

# **Treatment of Electronic Correlation in Magnetic Materials within the Fluctuation-Exchange Method**

von

Andreas Gierlich

**Diplomarbeit in Physik**

vorgelegt der

**Fakultät für Mathematik, Informatik und Naturwissenschaften**  
der Rheinisch-Westfälischen Technischen Hochschule Aachen

im

März 2007

angefertigt am

Institut für Festkörperforschung (IFF)  
Forschungszentrum Jülich



# Contents

<b>1</b>	<b>Introduction</b>	<b>1</b>
<b>2</b>	<b>Density-Functional Theory</b>	<b>7</b>
2.1	The Many-Body Problem . . . . .	7
2.2	The Theorems of Hohenberg and Kohn . . . . .	9
2.3	The Kohn-Sham Equation . . . . .	11
2.4	LSDA and GGA . . . . .	14
2.5	Calculation of the Equilibrium Lattice Constant . . . . .	15
<b>3</b>	<b>The FLAPW Method</b>	<b>17</b>
3.1	Solving the Kohn-Sham Equation with the APW Method . . . . .	17
3.2	The LAPW Basis Functions . . . . .	19
3.3	The Concept of FLAPW . . . . .	21
3.4	The Muffin-Tin $a$ and $b$ Coefficients . . . . .	21
3.5	Construction of the Electron Density inside the Muffin Tins . . . . .	23
3.6	Tight-binding Approximation within the FLAPW Framework . . . . .	25
<b>4</b>	<b>Green Functions</b>	<b>31</b>
4.1	Definition and Properties of Green Functions . . . . .	31
4.2	Electron Density and Spectral Function . . . . .	34
4.3	Green Functions within the TB-FLAPW Approach . . . . .	36
4.4	Mathematical Tools . . . . .	39
<b>5</b>	<b>Many-Body Perturbation Theory</b>	<b>41</b>
5.1	The Multiband Hubbard Hamiltonian . . . . .	42
5.2	Green Functions in Perturbation Theory . . . . .	45
5.2.1	A Green Function for the Multiband Hubbard Hamiltonian . . . . .	45
5.2.2	The Self-Energy and the Quasi-Particle Picture . . . . .	48
5.3	The Language of Feynman Diagrams . . . . .	49
5.3.1	Vocabulary of the Diagrammatic Language . . . . .	50
5.3.2	Two-Particle Propagator and Self-Energy . . . . .	53
5.4	The FLEX Method . . . . .	55
5.4.1	Equations for the Vertex Function $\Gamma$ . . . . .	56
5.4.2	The Horizontal Ladder Approximation . . . . .	59
5.4.3	Determining the Self-Energy within FLEX . . . . .	63

<b>6</b>	<b>Dynamical Mean-Field Theory</b>	<b>67</b>
6.1	Solution of the Multiband Hubbard Model within DMFT . . . . .	68
6.2	The DMFT-FLEX Solver . . . . .	73
<b>7</b>	<b>Preparatory Calculations within DFT</b>	<b>79</b>
7.1	Convergence Tests for the Parameters of the LAPW Basis . . . . .	79
7.1.1	Determining $K_{\max}$ and $l_{\max}$ . . . . .	81
7.1.2	Converged Number of $\mathbf{k}$ Points . . . . .	85
7.1.3	The Choice of the Exchange-Correlation Potential . . . . .	86
7.2	Transformation from the LAPW to the TB-FLAPW Basis . . . . .	87
<b>8</b>	<b>Benchmark Calculations within GGA+DMFT for Fe, Co and Ni</b>	<b>93</b>
8.1	Calculations . . . . .	93
8.1.1	Density of States (DOS) . . . . .	94
8.1.2	Band Structure and Spectral Function . . . . .	95
8.1.3	Total Spin-Magnetic Moments . . . . .	99
8.2	Results for Nickel (Ni) . . . . .	99
8.3	Results for Cobalt (Co) . . . . .	108
8.4	Results for Iron (Fe) . . . . .	114
<b>9</b>	<b>Auger Spectra of Fe, Co and Ni</b>	<b>119</b>
9.1	The Physics of the Auger Process . . . . .	119
9.2	A Model for Auger Spectra . . . . .	121
9.3	Calculations and Results . . . . .	124
<b>10</b>	<b>Chromium – A Case Study of AFM within GGA+DMFT</b>	<b>129</b>
10.1	A Model for Chromium as Commensurate AFM . . . . .	129
10.2	Calculating Commensurate AFM within GGA+DMFT . . . . .	130
10.3	Results for Chromium . . . . .	133
<b>11</b>	<b>Conclusion and Outlook</b>	<b>141</b>
<b>12</b>	<b>Acknowledgments - Danksagung</b>	<b>147</b>
	<b>Bibliography</b>	<b>151</b>

# 1 Introduction

**The Motivation** Magnetic materials like the late  $3d$  transition metals iron, cobalt and nickel are the key ingredients in the design of a vast number of modern applications today. Magnetic separators and magnetic holders have become irreplaceable tools in numerous industrial production processes, magnetic sensors are widely used in many fields of research, in medicine magnetic materials are used e.g. for magnetic coupling in blood pumps, loudspeakers and small electric motors are part of our every day life. Permanent magnets used in modern applications are usually compounds such as AlNiCo or NyFeB with complex crystal and electronic structure. Hence, it seems a little bit odd, that we still lack a complete understanding and a thorough quantitative description of even the simplest magnetic elements namely the  $3d$  metals Fe, Co and Ni.

The discovery of the giant magneto resistance (GMT) by Grünberg [BGSZ89] and simultaneously by Fert [BBF<sup>+</sup>88] in 1988 renewed the interest to study magnetic materials and to investigate the mechanisms causing magnetic properties on a nano-scale as well. These studies were fueled over the last two decades by new observations like the first measurement of the tunneling magneto resistance (TMR) in 1995 by Moodera, Kinder *et al* [MKWM95] almost 20 years after its theoretical prediction by Julliere [Jul75]. However, the magnetic materials and the mechanisms causing magnetic properties are often described only qualitatively in model calculations relying strongly on empirical parameters for the description of realistic materials. To apply the nano-scale magnetism sufficiently in new areas like spintronics it is vital to also improve on the quantitative description of these materials. It is thus most desirable to develop *ab initio* methods describing such materials. An *ab initio* approach will not only yield a parameter-free description of the magnetic materials Fe, Co and Ni to be studied here. The predictive power of an *ab initio* method in the analysis of new materials exceeds by far the possibilities accessible by model calculations with empirical input. A deeper understanding of the underlying physics of these magnetic properties in general and of the mechanisms determining the electronic structure of these materials in particular can be obtained best from an *ab initio* approach.

In the last 40 years density-functional theory (DFT) has become the by far most successful *ab initio* approach to describe the electronic structure of solids. Properties of weakly correlated solids are described quantitatively well by DFT in its two most common forms the local-density (LDA) and the generalized gradient (GGA) approximation. Fe, Co and Ni, however, are example materials featuring intermediately correlated electrons due to their partially filled  $d$  bands. These bands are

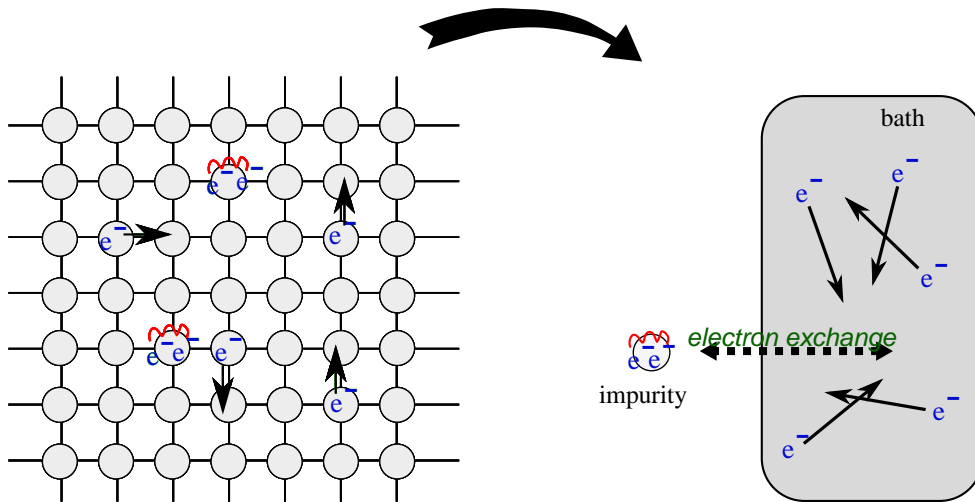
rather localized and narrow such that the electrons in these bands show signs of more atomic-like behavior as opposed to an itinerant character. Since LDA and GGA incorporate electronic correlation only rudimentarily, they fail to describe adequately the electronic structure of more correlated materials. For example, in Fe, Co and Ni the spin splitting is overestimated or the 6 eV satellite in nickel can not be obtained from calculations in LDA or GGA. Therefore, theoretical methods beyond DFT need to be deployed to properly describe the electronic structure of more correlated materials. In model calculations, the dynamical mean-field theory (DMFT) has already proved very successful in describing correlated electron systems. This gave rise to the idea to merge DFMT and DFT to combine the advantages from both methods: The predictive power of the *ab initio* approaches in DFT and the descriptive power of DMFT capturing true correlation effects.

The idea to combine LDA and DMFT in one LDA+DMFT method is less than a decade old and the method is in a stage of active development. It has already been applied successfully to various problems including electronic-structure calculations for  $\gamma$ -manganese [BDC<sup>+</sup>04] and  $\delta$ -Pu [PKL<sup>+</sup>06]. Most available implementations apply some drastic simplifications to the LDA+DFMT formalism, e.g. many codes are based on the atomic-sphere approximation in the LDA part like the approach by Lichtenstein *et al* [LK98]. Very recently, Grechnev *et al* reported on successfully combining DMFT with a full-potential LMTO-based LDA [GDMK<sup>+</sup>06]. Nevertheless, the LDA+DMFT method is at present the most universal technique for calculating the electronic structure of correlated solids.

**The Method** Dynamical mean-field theory (DMFT) is one of the most successful schemes developed over the past 18 years to treat electronic correlation. It evolved in the context of lattice models like the Hubbard model. An illustration of such a lattice model in two dimensions is given on the left side of figure 1.1. The electrons are assumed to be situated in the orbitals of the crystal atoms at each lattice site. They can move from an orbital on one site to an orbital at another site. For two electrons meeting on the same site the Coulomb repulsion between this pair of electrons, depicted by a red wiggly line in figure 1.1, yields an additional contribution to the total energy of the electronic system. In DMFT the lattice model is mapped onto an effective impurity problem consisting of a single correlated site in a self-consistent bath of non-interacting electrons. This mapping becomes exact in the limit of infinite lattice coordination. It is shown schematically in figure 1.1 how the two-dimensional lattice is mapped onto a single atom connected to a self-consistent bath. In the effective impurity model the movement of the electrons inside the bath is decoupled from the interaction between electrons taking place only at the impurity site. Consequently, spatial quantum fluctuations are frozen in the effective model. However, all local quantum fluctuations are completely retained since the single site can still exchange electrons with the surrounding self-consistent bath. Thus, all local correlation effects are fully accounted for within the framework of DMFT.

Although originally designed for model systems, DMFT can be merged with DFT

to study realistic materials in the *ab initio* context of LDA or GGA and include electron correlation into this context through DMFT. In this work a GGA is combined with DMFT and a new GGA+DMFT scheme is introduced. This is achieved by deriving a Hubbard-type lattice model from a tight-binding ansatz for the Kohn-Sham wave functions obtained from DFT calculation using the GGA. The model consists of two parts: a single-electron term describes the movement of the electrons between atomic orbitals and different lattice sites. This term can be completely determined from calculations in GGA. The second term of the Hubbard-type lattice model describes the interaction due to the Coulomb repulsion between two electrons meeting at the same lattice site. The resulting lattice model containing both the DFT description of a material and explicit interaction effects between the electrons can then be solved using DMFT. Within DMFT the model is first mapped onto an impurity model thus achieving the decoupling of the single-electron part and the interacting part of the model. The crucial point remaining is to solve the impurity problem self-consistently in other words a scheme to treat the local interaction processes has to be



**Lattice model.** Electrons are situated in the orbitals of the atoms on the lattice sites. They can move from site to site. If two electrons meet on the same site, the Coulomb repulsion between the electron pair symbolized by the red wiggles yields an additional contribution to the total energy of the electron system

**Effective impurity model.** The movement of the electrons in the bath is decoupled from the interaction between the electrons, because they can only interact at the single impurity site. Furthermore, local quantum fluctuations are retained due to the possibility of electron exchange between the impurity site and the bath.

**Figure 1.1:** Mapping of a two-dimensional lattice model onto a single-site impurity in a self-consistent bath.

found. The DMFT “solver” used in this thesis is the so-called fluctuation-exchange (FLEX) approach.

To find a description of the local interaction processes within FLEX, the many-electron problem must be restated first in terms of Green functions. The Green functions can be used in turn to derive a description of the interacting lattice electrons in terms of Feynman diagrams within many-body perturbation theory. The FLEX method is used to simplify this description of the lattice electrons and to derive expressions that can be solved within DMFT.

The FLEX method is an approximation scheme to select certain subclasses from all the diagrams describing the interacting lattice electrons. The diagrams in each subclass describe a certain many-body interaction process, namely the multiple scattering between two electrons, between an electron and a hole or between two holes. In addition to that, another subclass describing the screening of the Coulomb repulsion in a solid due to pair interaction is also taken into account. The diagrams of each subclass can be summed up to infinite order using geometric series yielding an analytic expression for each subclass of diagrams. If the FLEX method is deployed within the framework of DMFT, these analytic expressions are further simplified due to the mapping of the lattice electrons onto an impurity in a self-consistent bath, since interaction processes are restricted to the impurity site in the effective model. The mapping procedure therefore imposes a single-site approximation (SSA) on the diagrams describing the electronic interaction in the lattice system. The analytic expressions obtained from the summation over the diagrams of the lattice electrons can be solved in the SSA. The results are deployed in turn to derive a description of the self-consistent bath which is used then to derive a new solution for the lattice model. This scheme is iterated, until convergence is reached. Thus, the GGA+DMFT approach finally yields a description of realistic intermediately correlated electron systems.

The DMFT solver used in this work is based on a formulation of the FLEX approximation scheme as introduced by Babanov *et al* [BNSF71, BNSF73a, BNSF73b], which was extended for the present work to describe electronic systems with collinear spin structure. Other solvers derived from the FLEX approach as introduced by Bickers and Scalapino [BS89] have been developed by Lichtenstein *et al* presented in [KL99], [LK98] and by Lichtenstein, Katsnelson *et al* [LKK01]. In principle, DMFT solvers based e.g. on quantum Monte Carlo or exact diagonalization which should yield numerically exact solutions of the Hubbard-type lattice could also be used here. However, the exact diagonalization technique is limited by the exponential growth of the computations with the system size and the quantum Monte Carlo method is restricted to rather high temperatures by the minus-sign problem. Moreover, the diagrammatic approach using FLEX yields the advantage that the selected diagrams depict distinct physical processes. Describing the lattice electron systems in terms of these diagrams gives direct access to analyze the influence of the various interaction processes and to study their influence on the electronic correlation. This connection to the underlying physics of the interaction processes can be neither obtained from

---

quantum Monte Carlo nor from exact diagonalization techniques.

Alternative approaches to the GGA+DMFT method to derive an *ab initio* description of correlated electron systems have been proposed e.g. by Aryasetiawan [Ary92] describing the electronic structure of Ni with a combination of LDA and *GW*. Further progress has been made in this area recently, for example Biermann *et al* reported on the successful combination of *GW* with DMFT [BAG03] further discussed e.g. by Aryasetiawan [AIG<sup>+</sup>04]. However, the *GW* method also being a technique within diagrammatic perturbation theory fails to reproduce the 6eV Ni satellite because it only considers a subset of the diagrams covered by FLEX. It was shown by Springer, Aryasetiawan and Karlsson [SAK98] that inclusion of the *T*-matrix into this *GW* approach yields the satellite structure in the spectrum of Ni, but the *T*-matrix could not be included on an *ab initio* level. A recent presentation of first-principles *GW* calculations including the *T*-Matrix by Zhukov *et al* [ZCE04] document further progress in this area. As opposed to that, the *T*-matrix is contained in the FLEX method right from the start.

**The Structure** Finally I would like to give a brief overview on the structure of the thesis. Chapters 2 through 6 give an overview of the theoretical frameworks contained in GGA+DMFT and introduce the formalism of this method. Chapter 2 gives a brief introduction to DFT presenting the Kohn-Sham equations for collinear electronic systems, the GGA and the LSDA, the local spin-density approximation. Chapter 3 introduces the full-potential linearized augmented plane-wave (FLAPW) basis set used to solve the Kohn-Sham equations as well as the tight-binding (TB) FLAPW basis. Using the TB-FLAPW basis a Hubbard-type lattice model is derived. In chapter 4 Green-function approaches in electronic-structure calculations are discussed and a Green function for the lattice model within DFT is derived. Chapter 5 presents a Green-function approach for the Hubbard-type lattice model derived in chapter (3). Furthermore, the Feynman diagrams to describe the interacting electron problem are introduced and the FLEX approximation to select certain subclasses of diagrams is finally presented. The last chapter 6 of this theoretical introduction motivates the further treatment of the FLEX diagrams within DMFT and presents the iteration scheme to derive a self-consistent solution for interacting lattice electron systems within the GGA+DMFT approach. In the remaining chapters 7 through 10 I present my results of calculations carried out within the newly derived GGA+DMFT approach. In chapter 7 the calculations within DFT to obtain input data for the GGA+DMFT scheme are discussed focussing specifically on the choice of sensible input parameters for the DFT code FLEUR. Furthermore, the approximations necessary to derive the TB-FLAPW basis functions are discussed quantitatively. In chapter 8 benchmark calculations for Fe, Co and Ni within the GGA+DMFT are presented and compared with experimental data as well as DFT calculations. In the last two chapters some further applications of the GGA+DMFT method are presented. The application within the theory of Auger spectra is discussed and the Auger spectra of Fe, Co and Ni are calculated. An extension of

the GGA+DMFT scheme for the treatment of commensurate antiferromagnetism is presented in chapter 10. With the new scheme a case study for chrome with a commensurate antiferromagnetic structure was carried out and the results are presented in this chapter as well. I would like to summarize my results in the last chapter 11 and give a perspective of possible directions to be pursued in future work. It can be concluded that the GGA+DMFT method exhibits a high potential to gain further insight and a better understanding of the exciting field of many-body theory.

## 2 Density-Functional Theory

In condensed-matter physics one has to face the challenge to describe materials consisting of a vast number of particles (roughly  $10^{23} \text{ m}^{-3}$  in a solid). However, it is not only the sheer number of particles but rather the interplay between these particles, which makes it so difficult to find a description both accurate and feasible for these materials. Density-functional theory (DFT) provides means to achieve both feasibility and yet good agreement with experimental results in the theoretical study of many properties of such materials.

In this chapter I give a short introduction to DFT first stating the famous theorems of Hohenberg and Kohn, which represent the theoretical ground DFT was built upon. I will then derive the Kohn-Sham equation for spin-polarized systems. This equation is the mean-field DFT description of the many-body problem presented above, allowing for an approximate characterization of such systems with huge numbers of particles in terms of just one single electron. This will be the starting point for studying the magnetic materials in later chapters.

### 2.1 The Many-Body Problem

A non-relativistic description of a solid containing  $N_e$  electrons and  $N_A$  nuclei is given by the Schrödinger equation

$$\begin{aligned} \hat{H}_{\text{tot}} \Psi &= \left[ -\frac{\hbar^2}{2m} \sum_{i=1}^{N_e} \nabla_i^2 - \frac{\hbar^2}{2} \sum_{A=1}^{N_A} \frac{1}{M_A} \nabla_A^2 + \frac{e^2}{4\pi\epsilon_0} \sum_{i<j}^{N_e} \frac{1}{|\mathbf{r}_i - \mathbf{r}_j|} \right. \\ &\quad \left. + \frac{e^2}{4\pi\epsilon_0} \sum_{A<B}^{N_A} \frac{Z_A Z_B}{|\mathbf{R}_A - \mathbf{R}_B|} - \frac{e^2}{4\pi\epsilon_0} \sum_{i=1}^{N_e} \sum_{A=1}^{N_A} \frac{Z_A}{|\mathbf{R}_A - \mathbf{r}_i|} \right] \Psi \\ &= E_{\text{tot}} \Psi(\mathbf{r}_1, \dots, \mathbf{r}_{N_e}; \mathbf{R}_1, \dots, \mathbf{R}_{N_A}) \end{aligned} \quad (2.1)$$

with eigenfunctions  $\Psi$  and a total energy  $E_{\text{tot}}$ . The Schrödinger equation (2.1) captures both the kinetic energy of the electrons and nuclei within the first two terms and interactions between electrons with other electrons, nuclei with nuclei and finally between electrons and nuclei within the last three terms. The  $\{Z_A\}$  and  $\{M_A\}$  are the atomic numbers and the masses of the nuclei, the  $\{\mathbf{R}_A\}$  give the nuclei's positions,  $m$  denotes the mass of the electron while  $e$  is the elementary charge and the  $\{\mathbf{r}_i\}$  denote the positions of the electrons.

Throughout this thesis the SI units are used, thus  $\hbar$  denotes the Planck constant and  $\varepsilon_0$  is the dielectric constant of the vacuum. Furthermore, it should be mentioned that the description of non-relativistic effects was not included in the derivation of the equations in this introductory part to maintain a clear and transparent notation. In the calculations these effects were always accounted for. This is necessary since the FLAPW method I used here is an all-electron method and for the description of core electrons relativistic effects yield a contribution which is non-negligible.

Although equation (2.1) gives in principle an exact non-relativistic description of the particles and their interactions, it is of little use in practice. The many-particle eigenfunctions  $\Psi$  depend on the positions of all  $N_e \times N_A$  particles and in addition must be antisymmetrized to fulfill the Pauli principle. Due to the rapid increase of information contained in the eigenfunctions  $\Psi$  with respect to the number of particles, the amount of data get too large to be processed on a reasonable time scale for solid materials with a realistic number of particles.

In need to simplify equation (2.1) yet retain the important physics we shall first apply the Born-Oppenheimer approximation. Since the mass of the electron differs from the mass of a nucleus roughly by three to four orders of magnitude electrons respond almost instantaneously to changes in the positions of the atoms. Hence, the electrons approximately are in a stationary field of the nuclei at all times. Therefore, the nuclei may be considered to be classical particles and their positions  $\{\mathbf{R}_A\}$  can be taken as parameters that appear only in the potential of the electronic part of the Schrödinger equation. As a consequence of this approximation the ionic and electronic motion can be separated, electrons and nuclei can be considered as two independent systems and their behavior can be studied independently. Thus, for the rest of this thesis, the many-electron Schrödinger equation given by

$$\begin{aligned} \hat{H} \Psi_e &= \left[ -\frac{\hbar^2}{2m} \sum_{i=1}^{N_e} \nabla_i^2 + \frac{e^2}{4\pi\varepsilon_0} \sum_{i<j}^{N_e} \frac{1}{|\mathbf{r}_i - \mathbf{r}_j|} + \sum_{i=1}^{N_e} v_{\text{ext}}(\mathbf{r}_i) \right] \Psi_e \\ &= E \Psi_e(\mathbf{r}_1, \dots, \mathbf{r}_{N_e}) \end{aligned} \quad (2.2)$$

is the system to be discussed, where  $\Psi_e$  is the electronic wave functions and  $E$  is the total energy of the electronic system. The  $v_{\text{ext}}$  is the potential experienced by an electron in the field of all nuclei at positions  $\{\mathbf{R}_A\}$  with atomic numbers  $\{Z_A\}$

$$v_{\text{ext}}(\mathbf{r}) = -\frac{e^2}{4\pi\varepsilon_0} \sum_{A=1}^{N_A} \frac{Z_A}{|\mathbf{R}_A - \mathbf{r}|}. \quad (2.3)$$

Note that due to the Born-Oppenheimer approximation the  $\{\mathbf{R}_A\}$  are no longer variables but enter as parameters in  $v_{\text{ext}}(\mathbf{r})$ . This reduced description however still is too complex to be solved analytically or numerically for systems of relevant size.

In the 1920s Thomas and Fermi first came up with an alternative yet heuristic description of many-electron systems in terms of the electron density distribution  $n(\mathbf{r})$ . Formally, the electron density distribution (henceforth also referred to as electron

density or simply density) can be derived from the many-electron wave functions  $\Psi_e$  by

$$n(\mathbf{r}) = N_e \int \Psi_e(\mathbf{r}, \mathbf{r}_2, \dots, \mathbf{r}_{N_e}) \times \Psi_e^*(\mathbf{r}, \mathbf{r}_2, \dots, \mathbf{r}_{N_e}) d^3r_2 \dots d^3r_{N_e}. \quad (2.4)$$

It is assumed here that the many-electron wave functions are normalized to unity. Since electrons are indistinguishable it would make no difference whichever  $N_e - 1$  electron coordinates one chooses to integrate out.

The description of the many-electron problem in terms of the electron density yields the big advantage that one has to deal with  $N_e - 1$  less degrees of freedom compared to approaches dealing with the full many-electron wave function. But it took almost another 40 years until in 1964 Hohenberg and Kohn found a theoretical proof for their famous theorems [HK64] stating that the ground-state particle density  $n_0(\mathbf{r})$  is actually sufficient to uniquely determine the ground state properties of a many-electron system. That was the birth of density-functional theory.

## 2.2 The Theorems of Hohenberg and Kohn

According to the first theorem of Hohenberg and Kohn [HK64] the external potential  $v_{\text{ext}}(\mathbf{r}_i)$  in (2.2) is completely determined by the ground-state electron density  $n_0(\mathbf{r})$  (up to a trivial constant  $C$ ):

**Theorem 1.** (*existence theorem*)

*Let  $n_0(\mathbf{r})$  be the single-particle density of a non-degenerate ground state of an interacting electron system in an external potential  $v_{\text{ext}}(\mathbf{r})$  and let  $n'_0(\mathbf{r})$  correspond in the same manner to  $v'_{\text{ext}}(\mathbf{r})$ . Then  $n_0(\mathbf{r}) = n'_0(\mathbf{r})$  implies  $v_{\text{ext}}(\mathbf{r}) = v'_{\text{ext}}(\mathbf{r}) + C$ , where  $C$  is a constant.*

Hence, if the ground-state density is known, the external potential  $v_{\text{ext}}(\mathbf{r}_i)$  is implicitly determined. On the other hand the first and second term in the many-electron Hamiltonian depend only on the electrons' movements and interactions. Consequently, the knowledge of the ground-state density  $n_0(\mathbf{r})$  fixes the complete many-electron Hamiltonian,  $\hat{H} = \hat{H}[n_0(\mathbf{r})]$ .

If the ground-state electron density  $n_0(\mathbf{r})$  can be found without the help of the many-electron wave function  $\Psi_e$  in principle it is no longer necessary to find the many-electron wave function, because all ground-state characteristics of the system and in particular the total energy of the ground state can be calculated as functionals of the ground-state density. According to the second theorem of Hohenberg and Kohn this functional of the total energy can be used to determine the ground-state density without the knowledge of  $\Psi_e$ .

**Theorem 2.** (*variational principle*)

*The total energy functional  $E[n]$  of the  $N_e$ -electron system is minimized by*

*the ground-state electron density, if the trial densities  $n(\mathbf{r})$  are restricted by the conditions  $n(\mathbf{r}) \geq 0$  and  $\int n(\mathbf{r})d^3r = N_e$ .*

Thus, the determination of the ground-state electron density and the total energy becomes extremely simple compared to the problem of solving the  $3N_e$ -dimensional Schrödinger equation: the variation of the total-energy functional  $E[n]$  with respect to the electron density yields the ground-state electron density and consequently all other ground-state properties regardless of the number of particles involved. The only constraint is that the total number  $N_e$  of particles has to be kept constant. Hence, the search for a solution to the original problem (2.2) is greatly simplified. In practice, however, an explicit form for the functional of the total energy has yet to be found. Before deriving such an explicit form for the total-energy functional the electron's spin as additional degree of freedom of the electrons shall be included now. This spin-polarized formulation of the formalism will be used then throughout the whole thesis. It should be mentioned that inclusion of the spin is already an extension to the original formulation of the density-functional theory as introduced by Hohenberg and Kohn and Kohn and Sham [KS65]. This extension was first proposed by von Barth and Hedin [vBH72].

The spin of the electron has to be included to study the magnetization density of materials. In principle the magnetization density is a functional of the ground-state electron density like the total energy but like the functional of the total energy it is generally unknown. It could be quite difficult if not impossible to find this functional for the magnetization. All systems to be examined in this thesis have collinear structure that means the spin is oriented along one particular direction. The Hamiltonian of such systems is diagonal in the spin components of the wave function and can be solved independently for each spin component. Hence, the total electron density  $n(\mathbf{r})$  also becomes diagonal in spin space and can be split in a contribution of a spin-up density  $n_\uparrow(\mathbf{r})$  and a spin-down density  $n_\downarrow(\mathbf{r})$ . The functional of the total energy consequently becomes a functional of the spin-up and spin-down densities

$$n(\mathbf{r}) = n_\uparrow(\mathbf{r}) + n_\downarrow(\mathbf{r}), \quad E = E[n_\uparrow, n_\downarrow]. \quad (2.5)$$

Furthermore, the magnetization density  $m(\mathbf{r})$  can be calculated by simply evaluating the difference of the two spin densities

$$m(\mathbf{r}) = n_\uparrow(\mathbf{r}) - n_\downarrow(\mathbf{r}). \quad (2.6)$$

Thus, including the spin in the description of the system as an additional degree of freedom allows to examine the system's magnetization without knowledge of the respective functional. Therefore, the spin-polarized formulation of the DFT equations shall be used.

## 2.3 The Kohn-Sham Equation

In this section an explicit expression for the functional of the total energy in the form  $E[n_\uparrow, n_\downarrow]$  is derived. If  $|\Psi_e\rangle$  is an eigenstate of the many-electron Hamiltonian  $\hat{H}$  in equation (2.2), the total-energy functional can be written as

$$E[n_\uparrow, n_\downarrow] = T[n_\uparrow, n_\downarrow] + V_{ee}[n_\uparrow, n_\downarrow] + \int d^3r n(\mathbf{r}) v_{\text{ext}}(\mathbf{r}). \quad (2.7)$$

The first term on the right-hand side is the functional of the kinetic energy  $T$ , defined as

$$T[n_\uparrow, n_\downarrow] = -\frac{\hbar^2}{2m} \langle \Psi_e | \sum_i^{N_e} \nabla_i^2 | \Psi_e \rangle. \quad (2.8)$$

The second term contains the electron-electron interaction and can be written as

$$V_{ee}[n_\uparrow, n_\downarrow] = V_H[n_\uparrow, n_\downarrow] + W_{ee}[n_\uparrow, n_\downarrow]. \quad (2.9)$$

The first functional  $V_H[n_\uparrow, n_\downarrow]$  describes the classical Coulomb repulsion, which is identical with the term for direct electron-electron interaction in Hartree approximation

$$V_H[n_\uparrow, n_\downarrow] = \frac{1}{2} \frac{e^2}{4\pi\epsilon_0} \int \frac{n(\mathbf{r})n(\mathbf{r}')}{|\mathbf{r} - \mathbf{r}'|} d^3r d^3r'. \quad (2.10)$$

The functional  $W_{ee}[n_\uparrow, n_\downarrow]$  captures all remaining contributions to the electron interaction, which are of quantum mechanical origin.

Writing down expression (2.7) for the energy functional might have brought some clarity, but the functionals  $T[n_\uparrow, n_\downarrow]$  and  $W_{ee}[n_\uparrow, n_\downarrow]$  are only defined implicitly by means of the existence theorem. Explicit expressions for these functionals have yet to be found to calculate  $E[n_\uparrow, n_\downarrow]$  using (2.7).

Kohn and Sham suggested the existence of a non-interacting reference system [KS65] with the Hamiltonian

$$\hat{H}_\sigma^s = \sum_{i=1}^{N_e} \left[ -\frac{\hbar^2}{2m} \nabla_i^2 + v_\sigma^s(\mathbf{r}_i) \right] \quad (2.11)$$

in which there are no electron-electron repulsion terms, and for which the ground-state density is exactly identical to that of the real system. For this system there will be an exact determinantal ground-state wave function

$$\Psi_\sigma^s = \frac{1}{\sqrt{N_e!}} \det[\psi_{1\sigma}^s \psi_{2\sigma}^s \dots \psi_{N_e\sigma}^s] \quad (2.12)$$

where the  $\psi_{i\sigma}^s$  are the  $N_e$  lowest eigenfunctions of the one-electron Hamiltonian  $\hat{h}_\sigma^s$

$$\hat{h}_\sigma^s \psi_{i\sigma}^s = \left[ -\frac{\hbar^2}{2m} \nabla_i^2 + v_\sigma^s(\mathbf{r}_i) \right] \psi_{i\sigma}^s = \epsilon_{i\sigma} \psi_{i\sigma}^s. \quad (2.13)$$

The corresponding single-particle density is then given by

$$n_\sigma(\mathbf{r}) = \sum_{i=1}^{N_e} |\psi_{i\sigma}^s(\mathbf{r})|^2 \quad (2.14)$$

and the kinetic energy functional is

$$T^s[n_\uparrow, n_\downarrow] = -\frac{\hbar^2}{2m} \sum_{\sigma \in \{\uparrow, \downarrow\}} \sum_i \langle \psi_{i\sigma}^s | \nabla_i^2 | \psi_{i\sigma}^s \rangle. \quad (2.15)$$

The kinetic energy functional  $T^s[n_\uparrow, n_\downarrow]$  could be calculated straightforwardly once the eigenfunctions  $\psi_{i\sigma}^s$  are known. Although it is in principle not difficult to solve for the eigenfunctions of a one-electron problem such as (2.13), so far we do not know the explicit form of the potential  $v_\sigma^s(\mathbf{r}_i)$ . Furthermore, upon comparing the expression (2.15) for  $T^s[n_\uparrow, n_\downarrow]$  with (2.8) defining the actual kinetic energy functional  $T[n_\uparrow, n_\downarrow]$  to be calculated, one can see that they are not identical.

Kohn and Sham solved the latter problem in such a way that they used a separation other than (2.7) with  $T[n_\uparrow, n_\downarrow]$  replaced by  $T^s[n_\uparrow, n_\downarrow]$ . Then, they introduced the so-called exchange-correlation energy functional  $E_{xc}[n_\uparrow, n_\downarrow]$  by

$$E_{xc}[n_\uparrow, n_\downarrow] = T[n_\uparrow, n_\downarrow] - T^s[n_\uparrow, n_\downarrow] + W_{ee}[n_\uparrow, n_\downarrow]. \quad (2.16)$$

The functional  $E_{xc}[n_\uparrow, n_\downarrow]$  thus accounts for the difference in the functionals for the kinetic energy and also includes the still unknown functional  $W_{ee}$ . This can be seen directly, if the total energy functional (2.7) is expressed in terms of  $T^s[n_\uparrow, n_\downarrow]$  and  $E_{xc}[n_\uparrow, n_\downarrow]$

$$E[n_\uparrow, n_\downarrow] = T^s[n_\uparrow, n_\downarrow] + V_H[n_\uparrow, n_\downarrow] + \int d^3r n(\mathbf{r}) v_{\text{ext}}(\mathbf{r}) + E_{xc}[n_\uparrow, n_\downarrow]. \quad (2.17)$$

This form of the total-energy functional is now used to construct the potential of the reference system by applying the variational principle

$$\begin{aligned} \frac{\delta E[n_\uparrow, n_\downarrow]}{\delta n_\sigma(\mathbf{r})} &= \frac{\delta}{\delta n_\sigma(\mathbf{r})} \left[ \mu N_e - \mu \int n(\mathbf{r}) d^3r \right] \\ \Leftrightarrow v_{\text{ext}}(\mathbf{r}) + \frac{\delta T^s[n_\uparrow, n_\downarrow]}{\delta n_\sigma(\mathbf{r})} + \frac{e^2}{4\pi\epsilon_0} \int \frac{n(\mathbf{r}')}{|\mathbf{r} - \mathbf{r}'|} d^3r' + \frac{\delta E_{xc}[n_\uparrow, n_\downarrow]}{\delta n_\sigma(\mathbf{r})} &= -\mu. \end{aligned} \quad (2.18)$$

For the variation, the Lagrange parameter  $\mu$  was introduced to take into account the constraint from the second theorem of Hohenberg and Kohn that the number of particles in the system is to be conserved. Now, we compare expression (2.18) with the following equation for the system of non-interacting electrons moving in some effective potential named  $v_\sigma^{\text{eff}}(\mathbf{r})$

$$\frac{\delta E[n_\uparrow, n_\downarrow]}{\delta n_\sigma(\mathbf{r})} = v_\sigma^{\text{eff}}(\mathbf{r}) + \frac{\delta T^s[n_\uparrow, n_\downarrow]}{\delta n_\sigma(\mathbf{r})}. \quad (2.19)$$

The two mathematical problems are obviously identical provided that

$$v_{\sigma}^{\text{eff}}(\mathbf{r}) = v_{\text{ext}}(\mathbf{r}) + \frac{e^2}{4\pi\epsilon_0} \int \frac{n(\mathbf{r}')}{|\mathbf{r} - \mathbf{r}'|} d^3r' + \frac{\delta E_{\text{xc}}[n_{\uparrow}, n_{\downarrow}]}{\delta n_{\sigma}(\mathbf{r})}. \quad (2.20)$$

Thus, the electron density satisfying (2.18) can be obtained by solving a one-electron Schrödinger-type equation corresponding to non-interacting electrons moving in the potential  $v_{\sigma}^{\text{eff}}(\mathbf{r})$ .

$$\hat{h}_{\sigma}^{\text{eff}} \varphi_{i\sigma} = \left[ -\frac{\hbar^2}{2m} \nabla_i^2 + v_{\sigma}^{\text{eff}}(\mathbf{r}_i) \right] \varphi_{i\sigma} = \epsilon_{i\sigma} \varphi_{i\sigma}. \quad (2.21)$$

such that

$$n_{\sigma}(\mathbf{r}) = \sum_i^{\text{occ}} |\varphi_{i\sigma}(\mathbf{r})|^2 \quad (2.22)$$

where the sum runs over the lowest occupied electron states of the given spin direction. Formula (2.21) is the famous Kohn-Sham equation, the functions  $\varphi_{i\sigma}$  and the parameters  $\epsilon_{i\sigma}$  are called the Kohn-Sham eigenfunctions and Kohn-Sham eigenvalues respectively.

The many-electron problem (2.2) was thus boiled down to the solution of the Kohn-Sham equation. It has to be kept in mind though that equation (2.21) itself does not give a description of the physical system. It was derived from the variational principle for the reference system consisting of non-interacting particles which is a purely artificial construction. Despite the resemblance to a Schrödinger equation the functions  $\varphi_{i\sigma}$  thus are artificial quantities and have nothing to do with the wavefunction of the physical system. This holds true as well for the Kohn-Sham eigenvalues  $\epsilon_{i\sigma}$ . They were introduced as Lagrange parameters to solve the eigenvalue problem and have no physical meaning *a priori*. Nevertheless, in practice the  $\epsilon_{i\sigma}$  are often taken as excitation energies because comparison with experimental data showed that they are in good agreement with the energies found in experiments for many materials. But there is no theoretical link that the  $\epsilon_{i\sigma}$  are the excitation energies, they are interpreted as such. The eigenfunctions  $\varphi_{i\sigma}$  are interpreted as physical wave functions as well without any theoretical justification. The only quantity directly related to the physical system (2.2) is the ground-state spin-density  $n_{\sigma}(\mathbf{r})$ , which is constructed according to (2.22). This is due to the fact that the effective potential  $v_{\sigma}^{\text{eff}}$  was chosen precisely in such a way that the reference system yields the same ground-state spin-densities as the physical system.

Since the effective potential itself depends on the density, equations (2.21) and (2.22) have to be solved self consistently, which can be achieved by iteration. Usually starting densities for spin up and spin down are constructed using atomic-like orbitals, the effective potential is constructed and then (2.21) is solved with this potential. The resulting wave functions are then used to construct new densities and the whole procedure is repeated until the new densities equal the previous ones. The only remaining question now is how to construct the exchange-correlation functional.

## 2.4 Local-Spin-Density Approximation and Generalized Gradient Approximation

The effective potential  $v_\sigma^{\text{eff}}$  was defined as

$$v_\sigma^{\text{eff}}(\mathbf{r}) = v_{\text{ext}}(\mathbf{r}) + \frac{e^2}{4\pi\epsilon_0} \int \frac{n(\mathbf{r}')}{|\mathbf{r} - \mathbf{r}'|} d^3r' + \frac{\delta E_{\text{xc}}[n_\uparrow, n_\downarrow]}{\delta n_\sigma(\mathbf{r})}. \quad (\text{see 2.20})$$

The so-called exchange-correlation potential is defined from this expression as

$$v_\sigma^{\text{xc}}(\mathbf{r}) = \frac{\delta E_{\text{xc}}[n_\uparrow, n_\downarrow]}{\delta n_\sigma(\mathbf{r})} \quad (2.23)$$

All terms in the definition of  $v_\sigma^{\text{eff}}$  are known except for the exchange-correlation potential. It originates from the difference in the kinetic energy of the physical and the reference system and additionally accounts for all electron correlation effects beyond the Hartree term. The possible correlation effects are numerous, often depending on the specifics of the physical system. There is no procedure yet to account for all of them explicitly. However, approximations for  $E_{\text{xc}}[n_\uparrow, n_\downarrow]$  and  $v_\sigma^{\text{xc}}$  have been derived that are both simple and accurate enough such that finally a feasible description for the many-electron system is obtained. Below the two most common approximation used to determine  $E_{\text{xc}}[n_\uparrow, n_\downarrow]$  are presented.

Within the local-spin-density approximation (LSDA) the exact functional  $E_{\text{xc}}[n_\uparrow, n_\downarrow]$  for the exchange-correlation energy is replaced by

$$E_{\text{xc}}^{\text{LSDA}}[n_\uparrow, n_\downarrow] = \int n(\mathbf{r}) \epsilon_{\text{xc}}^{\text{LSDA}}(n_\uparrow(\mathbf{r}), n_\downarrow(\mathbf{r})) d^3r. \quad (2.24)$$

The idea leading to this approximation is to express  $E_{\text{xc}}[n_\uparrow, n_\downarrow]$  by the exchange-correlation energy of a homogeneous electron gas for which (2.24) becomes exact and can be determined numerically. The energy functional  $E_{\text{xc}}[n_\uparrow, n_\downarrow]$  of electronic systems with small deviations in the electron density are thus described by (2.24) in good approximation by calculating  $\epsilon_{\text{xc}}^{\text{LSDA}}(n_\uparrow(\mathbf{r}), n_\downarrow(\mathbf{r}))$  as a function (not a functional!) of the spin-densities of the system in question. The idea was originally proposed for non-spin-polarized systems by Kohn and Sham [KS65] and was generalized to describe systems with collinear structure by von Barth and Hedin [vBH72] and Pant and Rajagopal [PR72].

For systems with larger inhomogeneity, the integrand in (2.24) can also be replaced by a function of the spin-densities and its gradient

$$E_{\text{xc}}[n_\uparrow, n_\downarrow] \approx \int f(n_\uparrow(\mathbf{r}), n_\downarrow(\mathbf{r}), \nabla n_\uparrow(\mathbf{r}), \nabla n_\downarrow(\mathbf{r})) d^3r. \quad (2.25)$$

Whereas the function  $\epsilon_{\text{xc}}^{\text{LSDA}}$  in LSDA is derived upon a physical picture, the function  $f$  is not uniquely defined. Many different forms have been suggested for  $f$  based on

i.e. numerical fitting of experimental data or derived using general properties known for  $E_{xc}[n_\uparrow, n_\downarrow]$ . A widely accepted approach is the so-called generalized gradient approximation (GGA) suggested by Langreth *et al.* [LP80] and further developed i.e. by Perdew [Per85].

In this thesis, calculations were done using both LSDA and GGA. For the LSDA part an expression for  $\epsilon_{xc}^{\text{LSDA}}$  derived by Perdew and Zunger [PZ81] was used, which is a parametrization of a numerical simulation for  $\epsilon_{xc}^{\text{LSDA}}$  for the homogeneous electron gas by Ceperley and Alder [CA80] using the Quantum Monte Carlo method. Within GGA I compared two parametrizations of  $f$ , the first being derived from the same Monte Carlo simulations in 1992 by Perdew and Wang [PW92] and the second one being an improvement upon this parametrization published in 1996 by Perdew, Burke and Ernzerhof [PBE96].

## 2.5 Calculation of the Equilibrium Lattice Constant

In the previous sections a procedure was derived to approximately calculate the total-energy functional  $E[n_\uparrow, n_\downarrow]$ , that is used in turn to calculate the ground-state spin densities. The functional  $E[n_\uparrow, n_\downarrow]$  was introduced in (2.5) as the functional of the total energy of the electron system, which was derived from the combined description of the electronic and lattice system (2.1) by applying the Born-Oppenheimer approximation.

From this combined description (2.1) for the electronic and the lattice system, we would like to retrieve the term of the Coulomb interaction between the nuclei, which was given by

$$E_n[\{\mathbf{R}\}] = \frac{e^2}{4\pi\epsilon_0} \sum_{A<B}^{N_a} \frac{Z_A Z_B}{|\mathbf{R}_A - \mathbf{R}_B|}. \quad (2.26)$$

Combining this term with the energy functional  $E[n_\uparrow, n_\downarrow]$  a new energy functional  $\tilde{E}[n_\uparrow, n_\downarrow, \{\mathbf{R}\}]$  can be defined by

$$\tilde{E}[n_\uparrow, n_\downarrow, \{\mathbf{R}\}] = E[n_\uparrow, n_\downarrow] + E_n[\{\mathbf{R}\}]. \quad (2.27)$$

While the positions of the nuclei  $\{\mathbf{R}_A\}$  constituting the materials' lattice only enter as parameters in the former functional  $E[n_\uparrow, n_\downarrow]$ , they enter the new functional  $\tilde{E}[n_\uparrow, n_\downarrow, \{\mathbf{R}\}]$  as variables because of the term (2.26). If the variational principle is now applied to the new functional with respect to the nuclei's positions, the functional's value will be minimal for an atomic distance, that equals the equilibrium lattice constant of the material.



# 3 The FLAPW Method

The FLAPW method is a widely used *ab initio* technique to analyze various aspects of the electronic structure of materials on the footing of density-functional theory. The abbreviation FLAPW stands for full-potential linearized augmented plane wave which corresponds to a list of the key points of this method: in the setup of the eigenvalue problem the potential of the lattice atoms is taken into account without any approximations regarding its shape or asymptotic behavior. The basis set used then to represent the Kohn-Sham eigenfunctions consists of linearized augmented plane waves.

The FLAPW method can be applied to a huge variety of different classes of materials in many different ways (e.g. in order to calculate band structures, total energies etc.). In this thesis the FLAPW method is used solely to solve the Kohn-Sham equation presented in section 2.3 and to derive a new tight-binding-like basis set. Therefore it is not intended to present a thorough derivation of the full FLAPW method in this section, but merely to introduce those parts necessary to successfully apply the FLAPW method in the present context. Some key aspects of the predecessors of FLAPW, the APW and the LAPW methods, are discussed briefly focusing mainly on the introduction of the LAPW-basis set. A short description of the extension needed to derive the FLAPW method from the LAPW method is given afterwards. In the remainder of this section some details of the LAPW basis set are examined and the tight-binding like basis set within the framework of FLAPW is derived.

The contribution of many different authors finally led to what is presented here as FLAPW method and some of them shall be explicitly mentioned during the derivation in the following sections. In addition to that I would like to refer the interested reader to a detailed introductory article on FLAPW by Blügel and Bihlmayer in [BB06] and a book by David Singh [Sin94] where a detailed discussion of the LAPW method can be found.

## 3.1 Solving the Kohn-Sham Equation with the APW Method

There are numerous ways to solve eigenvalue problems like the Kohn-Sham equation. One widely used method is to expand the eigenfunctions  $\psi_{\mathbf{k},\nu}^{\sigma}(\mathbf{r})$  with Bloch vector  $\mathbf{k}$ , band index  $\nu$  and spin  $\sigma$  using some known set of basis functions  $\varphi_{\mathbf{G}}^{\sigma}(\mathbf{k}, \mathbf{r})$  that

satisfy the Bloch boundary conditions.

$$\psi_{\mathbf{k},\nu}^{\sigma}(\mathbf{r}) = \sum_{\mathbf{G}} c_{\mathbf{k},\nu}^{\mathbf{G}\sigma} \varphi_{\mathbf{G}}^{\sigma}(\mathbf{k}, \mathbf{r}). \quad (3.1)$$

Here  $\mathbf{G}$  are all reciprocal lattice vectors up to the largest value  $K_{\max}$  and  $c_{\mathbf{k},\nu}^{\mathbf{G}\sigma}$  are variational coefficients. For the sake of simplicity, the index  $\sigma$  is dropped from now on.

Naively thinking, one would assume that it is best to use plane waves as basis functions, because these functions are orthogonal, diagonal in momentum space and can be implemented easily due to their simplicity. However, the wave functions vary rapidly in the vicinity of the nuclei because of the singularity of the crystal potential at the ionic positions. Thus, the cut-off  $K_{\max}$  would need to be huge to accurately represent the wave functions and convergence would be very slow. One way to remove this deficiency is to use pseudo potentials that do not diverge at the nuclei's positions. This is usually done in practice, if plane waves are used as basis set. However, an accurate description of electrons that are more localized in the vicinity of the nuclei e.g. electrons in  $d$  and  $f$  orbitals still requires many plane waves, which makes the usage of pseudo potentials computationally demanding. Therefore we resign to another approach based on an idea from Slater [Sla37]. The corresponding technique is called the augmented plane wave method (APW).

Within the APW approach the plane waves are augmented in the region around the nuclei by another set of functions. In order to do so, space is divided into two regions: the so-called muffin-tin spheres situated around each nucleus and the remaining space between those spheres, which is called the interstitial region. The muffin tins are chosen such that they nearly touch to cover as much space as possible but to allow still for structural relaxations. The potential  $V(\mathbf{r}) = v_{\sigma}^{\text{eff}}(\mathbf{r})$  in the Hamiltonian of the Kohn-Sham equation (2.21) is then thought to be spherically symmetric inside the muffin tins and set to be constant in the interstitial region

$$V(\mathbf{r}) \approx \begin{cases} V_{\text{IS}}^0 = \text{const} & \text{interstitial region} \\ V_{\text{MT}}^0(r^{\mu}) & \text{muffin - tin } \mu \end{cases}. \quad (3.2)$$

In the interstitial region the Schrödinger equation is solved by plane waves since the potential is kept constant there. These plane waves are then augmented inside the muffin tins by first applying the Rayleigh decomposition of the plane waves inside each muffin tin

$$e^{i\mathbf{K}\mathbf{r}} = 4\pi \sum_L i^l j_l(rK) Y_L^*(\hat{\mathbf{K}}) Y_L(\hat{\mathbf{r}}), \quad (3.3)$$

where  $r = |\mathbf{r}|$ ,  $K = |\mathbf{K}|$  and  $\mathbf{K}$  abbreviates  $(\mathbf{G} + \mathbf{k})$  and then by replacing the Bessel functions  $j_l(Kr)$  by the radial functions  $u_l$ , which are solutions to the radial Schrödinger-like equations obtained for the radial potential  $V_{\text{MT}}^0(r^{\mu})$  inside each muffin tin

$$\left\{ -\frac{\hbar^2}{2m} \frac{\partial^2}{\partial r^{\mu 2}} + \frac{\hbar^2}{2m} \frac{l(l+1)}{r^{\mu 2}} + V_{\text{MT}}^0(r^{\mu}) - E \right\} r^{\mu} u_l(r^{\mu}, E) = 0. \quad (3.4)$$

The position  $\mathbf{r}^\mu$  inside the sphere  $\mu$  is given with respect to the center of each sphere, which is located at position  $\boldsymbol{\tau}^\mu$  in the unit cell. The  $l$  is interpreted as the quantum number of the regular solution  $u_l$  to the energy parameter  $E$  and  $L = (l, m)$  is introduced as a combined index for the quantum numbers  $l$  and  $m$ . Hence, the APW basis set is given by

$$\varphi_{\mathbf{G}}(\mathbf{k}, \mathbf{r}) = \begin{cases} \exp[i(\mathbf{k} + \mathbf{G}) \cdot \mathbf{r}] & \text{interstitial region} \\ \sum_L \tilde{A}_L^{\mu\mathbf{G}}(\mathbf{k}) u_l(r^\mu, E) Y_L(\hat{\mathbf{r}}^\mu) & \text{muffin-tin } \mu \end{cases} . \quad (3.5)$$

The coefficients  $\tilde{A}_L^{\mu\mathbf{G}}(\mathbf{k})$  are determined from the requirement that the wave functions have to be continuous at the boundary of the muffin-tin spheres.

The Hamiltonian in the Kohn-Sham equation (2.21) can now be set up in terms of this basis. This would lead to a standard secular problem if the energy  $E$  is kept fixed and only used as a parameter during the construction of the basis. However, the resulting APW basis set does not offer enough variational freedom if  $E$  is kept fixed. An accurate description can only be obtained if the energies are set to the corresponding band energies  $\epsilon_{\mathbf{k},\nu}$ . In this case however, the radial solutions  $u_l$  are functions of the band energies, the Hamiltonian matrix would as well depend on the  $\epsilon_{\mathbf{k},\nu}$  and can thus no longer be determined by a simple diagonalization. The solution of the secular equation becomes a non-linear problem which is computationally much more demanding than a secular problem. In addition to that, the APW method has some further drawbacks such as the asymptote problem can appear, that is, the radial function  $u_l$  is decoupled from the plane wave if  $u_l$  becomes zero at the sphere's boundary. These problems led to the suggestion of a linearization for the radial function thus giving rise to the LAPWs, the linearized augmented plane waves.

## 3.2 The LAPW Basis Functions

In the middle of the seventies linearized methods were invented by Andersen [And75], Koelling and Arbman [KA75] to treat the energy dependence of the augmented plane waves. Based on an idea of Marcus [Mar67] the energy-dependent radial basis functions of the APW basis are expanded using a Taylor series up to the first order

$$u_l(r^\mu, E) = u_l(r^\mu, E_l) + (E - E_l)\dot{u}_l(r^\mu, E_l) + \mathcal{O}((E - E_l)^2) . \quad (3.6)$$

The function  $\dot{u}_l$  denotes the energy derivative  $\dot{u}_l(r^\mu, E) = \partial u_l(r^\mu, E)/\partial E$  of  $u_l$  and  $\mathcal{O}((E - E_l)^2)$  contains all terms that are at least quadratic in the energy difference. The functions  $u_l$  of the APW basis are then replaced by  $u_l(E_l)$  and its energy derivative  $\dot{u}_l(E_l)$  but both evaluated at fixed energies  $E_l$ . Due to this linearization in the

energies the LAPW basis set is derived as

$$\varphi_{\mathbf{G}}(\mathbf{k}, \mathbf{r}) = \begin{cases} \exp[i(\mathbf{k} + \mathbf{G}) \cdot \mathbf{r}] & \text{interstitial region} \\ \sum_L (a_L^{\mu\mathbf{G}}(\mathbf{k}) u_l(r^\mu) + b_L^{\mu\mathbf{G}}(\mathbf{k}) \dot{u}_l(r^\mu)) Y_L(\hat{\mathbf{r}}^\mu) & \text{muffin-tin } \mu \end{cases} \quad (3.7)$$

The coefficients  $a_L^{\mu\mathbf{G}}(\mathbf{k})$  and  $b_L^{\mu\mathbf{G}}(\mathbf{k})$  are chosen such that the plane waves in the interstitial region are matched to the radial solution  $u_l$  as well as its derivative  $\dot{u}_l$  at the sphere's boundary. Since these coefficients play an important role, they are to be discussed in further detail in section 3.4. Some properties of the LAPW basis are discussed below.

Due to the approximation of the full energy-dependent radial functions by  $u_l(E_l)$  and  $\dot{u}_l(E_l)$ , the wave functions are affected by an error which is quadratic in the deviation of the energy parameter  $E_l$  from the energy  $E$ . However, the error enters in the eigenvalues itself only to fourth order. Consequently, spectra of the eigenvalues obtained from LDA calculations using the LAPW basis set are in quite good agreement with those results obtained from calculations using APWs especially since the energy parameters  $E_l$  are usually chosen to minimize the linearization error, i.e. in the center of gravity of the  $l$ -like bands. But most importantly the energy linearization removes the energy dependence of the Hamiltonian thus simplifying the eigenvalue problem to a standard problem of linear algebra. Thus, one of the major drawbacks of the APW method is removed. Furthermore, the LAPW method can be extended to non-spherical muffin-tin potentials with little difficulty, leading to the full-potential linearized augmented plane wave method (FLAPW). This will be discussed in the next section. Finally, it is worth mentioning that due to the linear combination of the  $u_l$  and  $\dot{u}_l$  in the muffin-tin regions also the asymptote problem from the APW method is removed, since in general the radial derivative and  $\dot{u}_l$  will be non-zero at the sphere's boundary even if the  $u_l$  happen to be zero there.

The energy derivative  $\dot{u}_l$  can be obtained evaluating the energy derivative of the radial Schrödinger equation (3.4) at the fixed energy  $E_l$ . If  $H_{\text{sp}}^\mu$  denotes the spherical Hamiltonian in equation (3.4) for muffin tin  $\mu$ , the energy derivative of the equation evaluated at the energy  $E_l$  is given by

$$H_{\text{sp}}^\mu \dot{u}_l^\mu = E_l \dot{u}_l^\mu + u_l^\mu. \quad (3.8)$$

The radial functions are usually normalized to 1 inside the muffin-tin spheres,

$$\int_0^{R_{\text{MT}}^\mu} r^2 (u_l^\mu)^2 dr = 1. \quad (3.9)$$

It can be shown using (3.8) and (3.9) that the energy derivatives  $\dot{u}_l$  are orthogonal to the radial functions, i.e.

$$\int_0^{R_{\text{MT}}^\mu} r^2 u_l^\mu \dot{u}_l^\mu dr = 0. \quad (3.10)$$

These relations will be useful when the LAPW basis set is applied later on.

### 3.3 The Concept of FLAPW

Within the full-potential LAPW-method (FLAPW) all shape-approximations to the potential are dropped and the potential is described in a realistic manner. This became possible with the development of a technique that allows to determine the Coulomb potential for a general periodic charge density without shape-approximations.

In the APW method the following approximation for the potential  $V(\mathbf{r})$  was used

$$V(\mathbf{r}) \approx \begin{cases} V_{\text{IS}}^0 = \text{const} & \text{interstitial region} \\ V_{\text{MT}}^0(r^\mu) & \text{muffin-tin } \mu \end{cases} . \quad (\text{see 3.2})$$

In the FLAPW method the constant interstitial potential  $V_{\text{IS}}^0$  is relaxed due to inclusion of a warped interstitial  $\sum_{\mathbf{G}} V_{\text{IS}}^{\mathbf{G}} e^{i\mathbf{G}\mathbf{r}}$  and inside the muffin-tin spheres the potential  $V_{\text{MT}}^0(r^\mu)$  is generalized by including non-spherical terms. The potential is then given by

$$V(\mathbf{r}) = \begin{cases} \sum_{\mathbf{G}} V_{\text{IS}}^{\mathbf{G}} e^{i\mathbf{G}\mathbf{r}} & \text{interstitial region} \\ \sum_L V_{\text{MT}}^L(r^\mu) Y_L(\hat{\mathbf{r}}^\mu) & \text{muffin-tin } \mu \end{cases} . \quad (3.11)$$

The electron density  $n(\mathbf{r})$  can be written similarly to equation (3.11) just by replacing all potentials  $V$  by densities  $n$ .

### 3.4 The Muffin-Tin a and b Coefficients

The  $a$  and  $b$  coefficients of the LAPW basis set 3.7 shall be derived in this section. They are constructed not only to meet the requirement of matching at the sphere boundaries. In addition the symmetry of the problem shall be exploited during the derivation. This leads to a quite elegant result saving memory and computer time however making the derivation a little more complicated.

The symmetry is exploited by mapping atoms, which are symmetry equivalent, onto each other by a space-group operation  $\{\Lambda|\mathbf{t}\}$ , where  $\Lambda$  is a rotational matrix and  $\mathbf{t}$  is a translation in space. The group of atoms that can be mapped onto each other by such an operation is called an atom type and can be represented by just one atom and the respective symmetry operations. For example, let  $\{\Lambda^\mu|\mathbf{t}^\mu\}$  be the operation mapping the atom surrounded by the muffin tin  $\mu$  onto its representative  $\alpha$ . The atom in  $\mu$  is assigned a local coordinate frame  $S^\mu$  with its origin situated at the atoms position given by  $\tau^\mu$  inside the unit cell. The local frame is chosen such that the unit vectors of this frame are mapped onto those of the global frame denoted by  $S^g$  using a symmetry operation  $\Lambda^g$  ( $\Lambda^g S^\mu = S^g$ ). For simplicity, we assume that the local frame  $S^\alpha$  of the representative atom  $\alpha$  is only translated with respect to the global frame  $S^g$ . Hence, the translation  $\mathbf{t}^\mu$  together with the rotation  $\Lambda^\mu$  maps  $S^\mu$  onto  $S^\alpha$  and by assumption it is  $\Lambda^\mu = \Lambda^g$ . If the potential (and other

quantities) inside the muffin tins are written in terms of the local coordinate systems, we find that  $V_{MT^\alpha}(\mathbf{r}^\alpha) = V_{MT^\mu}(\mathbf{r}^\mu)$ , where  $\mathbf{r}^\alpha$  and  $\mathbf{r}^\mu$  are expanded in terms of the local frames  $S^\alpha$  and  $S^\mu$  respectively. Consequently the radial functions  $u_l(r^\alpha)$  are the same for all atoms of the same type and must only be calculated once for the representative of each atom type.

This mapping procedure must now be incorporated in the derivation of the  $a$  and  $b$  coefficients. They ought to be chosen such that the solutions for the interstitial regions and the muffin tins match smoothly at the sphere's boundary. Again, the Rayleigh expansion 3.3 is used to decompose the plane waves into radial Bessel functions and spherical harmonics. If we look at the plane wave from the local frame of the atom  $\mu$ , the position  $\tau^\mu$  of the atom as well as  $\mathbf{K}$  are rotated by the symmetry operation  $\Lambda^\mu$ . Furthermore, the vector  $\mathbf{r}$  must be shifted since the origin of the new coordinate system  $S^\mu$  is situated at  $\tau^\mu$  inside the respective unit cell. The plane wave in the local frame inside the unit cell therefore has the form

$$e^{i(\Lambda^\mu \mathbf{K})(\mathbf{r} + \Lambda^\mu \tau^\mu)} \quad (3.12)$$

and the Rayleigh expansion of the plane wave in the local frame is given by

$$e^{i\mathbf{K}\tau^\mu} 4\pi \sum_L i^l j_l(rK) Y_L^*(\Lambda^\mu \hat{\mathbf{K}}) Y_L(\hat{\mathbf{r}}). \quad (3.13)$$

If the matching conditions are imposed now, the following two equations are obtained: First, the requirement of continuity of the wave functions at the sphere boundary leads to the equation

$$\begin{aligned} & \sum_L a_L^{\mu\mathbf{G}}(\mathbf{k}) u_l(R_{MT^\alpha}) Y_L(\hat{\mathbf{r}}) + b_L^{\mu\mathbf{G}}(\mathbf{k}) \dot{u}_l(R_{MT^\alpha}) Y_L(\hat{\mathbf{r}}) \\ & = e^{i\mathbf{K}\tau^\mu} 4\pi \sum_L i^l j_l(rK) Y_L^*(\Lambda^\mu \hat{\mathbf{K}}) Y_L(\hat{\mathbf{r}}), \end{aligned} \quad (3.14)$$

where  $R_{MT^\alpha}$  is the muffin-tin radius of the atom type  $\alpha$ . Secondly, the derivative of the wave function with respect to  $r$  must also be continuous. With  $\partial u / \partial r = u'$ , one obtains

$$\begin{aligned} & \sum_L a_L^{\mu\mathbf{G}}(\mathbf{k}) u'_l(R_{MT^\alpha}) Y_L(\hat{\mathbf{r}}) + b_L^{\mu\mathbf{G}}(\mathbf{k}) \dot{u}'_l(R_{MT^\alpha}) Y_L(\hat{\mathbf{r}}) \\ & = e^{i\mathbf{K}\tau^\mu} 4\pi \sum_L i^l j'_l(rK) Y_L^*(\Lambda^\mu \hat{\mathbf{K}}) Y_L(\hat{\mathbf{r}}) \end{aligned} \quad (3.15)$$

for each  $\mu$ ,  $\mathbf{K}$  and  $\mathbf{G}$ . Both conditions must be met simultaneously, which can only be accomplished if the coefficients of each spherical harmonic  $Y_L(\hat{\mathbf{r}})$  are equal. Solving

the resulting equations for  $a_L^{\mu\mathbf{G}}(\mathbf{k})$  and  $b_L^{\mu\mathbf{G}}(\mathbf{k})$  yields:

$$\begin{aligned} a_L^{\mu\mathbf{G}}(\mathbf{k}) &= e^{i\mathbf{K}\tau^\mu} 4\pi \frac{1}{W} i^l Y_L^*(\Lambda^\mu \hat{\mathbf{K}}) \\ &\quad [\dot{u}_l(R_{MT^\alpha}) K j_l'(R_{MT^\alpha} K) - \dot{u}_l'(R_{MT^\alpha}) j_l(R_{MT^\alpha} K)] \\ b_L^{\mu\mathbf{G}}(\mathbf{k}) &= e^{i\mathbf{K}\tau^\mu} 4\pi \frac{1}{W} i^l Y_L^*(\Lambda^\mu \hat{\mathbf{K}}) \\ &\quad [u_l'(R_{MT^\alpha}) j_l(R_{MT^\alpha} K) - u_l(R_{MT^\alpha}) K j_l'(R_{MT^\alpha} K)]. \end{aligned} \quad (3.16)$$

The Wronskian  $W$  is given by

$$W = [\dot{u}_l(R_{MT^\alpha}) u_l'(R_{MT^\alpha}) - u_l(R_{MT^\alpha}) \dot{u}_l'(R_{MT^\alpha})]. \quad (3.17)$$

### 3.5 Construction of the Electron Density inside the Muffin Tins

In spin-polarized density-functional calculations of an infinite periodic solid, the electron density is given by an integral over the first Brillouin zone

$$n(\mathbf{r}) = \frac{1}{V_{\text{BZ}}} \int_{\text{BZ}} \sum_{\nu, \epsilon_\nu < E_F} \sum_{\sigma \in \{\uparrow, \downarrow\}} |\psi_{\mathbf{k}, \nu}^\sigma(\mathbf{r})|^2 d^3k, \quad (3.18)$$

where  $\psi_{\mathbf{k}, \nu}^\sigma(\mathbf{r})$  are once more the eigenfunctions of the Kohn-Sham equation,  $V_{\text{BZ}}$  is the volume of the first Brillouin zone,  $\nu$  is the band index and  $E_F$  is the Fermi energy.

In the further course we like to explicitly determine the contributions of the distinct electronic eigenstates  $l = s, p, d$  to the electron density. Therefore, we are only interested in calculating the electron densities within the muffin-tin spheres, because the contributions from the interstitial region can not be attributed to a specific atom and in particular not to a specific l-quantum number. The expansion of the Kohn-Sham eigenfunctions (3.1) within the LAPW basis set in a sphere  $\mu$  is given by

$$\psi_{\mathbf{k}, \nu}^\mu(\mathbf{r}) = \sum_{\mathbf{G}} c_{\mathbf{k}, \nu}^{\mathbf{G}} \sum_L a_L^{\mu\mathbf{G}}(\mathbf{k}) u_l(r^\mu) Y_L(\hat{\mathbf{r}}^\mu) + b_L^{\mu\mathbf{G}}(\mathbf{k}) \dot{u}_l(r^\mu) Y_L(\hat{\mathbf{r}}^\mu) \quad (3.19)$$

The spin index is again dropped for convenience. The coefficients  $a_L^{\mu\mathbf{G}}(\mathbf{k})$  and  $b_L^{\mu\mathbf{G}}(\mathbf{k})$  are replaced by band-dependent  $A$ - and  $B$ -coefficient, obtained by summing over the plane waves

$$\psi_{\mathbf{k}, \nu}^\mu(\mathbf{r}) = \sum_L A_{L, \nu}^\mu(\mathbf{k}) u_l(r^\mu) Y_L(\hat{\mathbf{r}}^\mu) + B_{L, \nu}^\mu(\mathbf{k}) \dot{u}_l(r^\mu) Y_L(\hat{\mathbf{r}}^\mu), \quad (3.20)$$

with

$$A_{L, \nu}^\mu(\mathbf{k}) = \sum_{\mathbf{G}} c_{\mathbf{k}, \nu}^{\mathbf{G}} a_L^{\mu\mathbf{G}}(\mathbf{k}), \quad B_{L, \nu}^\mu(\mathbf{k}) = \sum_{\mathbf{G}} c_{\mathbf{k}, \nu}^{\mathbf{G}} b_L^{\mu\mathbf{G}}(\mathbf{k}). \quad (3.21)$$

If we substitute expression (3.20) into equation (3.18), the resulting expression for the electron density in the muffin-tin sphere  $\mu$  reads

$$n^\mu(\mathbf{r}^\mu) = \frac{1}{V_{\text{BZ}}} \int_{\text{BZ}} \sum_{\substack{\nu, \epsilon_\nu < E_{\text{F}} \\ \sigma \in \{\uparrow, \downarrow\}}} \left[ \sum_{L'} (A_{L',\nu}^{\mu\sigma}(\mathbf{k}) u_{l'}^\sigma(r^\mu) + B_{L',\nu}^{\mu\sigma}(\mathbf{k}) \dot{u}_{l'}^\sigma(r^\mu))^* Y_{L'}^*(\hat{\mathbf{r}}^\mu) \right. \\ \left. \sum_L (A_{L,\nu}^{\mu\sigma}(\mathbf{k}) u_l^\sigma(r^\mu) + B_{L,\nu}^{\mu\sigma}(\mathbf{k}) \dot{u}_l^\sigma(r^\mu)) Y_L(\hat{\mathbf{r}}^\mu) \right]. \quad (3.22)$$

From this general formula an "l-like" electron density further called orbital-resolved density can be derived. Since the wave functions inside the muffin-tin spheres are expanded using spherical harmonics, they can be split up into contributions with a certain  $l$  character

$$\psi_{\mathbf{k},\nu}^\mu(\mathbf{r}) = \sum_l \psi_{\mathbf{k},\nu,l}^\mu(\mathbf{r}). \quad (3.23)$$

If this is to be inserted into expression (3.22), it will contain cross terms with a mixture of different  $l$ 's, since the two sums run over  $l$  and  $l'$ . If, however, the density is integrated over the muffin tin, the cross-terms vanish due to the orthogonality of the spherical harmonics. The total electron density inside a sphere can thus be written as

$$n_\nu^\mu = \sum_l n_{\nu,l}^\mu, \quad n_{\nu,l}^\mu = \frac{1}{V_{\text{BZ}}} \int_{\text{BZ}} \int_{\text{MT}^\mu} |\psi_{\mathbf{k},\nu,l}^\mu(\mathbf{r})|^2 d^3r d^3k, \quad (3.24)$$

where  $n$  is called orbital-resolved electron density. Similarly, a  $\mathbf{k}$ -dependent orbital resolved density can be defined by.

$$n_{\nu,l}^\mu(\mathbf{k}) = \int_{\text{MT}^\mu} |\psi_{\mathbf{k},\nu,l}^\mu(\mathbf{r})|^2 d^3r. \quad (3.25)$$

Substitution of equation (3.20) into this expression yields

$$n_{\nu,l}^\mu(\mathbf{k}) = \sum_L \sum_{\sigma=\uparrow,\downarrow} |A_{L,\nu}^{\mu\sigma}(\mathbf{k})|^2 + |B_{L,\nu}^{\mu\sigma}(\mathbf{k})|^2 \dot{N}_l^\sigma, \quad (3.26)$$

where

$$\dot{N}_l = \int_0^{R_{\text{MT}^\mu}} (\dot{u}_l(\mathbf{r}))^2 r^2 dr. \quad (3.27)$$

Note that expression (3.26) was derived using the orthogonality of the spherical harmonics, the normalization of  $u_l$  (3.9) and the orthogonality of  $u_l$  and  $\dot{u}_l$  (3.10).

Numerical calculations for the materials studied in this thesis have shown that the contribution of the second term in (3.26) originating from the functions  $\dot{u}_l$  in the LAPW basis is quite small. If this term was omitted and the orbital resolved  $\mathbf{k}$ -dependent density was calculated by

$$n_{\nu,\mathbf{k},l}^\mu = \sum_{m=-l}^l \sum_{\sigma \in \{\uparrow, \downarrow\}} |A_{L,\nu}^{\mu\sigma}(\mathbf{k})|^2 \quad (3.28)$$

the deviation from the densities obtained with equation (3.26) were quite small, which can be seen from the results presented in chapter 7. Based on these findings a tight-binding-like basis set within the FLAPW framework shall be derived in the last section of this chapter.

### 3.6 Tight-binding Approximation within the FLAPW Framework

We are interested in the description of the electronic structure of  $3d$  metals especially in describing the behavior of the electrons in the  $d$ -bands of these materials. The  $d$  states are more localized in the vicinity of the nuclei of the atoms, hence, the electrons in these bands show a rather atomic-like character than itinerant behavior. The LAPW basis functions seem to be rather insufficient to catch the localized character of these electrons, since the basis functions being augmented plane waves clearly have non-local character. However, it is this localized character of the electrons that leads to electronic correlation effects to be described in chapter 5. In particular, the description of electronic correlation within many-body perturbation theory will be formulated in terms of interacting electrons situated in orbitals that are localized at the distinct sites of the crystal lattice. Thus, in need of a basis reflecting this localized character of the electrons the LAPW basis set will be modified in a tight-binding-like fashion leading to a new basis set. Furthermore, a tight-binding description of the many-electron system is introduced.

**Tight-binding-like basis set.** It is supposed in the tight-binding (TB) treatment of solids that the electronic interactions of the atoms in the solid are relatively small and that the electrons are largely localized in the vicinity of atoms. It is then a very good approximation to write the electronic wave functions as linear combinations of localized orbitals centered on each site. As a TB-like basis set we choose the functions

$$\chi_L^{\mu\sigma}(\mathbf{r}^\mu) = u_l^\sigma(r^\mu) Y_L(\hat{\mathbf{r}}^\mu), \tag{3.29}$$

where the radial functions  $u_l$  are the solution to the radial Schrödinger equation (3.4) evaluated at the fixed energies  $E_l$ . These functions are normalized to unity inside the muffin tins

$$\int_0^{R_{\text{MT}}^\mu} (\chi_L^{\mu\sigma}(\mathbf{r}^\mu))^* (\chi_{L'}^{\mu'\sigma'}(\mathbf{r}^{\mu'})) d^3r = \delta_{\mu\mu'} \delta_{LL'} \delta_{\sigma\sigma'} \tag{3.30}$$

which is a direct consequence of the normalization of the functions  $u_l$  (3.9) and the normalization of the spherical harmonics  $Y_L(\hat{\mathbf{r}}^\mu)$ .

If the expansion of the Kohn-Sham eigenfunctions  $\psi_{\mathbf{k},\nu}^{\mu\sigma}$  inside muffin tin  $\mu$  in terms of the LAPW basis is now compared to the expansion in terms of the new TB-like

basis

$$\begin{aligned}\psi_{\mathbf{k},\nu}^{\mu\sigma}(\mathbf{r}^\mu) &= \sum_L A_{L,\nu}^{\mu\sigma}(\mathbf{k}) u_l^\sigma(r^\mu) Y_L(\hat{\mathbf{r}}^\mu) + B_{L,\nu}^{\mu\sigma}(\mathbf{k}) \dot{u}_l^\sigma(r^\mu) Y_L(\hat{\mathbf{r}}^\mu) \\ &\approx \sum_L A_{L,\nu}^{\mu\sigma}(\mathbf{k}) \chi_L^{\mu\sigma}(\mathbf{r}^\mu).\end{aligned}\quad (3.31)$$

it becomes evident that the localized basis functions  $\chi_L^{\mu\sigma}$  are obtained from the LAPW basis by simply neglecting the  $\dot{u}_l$  term. Due to the neglect of the  $\dot{u}_l$  term the representation of the Kohn-Sham eigenfunctions in terms of the TB basis functions deviates from the representation employing the full LAPW basis. However, these deviations should be small close to the energies  $E_l$  that are used to evaluate the radial component  $u_l$  and its energy derivative  $\dot{u}_l$  in the linearization of the APWs (3.6). Since we are interested in calculating the electronic densities of states close to these energies  $E_l$ , the expansion of the Kohn-Sham eigenfunctions in terms of the functions  $\chi_L^{\mu\sigma}$  should therefore yield a good approximation to the representation by the full LAPW basis inside the muffin tin region. The difference between the two representations has been analyzed and the results presented in chapter 7 show that the deviations close to  $E_l$  are indeed small. Therefore, the functions  $\chi_L^{\mu\sigma}$  yield a sufficient representation of the Kohn-Sham eigenfunctions inside one muffin tin  $\mu$ .

It is furthermore assumed that the muffin-tin spheres occupy the majority of space due to the close-packed crystal structures of the 3d metals. Therefore, the major part of the electron density is situated within the muffin-tin spheres. Based on this assumption the interstitial space is neglected completely in the TB representation. Nevertheless, the TB basis functions  $\chi_L^{\mu\sigma}$  should still yield a sufficient description of the  $d$  electron states since these should be almost completely contained in the region of space covered by muffin tins due to their localized character. Results of further calculations also presented in chapter 7 show that the charges situated in the  $d$  states are indeed mainly contained inside the muffin tins.

The Kohn-Sham functions describing the whole region in space covered by muffin tins can now be expressed as a sum over all muffin tins  $\mu$  at positions  $\mathbf{R}^\mu$  of the TB representation of  $\psi_{\mathbf{k},\nu}^{\mu\sigma}$  inside one muffin tin  $\mu$

$$\psi_{\mathbf{k},\nu}^\sigma(\mathbf{r}) = \sum_{\mathbf{R}^\mu} \sum_L \tilde{A}_{L,\nu}^{\mathbf{R}^\mu,\mu\sigma}(\mathbf{k}) \chi_L^{\mu\sigma}(\mathbf{r}^\mu), \quad \mathbf{r} \in \text{muffin - tin region} . \quad (3.32)$$

The coefficients  $\tilde{A}_{L,\nu}^{\mathbf{R}^\mu,\mu\sigma}$  are derived from the coefficient in the LAPW representation of  $\psi_{\mathbf{k},\nu}^{\mu\sigma}$  (first line in (3.31)) by

$$\tilde{A}_{L,\nu}^{\mathbf{R}^\mu,\mu\sigma}(\mathbf{k}) = \frac{1}{\sqrt{N}} e^{i\mathbf{R}^\mu \mathbf{k}} A_{L,\nu}^{\mu\sigma}(\mathbf{k}), \quad (3.33)$$

where  $N$  is the number of atoms in the crystal. The factor  $1/\sqrt{N}$  must be introduced here for normalization purposes, because the Kohn-Sham wave functions are

normalized to unity with respect to the number of atoms in the crystal, whereas the function  $\chi_L^{\mu\sigma}$  are normalized to unity inside the muffin tin  $\mu$ .

Finally, we want to define eigenstates and creation and annihilation operators for the TB basis set. For the sake of clarity, this is only done for crystal structures that can be represented by unit cells containing only one atom. In this case, the lattice vectors can be chosen such that they point to the middle of each unit cell, where the center of the muffin tin is positioned. Hence, the index  $\mu$  can be dropped and the Kohn-Sham wave functions are represented by

$$\psi_{\mathbf{k},\nu}^{\sigma}(\mathbf{r}) = \sum_{\mathbf{R}} \sum_L \tilde{A}_{L,\nu}^{\mathbf{R},\sigma}(\mathbf{k}) \chi_L^{\sigma}(\mathbf{r}^{\mathbf{R}}), \quad \mathbf{r} \in \text{muffin - tin region}, \quad (3.34)$$

where  $\mathbf{r}^{\mathbf{R}}$  is the position inside the muffin tin situated at lattice site  $\mathbf{R}$ . If we now introduce the eigenstate  $|\mathbf{R}L\sigma\rangle$  of an electron sitting in the orbital  $L$  with spin  $\sigma$  in the muffin tin at position  $\mathbf{R}$  by

$$\chi_{\mathbf{R}L}^{\sigma}(\mathbf{r}^{\mathbf{R}}) = \langle \mathbf{r}^{\mathbf{R}} | \mathbf{R}L\sigma \rangle, \quad (3.35)$$

we can define creation and annihilation operators

$$c_{\mathbf{R}L\sigma}^{\dagger}, \quad c_{\mathbf{R}L\sigma}, \quad (3.36)$$

that create or annihilate an electron in the state given by  $|\mathbf{R}L\sigma\rangle$ . Because of (3.30) the canonical commutation rules hold for these operators

$$[c_{\mathbf{R}L\sigma}, c_{\mathbf{R}'L'\sigma'}] = [c_{\mathbf{R}L\sigma}^{\dagger}, c_{\mathbf{R}'L'\sigma'}^{\dagger}] = 0 \quad (3.37)$$

$$[c_{\mathbf{R}L\sigma}, c_{\mathbf{R}'L'\sigma'}^{\dagger}] = \delta_{\mathbf{R}\mathbf{R}'} \delta_{LL'} \delta_{\sigma\sigma'}. \quad (3.38)$$

**TB Hamiltonian.** We want to find an approximate representation of the Hamiltonian,

$$\hat{H} = \left[ -\frac{\hbar^2}{2m} \sum_{i=1}^{N_e} \nabla_i^2 + \frac{e^2}{4\pi\epsilon_0} \sum_{i<j}^{N_e} \frac{1}{|\mathbf{r}_i - \mathbf{r}_j|} + \sum_{i=1}^{N_e} v_{\text{ext}}(\mathbf{r}_i) \right] \quad (\text{see 2.2})$$

of the many-electron Schrödinger equation employing the TB basis and the creation and annihilation operators introduced above. The derivation is carried out only for structures with one atom per unit cell. The extension to the case of multiple atoms per unit cell can be done straightforwardly.

Below the Kohn-Sham equation is restated

$$\hat{h}_{\sigma}^{\text{eff}} \psi_{\mathbf{k},\nu}^{\sigma}(\mathbf{r}) = \left[ -\frac{\hbar^2}{2m} \nabla^2 + v_{\sigma}^{\text{eff}}(\mathbf{r}) \right] \psi_{\mathbf{k},\nu}^{\sigma}(\mathbf{r}) = \epsilon_{\mathbf{k},\nu}^{\sigma} \psi_{\mathbf{k},\nu}^{\sigma}(\mathbf{r}), \quad (\text{see 2.21})$$

where  $\epsilon_{\mathbf{k},\nu}^\sigma$  is the Kohn-Sham eigenvalue to the eigenfunction  $\psi_{\mathbf{k},\nu}^\sigma(\mathbf{r})$  and

$$\begin{aligned} v_\sigma^{\text{eff}}(\mathbf{r}) &= v_{\text{ext}}(\mathbf{r}) + v_{\text{H}}(\mathbf{r}) + v_\sigma^{\text{xc}}(\mathbf{r}) \\ v_{\text{H}}(\mathbf{r}) &= \frac{e^2}{4\pi\epsilon_0} \int \frac{n(\mathbf{r}')}{|\mathbf{r} - \mathbf{r}'|} d^3r', \quad v_\sigma^{\text{xc}}(\mathbf{r}) = \frac{\delta E_{\text{xc}}[n_\uparrow, n_\downarrow]}{\delta n_\sigma(\mathbf{r})} \end{aligned} \quad (3.39)$$

The Hamiltonian of the Kohn-Sham equation  $\hat{h}_\sigma^{\text{eff}}$  will be denoted by  $\hat{h}_\sigma^{\text{KS}}$  from now on. The electronic Hamiltonian  $\hat{H}$  of (2.2) can then be rewritten as

$$\hat{H} = \sum_{i=1}^{N_e} \sum_{\sigma=\uparrow,\downarrow} \left[ \hat{h}_\sigma^{\text{KS}}(\mathbf{r}_i) - v_{\text{H}}(\mathbf{r}_i) - v_\sigma^{\text{xc}}(\mathbf{r}_i) \right] + U_{\text{ee}}, \quad (3.40)$$

with

$$U_{\text{ee}} = \frac{e^2}{4\pi\epsilon_0} \sum_{i<j}^{N_e} \frac{1}{|\mathbf{r}_i - \mathbf{r}_j|}. \quad (3.41)$$

Based on this form of the Hamiltonian a new TB representation of the many-electron system can be introduced. Using the states  $|\mathbf{R}L\sigma\rangle$  and the operators  $c_{\mathbf{R}'L'\sigma}$  and  $c_{\mathbf{R}'L'\sigma}^\dagger$  a new TB-Hamiltonian  $\hat{H}^{\text{TB}}$  can be defined by

$$\begin{aligned} \hat{H}^{\text{TB}} &= \sum_{\mathbf{R}L,\mathbf{R}'L';\sigma'} H_{\mathbf{R}L,\mathbf{R}'L'}^{\text{DFT}\sigma} c_{\mathbf{R}L\sigma}^\dagger c_{\mathbf{R}'L'\sigma} - \sum_{\mathbf{R}L,\mathbf{R}'L';\sigma'} D_{\mathbf{R}L,\mathbf{R}'L'}^\sigma c_{\mathbf{R}L\sigma}^\dagger c_{\mathbf{R}'L'\sigma} \\ &+ \frac{1}{2} \sum_{\substack{\mathbf{R}_1\mathbf{R}_2\mathbf{R}_3\mathbf{R}_4 \\ L_1L_2L_3L_4,\sigma\sigma'}} U_{\mathbf{R}_1L_1\sigma,\mathbf{R}_2L_2\sigma',\mathbf{R}_3L_3\sigma,\mathbf{R}_4L_4\sigma'} c_{\mathbf{R}_1L_1\sigma}^\dagger c_{\mathbf{R}_2L_2\sigma'}^\dagger c_{\mathbf{R}_4L_4\sigma'} c_{\mathbf{R}_3L_3\sigma} \end{aligned} \quad (3.42)$$

with

$$H_{\mathbf{R}L,\mathbf{R}'L'}^{\text{DFT}\sigma} = \langle \mathbf{R}L\sigma | \hat{h}_\sigma^{\text{KS}} | \mathbf{R}'L'\sigma \rangle, \quad (3.43)$$

$$D_{\mathbf{R}L,\mathbf{R}'L'}^\sigma = \langle \mathbf{R}L\sigma | v_{\text{H}} + v_\sigma^{\text{xc}} | \mathbf{R}'L'\sigma \rangle, \quad (3.44)$$

and

$$U_{\mathbf{R}_1L_1\sigma,\mathbf{R}_2L_2\sigma',\mathbf{R}_3L_3\sigma,\mathbf{R}_4L_4\sigma'} = \langle \mathbf{R}_1L_1\sigma, \mathbf{R}_2L_2\sigma' | U_{\text{ee}} | \mathbf{R}_3L_3\sigma, \mathbf{R}_4L_4\sigma' \rangle. \quad (3.45)$$

Equations (3.43) - (3.45) are projections of the terms of the full many-electron Hamiltonian (3.40) onto the TB basis states, hence, the TB Hamiltonian  $\hat{H}^{\text{TB}}$  describes only those electrons situated inside the muffin-tins in states  $|\mathbf{R}L\sigma\rangle$ . In particular the charges situated in the interstitial region are not contained in the TB description given by  $\hat{H}^{\text{TB}}$  due to the construction of the TB basis states. The many-body correction to the DFT approach presented in chapter 5 starts from equation (3.42). Hence, this description for the electron system shall be examined a little closer in the remainder of this section.

The annihilation and creation operators in the first term of (3.42) describe the annihilation of an electron at one site  $\mathbf{R}'$  in the orbital  $L'$  with spin  $\sigma'$  which is

created then at another site  $\mathbf{R}$  in a state with  $L$  and  $\sigma$ . Hence, the term gives the kinetic energy of the electrons, since it describes the motion of them from one site to another. However, the matrix elements  $H_{\mathbf{R}L,\mathbf{R}'L'}^{\text{DFT}\sigma}$  are calculated using the Kohn-Sham Hamiltonian  $\hat{h}_\sigma^{\text{KS}}$  which also contains the effective potential  $v_\sigma^{\text{eff}}$ . Thus, the first term also yields the potential energy of an electron due to its static interaction with the charge background caused by the effective medium. Therefore, the second term, the so-called double-counting term, had to be introduced to subtract these electronic interaction, because they are not only captured by the first term due to the effective potential but they are also contained in the third term. The third term as presented in its most general form here accounts for all electron-electron interaction processes.

Closing this chapter, it is proved that the first term of (3.42) can be completely determined within the framework of DFT. In the same spirit, as the vector states  $|\mathbf{R}L\sigma\rangle$  were introduced, I define  $|\mathbf{k}\nu\sigma\rangle$  denoting the Kohn-Sham eigenfunctions  $\psi_{\mathbf{k},\nu}^\sigma(\mathbf{r})$  in state space by

$$\psi_{\mathbf{k},\nu}^\sigma(\mathbf{r}) = \langle \mathbf{r} | \mathbf{k}\nu\sigma \rangle, \quad \mathbf{r} \in \mathbb{R}. \quad (3.46)$$

If we furthermore introduce the abbreviation

$$\frac{1}{V_{\text{BZ}}} \int_{\text{BZ}} d^3k \quad \longrightarrow \quad \sum_{\mathbf{k}}, \quad (3.47)$$

the unity operator can be written as

$$\sum_{\mathbf{k}\nu\sigma} |\mathbf{k}\nu\sigma\rangle \langle \mathbf{k}\nu\sigma| = \mathbf{1}, \quad (3.48)$$

by exploiting the completeness relation of the basis set  $\{|\mathbf{k}\nu\sigma\rangle\}$ . The expansion coefficients defined in (3.33) are given by

$$\tilde{A}_{L,\nu}^{\mathbf{R},\sigma}(\mathbf{k}) = \langle \mathbf{R}L\sigma | \mathbf{k}\nu\sigma \rangle \quad (3.49)$$

yielding the projection of the Kohn-Sham eigenstate  $|\mathbf{k}\nu\sigma\rangle$  onto the TB state  $|\mathbf{R}L\sigma\rangle$ . Using these identities expression (3.43) can be evaluated:

$$\begin{aligned} H_{\mathbf{R}L,\mathbf{R}'L'}^{\text{DFT}\sigma} &= \langle \mathbf{R}L\sigma | \hat{h}_\sigma^{\text{KS}} | \mathbf{R}'L'\sigma \rangle \\ &= \langle \mathbf{R}L\sigma | \left( \sum_{\mathbf{k}\nu\sigma''} |\mathbf{k}\nu\sigma''\rangle \langle \mathbf{k}\nu\sigma''| \right) \hat{h}_\sigma^{\text{KS}} \left( \sum_{\mathbf{k}'\nu'\sigma'} |\mathbf{k}'\nu'\sigma'\rangle \langle \mathbf{k}'\nu'\sigma'| \right) | \mathbf{R}'L'\sigma \rangle \\ &= \sum_{\mathbf{k}\nu} \epsilon_{\mathbf{k},\nu}^\sigma \langle \mathbf{R}L\sigma | \mathbf{k}\nu\sigma \rangle \langle \mathbf{k}\nu\sigma | \mathbf{R}'L'\sigma \rangle \\ &= \sum_{\mathbf{k}\nu} \epsilon_{\mathbf{k},\nu}^\sigma \left( \tilde{A}_{L,\nu}^{\mathbf{R},\sigma}(\mathbf{k}) \right) \left( \tilde{A}_{L',\nu}^{\mathbf{R}',\sigma}(\mathbf{k}) \right)^*. \end{aligned} \quad (3.50)$$



## 4 Green Functions

Green functions are a now widely used alternative description of many-particle systems. All physical quantities which are obtained using a Hamiltonian-based description for such systems can also be obtained from a Green-function approach. Moreover, the Green-function approach allows to calculate physical quantities without the knowledge of the eigenvalues or eigenstates of the corresponding Hamiltonian description. This is of particular interest for those systems where true particle-particle interactions play an important role i.e. for the materials analyzed in this thesis, when effects due to electron correlations are taken into account explicitly. Those effects can not be described in a one-particle picture as used in DFT and in a Hamiltonian approach one would have to resign to the solution of the full many-electron Schrödinger equation (2.2). Since it was already argued in the previous chapters that the determination of the true many-electron wave functions can be extremely difficult, the Green-function approach seems to be an alternative worth thinking about for the description of many-particle systems.

In this chapter, a Green function is derived within the framework of the FLAPW method using the TB approach described in the previous chapter and some useful relations between the Green function and some observables measured in many-electron systems are presented. We start with the general definition of the Green function as used in many-particle physics.

### 4.1 Definition and Properties of Green Functions

Field operators acting on a system containing  $N$  electrons can be introduced as

$$\hat{\psi}^\dagger(\lambda), \quad \hat{\psi}(\lambda) \quad \text{with} \quad \lambda = (\mathbf{r}, \sigma). \quad (4.1)$$

These field operators describe the creation/annihilation of an electron at position  $\mathbf{r}$  with spin  $\sigma$ . Alternatively, the annihilation of one electron is interpreted as creation of a hole. The Hamiltonian of the  $N$ -electron system shall be denoted by  $\hat{H}$  and the ground state at time  $t'$  is given by  $|\Psi_0^N(t')\rangle$ . A Green function  $G^e(\lambda t, \lambda' t')$  for this system is now defined such that  $i\hbar G^e(\lambda t, \lambda' t')$  is the probability amplitude for an electron, which is added to  $|\Psi_0^N(t')\rangle$  in the state  $\lambda'$  at the time  $t'$  to be measured in the state  $\lambda$  at time  $t$ . The final state of the system at time  $t$  is then given by  $\hat{\psi}(\lambda)\hat{U}(t, t')\hat{\psi}^\dagger(\lambda')|\Psi_0^N(t')\rangle$ . Thus, the final state is constructed from the initial state by successively applying to it the electron creation operator  $\hat{\psi}^\dagger(\lambda')$ , the evolution

operator  $\hat{U}(t, t') = \exp[-i\hat{H}(t - t')/\hbar]$ , which takes the system from the initial time  $t'$  to a later time  $t > t'$ , and the electron annihilation operator  $\hat{\psi}(\lambda)$ . Since the probability amplitude between two states of a system is given by the overlap of these states, the Green function can now be defined as

$$\begin{aligned} G^e(\lambda t, \lambda' t') &= -\frac{i}{\hbar} \left\langle \Psi_0^N(t) \left| \hat{\psi}(\lambda) \hat{U}(t, t') \hat{\psi}^\dagger(\lambda') \right| \Psi_0^N(t') \right\rangle \theta(t - t') \\ &= -\frac{i}{\hbar} \left\langle \Psi_0^N \left| \hat{\psi}(\lambda t) \hat{\psi}^\dagger(\lambda' t') \right| \Psi_0^N \right\rangle \theta(t - t'), \end{aligned} \quad (4.2)$$

where  $\theta(t - t')$  is the Heaviside step function defined by

$$\theta(t - t') = \begin{cases} 1 & \text{if } t > t' \\ 0 & \text{if } t < t' \end{cases}. \quad (4.3)$$

From the first to the second line in (4.2) the field operators were changed from their representation in the Schrödinger picture to their representation in the Heisenberg picture, which are related by

$$|\Psi_H\rangle = \hat{U}(0, t) |\Psi_S(t)\rangle \quad \text{and} \quad \hat{O}_H(t) = \hat{U}(0, t) \hat{O}_S \hat{U}(t, 0). \quad (4.4)$$

As long as it is clear from the context, which representation of the operators is presently used, the indices H and S will be omitted.

Similarly to the propagation of an additional electron through the many-electron system, the propagation of a hole from  $(\lambda, t)$  to  $(\lambda', t')$  is described by the Green function

$$G^h(\lambda' t', \lambda t) = -\frac{i}{\hbar} \left\langle \Psi_0^N \left| \hat{\psi}^\dagger(\lambda' t') \hat{\psi}(\lambda t) \right| \Psi_0^N \right\rangle \theta(t' - t), \quad (4.5)$$

and the two Green functions are often combined to one time-ordered Green function

$$G(\lambda t, \lambda' t') = G^e(\lambda t, \lambda' t') - G^h(\lambda' t', \lambda t) = -\frac{i}{\hbar} \left\langle \Psi_0^N \left| \hat{T} \left[ \hat{\psi}(\lambda t) \hat{\psi}^\dagger(\lambda' t') \right] \right| \Psi_0^N \right\rangle, \quad (4.6)$$

where the time-ordering operator  $\hat{T}$  was used, which rearranges a series of field operators in order of ascending time arguments from right to left with a factor  $(-1)$  for each pair permutation. Depending on the time order, equation (4.6) describes either electron ( $t > t'$ ) or hole ( $t < t'$ ) propagation. To stretch the physical meaning of this Green function  $G(\lambda t, \lambda' t')$ , it is often called the one-particle propagator.

An equation of motion for the one-particle propagator can be derived using the following relations:

- The equation of motion for a Heisenberg operator  $\hat{O}$  in a system with Hamiltonian  $\mathcal{H}$  is given by

$$i\hbar \frac{d}{dt} \hat{O}(t) = [\hat{O}(t), \mathcal{H}]_- + i\hbar \frac{\partial \hat{O}(t)}{\partial t}, \quad (4.7)$$

where  $[...]_-$  is the commutator of the Hamiltonian and the operator.

- The time derivative of the Heaviside function is the delta function

$$\frac{d}{dt}\theta(t-t') = \delta(t-t') = -\frac{d}{dt'}\theta(t-t'). \quad (4.8)$$

- To simplify the notation, the ground-state  $|\Psi_0^N\rangle$  is abbreviated by  $|\rangle$  and  $\langle\Psi_0^N|$  by  $\langle$  respectively.

The equation of motion is then given by

$$\begin{aligned} i\hbar\frac{\partial}{\partial t}G(\lambda t, \lambda' t') &= \delta(t-t') \langle [\hat{\psi}(\lambda t), \hat{\psi}^\dagger(\lambda' t')]_+ \rangle - \frac{i}{\hbar} \left\langle \hat{T} \left[ \frac{\partial \hat{\psi}(\lambda t)}{\partial t} \hat{\psi}^\dagger(\lambda' t') \right] \right\rangle \\ &= \delta(t-t') \delta(\mathbf{r}-\mathbf{r}') \delta_{\sigma\sigma'} - \frac{i}{\hbar} \left\langle \hat{T} \left[ [\hat{\psi}(\lambda t), \hat{H}]_-; \hat{\psi}^\dagger(\lambda' t') \right] \right\rangle, \end{aligned} \quad (4.9)$$

where the anti-commutator relation  $[\dots]_+$  between the field operators was evaluated in the second step. The commutator in the second term  $[\hat{\psi}(\lambda t), \hat{H}]_-$  is in general also an operator such that the whole term is yet another Green function but now of higher order. One can set up a new equation of motion to obtain this Green function, which will lead to a similar relation with yet another Green function of even higher order. This will lead to an infinite chain of differential equations, hence, to determine the one particle propagator exactly an infinite number of differential equations has to be solved, which is just as impossible as finding the exact many-electron wave function. The big advantage of the Green-function approach lies in the splitting of the determination process into distinct differential equations. By breaking the infinite chain of equations at some point i.e. by approximating the Green function on this level of the hierarchy all Green functions of lower order can in principle be calculated. This procedure will be used in the next chapter.

We want to analyze only stationary systems for which the Hamiltonian  $\hat{H}$  is not explicitly time-dependent. Consequently, the Green function depends only on the time difference  $\tau = t - t'$  between the initial and the final state

$$G(\lambda t, \lambda' t') = G(\lambda, \lambda'; \tau). \quad (4.10)$$

Furthermore, with a set of state vectors  $\{|\Psi_j^{N\pm 1}\rangle\}$  introduced as the complete set of states of the  $(N \pm 1)$ -particle system, we can define the projections

$$\psi_j^{N-1}(\lambda) = \langle \Psi_j^{N-1} | \hat{\psi}(\lambda) | \Psi_0^N \rangle \quad \text{and} \quad \psi_j^{N+1}(\lambda) = \langle \Psi_0^N | \hat{\psi}(\lambda) | \Psi_j^{N+1} \rangle \quad (4.11)$$

with corresponding excitation energies

$$\epsilon_j^{N-1} = E_0^N - E_j^{N-1} \quad \text{and} \quad \epsilon_j^{N+1} = E_j^{N+1} - E_0^N, \quad (4.12)$$

for the  $(N \pm 1)$ -particle system. Inserting the closure relation  $\sum_i |\Psi_j^{N\pm 1}\rangle \langle \Psi_j^{N\pm 1}| = \mathbf{1}$  between the field operators of the time-ordered Green function  $G(\lambda, \lambda'; \tau)$  as defined

in (4.6) for a stationary system then leads to

$$G(\lambda, \lambda'; \tau) = -\frac{i}{\hbar} \sum_j \psi_j^{N+1}(\lambda) \psi_j^{N+1*}(\lambda') e^{-i\epsilon_j^{N+1}\tau/\hbar} \theta(\tau) + \frac{i}{\hbar} \sum_j \psi_j^{N-1*}(\lambda') \psi_j^{N-1}(\lambda) e^{-i\epsilon_j^{N-1}\tau/\hbar} \theta(-\tau). \quad (4.13)$$

It is convenient to switch to an energy representation of the Green function using the Fourier transformation,

$$G(\lambda, \lambda'; \tau) \xrightarrow{F.T.} G(\lambda, \lambda'; \epsilon). \quad (4.14)$$

The Fourier transformed depend only on one energy  $\epsilon$ . They are defined as

$$G(\lambda, \lambda'; \epsilon) = \int_{-\infty}^{\infty} d\tau e^{i\epsilon\tau/\hbar} G(\lambda, \lambda'; \tau) \quad (4.15)$$

$$G(\lambda, \lambda'; \tau) = \int_{-\infty}^{\infty} \frac{d\epsilon}{2\pi\hbar} e^{-i\epsilon\tau/\hbar} G(\lambda, \lambda'; \epsilon).$$

In turns, the right-hand site of (4.13) can also be Fourier transformed into energy space using the Fourier transformed of the Heaviside step function

$$\theta(\epsilon) = \int_{-\infty}^{\infty} d\tau e^{(i\epsilon\tau - \eta|\tau|)/\hbar} \theta(\tau) = \frac{i\hbar}{\epsilon + i\eta}, \quad (4.16)$$

where  $\eta$  is an infinitesimally small positive number. The Fourier transformation of (4.13) yields the so-called Lehmann representation of the Green function

$$G(\lambda, \lambda'; \epsilon) = \sum_j \frac{\psi_j^{N+1}(\lambda) \psi_j^{N+1*}(\lambda')}{\epsilon - \epsilon_j^{N+1} + i\eta} + \sum_j \frac{\psi_j^{N-1}(\lambda) \psi_j^{N-1*}(\lambda')}{\epsilon - \epsilon_j^{N-1} - i\eta}. \quad (4.17)$$

The sums run over the ground state and all excited states of the  $(N-1)$ - and  $(N+1)$ -particle system. The Green function has poles at all true many-particle excitation energies  $\epsilon_j^{N\pm 1}$ , hence, it contains all information about the complete one-particle excitation spectrum of the  $(N \pm 1)$ -particle system. In principle, the Green function can also be used to calculate the total energy of these systems but this is not to be discussed here. It should just be mentioned to emphasize once more that the Green function really yields all one-particle information that are in principle also accessible via a Hamiltonian approach.

## 4.2 Electron Density and Spectral Function

**The electron density.** The electron density  $n$  of a system containing  $N$  electrons can be calculated directly from the Green function of that system. From here on I

will use the following more convenient notation for the Lehmann representation of the time-ordered Green function

$$G(\lambda, \lambda'; \epsilon) = \sum_j \frac{\psi_j^{N\pm 1}(\lambda) \psi_j^{N\pm 1*}(\lambda')}{\epsilon - \epsilon_j^{N\pm 1} \pm i\eta} \quad (4.18)$$

where the two sums in (4.17) were summarized in one expression. To expand (4.18) and recover (4.17) the signs in the denominator as well as in the indices of the projections  $\psi_j^{N+1}$  and  $\psi_j^{N-1}$  have to be chosen accordingly.

With the identity

$$\frac{1}{x \pm i\eta} = \mathcal{P}\left(\frac{1}{x}\right) \mp i\pi\delta(x) \quad (4.19)$$

in the limit  $\eta \rightarrow 0^+$ , where  $\mathcal{P}(1/x)$  is the principal value of  $1/x$ , we can define the energy resolved density distribution of the electrons  $w(\epsilon, \lambda)$  by

$$\begin{aligned} w(\epsilon, \lambda) &= \mp \frac{1}{\pi} \text{Im} G(\lambda, \lambda; \epsilon) \\ &= \sum_j |\psi_j^{N\pm 1}(\lambda)|^2 \delta(\epsilon - \epsilon_j^{N\pm 1}). \end{aligned} \quad (4.20)$$

Energy integration of  $w(\epsilon, \lambda)$  up to Fermi energy  $E_F$  yields

$$\begin{aligned} n(\lambda) &= \int_{-\infty}^{E_F} w(\epsilon, \lambda) d\epsilon \\ &= \int_{-\infty}^{E_F} \sum_j |\psi_j^{N\pm 1}(\lambda)|^2 \delta(\epsilon - \epsilon_j^{N\pm 1}) d\epsilon \\ &= \sum_j^{\text{occ}} |\psi_j^{N-1}(\lambda)|^2, \end{aligned} \quad (4.21)$$

where the sum now runs over all states of the  $(N-1)$ -particle system, since the states represented by  $\{\psi_j^{N+1}\}$  all lie above the Fermi level and the states  $\{\psi_j^{N-1}\}$  represent the occupied one-electron orbitals below the Fermi level if the system is in the ground state. Expression (4.21) for the electron density  $n$  is formally identical with expression (2.22) for the electron density expressed in terms of the Kohn-Sham eigenfunctions, but the states  $\{\psi_j^{N-1}\}$  used here are projections of the real system. Thus, the expressions are not identical but should yield the same results, since the auxiliary system in DFT is explicitly constructed to yield the correct electron density of the real system.

From (4.20), the total density of states  $D(\epsilon)$  (DOS) can also be derived by

$$D(\epsilon) = \int_{-\infty}^{\infty} w(\epsilon, \lambda) d\lambda = \mp \frac{1}{\pi} \int_{-\infty}^{\infty} \text{Im} G(\lambda, \lambda; \epsilon) d\lambda, \quad (4.22)$$

where the integration over  $\lambda$  represents the integration over the spacial coordinates and summation over spins here. If the summation over the spins is not carried out, one can obtain a spin-resolved DOS. The DOS gives all possible electron states for the system regardless whether they are occupied or not.

**The spectral function.** The spectral function  $A(\lambda, \lambda'; \epsilon)$  for a  $N$ -electron system is defined as a sum over delta functions at the excitation energies

$$\begin{aligned} A(\lambda, \lambda'; \epsilon) = & \sum_j \psi_j^{N-1}(\lambda) \psi_j^{N-1*}(\lambda') \delta(\epsilon - \epsilon_j^{N-1}) \\ & + \sum_j \psi_j^{N+1}(\lambda) \psi_j^{N+1*}(\lambda') \delta(\epsilon - \epsilon_j^{N+1}) \end{aligned} \quad (4.23)$$

weighted by the products of the corresponding projections  $\psi_i^{N\pm 1}$ . Using the Lehmann representation (4.17) of the time-ordered Green function  $G(\lambda, \lambda'; \epsilon)$  and the identity (4.19) in the limit  $\eta \rightarrow 0^+$ , the spectral function can be written as

$$A(\lambda, \lambda'; \epsilon) = -\text{sgn}(\epsilon - E_F) \frac{1}{\pi} \text{Im} G(\lambda, \lambda'; \epsilon). \quad (4.24)$$

Thus, the spectral function can also be determined, if the Green function is known.

The spectral function gives the spectrum of the excited states that contribute to the electron or hole propagation. This can be seen from equation (4.23), since  $A(\lambda, \lambda'; \epsilon)$  will be non-zero only at the excitation energies  $\epsilon_j^{N\pm 1}$  due to the delta function. Within DFT, the spectra obtained from the spectral function really do have delta-peak structure. However, the situation will become more difficult, when the spectral function is derived from the Green function obtained in chapter 5 within many-body perturbation theory. Since the changes in the spectra due to many-body correction will be much easier to understand after related quantities have been introduced I postpone further discussion to chapter 8, where the results of calculations of the spectral function are presented.

### 4.3 Green Functions within the TB-FLAPW Approach

In this section a Green function is derived within the framework of DFT. Density-functional theory is a mean-field approach mapping the real system onto the effective system of non-interacting particles. Hence, the  $\psi_j^{N+1}(\lambda)$  and the  $\psi_j^{N-1}(\lambda)$  defined in (4.11) become simply the unoccupied and the occupied single-particle eigenfunctions of the Kohn-Sham equations, which were denoted by  $\psi_{\mathbf{k},\nu}^\sigma(\mathbf{r})$ . The  $\epsilon_j^{N\pm 1}$  are the corresponding single-particle Kohn-Sham eigenvalues given by  $\epsilon_{\mathbf{k},\nu}^\sigma$ . In the Lehmann representation of the time-ordered Green function (4.17) for a system described within DFT the sum over  $j$  is therefore replaced by the integral over the first Brillouin zone

(1<sup>st</sup> BZ), the sum over the band indices  $\nu$  and the sum over the spin  $\sigma$  where  $V_{\text{BZ}}$  is the volume of the first Brillouin zone:

$$\sum_j \xrightarrow{\text{DFT}} \frac{1}{V_{\text{BZ}}} \int_{\text{BZ}} d^3k \sum_{\nu} \longrightarrow \sum_{\mathbf{k}} \sum_{\nu} . \quad (4.25)$$

In the second step the abbreviation introduced in (3.47) was applied representing the Brillouin-zone integral as a sum over  $\mathbf{k}$  vectors. The sum over spin indices is not carried out, since I only want to describe systems with collinear spin structure and the Green function of these systems is diagonal in spin. A Kohn-Sham Green function for each spin  $\sigma$  can now be defined as

$$G^{\sigma}(\mathbf{r}, \mathbf{r}'; \epsilon) = \sum_{\mathbf{k}} \sum_{\nu} \frac{\psi_{\mathbf{k},\nu}^{\sigma}(\mathbf{r}) \psi_{\mathbf{k},\nu}^{\sigma*}(\mathbf{r}')}{\epsilon - \epsilon_{\mathbf{k},\nu}^{\sigma} \pm i\eta}, \quad \mathbf{r}, \mathbf{r}' \in \mathbb{R} . \quad (4.26)$$

This Green function is now to be expressed using the TB-FLAPW basis functions derived in section 3.6. By inserting the expansion (3.32) of the Kohn-Sham eigenfunctions in terms of the TB basis functions defined in (3.29) into (4.26) we obtain the following Green function

$$G^{0\sigma}(\mathbf{r}^{\mu}, \mathbf{r}^{\mu'}; \epsilon) = \sum_{\substack{\mathbf{R}^{\mu} \mu L \\ \mathbf{R}^{\mu'} \mu' L'}} \chi_L^{\mu\sigma}(\mathbf{r}^{\mu}) \left( \sum_{\mathbf{k}\nu} \frac{(\tilde{A}_{L,\nu}^{\mathbf{R}^{\mu},\mu\sigma}(\mathbf{k})) (\tilde{A}_{L',\nu}^{\mathbf{R}^{\mu'},\mu\sigma}(\mathbf{k}))^*}{\epsilon - \epsilon_{\mathbf{k},\nu}^{\sigma} \pm i\eta} \right) \chi_{L'}^{\mu'\sigma*}(\mathbf{r}^{\mu'}). \quad (4.27)$$

In contrast to the Green function (4.26) the new TB Green function (4.27) only describes a particle that is contained in the region of space covered by muffin tins which is denoted by replacing the arguments  $\mathbf{r}, \mathbf{r}'$  of the Green function (4.26) on the left-hand side by  $\mathbf{r}^{\mu}, \mathbf{r}^{\mu'}$  in (4.27). This is analogous to the TB Hamiltonian derived in the previous chapter, that also described only those particles inside the muffin-tin region. The term in brackets in (4.27) is now defined as DFT lattice Green function in the TB representation, which can be understood as matrix operator with matrix elements

$$G_{\mathbf{R}^{\mu} L, \mathbf{R}^{\mu'} L'}^{0\mu\mu'\sigma}(\epsilon) = \frac{1}{V_{\text{BZ}}} \int_{\text{BZ}} d^3k \sum_{\mathbf{k}\nu} \frac{(\tilde{A}_{L,\nu}^{\mathbf{R}^{\mu},\mu\sigma}(\mathbf{k})) (\tilde{A}_{L',\nu}^{\mathbf{R}^{\mu'},\mu\sigma}(\mathbf{k}))^*}{\epsilon - \epsilon_{\mathbf{k},\nu}^{\sigma} \pm i\eta} . \quad (4.28)$$

We thus obtain a Green function for each pair of muffin tins  $\{\mu, \mu'\}$  situated at the lattice sites  $\{\mathbf{R}^{\mu}, \mathbf{R}^{\mu'}\}$ . Within the TB-FLAPW description of the many-electron system, this lattice Green function can be again interpreted as a probability amplitude now giving the probability for the propagation of an electron or a hole with spin  $\sigma$  from its initial state in the orbital  $L'$  of the atom  $\mu'$  at lattice site  $\mathbf{R}^{\mu'}$  to the orbital  $L$  of the atom  $\mu$  at lattice site  $\mathbf{R}^{\mu}$ . The index  $^0$  in the notation for the DFT lattice Green function is introduced here to distinguish it from quantities which will be introduced later. The Green function (4.27) was derived for the general case of  $\mu$

atoms per unit cell. If the crystal structure of the electronic system is described by unit cells containing only one atom the index  $\mu$  can be dropped in the notation of the above quantities and a lattice Green function is obtained with matrix elements of the form

$$G_{\mathbf{R}L, \mathbf{R}'L'}^{0\sigma}(\epsilon) = \frac{1}{V_{\text{BZ}}} \int_{\text{BZ}} d^3k \sum_{\nu} \frac{(\tilde{A}_{L,\nu}^{\mathbf{R},\sigma}(\mathbf{k})) (\tilde{A}_{L',\nu}^{\mathbf{R}',\sigma}(\mathbf{k}))^*}{\epsilon - \epsilon_{\mathbf{k},\nu}^{\sigma} \pm i\eta}. \quad (4.29)$$

The 3d metals iron, cobalt and nickel to be studied in latter chapters all form a crystals consisting of unit cells with only one atom (iron in bcc structure, nickel and cobalt in fcc structure). Furthermore, the fcc and the bcc crystal structure belong to the cubic group. If we assume that the crystal field yields the largest contribution to the crystal potential the 5  $d$  states at each atomic site split into three times degenerated  $t_{2g}$  states and two times degenerated  $e_g$  states. Moreover, the TB states  $|\mathbf{R}L\sigma\rangle$  at a distinct site  $\mathbf{R}$  are orthogonal for different quantum numbers  $L = (l, m)$ . However, if there is no overlap between different orbitals denoted by  $L$  the transition amplitude between those states is zero and consequently the on-site block with  $\mathbf{R} = \mathbf{R}'$  of the lattice Green function is diagonal in the subspace spanned by the TB states denoted by different  $L$

$$G_{\mathbf{R}L, \mathbf{R}'L'}^{0\sigma}(\epsilon) = G_{\mathbf{R}L, \mathbf{R}L}^{0\sigma}(\epsilon) \delta_{LL'}. \quad (4.30)$$

The fact that the submatrix is diagonal will be used later on to simplify the equations derived within many-body perturbation theory.

It will be convenient to derive also a  $\mathbf{k}$ -dependent lattice Green function. For an arbitrary operator  $\hat{O}(\epsilon)$  with matrix elements  $O_{\mathbf{R}L, \mathbf{R}'L'}(\epsilon)$  a lattice Fourier transformation is defined by

$$O_{L,L'}(\mathbf{k}; \epsilon) = \sum_{\mathbf{T} = \mathbf{R}' - \mathbf{R}} e^{i(\mathbf{R}' - \mathbf{R})\mathbf{k}} O_{\mathbf{R}L, \mathbf{R}'L'}(\epsilon). \quad (4.31)$$

$$O_{\mathbf{R}L, \mathbf{R}'L'}(\epsilon) = \frac{1}{V_{\text{BZ}}} \int_{V_{\text{BZ}}} d^3k e^{i(\mathbf{R}' - \mathbf{R})\mathbf{k}} O_{L,L'}(\mathbf{k}; \epsilon) \quad (4.32)$$

Looking closely at the matrix elements  $G_{\mathbf{R}^{\mu}L, \mathbf{R}'^{\mu'}L'}^{0\mu\mu'\sigma}(\epsilon)$  of the lattice Green function, and inserting the definition (3.33) of the coefficients  $\tilde{A}_{L,\nu}^{\mathbf{R},\mu\sigma}(\mathbf{k})$

$$G_{\mathbf{R}^{\mu}L, \mathbf{R}'^{\mu'}L'}^{0\mu\mu'\sigma}(\epsilon) = \frac{1}{V_{\text{BZ}}} \int_{V_{\text{BZ}}} d^3k \sum_{\nu} \frac{1}{\sqrt{N}} e^{-i\mathbf{R}^{\mu}\mathbf{k}} \frac{(A_{L,\nu}^{\mu\sigma}(\mathbf{k})) (A_{L',\nu}^{\mu'\sigma}(\mathbf{k}))^*}{\epsilon - \epsilon_{\mathbf{k},\nu}^{\sigma} \pm i\eta} \frac{1}{\sqrt{N}} e^{i\mathbf{R}'^{\mu'}\mathbf{k}} \quad (4.33)$$

already yields the expression for the Fourier transform of the DFT lattice Green function

$$G_{LL'}^{0\mu\mu'\sigma}(\mathbf{k}; \epsilon) = \frac{1}{N} \sum_{\nu} \frac{(A_{L,\nu}^{\mu\sigma}(\mathbf{k})) (A_{L',\nu}^{\mu'\sigma}(\mathbf{k}))^*}{\epsilon - \epsilon_{\mathbf{k},\nu}^{\sigma} \pm i\eta}. \quad (4.34)$$

Again, for the case of one atom per unit cell the index  $\mu$  can be dropped and the Fourier transform of the DFT lattice Green function is given by

$$G_{LL'}^{0\sigma}(\mathbf{k}; \epsilon) = \frac{1}{N} \sum_{\nu} \frac{(A_{L,\nu}^{\sigma}(\mathbf{k}))(A_{L',\nu}^{\sigma}(\mathbf{k}))^*}{\epsilon - \epsilon_{\mathbf{k},\nu}^{\sigma} \pm i\eta}. \quad (4.35)$$

## 4.4 Mathematical Tools

In the last section of this chapter, some mathematical identities for complex functions are presented. They can be applied to Green functions and have been used extensively during the implementation and also for the numerical calculations to simplify the formulation and speed up the calculations.

We have introduced the three Green functions in equations (4.2), (4.5) and (4.6) as the electron, the hole and the time-ordered Green function, where the later one can be understood as a combination of the prior two. The time-ordered Green function  $G(\lambda, \lambda'; \epsilon)$  is the basic quantity for the formulation of the diagrammatic perturbation theory presented in the next chapter. However, this Green function has poles in the lower and upper complex half planes as can be seen from the Lehmann representation (4.17) of that function. However, many quantities derived from the Green function can be obtained much easier using the so-called retarded Green function, since it is an analytic function in the upper half plane of the complex plane. This can be seen best from a Lehmann representation of the retarded Green function, which can be defined for an  $N$ -electron systems using the projections  $\psi_j^{N-1}$  and  $\psi_j^{N+1}$  from (4.11) as

$$G^{\text{ret}}(\lambda, \lambda'; \epsilon) = \sum_j \frac{\psi_j^{N+1}(\lambda)\psi_j^{N+1*}(\lambda')}{\epsilon - \epsilon_j^{N+1} + i\eta} + \sum_j \frac{\psi_j^{N-1}(\lambda)\psi_j^{N-1*}(\lambda')}{\epsilon - \epsilon_j^{N-1} + i\eta}. \quad (4.36)$$

In Lehmann representation, the only difference between the time-ordered and the retarded Green function is the different sign of the imaginary part of the denominator in the first sum. All quantities expressed in terms of the time-ordered Green function can therefore be rewritten using the retarded Green function, since the following relation holds:

$$G(\lambda, \lambda'; \epsilon) = \text{Re } G^{\text{ret}}(\lambda, \lambda'; \epsilon) + i \text{sgn}(\epsilon - E_F) \text{Im } G^{\text{ret}}(\lambda, \lambda'; \epsilon) \quad (4.37)$$

It can be shown that this relation also holds for other quantities introduced later, that can be defined as retarded and time-ordered quantities. Thus, many calculations can be performed using the retarded quantities which often simplifies the calculation because of the different analytical behavior of the retarded quantities.

Calculations can often be simplified even more when using retarded quantities, since the whole complex quantity is already determined by the imaginary or the real part of the quantity. If either one part has been calculated, the other one is found

by calculating the Hilbert transformed of the known part. For a complex function  $f(z)$  with  $z = \epsilon + i\eta$  which is analytic in the upper complex half plane and meets the condition

$$\lim_{\text{Im } z > 0, z \rightarrow \infty} f(z) = 0 \quad (4.38)$$

the Hilbert transformation is given by

$$\text{Re}f(\epsilon) = \mathcal{P} \int_{-\infty}^{\infty} \frac{d\epsilon' \text{Im}f(\epsilon')}{\pi (\epsilon' - \epsilon)}, \quad (4.39)$$

$$\text{Im}f(\epsilon) = -\mathcal{P} \int_{-\infty}^{\infty} \frac{d\epsilon' \text{Re}f(\epsilon')}{\pi (\epsilon' - \epsilon)}, \quad (4.40)$$

where  $\mathcal{P}$  denotes the Cauchy principal value of the integral defined as

$$\mathcal{P} \int_a^b dx \frac{f(x)}{x - c} = \lim_{\delta \rightarrow 0} \left[ \int_a^{\xi - \delta} dx \frac{f(x)}{x - \xi} - \int_{\xi + \delta}^b dx \frac{f(x)}{x - \xi} \right]. \quad (4.41)$$

# 5 Many-Body Perturbation Theory

I like to return to the many-electron Schrödinger equation (2.2). The Hamiltonian of (2.2) was approximated within the tight-binding formulation by

$$\begin{aligned} \hat{H}^{\text{TB}} = & \sum_{\mathbf{R}L, \mathbf{R}'L'; \sigma'} H_{\mathbf{R}L, \mathbf{R}'L'}^{\text{DFT} \sigma} c_{\mathbf{R}L\sigma}^\dagger c_{\mathbf{R}'L'\sigma} - \sum_{\mathbf{R}L, \mathbf{R}'L'; \sigma'} D_{\mathbf{R}L, \mathbf{R}'L'}^\sigma c_{\mathbf{R}L\sigma}^\dagger c_{\mathbf{R}'L'\sigma} \\ & + \frac{1}{2} \sum_{\substack{\mathbf{R}_1 \mathbf{R}_2 \mathbf{R}_3 \mathbf{R}_4 \\ L_1 L_2 L_3 L_4, \sigma \sigma'}} U_{\mathbf{R}_1 L_1 \sigma, \mathbf{R}_2 L_2 \sigma', \mathbf{R}_3 L_3 \sigma, \mathbf{R}_4 L_4 \sigma'} c_{\mathbf{R}_1 L_1 \sigma}^\dagger c_{\mathbf{R}_2 L_2 \sigma'}^\dagger c_{\mathbf{R}_4 L_4 \sigma'} c_{\mathbf{R}_3 L_3 \sigma} \end{aligned} \quad (5.1)$$

(see chapter 3). In chapter 2, density-functional theory was introduced as well to obtain an accurate and feasible approximation to the many-electron Schrödinger equation (2.2). DFT being a mean-field approach describes the many-electron problem in terms of a single electron moving in a combined potential of the nuclei and a contribution due to averaging over all other electrons. Thus, in the DFT description some static interaction between the one electron with the charge background of the other electrons in the crystal is contained due to the exchange-correlation potential but true pair interaction is not contained. This is consistent with the findings at the end of chapter 3, section 3.6 that the first term of the Hamiltonian (5.1) can be determined within the framework of DFT. The second and especially the third term describing pair interaction are however not contained in the DFT description.

If electrons are confined to more localized orbitals such as the  $d$ -orbitals of the  $3d$  transition metals or the  $f$ -orbitals of the rare-earth elements, the electronic correlation described by the contribution of the third term in the Hamiltonian (5.1) can no longer be approximated sufficiently in a mean-field type single-particle approach. For example, the LDA band structure for  $f$ -electron systems is in strong disagreement with the band structure measured in experiments for  $f$ -electron systems. In this thesis, I like to study  $3d$  transition metals focusing specifically on electronic correlation occurring in these systems. Thus, it is necessary to find means to go beyond the mean-field DFT description of these systems and explicitly take the third term in (5.1) into accounts.

In general, the DFT description for the  $3d$  transition metals already yields rather accurate results. This is due to the fact that the  $d$ -orbitals are not so strongly localized, hence, the electronic correlation is moderate in these systems compared e.g. to the correlation effects occurring in  $f$ -electron systems. Therefore, in the approach presented here, the systems will be first characterized by a DFT description and then true electron-electron interactions are added to the description within the framework

of diagrammatic many-body perturbation theory. The diagrammatic technique to be used is called fluctuation-exchange (FLEX) method, which is thought to work well in the regime of not too strongly correlated electron systems.

In the first part of this chapter, a new model to describe the interacting electron system as well as a Green function for this model is derived. In the second part, Feynman diagrams are introduced as new means to describe the effects contained in this model. Within the FLEX method presented afterwards, a description of the electron system can then be obtained that incorporates true pair interaction effects.

## 5.1 The Multiband Hubbard Hamiltonian

In order to derive a model that incorporates pair interaction beyond the DFT description of a system lets have another look at the TB approximation of Hamiltonian of the many-electron Schrödinger equation (5.1). The first term is determined in the framework of DFT. The discussion of the second term, the so-called double-counting term, is postponed to the end of the section. The third term of (5.1) contains all pair interaction between electrons. Hence, this term should be at least included partially into the description of the system. When considering specifically the interaction among the valance electrons of  $3d$  transition metals, the following assumptions can be made:

- The  $s$ - and  $p$ -bands are delocalized over the whole crystal structure and can be very well described by the one-particle picture of the DFT mean-field description. Furthermore, for the ground state at temperature  $T = 0$  as discussed here, the  $s$ - and  $p$ -bands that do contain electrons have a small density of states around the Fermi level. Hence, their contribution to interaction processes around the Fermi level will be small.
- The  $d$  bands of the  $3d$  metals are localized in the vicinity of the lattice atoms. The electrons in these bands “see” each other, since they are confined to these localized orbitals. The Coulomb repulsion among the  $d$ -band electrons should therefore yield an important contribution to the interaction term. However, due to the localization of the bands, the intra-atomic contribution usually is an order of magnitude higher than the contributions of the inter-atomic terms.

Under these assumption the last term in (5.1) can be already greatly simplified by taking into account only contributions due to the on-site Coulomb repulsion between  $d$  electrons neglecting all other contributions. The terms remaining on each site are then composed of a sum over the product of creation and annihilation operators with the on-site matrix elements of the Coulomb repulsion given by

$$U_{\mathbf{R};L_1L_2L_3L_4,\sigma\sigma'} = \langle L_1\sigma, L_2\sigma' | U_{ee} | L_3\sigma, L_4\sigma' \rangle. \quad (5.2)$$

where the  $\{L\}$  denote only  $d$  orbitals now and the site index  $\mathbf{R}$  was dropped, since the remaining terms are site-diagonal. Finally, the long-range character of the Coulomb interaction  $U_{ee} \sim 1/|\mathbf{r}_i - \mathbf{r}_j|$  is neglected and the remaining matrix elements are approximated only in terms of two parameters called Hubbard  $U$  and Hubbard  $J$

$$U_{\mathbf{R};L_1L_2L_3L_4,\sigma\sigma'} \approx \delta_{L_1L_3}\delta_{L_2L_4}(1 - \delta_{L_1L_2}\delta_{\sigma\sigma'})U + \delta_{L_1L_4}\delta_{L_2L_3}(1 - \delta_{L_1L_2})\delta_{\sigma\sigma'}J. \quad (5.3)$$

The  $U$  and  $J$  have to be determined individually for each system. A short discussion about the peculiarities in the procedure to determine  $U$  and  $J$  can be found at the end of this section.

The new model to describe the electronic structure of  $3d$  transition metals is now given by

$$\begin{aligned} \hat{H}^{\text{Hubb}} = & \sum_{\mathbf{R}L,\mathbf{R}'L';\sigma} H_{\mathbf{R}L,\mathbf{R}'L'}^{\text{DFT}\sigma} c_{\mathbf{R}L\sigma}^\dagger c_{\mathbf{R}'L'\sigma} \\ & + \frac{1}{2}U \sum_{\mathbf{R}\tilde{L}\tilde{L}'\sigma\sigma'} (1 - \delta_{\tilde{L}\tilde{L}'}\delta_{\sigma\sigma'}) c_{\mathbf{R}\tilde{L}\sigma}^\dagger c_{\mathbf{R}\tilde{L}'\sigma}^\dagger c_{\mathbf{R}\tilde{L}'\sigma} c_{\mathbf{R}\tilde{L}\sigma} \\ & + \frac{1}{2}J \sum_{\mathbf{R}\tilde{L}\tilde{L}'\sigma} (1 - \delta_{\tilde{L}\tilde{L}'}) c_{\mathbf{R}\tilde{L}\sigma}^\dagger c_{\mathbf{R}\tilde{L}'\sigma}^\dagger c_{\mathbf{R}\tilde{L}\sigma} c_{\mathbf{R}\tilde{L}'\sigma}. \end{aligned} \quad (5.4)$$

where the sum over  $L$  and  $L'$  in the first term runs over indices  $l, m$  and  $l', m'$  representing  $s, p$  and  $d$  states, whereas the sum over  $\tilde{L}$  and  $\tilde{L}'$  in the second and third term only runs over indices  $l, m$  and  $l', m'$  representing  $d$  states.

This new Hamiltonian is a multiband Hubbard-type model with a structure similar to that of the famous Hubbard model, which was originally introduced by J. Hubbard [Hub63], [Hub64a] and [Hub64b] for a system containing only a single band with one orbital per site. The Hubbard model is the simplest model to incorporate itinerant electrons, Coulomb repulsion and lattice effects. It contains rich physics and has been successfully used to study phenomena of correlated electrons such as high- $T_c$  superconductivity or Mott transitions in transition metal oxides. Despite its simplicity, an exact solution has been only derived so far for the ground state of the one dimensional model [LW68]. Thus, one has to resign to solve the model numerically or by applying approximate solution techniques such as the many-body perturbation theory used in this thesis.

The ansatz to approximate the Coulomb repulsion by a single parameter  $U$  was first proposed by Hubbard for the single-band Hubbard model. For a single-band model the  $L$  quantum number is the same for all four states contributing to the matrix element

$$U_{\mathbf{R};L;\sigma\sigma'} = \langle L\sigma, L\sigma' | U_{ee} | L\sigma, L\sigma' \rangle. \quad (5.5)$$

The on-site Coulomb repulsion of two electrons in the orbital  $L$  is thought to yield the largest contribution, such that all other contributions can be neglected. If  $U_{ee}$  is therefore approximated by a parameter for the on-site matrix element and is set

to zero for all other matrix elements, the remaining term has the same structure as the second term of the new model (5.4) containing the parameter  $U$ . Note that a term with a  $J$ -like interaction can not occur in the single-band model, since it describes the interaction between particles having the same spin, which may not occupy the same orbital due to the Pauli principle. In further discussion, the  $U$  and  $J$  will also be referred to as the direct and the exchange interaction. The choice of this nomenclature will become clearer within the diagrammatic description of the problem to be introduced in section 5.4 of this chapter. It should only be mentioned here that this nomenclature is not to be confused with that used in Hartree-Fock theory. Although the interaction terms within both theories are derived upon the same interaction mechanisms, they are usually calculated differently, hence they are not entirely identical.

Changing from the one-band model back to the multiband model (5.4) I would like to examine the form of the approximation to the on-site Coulomb matrix elements in (5.3) a little more in detail. By inserting (5.3) into the many-electron Hamiltonian only the interactions between particles that occupy the same state before and after the interaction are retained. In other words, of all possible interactions between two particles only the correlations between particle densities are retained. This approximation to the Coulomb matrix elements is motivated by the symmetry of the crystal structure of the materials to be examined. It was already mentioned in chapter 4 that cubic symmetry is assumed for all calculations and as a consequence the electronic  $d$  states split into  $t_{2g}$  and  $e_g$  states which are orthogonal to each other. If the additional interaction among the electrons occupying the  $d$  states is small compared to the potential of the crystal field, the degeneracy of the  $d$  states is not lifted. Moreover it can be assumed, that the interaction does not cause the distinct orbitals to overlap. However, if no overlap between the states exists no transition between different states can take place and the only non-zero terms of the Coulomb matrix are those describing the interaction between particle densities.

If the multiband Hubbard model 5.4 is used to approximately describe the electronic structure of realistic systems, the parameters  $U$  and  $J$  have to be determined for realistic systems. It turns out that the screening of the Coulomb repulsion has a very large effect especially on the value of  $U$ . If  $U$  is to be approximated by the unscreened value of the Coulomb interaction, one obtains values in the range of tens of electron volts. Instead, the screened value of  $U$  in correlated materials is typically a few electron volts. There are three main screening mechanisms:

1. the redistribution of  $s$  and  $d$  electrons on the atom,
2. the redistribution of electrons on neighboring atoms, and
3. the change of atomic wave functions that tends to minimize the energy of electrons occupying the given atom.

These effects must also be accounted for in the determination of  $J$ , although the exchange interaction is less affected by the screening. A variety of approaches exists

to take the screening effects into account when calculating  $U$  and  $J$  and there is no unique way of determining  $U$  and  $J$ . A detailed discussion of such methods is beyond the scope of this work. Therefore, I would like only to refer to the literature i.e. [SDA94] where descriptions of these techniques as well as a broad range of values for the parameters for  $d$  electrons of  $3d$  metals can be found.

To conclude this section, I like to return once more to the Hamiltonian (5.1). Comparing (5.1) to the new Hamiltonian (5.4) reveals that the second term of (5.1) was simply neglected in the modeling of (5.4). This term, the so-called double counting term, which was introduced in (5.1) to subtract the static interactions between the electrons, since they are contained twice in (5.1) once in the first term due to the DFT description but also in the third term that describes all pair interaction between the electrons. The contribution to the total energy of this term is by far not negligible. The treatment of this term within the modeling however is very difficult and it turns out to be a delicate topic, which has been discussed thoroughly in the literature i.e. [AZA91] or [LKK01]. To take the contribution of this term into account so-called double counting corrections can be introduced. For the present case a double counting correction will be suggested in the context of diagrammatic perturbation theory to be presented later in this chapter to correct the error, that was made by simply neglecting the double-counting term in the modeling of (5.4).

## 5.2 Green Functions in Perturbation Theory

The diagrammatic perturbation theory to be applied to the new model (5.4) is formulated in terms of Green functions. Therefore, a Green function for the multiband Hubbard model will be derived in this section. Afterwards I present an interpretation of this Green function and related quantities within the so-called *quasi-particle* picture.

### 5.2.1 A Green Function for the Multiband Hubbard Hamiltonian

The general definition of the time-ordered one-particle Green function (4.6) can be applied to write down an expression for the Green function of the multiband Hubbard model. The Green function is formulated in terms of the TB-FLAPW basis introduced in section 3.6 in chapter 3 with the creation and annihilation operators  $c_{\mathbf{R}L\sigma}^\dagger$  and  $c_{\mathbf{R}L\sigma}$  for the corresponding TB-FLAPW vector states  $|\mathbf{R}L\sigma\rangle$

$$G_{\mathbf{R}L,\mathbf{R}'L'}^\sigma(t-t') = -\frac{i}{\hbar} \langle |\hat{T}[c_{\mathbf{R}L\sigma}(t) c_{\mathbf{R}'L'\sigma}^\dagger(t')] | \rangle. \quad (5.6)$$

Since I express the new Green function with the operators of a lattice-type basis, I chose the notation  $G_{\mathbf{R}L,\mathbf{R}'L'}^\sigma$  for the new Green function in analogy to the notation used for the DFT lattice Green function  $G_{\mathbf{R}L,\mathbf{R}'L'}^{0\sigma}$  derived from the TB-FLAPW ansatz in section 4.3 of chapter 4. However, these lattice Green functions are by

no means identical, since  $G_{\mathbf{R}L, \mathbf{R}'L'}^\sigma$  describes an interacting system and  $G_{\mathbf{R}L, \mathbf{R}'L'}^{0\sigma}$  was totally determined by quantities from the DFT description, thus containing no interactions beyond the static mean field considered in DFT. Since the new Green function is used only to calculate collinear systems, it is convenient to calculate it for each spin separately, since it is diagonal in spin space.

To derive an explicit formula for  $G_{\mathbf{R}L, \mathbf{R}'L'}^\sigma(t-t')$  we start from the equation of motion for the one-particle propagator

$$i\hbar \frac{\partial}{\partial t} G(\lambda t, \lambda' t') = \delta(t-t')\delta(\lambda-\lambda') - \frac{i}{\hbar} \left\langle \hat{T} \left[ [\hat{\psi}(\lambda t), \hat{H}]_-; \hat{\psi}^\dagger(\lambda' t') \right] \right\rangle. \quad (\text{see 4})$$

If the Hamiltonian  $\hat{H}$  is replaced by the model Hamiltonian  $\hat{H}^{\text{Hubb}}$  and the field operators  $\hat{\psi}^\dagger$  and  $\hat{\psi}$  are replaced by the creation and annihilation operators  $c_{\mathbf{R}L\sigma}^\dagger$  and  $c_{\mathbf{R}L\sigma}$  a differential equation for the new lattice Green function is obtained

$$\begin{aligned} & i\hbar \frac{\partial}{\partial t} G_{\mathbf{R}L, \mathbf{R}'L'}^\sigma(t-t') \\ &= \delta(t-t')\delta_{\mathbf{R}\mathbf{R}'}\delta_{LL'} - \frac{i}{\hbar} \left\langle \hat{T} \left[ [c_{\mathbf{R}L\sigma}(t), \hat{H}^{\text{Hubb}}]_-; c_{\mathbf{R}'L'\sigma}^\dagger(t') \right] \right\rangle. \end{aligned}$$

The evaluation of the commutator in the second line is lengthy but straightforward. Therefore, I only state the result here:

$$\begin{aligned} & \left\langle \hat{T} \left[ [c_{\mathbf{R}L\sigma}(t), \hat{H}^{\text{Hubb}}]_-; c_{\mathbf{R}'L'\sigma}^\dagger(t') \right] \right\rangle \\ &= \sum_{\mathbf{R}''L''} H_{\mathbf{R}L, \mathbf{R}''L''}^{\text{DFT}\sigma} \left\langle \left| \hat{T} [c_{\mathbf{R}''L''\sigma}(t) c_{\mathbf{R}'L'\sigma}^\dagger(t')] \right| \right\rangle \\ &+ U \sum_{L''\sigma''} (1 - \delta_{LL''}\delta_{\sigma\sigma''}) \left\langle \left| \hat{T} [c_{\mathbf{R}L''\sigma''}^\dagger(t) c_{\mathbf{R}L''\sigma''}(t) c_{\mathbf{R}L\sigma}(t) c_{\mathbf{R}'L'\sigma}^\dagger(t')] \right| \right\rangle \\ &+ J \sum_{L''} (1 - \delta_{LL''}) \left\langle \left| \hat{T} [c_{\mathbf{R}L''\sigma}^\dagger(t) c_{\mathbf{R}L''\sigma}(t) c_{\mathbf{R}L\sigma}(t) c_{\mathbf{R}'L'\sigma}^\dagger(t')] \right| \right\rangle. \end{aligned} \quad (5.7)$$

The term in the second line can be substituted by the definition (5.6) of the Green function. The commutators in the third and fourth line are replaced by the newly defined quantity

$$K_{\mathbf{R}L, \mathbf{R}'L'; L''}^{\sigma\sigma''}(t-t') = -\frac{1}{\hbar^2} \left\langle \left| \hat{T} [c_{\mathbf{R}L''\sigma''}^\dagger(t) c_{\mathbf{R}L''\sigma''}(t) c_{\mathbf{R}L\sigma}(t) c_{\mathbf{R}'L'\sigma}^\dagger(t')] \right| \right\rangle \quad (5.8)$$

This is all to be inserted in equation (5.7). The Fourier transform of (5.7) is then given by

$$\begin{aligned} \epsilon G_{\mathbf{R}L, \mathbf{R}'L'}^\sigma(\epsilon) &= \delta_{\mathbf{R}\mathbf{R}'}\delta_{LL'} + \sum_{\mathbf{R}''L''} H_{\mathbf{R}L, \mathbf{R}''L''}^{\text{DFT}\sigma} G_{\mathbf{R}''L'', \mathbf{R}'L'}^\sigma(\epsilon) \\ &+ i\hbar U \sum_{L''\sigma''} (1 - \delta_{LL''}\delta_{\sigma\sigma''}) K_{\mathbf{R}L, \mathbf{R}'L'; L''}^{\sigma\sigma''}(\epsilon) \\ &+ i\hbar J \sum_{L''} (1 - \delta_{LL''}) K_{\mathbf{R}L, \mathbf{R}'L'; L''}^\sigma(\epsilon). \end{aligned} \quad (5.9)$$

The last two terms can be summarized by introducing a combined interaction  $v$  as

$$v_{LL'}^{\sigma\sigma'} = U(1 - \delta_{LL'}\delta_{\sigma\sigma'}) + J\delta_{\sigma\sigma'}(1 - \delta_{LL'}), \quad (5.10)$$

leading to

$$\begin{aligned} \epsilon G_{\mathbf{R}L, \mathbf{R}'L'}^{\sigma}(\epsilon) &= \delta_{\mathbf{R}\mathbf{R}'}\delta_{LL'} + \sum_{\mathbf{R}''L''} H_{\mathbf{R}L, \mathbf{R}''L''}^{\text{DFT}\sigma} G_{\mathbf{R}''L'', \mathbf{R}'L'}^{\sigma}(\epsilon) \\ &+ i\hbar \sum_{L''\sigma''} v_{LL''}^{\sigma\sigma''} K_{\mathbf{R}L, \mathbf{R}'L'; L''}^{\sigma\sigma''}(\epsilon). \end{aligned} \quad (5.11)$$

For the final step I use the relation

$$\sum_{\mathbf{R}''L''} \left( G_{\mathbf{R}L, \mathbf{R}''L''}^{0\sigma}(\epsilon) \right) \left( \epsilon\delta_{\mathbf{R}''\mathbf{R}'}\delta_{L''L'} - H_{\mathbf{R}''L'', \mathbf{R}'L'}^{\text{DFT}\sigma} \right) = \delta_{\mathbf{R}\mathbf{R}'}\delta_{LL'}. \quad (5.12)$$

(Relation (5.12) can be proved by simply evaluating the left-hand site.) The new lattice Green function is now given by

$$\begin{aligned} G_{\mathbf{R}L, \mathbf{R}'L'}^{\sigma}(\epsilon) &= G_{\mathbf{R}L, \mathbf{R}'L'}^{0\sigma}(\epsilon) \\ &+ i\hbar \sum_{L''\sigma''} G_{\mathbf{R}L, \mathbf{R}''L''}^{0\sigma}(\epsilon) \left( \sum_{L'''\sigma'''} v_{L''L'''}^{\sigma''\sigma'''} K_{\mathbf{R}''L'', \mathbf{R}'L'; L'''}^{\sigma''\sigma'''}(\epsilon) \right). \end{aligned} \quad (5.13)$$

Thus, the lattice Green function of the interacting system can be expressed in terms of the DFT lattice Green function of the non-interacting system and the quantity  $K_{\mathbf{R}L, \mathbf{R}'L'; L''}^{\sigma\sigma''}$  defined in (5.8). This quantity is also a Green function, which should be clear from its definition. Since it contains two creation and annihilation operators, it is a two-particle Green function further called two-particle propagator. The new one-particle propagator thus can be expressed using the two-particle propagator, which was to be expected according to the general discussion of the equation of motion in chapter 4. However, instead of solving another equation of motion to obtain the two-particle propagator, the chain of differential equations for the higher order Green functions is to be broken using the following relation

$$\sum_{L''\sigma''} v_{L''L'}^{\sigma\sigma''} K_{\mathbf{R}L, \mathbf{R}'L'; L''}^{\sigma\sigma''}(\epsilon) = -\frac{i}{\hbar} \sum_{\mathbf{R}''L''} \Sigma_{\mathbf{R}L, \mathbf{R}''L''}^{\sigma}(\epsilon) G_{\mathbf{R}''L'', \mathbf{R}'L'}^{\sigma}(\epsilon), \quad (5.14)$$

by introducing yet another new quantity  $\Sigma_{\mathbf{R}L, \mathbf{R}'L'}^{\sigma}(\epsilon)$ , the so-called *self-energy*. If (5.14) is substituted in (5.13) the famous Dyson equation is obtained

$$G_{\mathbf{R}L, \mathbf{R}'L'}^{\sigma}(\epsilon) = G_{\mathbf{R}L, \mathbf{R}'L'}^{0\sigma}(\epsilon) + \sum_{\substack{\mathbf{R}''\mathbf{R}''' \\ L''L'''}} G_{\mathbf{R}L, \mathbf{R}''L''}^{0\sigma}(\epsilon) \Sigma_{\mathbf{R}''L'', \mathbf{R}'''L'''}^{\sigma}(\epsilon) G_{\mathbf{R}'''L''', \mathbf{R}'L'}^{\sigma}(\epsilon) \quad (5.15)$$

If we now switch to a matrix notation of the Dyson equation

$$\hat{G}^{\sigma}(\epsilon) = \hat{G}^{0\sigma}(\epsilon) + \hat{G}^{0\sigma}(\epsilon) \hat{\Sigma}^{\sigma}(\epsilon) \hat{G}^{\sigma}(\epsilon) \quad (5.16)$$

with the new Green function  $\hat{G}^\sigma$ , the DFT Green function  $\hat{G}^{0\sigma}$  and the self-energy  $\hat{\Sigma}^\sigma$  considered to be matrix operators with elements for each combination of orbital indices  $L$  and  $L'$  and each pair of lattice sites  $\mathbf{R}$  and  $\mathbf{R}'$ , the Dyson equation directly yields

$$\hat{G}^\sigma(\epsilon) = \left[ \left[ \hat{G}^{0\sigma}(\epsilon) \right]^{-1} - \hat{\Sigma}^\sigma(\epsilon) \right]^{-1}. \quad (5.17)$$

for the operator of the new lattice Green function. To obtain a closed set of equations, an expression for the self-energy is derived from (5.14)

$$\Sigma_{\mathbf{R}L,\mathbf{R}'L'}^\sigma(\epsilon) = i\hbar \sum_{\substack{\mathbf{R}''L'' \\ L''\sigma''}} \left( v_{LL''}^{\sigma\sigma''} K_{\mathbf{R}L,\mathbf{R}''L'';L''}^{\sigma\sigma''}(\epsilon) \right) \left( G_{\mathbf{R}''L'',\mathbf{R}'L'}^\sigma(\epsilon) \right)^{-1}. \quad (5.18)$$

In the following section, I introduce the FLEX method to calculate the two-particle propagator (5.8), which is inserted into (5.18) to obtain the self-energy. With the self-energy the new lattice Green function can then be calculated which will be used in turn to calculate electron densities and spectral functions. Note that the equations (5.17) and (5.18) have to be solved self-consistently, since the self-energy itself is expressed in terms of the new lattice Green function. Before a solution of (5.18) is derived, I like to examine some properties of the self-energy, which can be best understood within the quasi-particle picture.

## 5.2.2 The Self-Energy and the Quasi-Particle Picture

If an electron or a hole moves through a crystal, the interaction with the other particles of the crystal will lead to a redistribution of those particles, such that the moving electron or hole will be surrounded by particles of the opposite charge. But the cloud of particles surrounding the initial particle in turn influences the movement of the initial particle. If the particle together with the cloud is understood as one entity called the quasi-particle, the real part of the self-energy gives the energy of this particle. The name ‘‘self-energy’’ thus originates from this quasi-particle picture, where it is interpreted as the energy of a particle caused by the particle itself due to interaction of the particle with its environment. The one-particle propagator of the interacting system is therefore also called the quasi-particle propagator.

If equation (5.17) is restated in the following way

$$\hat{G}^\sigma(\epsilon) = \hat{G}^{0\sigma}(\epsilon) \left[ 1 - \hat{G}^{0\sigma}(\epsilon) \hat{\Sigma}^\sigma(\epsilon) \right]^{-1} \quad (5.19)$$

it can be seen on the other hand that the one-particle propagator of the interacting system is obtained due to renormalization of the DFT Green function. The new Green function is therefore also called the renormalized Green function and the DFT Green function is called the unrenormalized Green function respectively. The quasi-particle picture then gives rise to the interpretation of the renormalized Green function as

propagator of a dressed particle, whereas the DFT Green function is the bare particle propagator in this interpretation. From the Dyson equation (5.16) however another interpretation of the self-energy can be derived related to the interpretation of the new lattice Green function as renormalized quantity. This is achieved by writing the Dyson equation as a geometric series by subsequently replacing  $\hat{G}^\sigma$  on the right-hand side of (5.16) by  $\hat{G}^{0\sigma} + \hat{G}^{0\sigma}\hat{\Sigma}^\sigma\hat{G}^\sigma$ , which leads to an infinite summation starting with the following terms

$$\hat{G}^\sigma(\epsilon) = \hat{G}^{0\sigma}(\epsilon) + \hat{G}^{0\sigma}(\epsilon)\hat{\Sigma}^\sigma(\epsilon)\hat{G}^\sigma(\epsilon) + \hat{G}^{0\sigma}(\epsilon)\hat{\Sigma}^\sigma(\epsilon)\hat{G}^\sigma\hat{\Sigma}^\sigma(\epsilon)\hat{G}^\sigma(\epsilon) + \dots \quad (5.20)$$

This is a typical equation of scattering theory, where the different terms of the geometric series describe single, double, triple, etc., scattering processes, and  $\hat{\Sigma}^\sigma$  is the scattering potential. The renormalized Green function  $\hat{G}^\sigma$  is expressed here by the unrenormalized Green function  $\hat{G}^{0\sigma}$  and all interaction processes of the unrenormalized Green function, which are contained in the self-energy  $\hat{\Sigma}^\sigma$ . In analogy to this interpretation of the self-energy, an expression of the two-particle propagator in terms of the vertex function will be introduced in the next section.

For now, I like to return once more to the quasi-particle picture. The quasi-particle loses energy due to interaction with its environment, hence, it will decay and has a finite life-time  $\tau$ . It can be shown that the imaginary part of the self-energy is inversely proportional to the life-time of the quasi-particle

$$\frac{1}{\tau} \sim \text{Im} \hat{\Sigma}^\sigma(\epsilon) . \quad (5.21)$$

When describing the system in terms of real particles, the decay of the quasi-particle is equivalent to the decay of an excited state and the excitation energy is redistributed within the crystal due to the interaction of the particles of the crystal among themselves. Because of the finite life-time of the quasi-particles or likewise because of the decay of excited states the peaks seen in photo-emission spectra have finite height and finite width. The spectral function calculated from the quasi-particle propagator shows the same features, since it incorporates the interaction among the particles. Within the quasi-particle picture it can be also understood now why these features are not reproduced when using the DFT Green function to derive the spectral functions, since the bare particle propagator does not describe the physical mechanisms giving rise to these features in the spectra.

## 5.3 The Language of Feynman Diagrams

In this small section, I want to present the diagrammatic notation I use to formulate equations in terms of diagrams. I assume that the reader is already acquainted with the rules of drawing diagrams and with their application in the context of many-body perturbation theory. Thus, this section is by no means a general introduction to the topic of Feynman diagrams because this would be well beyond the scope of this work.

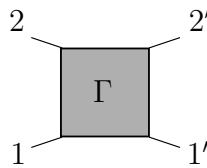
For an intuitive approach to Feynman diagrams I can refer the reader to the book by Mattuck [Mat67] and for a more mathematical introduction to the book by Fetter and Walecka [FW71].

The first part of this section is a compendium of the symbols to be used in the drawing of diagrams. In the second part, a diagrammatic expression of equation (5.18) for the self-energy in terms of the two-particle propagator is derived.

### 5.3.1 Vocabulary of the Diagrammatic Language

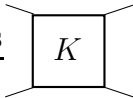
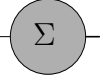
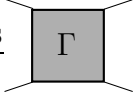
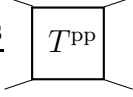
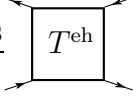
The intriguing idea of the diagrammatic notation of equations is to replace lengthy and complicated mathematical expressions by simple drawings. Of course, the math is still there but hidden in the diagrams, in the rules how to draw them and last but not least in the rules how to translate them back into formulas. The table of diagrammatic symbols 5.1 thus is not only a listing of all symbols to be used in this chapter. It also contains the prescription how to translate these symbols into a mathematical formula and in addition it gives a short description of all symbols. The list can be applied to translate whole equations from diagrammatic notation into a mathematical formulation using the following set of rules:

1. Each symbol in the equation is to be replaced by the corresponding expression listed in table 5.1. For convenience, the prefactors are already listed there as well.
2. The entries and exits of the diagrams in table 5.1 are labeled by the numbers  $1, 1', \dots$ . Each number represents the variables  $\mathbf{R}$ ,  $L$  and  $\sigma$  that have to be inserted into the mathematical expression instead of the label. The numbering of a diagram with two entries and two exits is always done as in the following example for the vertex function  $\Gamma$ :



3. Finally, a sum/an integration has to be carried out over all internal indices of the diagrammatic equation.

I like to mention explicitly that no time axis is associated when composing the diagrams. The diagrams are drawn using only the conventions of graph theory for drawing connected graphs and the symbols do not carry any additional meaning other than the one introduced in table 5.1. Consequently, the Green-function line represents both electrons and holes. For example, if all lines in a diagram carrying arrows that point into the same direction, the processes depicted in the diagram can

Symbol	Formula	Description
	$iG_{1,1'}(\epsilon)$	$G$ : Green function of the interacting system
	$i^2 K_{12,1'2'}(\epsilon_1, \epsilon_2; \epsilon_1 + \epsilon, \epsilon_2 \pm \epsilon)$	$K$ : two-particle propagator
	$-iv$	$v$ : pair interaction
	$\langle 12   -iv   1'2' \rangle - \langle 12   -iv   2'1' \rangle$	$\bar{V}$ : antisymmetrized pair interaction
	$-i\Sigma_{1,1'}(\epsilon)$	$\Sigma$ : self-energy
	$\langle 12   i\Gamma(\epsilon_1, \epsilon_2; \epsilon_1 + \epsilon, \epsilon_2 - \epsilon)   1'2' \rangle$	$\Gamma$ : vertex function
	$\langle 12   -iT^{\text{pp}}(\epsilon)   1'2' \rangle$	$T^{\text{pp}}$ : particle-particle T-matrix
	$\langle 12   -iT^{\text{eh}}(\epsilon)   1'2' \rangle$	$T^{\text{eh}}$ : electron-hole T-matrix

**Figure 5.1:** List of all diagrammatic symbols used in this chapter.

take place between two particles with the same charge. Thus, the same diagram describes the process between two electrons and also between two holes. If a Green-function line or an entry or an exit in a diagram does not carry any arrow, it means that the same diagram can be drawn with arrows pointing in one direction and also with the arrows pointing into the other direction.

The wiggly line in the list of diagrammatic symbols represents the pair interaction. It can symbolize either the direct or the exchange interaction, hence it corresponds to the combined interaction  $v$  defined in (5.10). If the interaction vertex is drawn explicitly for the direct and the exchange interaction

$$\begin{array}{ccc}
 \begin{array}{c} L\sigma \quad L\sigma \\ \swarrow \quad \searrow \\ \text{wiggly line} \\ \swarrow \quad \searrow \\ L'\sigma' \quad L'\sigma' \end{array} & & \begin{array}{c} Ls \quad L'\sigma \\ \swarrow \quad \searrow \\ \text{wiggly line} \\ \swarrow \quad \searrow \\ L'\sigma \quad Ls \end{array} \\
 & & (5.22)
 \end{array}$$

where in these example graphs the entries and exits of the vertices were explicitly denoted by the states of the incoming and outgoing particles, it becomes obvious why the interaction was called direct for one case and exchange for the other: In the first case, the interaction takes place between particles which are in the same state before and after the interaction. During the exchange interaction one particle changes from its initial state to the initial state of the other particle and vice versa. Therefore, the exchange interaction can only occur between particles having the same spin and the same charge, whereas the direct interaction can also occur between particles with opposite charge.

The definition of the antisymmetrized interaction  $\bar{V}$  from table 5.1 can be written in terms of diagrams as

$$\begin{array}{ccc}
 \begin{array}{c} \square \\ \swarrow \quad \searrow \\ \swarrow \quad \searrow \end{array} & = & \begin{array}{c} \swarrow \quad \searrow \\ \text{wiggly line} \\ \swarrow \quad \searrow \end{array} - \begin{array}{c} \swarrow \quad \searrow \\ \text{wiggly line} \\ \swarrow \quad \searrow \end{array} \\
 & & (5.23)
 \end{array}$$

The matrix elements of the Coulomb repulsion are to be replaced by the direct interaction term of the multiband Hubbard model, since the antisymmetrized pair interaction is introduced here solely for interactions between an electron and a hole. Hence, the lines of incoming and outgoing states are marked with arrows pointing into opposite directions. It should be mentioned that this quantity is only a combination of the (non-symmetrized) pair interaction and thus it does not describe any new kind of interaction. It is only a different way to represent the pair interaction  $V$  in diagrammatic language but it can simplify the drawing of diagrams significantly.

### 5.3.2 Two-Particle Propagator and Self-Energy

In the previous section, I derived an expression for the self-energy in terms of the interacting Green function and the two particle propagator

$$\Sigma_{\lambda,\lambda'}^{\sigma}(\epsilon) = i\hbar \sum_{\lambda''\lambda''',\sigma} \left( v_{\lambda\lambda''}^{\sigma\sigma'} K_{\lambda\lambda''\lambda'''}^{\sigma\sigma'}(\epsilon) \right) \left( G_{\lambda'''\lambda'}^{\sigma'}(\epsilon) \right)^{-1}, \quad (\text{see 5.18})$$

where the indices  $\mathbf{R}$  and  $L$  in equation (5.18) are replaced by the multiindex  $\lambda$  here to simplify the notation. So far, this expression for the self-energy is of little use, since both the two-particle propagator as well as the interacting Green function are unknown.

However, we can rewrite this equation in terms of diagrams now. In order to do so, I introduce the following picture for the self-convoluted two-particle propagator  $K_{\lambda\lambda''\lambda'''}^{\sigma\sigma'}$ , which is a two-particle propagator with one entry and one exit at the same site  $\lambda$  by

$$K_{\lambda_1\lambda_2;\lambda_1'\lambda_2'}^{\sigma\sigma'} = \begin{array}{c} \lambda_2\sigma' \\ \square \\ \lambda_1\sigma \end{array} \xrightarrow{\text{self convolution}} \begin{array}{c} \lambda'''\sigma' \\ \text{---} \\ \square \\ \lambda\sigma \end{array} = K_{\lambda\lambda''\lambda'''}^{\sigma\sigma'} \quad (5.24)$$

Note that the closed loop is not a Green-function line added to the non-self-convoluted diagram but it is a Green-function line that is already contained in the two-particle propagator. With this definition, the diagrammatic expression for the self-energy in terms of the two-particle propagator and the one-particle propagator is given by

$$\Sigma = \begin{array}{c} \text{---} \\ \text{---} \\ \text{---} \end{array} \text{---} \Sigma \text{---} \begin{array}{c} \text{---} \\ \text{---} \\ \text{---} \end{array} = \begin{array}{c} \text{---} \\ \text{---} \\ \text{---} \end{array} \begin{array}{c} \text{---} \\ \square \\ \text{---} \end{array} \begin{array}{c} \lambda'''\sigma' \\ \text{---} \\ \lambda\sigma \end{array} \left[ \text{---} \right]^{-1} \quad (5.25)$$

In the next step, an diagrammatic expansion for the two-particle propagator is introduced. From the general definition (5.8) of the two-particle propagator, it is known that  $K$  must contain all two-particle processes. Therefore the two-particle propagator is expanded here in terms of two non-interacting one-particle propagators and

the vertex function  $\Gamma$

$$\begin{aligned}
 \boxed{K} &= \begin{array}{c} \longrightarrow \\ \longrightarrow \end{array} - \begin{array}{c} \diagdown \\ \diagup \end{array} + \begin{array}{c} \longleftarrow \\ \longrightarrow \end{array} \\
 &+ \begin{array}{c} \longrightarrow \\ \longrightarrow \\ \Gamma \end{array} - \begin{array}{c} \longrightarrow \\ \longrightarrow \\ \Gamma \\ \diagdown \\ \diagup \end{array} \\
 &+ \begin{array}{c} \longrightarrow \\ \longleftarrow \\ \Gamma \end{array}
 \end{aligned} \tag{5.26}$$

In analogy to the self-energy containing all interaction processes between one particle and the surrounding medium, the vertex function is to contain all pair interaction processes between two particles. Note that in the expansion of the two-particle propagator as well as in all diagrams derived from equation (5.26) the one-particle Green functions of the interacting system has to be used. Furthermore, it should be mentioned that the first three terms are not simply products of two Green-function lines but these products have to be convoluted as well. Thus, term one and two are all contained in the bare particle-particle propagator, defined by

$$\Psi_{\lambda_1\lambda_2;\lambda'_1\lambda'_2}^{\sigma\sigma'}(\epsilon) = i \int_{-\infty}^{\infty} \frac{d\epsilon'}{2\pi} G_{\lambda_1\lambda'_1}^{\sigma}(\epsilon - \epsilon') G_{\lambda_2\lambda'_2}^{\sigma'}(\epsilon') \tag{5.27}$$

whereas the third term is the bare electron-hole propagator

$$\Phi_{\lambda_1\lambda_2;\lambda'_1\lambda'_2}^{\sigma\sigma'}(\epsilon) = i \int_{-\infty}^{\infty} \frac{d\epsilon'}{2\pi} G_{\lambda_1\lambda'_1}^{\sigma}(\epsilon + \epsilon') G_{\lambda_2\lambda'_2}^{\sigma'}(\epsilon'). \tag{5.28}$$

If the expansion for the two-particle propagator (5.26) is inserted into equation (5.25), the self-energy is expressed in terms of the vertex function and the one-particle propagator

$$\begin{aligned}
 \text{---} \Sigma \text{---} &= \begin{array}{c} \circlearrowleft \\ \text{---} \\ \text{---} \end{array} - \begin{array}{c} \text{---} \\ \text{---} \\ \text{---} \end{array} + \begin{array}{c} \text{---} \\ \text{---} \\ \Gamma \\ \text{---} \end{array} \\
 &+ \begin{array}{c} \text{---} \\ \text{---} \\ \Gamma \\ \text{---} \end{array} - \begin{array}{c} \text{---} \\ \text{---} \\ \Gamma \\ \text{---} \end{array}
 \end{aligned} \tag{5.29}$$

The first two terms yield the contribution to the self-energy due to the static interaction with the charge background caused by other particles in the system, which can also be obtained from Hartree-Fock theory. Furthermore, this contribution is already partly contained in the DFT description of the system. This is to be kept in mind and will be treated when a double-counting correction is introduced.

In the last three terms two Green-function lines are connected to the vertex function  $\Gamma$ , which stands for the fluctuation-exchange interaction between these two particles. Thus, this part in each diagram depicts pair fluctuation-exchange interaction processes. These pair interaction processes in each diagram are contracted with another Green-function line to yield the contributions to the self-energy. Hence, the last three terms describe the contribution to the self-energy due to the interaction of a quasi-particle with all pair fluctuation processes. This expression for the self-energy will be further evaluated within the framework of the FLEX method.

## 5.4 The FLEX Method

The fluctuation-exchange (FLEX) method is a simple approximation to determine the vertex function describing the exchange fluctuation interaction between a pair of quasi-particles retaining the correlation between these particles. Within FLEX an expression for the vertex function is obtained by expansion in terms of Feynman diagrams and then by selecting sub-classes of these diagrams, which are summed up to infinite order using geometric series. The diagrams are selected such that only these fluctuations between the pair of particles are taken into account which correspond to multiple scattering processes of these particles. The selected diagrams are thought to describe processes important for materials within the regime of the weak and intermediate correlation. However, if the correlation strength becomes stronger, the FLEX description becomes more and more insufficient, because it does not reproduce the Mott metal-insulator transition since the diagrams yielding an important contribution to the description of the transition are not contained in the subclasses of the FLEX diagrams.

The FLEX method was introduced by Bickers and Scalapino in 1989 [BS89], who also named the method FLEX. However, the same diagrams and equations were already derived between 1971 and 1973 by Y. U. Babanov *et al.* [BNSF71], [BNSF73a] and [BNSF73b]. The derivation of FLEX presented here is based on the works by Y. U. Babanov *et al.* using their notation of FLEX, because it is much simpler and much more transparent than the derivation and notation used by Bickers and Scalapino while yielding the same results. Furthermore, the FLEX equations will be derived here for the description of collinear systems, which is an extension to the original formulation of both groups of authors. A similar yet not identical extension of the original FLEX method to spin-polarized systems was introduced by Katsnelson and Lichtenstein [LK98] and [KL99], which is named SPTF for "Spin-polarized T-matrix FLEX" method.

I will first derive a set of equations to calculate the vertex function. These expressions are further simplified using the so-called *ladder approximation* and finally the approximated vertex-function will be used to find an expression to determine the self-energy of the multiband Hubbard model.

### 5.4.1 Equations for the Vertex Function $\Gamma$

The vertex function  $\Gamma$  is a connected quadrupole with two entry and two exit vertices. For the sake of clarity, I like to point out again that the entries and exits are labeled according to the following definition

$$\langle 12 | i\Gamma | 1'2' \rangle \equiv \begin{array}{c} 2 \qquad 2' \\ \diagdown \quad \diagup \\ \Gamma \\ \diagup \quad \diagdown \\ 1 \qquad 1' \end{array} . \quad (5.30)$$

The diagrammatic expansion of the vertex function contains many different diagrams. The set of all this diagrams shall be denoted by  $M$ . Three ways of cutting the diagrams contained in  $M$  along two Green-function lines can be distinguished:

1. a cut of the first kind separates the entries  $(1, 2)$  from the exits  $(1', 2')$ ,
2. a cut of the second kind separates the vertices  $(1, 1')$  from  $(2, 2')$ ,
3. a cut of the third kind separates the endings  $(1, 2')$  from  $(2, 1')$ .

All diagrams contained in  $M$  can now be classified with respect to the possibility if they can be separated by a cut of kind  $i$ ,  $i = 1, 2, 3$  or if they can not be separated. Hence, the following subsets of diagrams can be defined:

- set  $m_i$  contains all diagrams that can be separated by a cut of the  $i$ 'th kind,
- set  $M_i$  denotes all diagrams that can NOT be separated by a cut of the  $i$ 'th kind and
- set  $R$  contains all diagrams that can NOT be separated by a cut of ANY kind.

To make this classification a little more transparent, some first and second order diagrams of the expansion of the vertex function are depicted in figure 5.2. The diagrams of the first order  $1a$  and  $1b$  contain no Green-function lines, hence they can not be cut along such lines. Therefore, they belong to subset  $R$  and to all subsets  $M_1, M_2, M_3$ . The diagram  $2a$  belong to  $m_1, M_2, M_3$ ,  $2b$  belongs to  $m_2, M_1, M_3$  and  $2c$  belongs to  $m_3, M_1, M_2$ .

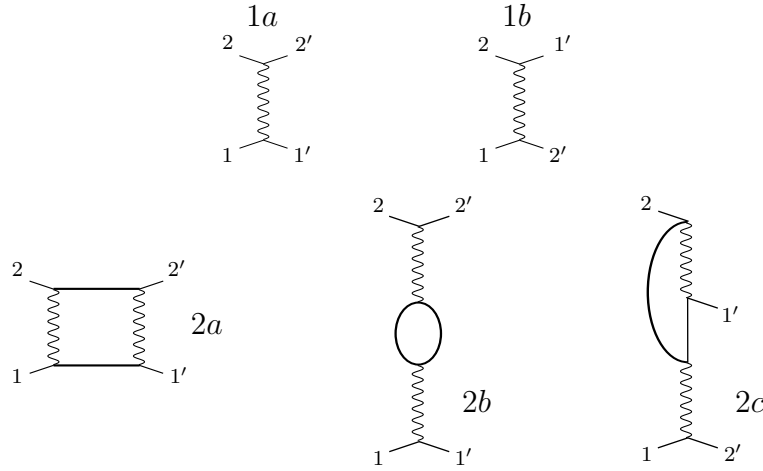


**Figure 5.2:** Selected first and second order diagrams of the vertex function

From the classification of diagrams, it should be obvious that all diagrams have to be contained at least in one subset. In figure 5.3 it is shown graphically how the complete set of diagrams  $M$  composing  $\Gamma$  can be separated into the subsets of diagrams. All diagrams contained in subset  $M_1$  for example can not be separated per definition by a cut of kind 1 but they might be separated with respect to the cuts of kind 2 and 3. Thus, each subset  $M_i$  is composed of the other subsets  $m_j, j \neq i$  and  $R$

$$M_1 = R + m_2 + m_3, \quad M_2 = R + m_1 + m_3, \quad M_3 = R + m_1 + m_2. \quad (5.31)$$

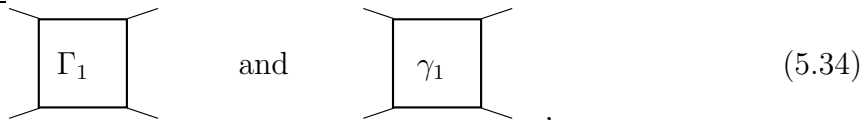
Furthermore, the whole set of all diagrams of  $M$  can obviously be constructed of the subsets  $m_i$  and  $R$ :

$$M = R + m_1 + m_2 + m_3. \quad (5.32)$$

which yields together with (5.31)

$$M = M_i + m_i, \quad i = 1, 2, 3. \quad (5.33)$$

Equation (5.33) is now used to derive a closed integral equation for the vertex function  $\Gamma$ . In order to do that, I introduce two vertex functions



which are to contain all processes described by all diagrams contained in the subsets  $M_1$  and  $m_1$  respectively. Per definition,  $\gamma_1$  contains all graphs, which can be separated by cutting two Green-function lines using a cut of kind 1. The diagrammatic

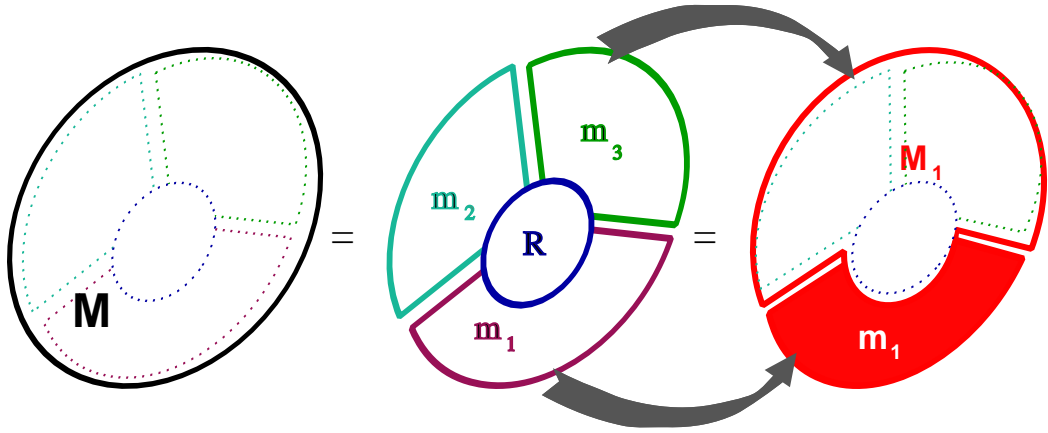


**Figure 5.3:** Relations between the subsets of diagrams composing  $\Gamma$

expansion of vertex function  $\gamma_1$  is therefore given by an infinite sum of diagrams, where the first terms are depicted by

$$\boxed{\gamma_1} = \boxed{\Gamma_1} \boxed{\Gamma_1} + \boxed{\Gamma_1} \boxed{\Gamma_1} \boxed{\Gamma_1} + \boxed{\Gamma_1} \boxed{\Gamma_1} \boxed{\Gamma_1} \boxed{\Gamma_1} + \dots \quad (5.35)$$

The relation between the subsets of diagrams (5.33) is used to rewrite this infinite series in terms of the vertex function  $\Gamma$

$$\begin{aligned} \boxed{\gamma_1} &= \boxed{\Gamma_1} \boxed{\Gamma_1} + \boxed{\Gamma_1} \boxed{\gamma_1} \\ &= \boxed{\Gamma_1} \times \left( \boxed{\Gamma_1} + \boxed{\gamma_1} \right) \\ &= \boxed{\Gamma_1} \boxed{\Gamma} \end{aligned} \quad (5.36)$$

and a closed integral equation for  $\Gamma$  can be obtained by inserting (5.36) into (5.33).

$$\begin{aligned} \boxed{\Gamma} &= \boxed{\Gamma_1} + \boxed{\gamma_1} \\ &= \boxed{\Gamma_1} + \boxed{\Gamma_1} \boxed{\Gamma} \end{aligned} \quad (5.37)$$

This equation is the so-called *horizontal equation* [BNSF71]. For the sake of completeness it should be mentioned here that two other integral equations for  $\Gamma$  can also

be derived in a similar way based on cuts of kind 2 and 3. They were named *vertical* and *parquet equation*. However, these equations will not be discussed here because they are not used in the FLEX method. In the next sections, an approximation for  $\Gamma_1$  is suggested such that (5.37) can be used to determine the vertex function.

### 5.4.2 The Horizontal Ladder Approximation

The name *horizontal ladder approximation* was also introduced by Babanov *et al.* and denotes the procedure to replace the vertex function  $\Gamma_1$  in the horizontal equation (5.37) by its lowest-order diagram which is simply the interaction  $v$  (or the antisymmetrized interaction  $\bar{V}$ ). This procedure leads to a selection of subsets of diagrams contained in the diagrammatic expansion of the vertex function  $\Gamma$ . One of these subsets contains the diagrams known as ladder diagrams which are retained in the “conventional” ladder approximation but in the horizontal ladder approximation in the sense of Babanov *et al.* a variety of additional diagrams is also retained as can be seen below. If this approximation is imposed, the remaining diagrams can be divided into two subsets:

- **Particle-Particle Channel:** This set contains only diagrams that describe processes between two particles with the same charge (either one electron with another electron or a hole with another hole).
- **Electron-Hole Channel:** This set contains only diagrams that describe processes between an electron and a hole.

The horizontal ladder approximation only retains diagrams from the expansion of  $\Gamma$ , that belong to either one subset. Speaking from a more physical point of view, in the description of a system with the FLEX method there are no processes contained where the interaction of a particle pair with identical charges is combined with the interaction of an electron-hole pair in one single process. For the discussion of the ladder approximation it is convenient to analyze the diagrammatic equations for each channel separately.

**Particle-Particle Channel.** If we consider only those diagrams with Green-function lines carrying arrows which point into the same direction, replacing the vertex function  $\Gamma_1$  in (5.37) by the interaction line  $v$  yields the horizontal ladder approximation for the particle-particle vertex function. The first term of the infinite sum of diagrams can be depicted as

$$\boxed{\Gamma} \approx \text{wavy line} + \text{two wavy lines with arrows} + \text{two wavy lines with arrows and a loop} + \dots = \boxed{T^{\text{PP}}} , \quad (5.38)$$

where the particle-particle T-matrix  $T^{\text{PP}}$  was introduced as the quantity containing the result of the summation over the infinite number of diagrams. All diagrams to

be contained in  $T^{\text{pp}}$  are made up of vertical interaction lines connected by a pair of horizontal Green-function lines. Because of this structure the diagrams are called ladder diagrams and the name *ladder approximation* originates from this subset of diagrams. The infinite sum of ladder diagrams in (5.38) corresponds to a geometric series. Thus, a closed integral equation for the particle-particle T-matrix can be obtained

$$T^{\text{pp}} = \text{wavy line} + \text{wavy line} \text{---} \text{solid line} \text{---} \text{wavy line} . \quad (5.39)$$

To derive a mathematical formula for  $T^{\text{pp}}$  from (5.39) the particle-particle propagator  $\Psi$  defined in (5.27) can be used to express  $T^{\text{pp}}$  in matrix operator notation as

$$\begin{aligned} T^{\text{pp}}(\epsilon) &= v + v \hat{\Psi}(\epsilon) T^{\text{pp}}(\epsilon) \\ &= v + v \hat{\Psi}(\epsilon) v + v \hat{\Psi}(\epsilon) v \hat{\Psi}(\epsilon) v + v \hat{\Psi}(\epsilon) v \hat{\Psi}(\epsilon) v \hat{\Psi}(\epsilon) v + \dots \end{aligned} \quad (5.40)$$

which can be solved using the geometric series yielding.

$$T^{\text{pp}}(\epsilon) = v [1 - \Psi(\epsilon) v]^{-1} . \quad (5.41)$$

The vertex function in the particle-particle channel is thus approximated by a sum over ladder diagrams yielding the particle-particle T-matrix  $T^{\text{pp}}$ . In figure 5.4 the first three lowest-order diagrams forming the ladder diagram series are depicted. These ladder diagrams describe the repeated scattering of two particles with the same charge. In diluted electron systems with a short-range repulsive potential the electron-electron ladder diagrams are the leading term in the diagrammatic expansion of the exact self-energy (see i.e. [FW71]). Hence, the electron-electron ladder diagrams from the particle-particle channel yield a good description for the electron system in the limit of small electron densities. The expansion of the self-energy in terms of the electron-electron ladder approximation is conventionally referred to as “the” ladder approximation. The horizontal ladder approximation in the sense of Babanov *et al.* contains already more types of diagrams in the particle-particle channel namely the hole-hole ladder approximation and in addition to that contains a whole subset of diagrams in the electron-hole channel which are not retained in the conventional ladder approximation. These diagrams belong to the electron-hole channel.

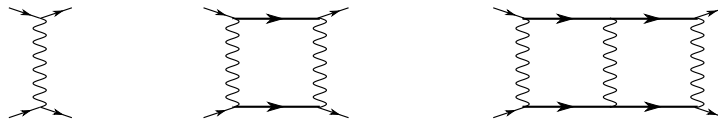


**Figure 5.4:** First, second and third order ladder diagram

**Electron-Hole Channel.** In this channel the vertex function  $\Gamma_1$  in (5.37) is replaced by the symmetrized interaction defined in (5.23). This also yields an infinite sum over diagrams

$$\boxed{\Gamma} \approx \text{diagram 1} + \text{diagram 2} + \text{diagram 3} + \dots = \boxed{T^{eh}} \quad (5.42)$$

where the electron-hole T-matrix  $T^{eh}$  was introduced. A closed integral equation for this T-matrix is given by

$$\boxed{T^{eh}} = \text{diagram 1} + \text{diagram 2} \quad (5.43)$$

I like to further expand the electron-hole T-matrix by inserting the definition of the antisymmetrized interaction (5.37). Furthermore, I like to make use of the underlying cubic symmetry of the crystal. It was already discussed in chapter 4 upon introducing the DFT lattice Green function that the electronic states at one atomic site do not overlap due to the cubic symmetry. Therefore, if an electron and a hole interact the final state of the electron and the hole has to be identical to the initial states for both particles if only those process between particles at the same lattice site are consider. If the electron-hole T-matrix is expanded only in terms of Green functions of particles located at the same lattice site only two subsets of all the diagrams contained in the expansion of  $T^{eh}$  are retained. One subset contains only diagrams with vertical interaction lines further referred to as electron-hole channel 1 (eh1) and the other subset contains only horizontal interaction lines and shall be denoted as electron-hole channel 2 (eh2). Due to the symmetry local processes between an electron and a hole described by diagrams containing horizontal and vertical interaction lines at the same time can not occur.

For each subsets of diagrams a closed integral equation of the same form as equation (5.43) can be derived. Consequently, two electron-hole T-matrices further denoted as  $T_1^{eh}$  and  $T_2^{eh}$  can be introduced by

$$\boxed{T_1^{eh}} = \text{diagram 1} + \text{diagram 2} \quad (5.44)$$

for the electron-hole channel 1 and for the electron-hole channel 2 by

$$\boxed{T_2^{eh}} = \text{diagram 1} + \text{diagram 2} \quad (5.45)$$

I like to point out once more that by replacing the full electron-hole T-matrix  $T^{eh}$  by  $T_1^{eh}$  and  $T_2^{eh}$  an additional approximation is introduced which is identical to neglecting all diagrams in the expansion of  $T^{eh}$  describing inter-atomic processes. However, it

will be demonstrated in the next chapter, that this approximation is justified if the diagrams are finally evaluated within the framework of dynamical mean-field theory.

Figure 5.5 shows some examples of diagrams from the electron-hole channel 1 in the first row and from the electron-hole channel 2 in the second line. The diagrams from the electron-hole channel 1 have the same structure as the diagrams in the particle-particle channel and describe multiple scattering processes between an electron and a hole. The diagrams of the second electron-hole channel are all composed of one interaction lines with a certain number of electron-hole bubble inserted into the line. In the lowest order one electron-hole bubble is inserted as depicted in the first example graph in 5.5 and for higher orders more electron-hole bubbles are inserted. These diagrams depict the screening of the Coulomb repulsion due to pair interaction fluctuations and have the same topology as the diagrams that yield the self-energy in the *GW* method. These diagrams are known to give an important contribution to the self-energy of the degenerated high-density electron gas (see i.e. [FW71]). In the limit of high electron density, this subclass of diagrams contribute the leading term to the diagrammatic expansion of the exact self-energy. Since the FLEX method contains both subclasses of diagrams yielding the exact self-energy in the case of low and high electron densities FLEX is also thought to yield an accurate extrapolation for system with intermediate densities.

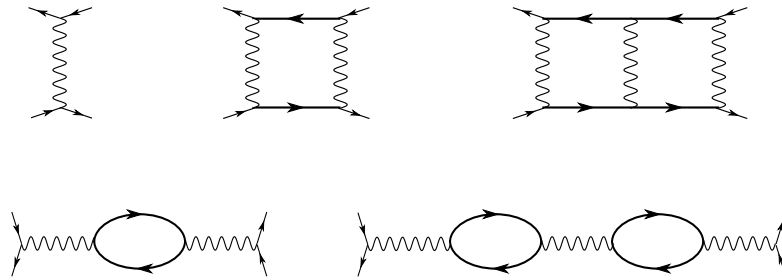


**Figure 5.5:** The first row shows example graphs from the eh1-channel, the second row shows two graphs from the eh2-channel

### 5.4.3 Determining the Self-Energy within FLEX

I return now to the diagrammatic expansion of the self-energy  $\Sigma^\sigma$  in terms of the vertex function  $\Gamma$  given by

$$\Sigma = \text{bubble} - \text{self-energy loop} + \text{Γ with bubble} + \text{Γ with bubble and loop} \quad (\text{see 5.29})$$

If the FLEX approximation to the vertex function is inserted into this expression, the self-energy can be decomposed into a sum over four different terms, which are depicted below.

The first contribution  $\Sigma^{\sigma \text{ HF}}$  contains the first two graphs, which could be also obtained within Hartree-Fock theory

$$\Sigma^{\sigma \text{ HF}} = \text{bubble} - \text{self-energy loop} \quad (5.46)$$

The second order terms from the expansion of the vertex function are summarized in  $\Sigma^{\sigma (2)}$  and can be drawn as

$$\Sigma^{\sigma (2)} = \text{bubble with wavy lines} - \text{crossed lines} \quad (5.47)$$

The last two contributions originate from the particle-particle T-matrix

$$\Sigma^{\sigma \text{ PP}} = \text{T}^{\text{PP}} \text{ with bubble} - \text{T}^{\text{PP}} \text{ with bubble and loop} \quad (5.48)$$

and from the electron-hole T-matrix

$$\Sigma^{\sigma \text{ eh}} = \text{T}^{\text{eh}} \text{ with bubble} \quad (5.49)$$

where the contribution from the electron-hole channel is depicted here using the full electron-hole T-matrix calculated from the antisymmetrized interaction. If only local electron-hole interactions are taken into account the single term above can be replaced by a sum over two terms of the same structure for the electron-hole channel 1 and the electron-hole channel 2 respectively yielding two contributions  $\Sigma^{\sigma \text{ eh}1}$  and  $\Sigma^{\sigma \text{ eh}2}$  to the full FLEX self-energy where the first contribution is obtained by replacing  $T^{\text{eh}}$  in (5.49) by  $T^{\text{eh}1}$  and the second by inserting  $T^{\text{eh}2}$  instead of  $T^{\text{eh}}$  in (5.49).

An diagrammatic expansion of the FLEX self-energy is thus obtained by summing up the different parts depicted above. If all double-counting corrections are taken into account, the FLEX self-energy is given by

$$\Sigma_{\lambda\lambda'}^{\sigma}(\epsilon) = \Sigma_{\lambda\lambda'}^{\sigma(2)}(\epsilon) + \Sigma_{\lambda\lambda'}^{\sigma \text{ PP}(3)}(\epsilon) + \Sigma_{\lambda\lambda'}^{\sigma \text{ eh}(3)}(\epsilon). \quad (5.50)$$

The double-counting corrections can be carried out in two steps.

The first order term of the diagrammatic expansion of the self-energy contributions from the particle-particle channel and the electron-hole channel yield the same contribution as contained in  $\Sigma^{\sigma \text{ HF}}$  and the second order term leads to diagrammatic contributions to the self-energy of the same kind as  $\Sigma^{\sigma(2)}$ . Hence, in order to avoid multiple counting of contributions like  $\Sigma^{\sigma \text{ HF}}$  and  $\Sigma^{\sigma(2)}$  to the self-energy the second and third term are included here starting from third-order graphs as denoted by the superscript <sup>(3)</sup>.

Secondly, the Hartree-Fock self-energy contribution is completely neglected in the calculation of the self-energy in order to take care of the *double-counting correction* introduced at the very beginning of this chapter in the TB description of the electronic system (5.1). The double-counting correction term was introduced in (5.1) to formally subtract the contributions describing electronic correlation which are contained in the electron-electron interaction term but which are also contained already in the DFT description of the system. DFT calculations carried out in the GGA in the present context yield a local single-particle mean field description of the electronic system. On the other hand, describing the electronic system approximately only in terms of the Hartree-Fock (HF) diagrams also leads to a mean-field type yet non-local description of the electronic system. Thus, within GGA and the HF approximation the electronic system is described in a mean-field type manner. In particular, both descriptions do not take into account correlation effects originating from true particle-particle interaction. Hence, if the self-energy is calculated using (5.50) it will only contain contributions neither contained in the DFT description nor contained in the Hartree-Fock term and by assuming that the DFT mean-field description is of the same type than the HF description the latter is not taken into account. It is however clear that the two contributions from the HF diagrams and from the GGA will not cancel out completely and might even differ substantially since both the HF approximation and the GGA are obtained by applying completely different approximation techniques.

In general, if we assume for a moment that the exact self-energy of the interacting system is known, it can be seen directly, that the contributions from the exchange-correlation potential would have to be completely omitted from the description of

the system since the following relations hold: The connection between the interacting Green function  $G$  of an arbitrary electronic system and the bare Green function  $G_0$  describing a non-interacting particle is given by

$$G(\epsilon) = G_0(\epsilon) + G_0(\epsilon)\Sigma(\epsilon)G(\epsilon), \quad (5.51)$$

where  $\Sigma$  now is the exact self-energy of the interacting system. For the Kohn-Sham Green function  $G_{\text{KS}}$  a similar equation is valid

$$G_{\text{KS}}(\epsilon) = G_0(\epsilon) + G_0(\epsilon)V_{\text{xc}}G_{\text{KS}}(\epsilon), \quad (5.52)$$

where  $V_{\text{xc}}$  is the exact exchange-correlation potential. It follows immediately, that  $G$  can be obtained from  $G_{\text{KS}}$  by

$$G(\epsilon) = G_{\text{KS}}(\epsilon) + G_{\text{KS}}(\epsilon)[\Sigma(\epsilon) - V_{\text{xc}}]G(\epsilon). \quad (5.53)$$

Hence, if  $\Sigma$  and  $V_{\text{xc}}$  could be determined exactly the double-counting correction can be carried out straightforwardly. However, in practice the self-energy is only determined approximately e.g. by evaluating only the contribution of certain subsets of diagrams contained in the diagrammatic expansion of the self-energy. On the other hand, the exact exchange-correlation potential  $V_{\text{xc}}$  is also not known but is approximated by a parametrizations of  $V_{\text{xc}}$  in the LDA or GGA. Whereas the diagrammatic contributions to the self-energy are explicitly calculated for particles in certain states yet not all diagrams in the expansion of  $\Sigma$  are calculated the parametrization of  $V_{\text{xc}}$  in general makes it impossible to single out the contributions of distinct electronic states to the approximate form of the exchange-correlation potential. There are most like contributions contained already in the lowest order (Hartree-Fock) diagrams of the self-energy that are not contained in the parametrized  $V_{\text{xc}}$  and vice versa. Consequently, simply subtracting  $V_{\text{xc}}$  from  $\Sigma$  will no longer yield the correct description of the electron system. One might however still argue, that the HF approximation is consistent with the perturbative many-body approach whereas the DFT description is not and thus the Green function  $G_0$  would better be determined from the HF approximation. However, the self-energy correction obtained from the FLEX method is treated as a perturbation to the non-interacting system and the quality of such an perturbative approach depends on the choice of the starting point. Since it is well known that LDA or GGA for metals yield a description much more in agreement with experiments than the HF approximation, the LDA or GGA description is the favorable starting point. To conclude this discussion it might be worth mentioning that all possibilities considered by other authors to introduce double-counting correction terms in practical calculations are equally based on an approximate scheme and no procedure has been found yet to derive an analytic expression for the double-counting correction, so that there remains some degree of arbitrariness how to incorporate the double-counting correction.



# 6 Dynamical Mean-Field Theory

The introduction of the multiband Hubbard model (5.4) allowed to include the pair interaction explicitly into the mean-field DFT description. By applying the FLEX method an expression for the self-energy was derived to approximately determine the self-energy and in turn to calculate the one-particle Green function of this new model. However, a huge computational effort is necessary to calculate the full non-local FLEX self-energy  $\Sigma_{\mathbf{R}L,\mathbf{R}'L'}^\sigma(\epsilon)$  or likewise the momentum-dependent Fourier transform  $\Sigma_{L,L'}^\sigma(\mathbf{k};\epsilon)$ . Therefore, the self-energy is to be calculated using a single-site approximation (SSA) such that only the on-site part of the self-energy is to be calculated and the off-site matrix elements are set to zero. This is of course equivalent to the neglect of the  $\mathbf{k}$ -dependence of the Fourier transform. However, instead of simply neglecting the  $\mathbf{k}$ -dependence of the self-energy, the SSA is to be applied in a way that corresponds to the so-called dynamical mean-field theory (DMFT). This will finally lead to a combined GGA+DMFT scheme to determine the electronic structure of the materials of interest.

The development of DMFT was triggered by Metzner and Vollhardt in 1989 [MV89], who introduced a new limit to correlated electron systems, the limit of infinite dimensions  $d \rightarrow \infty$  or equivalently an infinite number of neighboring lattice sites. Although the itinerant character of the electrons and the effects of the pair interaction is maintained, in this limit the description of the system yields a simplified, momentum-independent self-energy. The second cornerstone of DMFT was then laid by the works of Ohkawa in 1991 [Ohk91] and 1992 [Ohk92] and Georges and Kotliar in 1992 [GK92], who showed that a many-body model like the Hubbard model can be mapped onto an Anderson impurity model subject to a self-consistent bath for  $d \rightarrow \infty$ . Thus, reliable techniques for treating impurity models, that had been developed for over 30 years, could now be used to study correlated electrons in large dimensions. Georges and Kotliar were also able to show a precise correspondence of this description of correlated electron systems to the classical mean-field theory. However, as opposed to the classical case the on-site quantum problem remains a many-body problem such that only spatial fluctuations are frozen in this approach, but local quantum fluctuations are fully taken into account. Therefore, this method is called the *dynamical* mean-field theory leading to a neglect of the  $\mathbf{k}$ -dependence of the self-energy whereas the energy dependence of the self-energy is retained.

In this chapter, I want to first motivate the SSA of the self-energy obtained in the framework of DMFT for the multiband Hubbard model in the limit of infinite dimensions. By applying the SSA to a system with finite dimensions the set of

dynamical mean-field equations is obtained which has to be solved self-consistently. Based on these equations I then derive an GGA+DMFT description for spin-polarized systems in combination with prior GGA calculations. In the last part of the chapter I will present some details of the implementation of this GGA+DMFT scheme as well as the equations used to calculate the self-energy numerically using the FLEX method within the framework of DMFT.

## 6.1 Solution of the Multiband Hubbard Model within DMFT

In the review article [GKKR96] by Georges *et al.* the DMFT equations are derived from the analogy to classical mean-field theory and then applied to specific problems. Since this deductive ansatz to introduce DMFT is very general I do not believe it to be very instructive to resume this ansatz to explain DMFT as it is used in this thesis. To avoid the abstract formalism of the general formulation of DMFT, I will hence present the basic ideas of DMFT directly in connection with their application to the multiband Hubbard model. Furthermore, I like to introduce dynamical mean-field theory much more in accordance to the way it was originally developed. Hence, I first analyze the behavior of the Hubbard model in the limit of large dimensions and then discuss the dynamical mean-field equations obtain for a system with finite dimensions. (This ansatz follows up closely the introduction of DMFT in the review article by Held [HNK<sup>+</sup>06].) In the remainder of this section the DMFT mean-field equations are than used to formulate the GGA+DMFT self-consistency scheme which is an iterative scheme to determine the interacting lattice Green function of the multiband Hubbard model.

**The multiband Hubbard Model in infinite Dimensions.** Let me first restate the multiband Hubbard model as derived in chapter 5

$$\begin{aligned}
\hat{H}^{\text{Hubb}} = & \sum_{\mathbf{R}L, \mathbf{R}'L'; \sigma} H_{\mathbf{R}L, \mathbf{R}'L'}^{\text{DFT} \sigma} c_{\mathbf{R}L\sigma}^\dagger c_{\mathbf{R}'L'\sigma} \\
& + \frac{1}{2} U \sum_{\mathbf{R}\tilde{L}\tilde{L}'\sigma\sigma'} (1 - \delta_{\tilde{L}\tilde{L}'} \delta_{\sigma\sigma'}) c_{\mathbf{R}\tilde{L}\sigma}^\dagger c_{\mathbf{R}\tilde{L}'\sigma'}^\dagger c_{\mathbf{R}\tilde{L}'\sigma'} c_{\mathbf{R}\tilde{L}\sigma} \quad (\text{see 5.4}) \\
& + \frac{1}{2} J \sum_{\mathbf{R}\tilde{L}\tilde{L}'\sigma} (1 - \delta_{\tilde{L}\tilde{L}'}) c_{\mathbf{R}\tilde{L}\sigma}^\dagger c_{\mathbf{R}\tilde{L}'\sigma}^\dagger c_{\mathbf{R}\tilde{L}\sigma} c_{\mathbf{R}\tilde{L}'\sigma}.
\end{aligned}$$

The matrix elements  $H_{\mathbf{R}L, \mathbf{R}'L'}^{\text{DFT} \sigma}$  in the first term describe the overlap between the electronic eigenstate with the quantum numbers  $L, L'$  at site  $\mathbf{R}$  as well as the overlap of these states with those on all other sites  $\mathbf{R}'$ . The creation and annihilation operator in this term describe so to speak the “annihilation” of an electron in one state, which is then “created” again in another state. Therefore, the first term of the Hubbard

model is often called the hopping term and the  $H^{\text{DFT}\sigma}$  is often referred to as hopping matrix in this context. I resign to this nomenclature and I also like to switch to the conventional notation

$$H_{\mathbf{R}L, \mathbf{R}'L'}^{\text{DFT}\sigma} \rightarrow t_{\mathbf{R}L, \mathbf{R}'L'}^\sigma \quad (6.1)$$

for the elements of the hopping matrix  $t^\sigma$ . To simplify the notation in the further discussion I like to assume that the hopping from and to a site  $\mathbf{R}$  does only take place between this site and its nearest neighboring sites at positions  $\{\mathbf{R}'\}$ . All  $\mathcal{Z}_{\|\mathbf{R}-\mathbf{R}'\|}$  neighboring sites are of course situated in the same distance  $\|\mathbf{R}-\mathbf{R}'\|$  to site  $\mathbf{R}$ . In a Gedanken experiment a huge number of additional next nearest neighbors also situated in the same distance to site  $\mathbf{R}$  shall be added to the lattice. How do the terms of the Hamiltonian above scale, if the number  $\mathcal{Z}_{\|\mathbf{R}-\mathbf{R}'\|}$  of nearest neighbors increases up to infinity?

Since the second and third term, which give the potential energy per site originating from the pair interaction, are purely local, the adding of additional neighboring sites will have no effect on these terms. The sum in the first term however runs over as many terms as there are nearest neighboring sites, thus, this term diverges in the limit  $\mathcal{Z}_{\|\mathbf{R}-\mathbf{R}'\|} \rightarrow \infty$ . Hence, the hopping matrix elements have to be rescaled to ensure that the density of states has a well defined limit for  $\mathcal{Z}_{\|\mathbf{R}-\mathbf{R}'\|} \rightarrow \infty$ . It was proved by Metzner and Vollhardt [MV89], that the proper scaling for a cubic lattice is given by

$$t_{\mathbf{R}L, \mathbf{R}'L'}^\sigma = \frac{\tilde{t}_{\mathbf{R}L, \mathbf{R}'L'}^\sigma}{\sqrt{\mathcal{Z}_{\|\mathbf{R}-\mathbf{R}'\|}}} \quad (6.2)$$

where  $\tilde{t}_{\mathbf{R}L, \mathbf{R}'L'}^\sigma$  is a constant. With this scaling factor, the first term of the Hubbard model stays finite in the limit of infinite coordination of the atom at site  $\mathbf{R}$ . Due to the direct connection between the hopping matrix and the Green function from the non-interacting DFT description of the system

$$\sum_{\mathbf{R}''L''} \left( G_{\mathbf{R}L, \mathbf{R}''L''}^{0\sigma}(\epsilon) \right) \left( \epsilon \delta_{\mathbf{R}''\mathbf{R}'} \delta_{L''L'} - t_{\mathbf{R}L\sigma, \mathbf{R}'L'\sigma'} \right) = \delta_{\mathbf{R}\mathbf{R}'} \delta_{LL'} \quad (6.3)$$

which was introduced in equation (5.12) in chapter 5 the Green function from the non-interacting system must scale in the exact same way

$$G_{\mathbf{R}L, \mathbf{R}'L'}^{0\sigma}(\epsilon) \sim \frac{1}{\sqrt{\mathcal{Z}_{\|\mathbf{R}-\mathbf{R}'\|}}} \quad (6.4)$$

Based on the connection between the non-interacting Green function  $G^{0\sigma}$  and the Green function of the interacting system  $G^\sigma$  given by the Dyson equation (5.17), the assumption is made that the interacting lattice Green function as well shows a scaling behavior

$$G_{\mathbf{R}L, \mathbf{R}'L'}^\sigma(\epsilon) \sim \frac{1}{\sqrt{\mathcal{Z}_{\|\mathbf{R}-\mathbf{R}'\|}}} \quad (6.5)$$

We can now analyze the effect of this scaling behavior of  $G^{0\sigma}$  and  $G^\sigma$  on the self-energy  $\Sigma^\sigma$  of the Hubbard model in the form it was derived within the framework of the FLEX method.

Due to the local nature of the interaction vertices in the Hubbard model, only the particle-particle ladder diagrams and the electron-hole ladder diagrams in the diagrammatic expansion of the self-energy within FLEX yield contributions of diagrams, which contain Green function lines connecting different sites. The example diagram depicted in figure 6.1 is the lowest-order ladder diagram contained in the diagrammatic expansion of the self-energy. It is the same for the particle-particle channel as well as the electron-hole channel. It is drawn with Green-function lines that connect the neighboring site  $\mathbf{R}'$  with site  $\mathbf{R}$ . In this diagram as well as in all higher-order

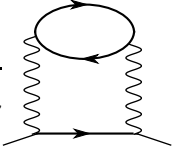


**Figure 6.1:** 2nd order contribution to the self-energy

diagrams, neighboring sites are always connected (directly or indirectly via additional sites) by three Green function lines, which all yield a scaling factor of  $1/\sqrt{\mathcal{Z}_{\|\mathbf{R}-\mathbf{R}'\|}}$ . There are of course  $\mathcal{Z}_{\|\mathbf{R}-\mathbf{R}'\|}$  equivalent contributions from each site  $\mathbf{R}' \neq \mathbf{R}$ , thus, the overall scaling for the summed contribution of all equivalent sites  $\mathbf{R}' \neq \mathbf{R}$  to the self-energy goes like  $1/\sqrt{\mathcal{Z}_{\|\mathbf{R}-\mathbf{R}'\|}}$ . These contributions become irrelevant for  $\mathcal{Z}_{\|\mathbf{R}-\mathbf{R}'\|} \rightarrow \infty$  and consequently, only the contributions of local diagrams to the self-energy remain. Thus the self-energy becomes purely local in the limit  $\mathcal{Z}_{\|\mathbf{R}-\mathbf{R}'\|} \rightarrow \infty$

$$\Sigma_{\mathbf{R}L,\mathbf{R}'L'}^\sigma(\epsilon) \xrightarrow{\mathcal{Z}_{\|\mathbf{R}-\mathbf{R}'\|} \rightarrow \infty} \Sigma_{\mathbf{R};LL'}^\sigma(\epsilon)\delta_{\mathbf{R}\mathbf{R}'} \quad (6.6)$$

or likewise the Fourier transform becomes  $\mathbf{k}$ -independent

$$\Sigma_{L,L'}^\sigma(\mathbf{k}; \epsilon) \xrightarrow{\mathcal{Z}_{\|\mathbf{R}-\mathbf{R}'\|} \rightarrow \infty} \Sigma_{LL'}^\sigma(\epsilon). \quad (6.7)$$

From this and the Dyson equation, it follows that  $G_{\mathbf{R}L,\mathbf{R}'L'}^\sigma \sim 1/\sqrt{\mathcal{Z}_{\|\mathbf{R}-\mathbf{R}'\|}}$ , which is consistent with the assumption made above. Thus, also the non-local elements of the one-particle propagator become negligible in the limit of large dimension. An electron may still leave the site  $\mathbf{R}$ , interact with electrons at other sites and return to site  $\mathbf{R}$ , but this is all contained in the on-site matrix elements  $G_{\mathbf{R};LL'}^\sigma\delta_{\mathbf{R}\mathbf{R}'}$  of the interacting Green function.

The single-site approximation for  $\Sigma^\sigma$  and  $G^\sigma$  becomes exact in the limit  $\mathcal{Z}_{\|\mathbf{R}-\mathbf{R}'\|} \rightarrow \infty$  and the whole dynamic of the lattice model is reduced to the dynamic at the single site. This resembles the situation described by an impurity problem. The local part of  $G^\sigma$  plays the role of the interacting impurity Green function, the local part of  $\Sigma^\sigma$  is the impurity self-energy and the bare impurity Green function is obtained from Dyson equation

$$[G_{\mathbf{R};LL'}^{0\sigma}(\epsilon)]^{-1} = [G_{\mathbf{R};LL'}^\sigma(\epsilon)]^{-1} + \Sigma_{\mathbf{R};LL'}^\sigma(\epsilon), \quad (6.8)$$

and  $G_{\mathbf{R};LL'}^{0\sigma}$  is of course the local part of the bare lattice Green function  $G^{0\sigma}$ .

**The DMFT equations.** In contrast to a lattice system in the limit of infinitely many neighboring sites in a finite dimensional system the interacting lattice Green function in  $\mathbf{k}$  space is as well connected to the self-energy and the bare lattice Green function via Dyson equation

$$\hat{G}^\sigma(\mathbf{k}; \epsilon) = \left[ \left[ \hat{G}^{0\sigma}(\mathbf{k}; \epsilon) \right]^{-1} - \hat{\Sigma}^\sigma(\mathbf{k}; \epsilon) \right]^{-1}. \quad (6.9)$$

However, in a finite dimensional system all quantities are  $\mathbf{k}$ -dependent or likewise they have non-local elements when transformed into real space. Note that all quantities in the above equation are matrix operators with matrix elements in the orbital indices  $L$  and  $L'$  for each spin and each  $\mathbf{k}$ -vector.

In 3 dimensional systems with high lattice coordination (i.e. body-centered cubic:  $\mathcal{Z}_{\|\mathbf{R}-\mathbf{R}'\|} = 8$ , face-centered cubic:  $\mathcal{Z}_{\|\mathbf{R}-\mathbf{R}'\|} = 12$ ) the suppression of the off-site contribution to the self-energy due to the scaling factor  $1/\sqrt{\mathcal{Z}_{\|\mathbf{R}-\mathbf{R}'\|}}$  is already large. Hence, the SSA can be applied to the self-energy of these systems approximating the full non-local or likewise  $\mathbf{k}$ -dependent self-energy by a local or non- $\mathbf{k}$ -dependent self-energy. The first DMFT equation is obtained by replacing  $\hat{\Sigma}^\sigma(\mathbf{k}; \epsilon)$  in (6.9) by this non- $\mathbf{k}$ -dependent self-energy yielding

$$\hat{G}^\sigma(\mathbf{k}; \epsilon) = \left[ \left[ \hat{G}^{0\sigma}(\mathbf{k}; \epsilon) \right]^{-1} - \hat{\Sigma}^\sigma(\epsilon) \right]^{-1}. \quad (6.10)$$

The local self-energy can again be interpreted as the self-energy of a single-site impurity problem and an effective bare impurity Greens function  $\mathcal{G}^{0\sigma}$  can be introduced by

$$\left[ \hat{G}_{\mathbf{R};LL'}^{0\sigma}(\epsilon) \right]^{-1} = \left[ G_{\mathbf{R};LL'}^\sigma(\epsilon) \right]^{-1} + \Sigma_{\mathbf{R};LL'}^\sigma. \quad (6.11)$$

In contrast to the discussion of the lattice system in infinite dimension in finite dimensional systems the bare impurity Greens function  $\mathcal{G}^{0\sigma}$  also called bath Green function differs from the bare Green function  $\hat{G}^{0\sigma}$  of the lattice because the latter in general contains also non-local terms. However, we can choose the local interacting Green function  $G_{\mathbf{R};LL'}^\sigma(\epsilon)$  in (6.11) such that the mapping of the lattice model onto the single site impurity problem becomes exact in the limit of infinite dimension. It can be proved that the mapping becomes exact if the local part of the interacting lattice Green function  $G^\sigma$  obtained by

$$G_{\mathbf{R};LL'}^\sigma(\epsilon) = \sum_{\mathbf{k}} G_{LL'}^\sigma(\mathbf{k}; \epsilon) \quad (6.12)$$

is inserted into (6.11). (Details of the proof e.g. based on the cavity method can be found in the review article [GKKR96] by Georges *et al.*).

The bare lattice Green function  $G^{0\sigma}$  can be obtained via Lehmann representation as described in chapter 4 by

$$G_{LL'}^{0\sigma}(\mathbf{k}; \epsilon) = \frac{1}{N} \sum_{\nu} \frac{(A_{L,\nu}^\sigma(\mathbf{k}))(A_{L',\nu}^\sigma(\mathbf{k}))^*}{\epsilon - \epsilon_{\mathbf{k},\nu}^\sigma + i\eta}. \quad (\text{see 4.34})$$

with the muffin-tin coefficients  $A_{L,\nu}^\sigma(\mathbf{k})$  and the Kohn-Sham eigenvalues  $\epsilon_{\mathbf{k},\nu}^\sigma$  taken from DFT calculations. If the local self-energy can also be determined equation (6.10) through (6.12) forming a closed set of mean-field equations can be solved self-consistently to determine the interacting lattice Green function  $G^\sigma$ . In the remainder of this section I like to introduce the GGA+DMFT scheme to iteratively solve the the DMFT mean-field equation self-consistently. The detailed description how the self-energy is obtained in the present approach employing the FLEX method within DMFT is then presented in the last section of this chapter.

**The GGA+DMFT Self-Consistency Scheme** In this section it is discussed how all parts from previous chapters can be merged together in one algorithm to calculate the electronic structure of selected magnetic materials. In order to obtain a self-consistent solution, an iterative procedure is used. A flow diagram of this procedure is depicted in figure 6.2.

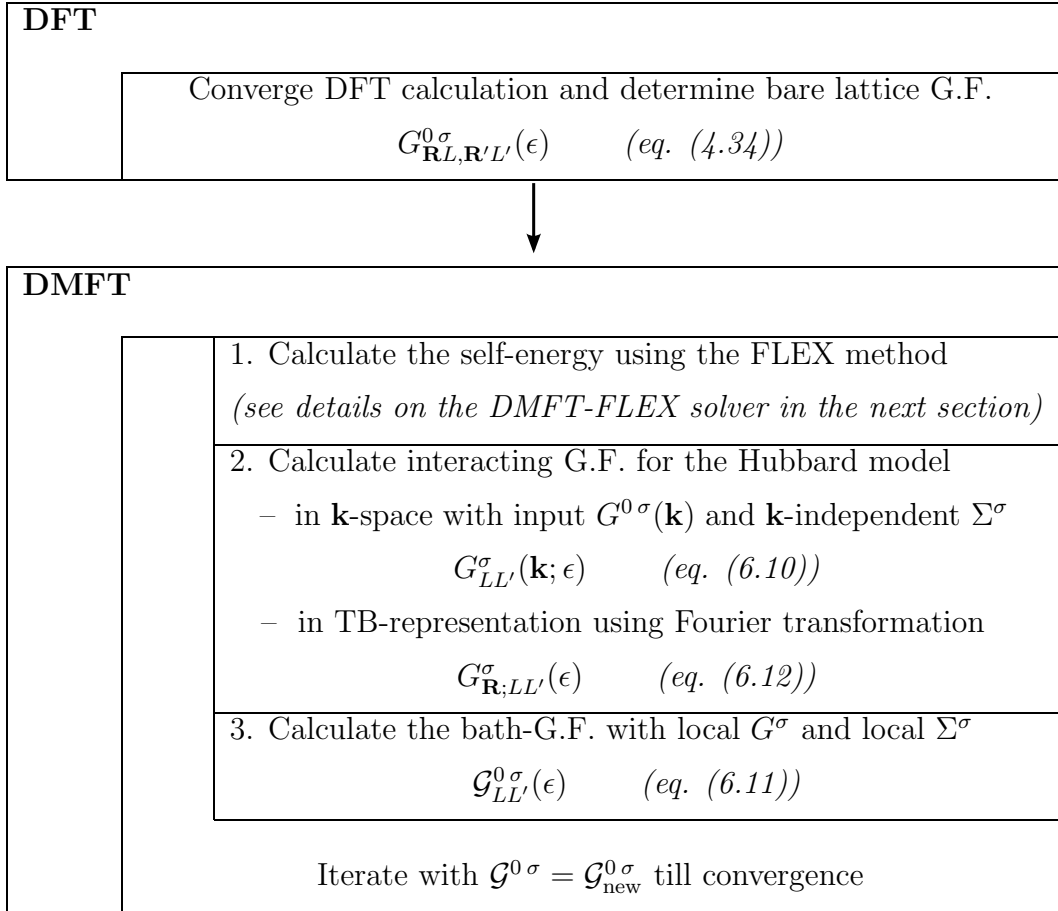


**Figure 6.2:** Flow diagram of the GGA+DMFT self-consistency cycle

From figure 6.2 it can be seen how the results obtained in the DFT description of a system are connected to the many-body perturbation theory applied within the framework of DMFT. It also lists the steps of the self-consistency cycle to solve the DMFT equations presented in the previous section. This part of the GGA+DMFT algorithm containing the DMFT self-consistency cycle was implemented straightforwardly in the FLEX solver presented in the next section. Iterations in the DMFT self-consistency cycle are carried out until the self-energy is converged up to the order of  $10^{-9}$ .

To conclude this section I would like to point out explicitly that the GGA+DMFT approach presented here differs from other GGA+DMFT approaches presented e.g. in the review article by Held [HNK<sup>+</sup>06]. In the present approach only the many-body corrections to the DFT description are calculated self-consistently as opposed to recalculating also the DFT quantities with the results obtained from one iteration step in the many-body iteration scheme. The approach presented here thus might better be described as DMFT on top of GGA. It can be expected however for the systems under consideration that a full self-consistent calculation including the recalculation of the DFT results will not yield substantially different results in the present context, since the correlation effects included via the extension of the DFT description within DMFT are rather weak. Thus, the DMFT calculations for these systems will mainly yield minor corrections to the DFT description such that a recalculation of the DFT results is not necessary for the systems under consideration.

## 6.2 The DMFT-FLEX Solver

Within the framework of DMFT the expression of the FLEX self-energy presented at the end of chapter 5 in terms of Feynman diagrams can be restated as analytical expressions that are evaluated numerically in a straightforward manner in the DMFT-FLEX solver. I will first derive these analytical expressions used to calculate the self-energy. I will then discuss some of the additional approximations entering the evaluation of the FLEX diagrams for the self-energy when these diagrams are evaluated in the framework of DMFT.

In chapter 5 an expansion of the self-energy that can formally be written as a sum over three terms

$$\Sigma_{\lambda\lambda'}^{\sigma}(\epsilon) = \Sigma_{\lambda\lambda'}^{\sigma(2)}(\epsilon) + \Sigma_{\lambda\lambda'}^{\sigma\text{pp}(3)}(\epsilon) + \Sigma_{\lambda\lambda'}^{\sigma\text{eh}(3)}(\epsilon). \quad (\text{see 5.50})$$

where each term has been defined in terms of Feynman diagrams in chapter 5 in the equations (5.47), (5.48) and (5.49). Each multiindex  $\lambda$  stands for the site-index  $\mathbf{R}$  and the orbital index  $L$ .

Starting from this expression for the self-energy the following steps are taken to translate the diagrammatic expression denoted by the three terms in (5.50) into analytic expressions:

1. The SSA from DMFT is applied. Consequently, only the on-site matrix elements of the self-energy contributions in (5.50) with  $\mathbf{R} = \mathbf{R}'$  are retained since all elements with  $\mathbf{R} \neq \mathbf{R}'$  are put to zero. Another consequences for the translation of the diagrammatic expression of the third contribution in (5.50) originating from the electron-hole channel is that this term becomes identical to the sum over the two contributions from the electron-hole channel 1 and electron-hole channel 2 as discussed in chapter 5.
2. If the cubic symmetry of the underlying crystal lattices is exploited taking into account that the self-energy is only calculated for particles occupying  $d$  states which split into non-overlapping  $t_{2g}$  and  $e_g$  states due to the crystal field, the self-energy matrices become diagonal in the subspace spanned by the  $t_{2g}$  and  $e_g$  states and for each spin direction only one self-energy contribution for each state  $t_{2g}$  and  $e_g$  has to be calculated. If the following notation for the site and  $L$ -diagonal self-energy contributions is introduced

$$\Sigma_{\mathbf{R}L, \mathbf{R}L}^{\sigma}(\epsilon) = \Sigma_{\mathbf{R}L}^{\sigma}(\epsilon) \quad (6.13)$$

the full self-energy can now be formally written as a sum over four terms

$$\Sigma_{\mathbf{R}L}^{\sigma}(\epsilon) = \Sigma_{\mathbf{R}L}^{\sigma(2)}(\epsilon) + \Sigma_{\mathbf{R}L}^{\sigma \text{ pp}(3)}(\epsilon) + \Sigma_{\mathbf{R}L}^{\sigma \text{ eh}1(3)}(\epsilon) + \Sigma_{\mathbf{R}L}^{\sigma \text{ eh}2(3)}(\epsilon), \quad (6.14)$$

where the index  $L$  now denotes either a  $t_{2g}$  or  $e_g$  state. Note that up to now only the diagrammatic expressions have been modified but they haven't been translated yet.

3. The diagrammatic expressions for the four terms in the sum presented above are drawn using time-ordered quantities. However, each time-ordered quantity can be expressed by retarded quantities as pointed out in chapter 4 using the identity

$$\begin{aligned} G^t(\lambda, \lambda'; \epsilon) &= \text{Re } G^{\text{ret}}(\lambda, \lambda'; \epsilon) + i \text{sgn}(\epsilon - E_{\text{F}}) \text{Im } G^{\text{ret}}(\lambda, \lambda'; \epsilon) \\ &= G_1(\lambda, \lambda'; \epsilon) + i \text{sgn}(\epsilon - E_{\text{F}}) G_2(\lambda, \lambda'; \epsilon). \end{aligned} \quad (6.15)$$

The imaginary part of a retarded function shall be denoted by the index two and the real part by index one. All analytic expressions will be written down using the imaginary part of a retarded quantity. If necessary, the real part can be obtained using the Hilbert transformation (4.40). By switching from time-ordered two retarded quantities the energy integrals in the analytic expressions for the diagrams are simplified since the retarded quantities are analytical functions of the complex energy  $\epsilon + i\eta$  in the upper half-plane as opposed to the time-ordered quantities which are non-analytic functions in the whole complex energy plane.

4. The interaction lines in the formulas will be translated using the matrix  $v$ , which stands for the matrix introduced in chapter 5 with matrix elements

$$v_{LL'}^{\sigma\sigma'} = U(1 - \delta_{LL'}\delta_{\sigma\sigma'}) + J\delta_{\sigma\sigma'}(1 - \delta_{LL'}). \quad (\text{see 5.10})$$

5. The symbol  $\hat{\phantom{x}}$  denoting matrix operators in previous chapters is dropped here to avoid overloading the formulas. In addition to that all quantities are presented here as matrix operators to also avoid overloading the notation. The matrices representing the one-particle quantities  $\Sigma^\sigma$  and the Green functions are  $5 \times 5$  matrices in the subspace spanned by the  $t_{2g}$  and  $e_g$  states whereas the two-particle quantities like the T-matrices, the bare particle-particle and the bare particle-hole propagator are matrices with elements carrying four distinct indices denoting  $t_{2g}$  or  $e_g$  states.
6. Finally within the framework of DMFT all Green function lines in the self-energy diagrams retained from the FLEX method are translated into formulas using the bath Green function  $\mathcal{G}^{0\sigma}$  instead of the interacting lattice Green function  $G^\sigma$ .

After going through all these steps analytic expression for the four terms in (6.14) can finally be written down.

**Self-energy contribution from the second order diagrams.** To evaluate the self-energy contribution  $\Sigma^{\sigma(2)}$  from the second order diagrams first the retarded bare particle-particle propagator is calculated as

$$\Psi_2^{\sigma\sigma'}(\epsilon) = - \int_{E_F}^{\epsilon - E_F} \frac{d\epsilon'}{\pi} \mathcal{G}_2^{0\sigma}(\epsilon - \epsilon') \mathcal{G}_2^{0\sigma'}(\epsilon'). \quad (6.16)$$

This is used to calculate  $\Sigma^{\sigma(2)}$  as

$$\Sigma_2^{\sigma(2)}(\epsilon) = - \int_{2E_F - \epsilon}^{\epsilon} \frac{d\epsilon'}{\pi} \sum_{\sigma'} v^{\sigma\sigma'} \Psi_2^{\sigma\sigma'}(\epsilon - \epsilon') v^{\sigma\sigma'} \mathcal{G}_2^{0\sigma'}(\epsilon'). \quad (6.17)$$

**Self-energy contribution from the particle-particle channel.** To calculate the retarded self-energy contribution from the particle-particle channel the particle-particle T-matrix is calculated as described in chapter 5 starting from third order

$$T^{\text{pp}(3)}(\epsilon) = v\Psi(\epsilon)v\Psi(\epsilon)v[1 - \Psi(\epsilon)v]^{-1} \quad (6.18)$$

and the retarded self-energy contribution from the particle-particle channel  $\Sigma^{\sigma(\text{pp})}$  is given by

$$\Sigma_2^{\sigma(\text{pp}(3))}(\epsilon) = - \int_{2E_F - \epsilon}^{\epsilon} \frac{d\epsilon'}{\pi} \sum_{\sigma'} T_2^{\sigma\sigma'\text{pp}(3)}(\epsilon + \epsilon') \mathcal{G}_2^{0\sigma'}(\epsilon'). \quad (6.19)$$

**Self-energy contribution from the electron-hole channels 1 and 2.** To derive analytic expressions for the two contribution to the self-energy from the electron-hole channel 1 and 2, first the retarded electron-hole propagator is calculated

$$\Phi_2^{\sigma\sigma'}(\epsilon) = \int_{E_F - \epsilon}^{E_F} \frac{d\epsilon'}{\pi} \mathcal{G}_2^{0\sigma'}(\epsilon + \epsilon') \mathcal{G}_2^{0\sigma}(\epsilon'). \quad (6.20)$$

To obtain the self-energy contribution from the electron-hole channel 1 the electron-hole 1 T-matrix starting from the third order term is obtained from

$$T^{\text{eh}1(3)}(\epsilon) = v\Phi(\epsilon)v\Phi(\epsilon)v [1 + \Phi(\epsilon)v]^{-1} \quad (6.21)$$

and the self-energy contribution of this channel is then given by

$$\Sigma_2^{\sigma \text{eh}1}(\epsilon) = \int_{E_F}^{\epsilon} \frac{d\epsilon'}{\pi} \sum_{\sigma'} T_2^{\sigma\sigma'\text{eh}1(3)}(\epsilon - \epsilon') \mathcal{G}_2^{0\sigma'}(\epsilon'). \quad (6.22)$$

To evaluate the contribution to the self-energy of the second electron-hole channel the full electron-hole T-matrix employing the antisymmetrized interaction  $\bar{V}$  defined in (5.23) is first calculated starting also from third order

$$T^{\text{eh}(3)}(\epsilon) = \bar{V}\Phi(\epsilon)\bar{V}\Phi(\epsilon)\bar{V} [1 + \Phi(\epsilon)\bar{V}]^{-1} \quad (6.23)$$

The diagrams from the electron-hole channel 2 are now evaluated using the full electron-hole T-matrix  $T^{\text{eh}(3)}$  instead of  $T^{\text{eh}2(3)}$ . However, due to the symmetry of all quantities the convolution of  $T^{\text{eh}(3)}$  with the Green function in the expression below leads to cancellation of all diagrams contained in the expansion of  $T^{\text{eh}(3)}$  except for those diagrams contained in  $T^{\text{eh}2(3)}$ . Hence, the first and second line in the formula below are identical and the formula is the correct translation of the diagrammatic contribution to the self-energy from the electron-hole channel 2:

$$\begin{aligned} \Sigma_2^{\sigma \text{eh}2}(\epsilon) &= \int_{E_F}^{\epsilon} \frac{d\epsilon'}{\pi} T_2^{\sigma\sigma\text{eh}(3)}(\epsilon - \epsilon') \mathcal{G}_2^{0\sigma}(\epsilon') \\ &= \int_{E_F}^{\epsilon} \frac{d\epsilon'}{\pi} T_2^{\sigma\sigma\text{eh}2(3)}(\epsilon - \epsilon') \mathcal{G}_2^{0\sigma}(\epsilon'). \end{aligned} \quad (6.24)$$

Equations (6.16) – (6.24) are recalculated in each iteration step employing the new bath Green function obtained from solving the DMFT equations of the DMFT self-consistency cycle. In the zeroth order step the bare lattice Green function is used to evaluate the expressions and to obtain the initial expression for the self-energy.

To translate the diagrammatic expressions in the expansion of the self-energy (5.50) into formulas within the framework of DMFT two additional approximation were used:

- The self-energy is calculated in single-site approximation.
- The diagrams are evaluated using the bath Green function  $\mathcal{G}^{0\sigma}$  instead of the interacting Green function  $G^\sigma$  of the crystal lattice.

In the SSA the  $\mathbf{k}$ -dependence of the self-energy becomes negligible as demonstrated in the first section of this chapter. This does not only simplify the formulation of expressions to calculate  $\Sigma^\sigma$ , but it also reduces the computational resources necessary

to evaluate these expression substantially. It has also been pointed out that the SSA is supposed to yield rather accurate results for systems with highly coordinated crystal structure as discussed in this thesis. Therefore, we assume the SSA to be well applicable in our context. However, some phenomena i.e. spin-wave excitations could only be studied, if the  $\mathbf{k}$ -dependence would be included in the description of the systems. In general, all effects related to the  $\mathbf{k}$ -dependence of the self-energy are of course lost, if the SSA is imposed, but these effects need not to be included to study i.e. the densities of states for the different spin orientation which is to be done here.

As to the second point it can be stated that using the bath Green function  $\mathcal{G}^{0\sigma}$  instead of the interacting lattice Green function seems to be the “canonical” procedure within DMFT which is applied by various authors e.g. in [KL99, LKK01]. However, at this point it remains an open question why this is done or if this has to be done or likewise if this yields a better or worse description of the electronic structure. Katsnelson and Lichtenstein discussed in [KL99] that the vertex function is partially renormalized if the bath Green function is used to calculate the FLEX diagrams instead of the interacting lattice Green function but they present no rigid argument why this should be the case. On the other hand, the evaluation of the FLEX diagrams employing the bath Green function leads to an approximate expression for the full lattice self-energy which is not conserving in the sense of Kadanoff and Baym (or “ $\Phi$ -derivable”). Due to a lack of time calculations to compare different levels of self-consistency could not be carried out and all diagrams were evaluated using  $\mathcal{G}^{0\sigma}$  as suggested in the literature.



# 7 Preparatory Calculations within DFT

In this chapter I will first describe the convergence tests carried out with a given DFT implementation, the FLEUR code, to obtain a robust description of the electron systems within DFT of the materials to be studied. These data will be used as input for the DMFT part of the GGA+DMFT scheme. To provide an insight of how the converged data were obtained I discuss example calculations for Fe and Ni.

In the second part of the chapter, the approximations are examined which enter into the implementation of the GGA+DMFT scheme by transforming the data obtained from FLEUR in an LAPW basis into a representation using the TB-FLAPW basis. The latter was introduced at the end of chapter 3. I present a quantitative analysis of the changes due to the basis transformation by comparing the density of states (DOS) of Fe, Co and Ni using both basis sets. It is demonstrated that the representation in terms of the TB-FLAPW basis is well applicable for materials with a close-packed crystal structure.

## 7.1 Convergence Tests for the Parameters of the LAPW Basis

All DFT calculations were carried out using the FLEUR code, which employs a basis set of linearized augmented plane waves (LAPWs) to represent the Kohn-Sham eigenfunctions  $\psi_{\mathbf{k},\nu}^\sigma$ . The expansion of the eigenfunctions in terms of the LAPW basis was already presented in chapter 3

$$\psi_{\mathbf{k},\nu}^\sigma(\mathbf{r}) = \sum_{\mathbf{G}} c_{\mathbf{k},\nu}^{\mathbf{G}\sigma} \varphi_{\mathbf{G}}^\sigma(\mathbf{k}, \mathbf{r}), \quad (\text{see 3.1})$$

where the linearized augmented plane waves were introduced as

$$\varphi_{\mathbf{G}}(\mathbf{k}, \mathbf{r}) = \begin{cases} \exp[i(\mathbf{k} + \mathbf{G}) \cdot \mathbf{r}] & \text{interstitial region} \\ \sum_L (a_L^{\mu\mathbf{G}}(\mathbf{k}) u_l(r^\mu) + b_L^{\mu\mathbf{G}}(\mathbf{k}) \dot{u}_l(r^\mu)) Y_L(\hat{\mathbf{r}}^\mu) & \text{muffin-tin } \mu \end{cases} \quad (\text{see 3.7})$$

In principle, the summations over  $\mathbf{G}$  and  $L$  run over infinitely many terms but they have to be restricted to a finite number of terms to be implemented. This is achieved

by an appropriate choice of cut-off values  $K_{\max}$  and  $l_{\max}$  with  $|\mathbf{k} + \mathbf{G}| \leq K_{\max}$  and  $0 \leq l \leq l_{\max}$ ,  $-l \leq m \leq l$  for the first and second summation. If the results derived from the eigenfunctions represented in the LAPW basis do not change significantly when more terms are added in the expansions, the representation can be considered converged within numerical accuracy. The procedure to determine  $K_{\max}$  and  $l_{\max}$  is described in detail below.

The calculations are carried out numerically in FLEUR by evaluating the Kohn-Sham eigenfunctions on a mesh of equidistant points in  $\mathbf{k}$  space. The mesh is constructed to cover the irreducible part of the first Brillouin zone (1<sup>st</sup> BZ). The number of mesh points and consequently the distance between the points has to be chosen such that the total-energy functional does not change if the number of  $\mathbf{k}$  points is increased further. For the calculation of the density of states (DOS) however a bigger set of  $\mathbf{k}$  points is necessary, since the DOS also depends on the energy and the energy eigenvalues are determined for each  $\mathbf{k}$  point on the discrete mesh. Hence, the number of  $\mathbf{k}$  points must be significantly larger to obtain a sufficient level of accuracy. In the table at the end of this section both values for the number of  $\mathbf{k}$  points are listed: the number to converge the total energy calculations (listed as ‘ $\mathbf{k}$  point, total energy’) and the number to calculate the DOS (listed as ‘FLEX input’). This number of  $\mathbf{k}$  points used to calculate the DOS within DFT is also used to calculate the eigenvalues and coefficients of the eigenfunctions of the Kohn-Sham equation used to construct the DFT lattice Green function as well as to determine the interacting lattice Green function in  $\mathbf{k}$  space.

Furthermore, an input value for the lattice constant of the materials to be analyzed has to be chosen and the muffin-tin radius  $R_{\text{MT}}$  has to be determined. It was described in the last section of chapter 2 that the equilibrium lattice constant could be determined from calculations within DFT. However, these theoretically determined lattice constants depend on the choice of the parametrization of the exchange correlation potential as will be discussed below. With approximate functionals the equilibrium lattice constants are usually not identical to the lattice constants measured in experiments. To be able to compare results to experimental findings I used the experimental value for the lattice constant in all calculations. The muffin-tin radius  $R_{\text{MT}}$  is chosen, such that as much space as possible is covered by the muffin tins but they do not overlap.

Finally, to choose a parametrization for the exchange-correlation potential for the DFT calculations, I determined the equilibrium lattice constants from FLEUR calculations using three different parametrizations of the exchange-correlation potential, the LDA and two different GGAs. Based on these test calculations I used the parametrization within GGA suggested by Perdew, Burke and Ernzerhof [PBE96] in all further calculations, since it yielded the equilibrium lattice constants closest to the experimental value for all three materials to be studied.

In the table below, the results of all convergence tests carried out in calculations for Fe, Co and Ni are presented. These parameters were used to generate the DFT

input for the GGA+DMFT calculations presented in the next chapter.

Material	Lattice Const. [ $a_B$ ]	$R_{MT}$ [ $a_B$ ]	$K_{max}$	$l_{max}$	k points	
					total energy	FLEX input
Iron	5.42	2.3465	4.2	8	322	1892
Cobalt	6.69	2.3650	4.2	8	–	2480
Nickel	6.66	2.3540	4.2	8	280	2480

Note that only bulk crystal calculations were performed. Iron was calculated the bcc structure, nickel and cobalt in the fcc structure. The experimental values of the lattice constants can be found in [Wij86]. I will now discuss the convergence tests in detail and give some examples of results from calculations for Fe and Ni.

### 7.1.1 Determining $K_{max}$ and $l_{max}$

The value of  $K_{max}$  determines the number of augmented plane waves used to represent a Kohn-Sham eigenfunction and  $l_{max}$  determines the number of radial functions used to augment the plane waves inside the muffin-tin regions. Both  $K_{max}$  and  $l_{max}$  are

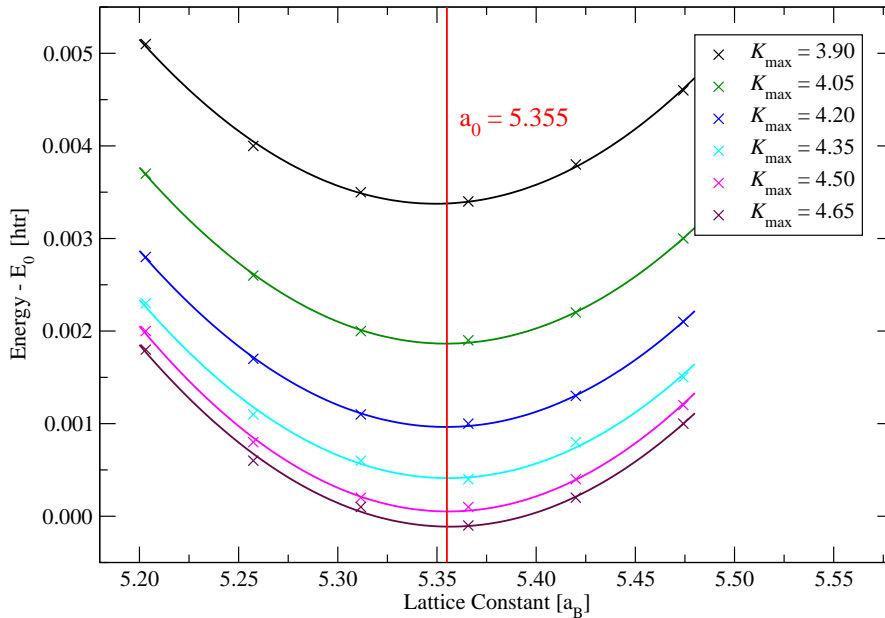


**Figure 7.1:** Data of convergence tests for  $K_{max}$  and parabola fits from bulk crystal calculations of iron. To better display the data, the values are all shifted by a constant  $E_0 = 1272.811$  htr. The value for  $a_0$  is the converged equilibrium lattice constant.

obtained by calculating the total energy in FLEUR for a number of different values of the lattice constant below and above the equilibrium lattice constant  $a_0$  for a fixed choice of the exchange-correlation potential and a fixed number of  $\mathbf{k}$  points. If the value for  $l_{\max}$  is also kept fixed a different parabola for each choice of  $K_{\max}$  is obtained. Likewise, if  $K_{\max}$  is kept fixed, parabolas for different values of  $l_{\max}$  can be plotted. I first examine the results for the convergence tests for  $K_{\max}$ . Figure 7.1 shows as an example the calculations for iron for a fixed value of  $l_{\max} = 8$  and a total number of 322  $\mathbf{k}$  points.

The converged value for  $K_{\max}$  is obtained by converging the value of the equilibrium lattice constant  $a_0$ . The equilibrium lattice constant depends on the chemical bonds, which are composed mainly by the  $s$  and  $p$  electrons in transition metals. Electrons in  $s$  and  $p$  states are fairly delocalized over the crystal lattice. Thus, the accuracy of the representation of the  $s$  and  $p$  wave functions in the LAPW basis depends primarily on the total number of augmented plane waves used in the expansion of the Kohn-Sham eigenfunctions. If the representation in the LAPW basis of the  $s$  and  $p$  wave functions that contribute to the chemical bonds inside the material becomes numerically exact, the value of  $a_0$  will not change further, if more plane waves are included in the expansion. Thus, both values for  $a_0$  and  $K_{\max}$  are converged if the

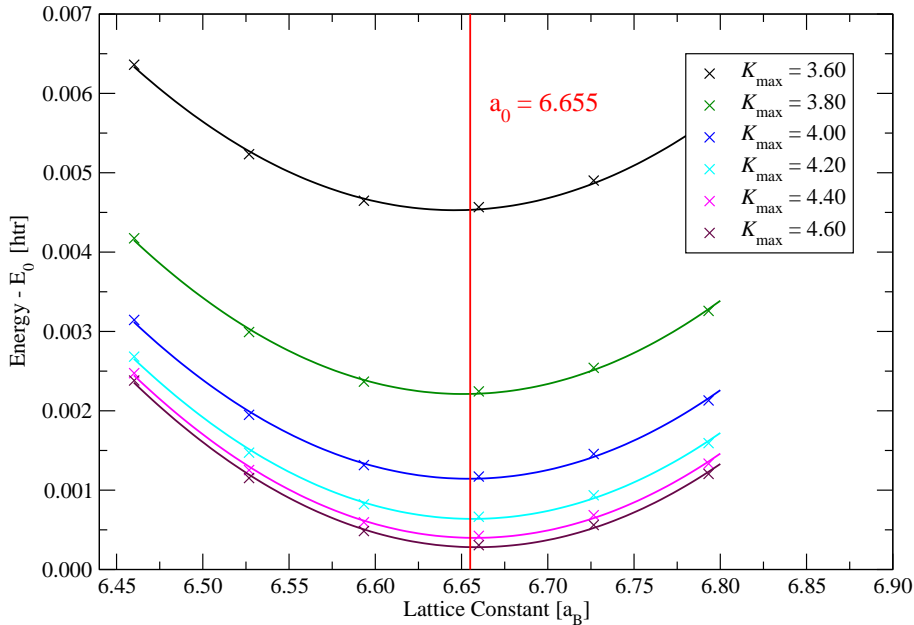


**Figure 7.2:** Data of convergence tests for  $K_{\max}$  and parabola fits from bulk crystal calculations of nickel. To better display the data, the values are all shifted by a constant  $E_0 = 1520.8399$  htr. The value for  $a_0$  is the converged equilibrium lattice constant.

position of the minima of the parabolas does not change when  $K_{\max}$  is increased further. It can be seen in figure 7.1 that convergence of  $a_0$  is reached for a value of  $K_{\max}$  larger or equal to 4.2. This has been confirmed by calculating the minima of the parabolas obtained by fitting a quadratic function to the results of each FLEUR calculation. Results obtained from calculations for nickel with  $l_{\max} = 8$  and 280  $\mathbf{k}$  points are shown in figure 7.2. Again convergence is reached if  $K_{\max}$  is larger or equal to 4.2.

It might seem odd that the minimum of the total energy still decreases, if  $K_{\max}$  is further increased although convergence of  $a_0$  is reached. This is due to the fact that the total energy is calculated as a functional of the electron density of all electrons which is proportional to the sum of the squares of all occupied Kohn-Sham eigenfunctions (see equation (2.22)). The minimum of the total-energy functional can be obtained from the functional derivative of the total energy with respect to the electron density. Adding more variational degrees of freedom to the electron density by increasing  $K_{\max}$  will therefore always yield a smaller value for the minimum of the total energy. Thus, the decrease of the total energy is independent of the convergence of  $a_0$  and  $K_{\max}$ .

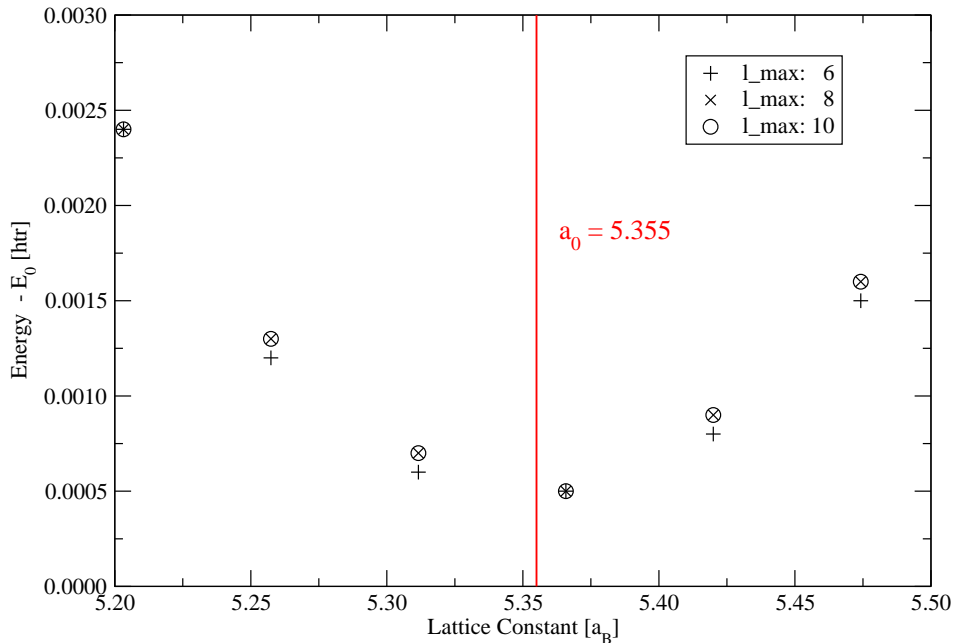


**Figure 7.3:** Data of convergence tests for  $l_{\max}$  from bulk crystal calculations of iron. To better display the data, the values are all shifted by a constant  $E_0 = 1272.811$  htr. The value for  $a_0$  is the converged lattice constant.

In figure 7.3 calculations of the total energy for iron with  $K_{\max} = 4.2$  and 322  $\mathbf{k}$  points are presented for different values of  $l_{\max}$ . Since the electron density is proportional to the square of all occupied Kohn-Sham eigenfunctions, convergence of  $l_{\max}$  is reached if the minimum of the total energy does not change further upon increasing the value of  $l_{\max}$  for a given value of  $K_{\max}$ . The minimum of all three data sets in 7.3 does not change for the different values of  $l_{\max}$ , hence, convergence is already reached with a choice of  $l_{\max} = 6$ . This was to be expected, since the electronic states in  $3d$  transition metals are occupied for  $l$ -quantum numbers up to 2. For free atoms with a spherically symmetric potential a value of 2 for  $l_{\max}$  should hence be sufficient to account for all occupied electronic states contributing in the calculation of the total energy. Due to the anisotropic potential in a crystal environment a slightly higher value for  $l_{\max}$  is necessary to describe distortions of the wave functions but these deviations should only have a small impact on the description of the materials studied here. However, an additional difficulty arises from the fact, that the wave functions when represented by a finite sum over  $l_{\max}$  terms inside the muffin tins are not continuous at the sphere's boundaries any more as they should be per definitionem. Although the total energy does not change any more for a choice of  $l_{\max}$  between 6 and 10 this additional problem has to be taken into account by choosing  $l_{\max}$  large enough such that the continuation into the interstitial space is as smooth as possible while keeping the numerical effort at a tolerable level. Therefore,  $l_{\max} = 8$  was used in the calculations for all materials.

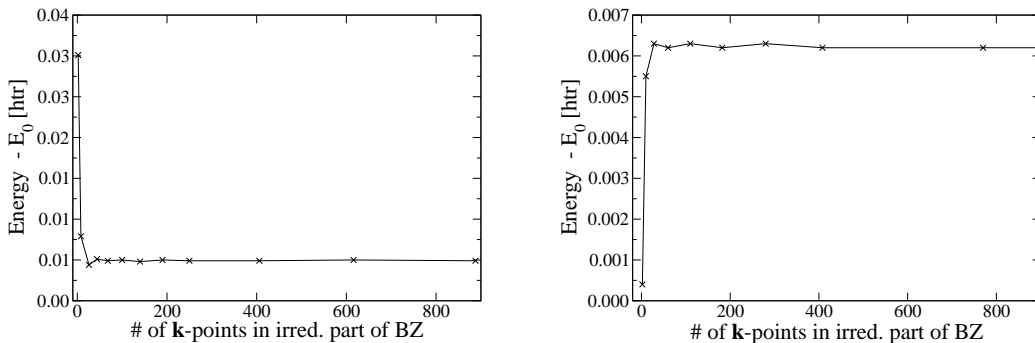


**Figure 7.4:** Results of convergence tests for the number of  $\mathbf{k}$  points from bulk crystal calculations of iron (left) and nickel (right). For Fe the parameters  $K_{\max} = 4.2$  and  $l_{\max} = 8$  were used and for Ni  $K_{\max} = 4.0$  and  $l_{\max} = 8$ .

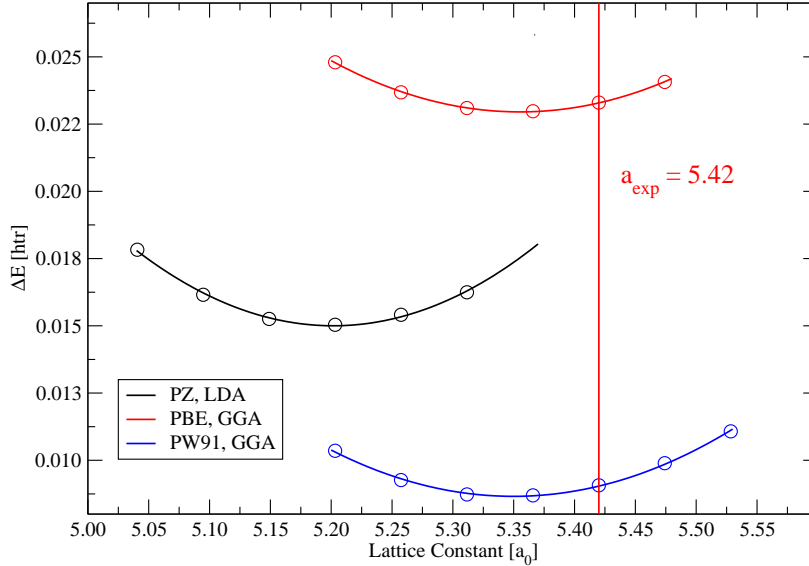


**Figure 7.5:** Results of convergence tests for the best choice of a parametrization for the exchange-correlation potential  $v_{xc}$  from bulk crystal calculations of iron. The value for  $a_{\text{exp}}$  denotes the lattice constant as obtained from experiments. Parameters used in the calculations:  $K_{\text{max}} = 4.2$ ,  $l_{\text{max}} = 8$ , number of  $\mathbf{k}$  points is 322.

### 7.1.2 Converged Number of $\mathbf{k}$ Points

The augmented plane waves  $\varphi_{\mathbf{G}}^{\sigma}(\mathbf{k}, \mathbf{r})$  are not calculated in FLEUR as analytical functions in  $\mathbf{k}$  space but they are calculated numerically and represented by a set of values  $\{\varphi_{\mathbf{k}_i}^{\sigma}(\mathbf{r})\}$  when  $\mathbf{G}$  is kept fixed and the  $\varphi_{\mathbf{k}_i}^{\sigma}$  are obtained from evaluating the function  $\varphi_{\mathbf{G}}^{\sigma}(\mathbf{k}, \mathbf{r})$  at certain points  $\mathbf{k}_i$  distributed on an equidistant mesh covering the 1<sup>st</sup> BZ. To obtain a set of values  $\{\varphi_{\mathbf{k}_i}^{\sigma}(\mathbf{r})\}$  that represents the wave functions with sufficient numerical accuracy, the number  $N_{\mathbf{k}}$  of  $\mathbf{k}$  points must be chosen large enough, but it may not be chosen too large because calculations would become too time consuming. The number  $N_{\mathbf{k}}$  of  $\mathbf{k}$  points is obtained by calculating the total energy in FLEUR for different values of  $N_{\mathbf{k}}$  with  $K_{\text{max}}$  and  $l_{\text{max}}$  kept fixed. Convergence is reached, if the value of the total energy does not change further with increasing number  $N_{\mathbf{k}}$  of  $\mathbf{k}$  points within a range of 0.001 htr around the converged value of the total energy. Examples of calculations for Fe and Ni can be seen in figure 7.4. The values for  $N_{\mathbf{k}}$  of  $\mathbf{k}$  obtained for Fe, Co and Ni are listed in the table at the beginning of this section. Note that  $N_{\mathbf{k}}$  is the number of  $\mathbf{k}$  points used to solve the Kohn-Sham equation self-consistently in FLEUR. As discussed above the density of states as well as the input values for the DMFT part of the GGA+DMFT scheme were generated with a larger number of  $\mathbf{k}$  points.

### 7.1.3 The Choice of the Exchange-Correlation Potential

Since the results obtained from the new GGA+DMFT scheme are to be compared with experimental data, the experimental value for the lattice constant  $a_{\text{exp}}$  was used as input value for all materials in all calculations. However, it was already mentioned briefly in the introduction of this section, that different parametrizations of the exchange-correlation potential  $v_{\text{xc}}$  usually yield different values for the theoretically determined equilibrium lattice constant  $a_0$ . Therefore, a parametrization of  $v_{\text{xc}}$  yielding a value for  $a_0$  close to the experimental value is preferable because it keeps the calculations as close as possible to the theoretical equilibrium. For a fixed number of  $\mathbf{k}$  points and fixed values for  $K_{\text{max}}$  and  $l_{\text{max}}$ , the total energy was determined with FLEUR for different values of the lattice constant and for a total of three different choices of the parametrization of  $v_{\text{xc}}$ . The figures 7.5 and 7.6 show the results of calculations performed for iron and nickel.

I used one parametrizations of  $v_{\text{xc}}$  in the LDA denoted by PZ, which was originally introduced by Perdew and Zunger [PZ81] and two parametrizations in the GGA, the first one denoted by PW91 and the second one by PBE introduced both by Perdew *et al.* [PW92, PBE96]. The absolute values of the total energy obtained from calculations with the different parametrization for  $v_{\text{xc}}$  differ so much that I had

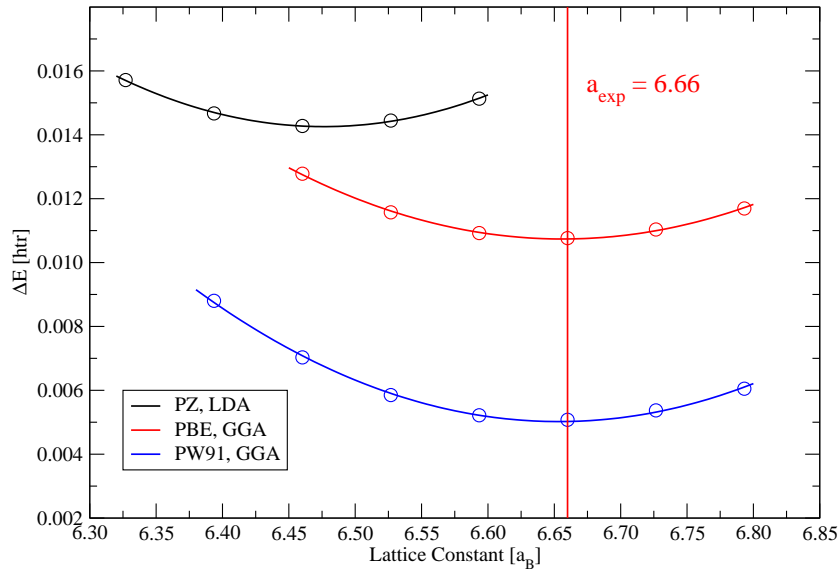


**Figure 7.6:** Results of convergence tests for the best choice of a parametrization for the exchange-correlation potential  $v_{\text{xc}}$  from bulk crystal calculations of nickel. The value for  $a_{\text{exp}}$  denotes the lattice constant as obtained from experiments. Parameters used in the calculations:  $K_{\text{max}} = 4.2$ ,  $l_{\text{max}} = 8$ , number of  $\mathbf{k}$  points is 280.

to shift the curves on the energy axis to plot all of them in one graph. Therefore, I plotted only differences in the total energy instead of the absolute values. The lattice constants are not affected by this rescaling, since I compared the position of the energy minimum at  $a_0$  with the value for the lattice constant  $a_{\text{exp}}$  obtained from experiments [Wij86]. The parametrization PBE yields the value for  $a_0$ , which comes closest to  $a_{\text{exp}}$ , hence, PBE was used in all further DFT calculations.

## 7.2 Transformation from the LAPW to the TB-FLAPW Basis

In this section, I would like to discuss the two approximations entering into the description of the electronic system of a certain material if a basis transformation from the representation in the LAPW basis to a representation in the tight-binding(TB)-FLAPW basis introduced in chapter 3 is carried out. This transformation is necessary since the lattice electron model defined in chapter 5 in equation (5.4) describing the electronic system within DMFT as well as the lattice Green functions used to solve the model are written in terms of the TB-FLAPW basis. The TB-FLAPW basis functions are obtained from the LAPW basis functions

- by neglecting the term containing the energy derivative of the radial function  $\dot{u}_l$  in the LAPW basis in the muffin-tin regions and
- by neglecting the plane wave contributions in the LAPW basis from the interstitial region.

The consequences of these approximations are to be examined now.

As for the first approximation, the results from various calculations prove that Fe, Co and Ni are well described in terms of the TB-FLAPW basis inside the muffin-tin regions, since the changes due to the neglect of the term containing the energy derivative of the radial function in the LAPW basis are rather small. To demonstrate this I present results of calculations of the spin-resolved density of states  $D^\sigma$  of the electrons inside the muffin-tin regions denoted as  $MT D^\sigma$  using an expansion of the Kohn-Sham functions in terms of the LAPW basis. These calculations are compared with the density of states  $D_{\text{TB}}^\sigma$  obtained from a representation of the Kohn-Sham functions in terms of the TB-FLAPW basis. The densities of states are obtained directly from the Kohn-Sham eigenfunctions written in terms of one basis set or the other as

$$D^\sigma(\epsilon) = \sum_{L\nu\mu} \frac{1}{V_{\text{BZ}}} \int_{\text{BZ}} d^3k \left[ |A_{l,\nu}^{\mu\sigma}(\mathbf{k})|^2 + |B_{l,\nu}^{\mu\sigma}(\mathbf{k})|^2 \int_0^{R_{\text{MT}}} r^2 dr |\dot{u}_{l\sigma}(r)|^2 \right] \delta(\epsilon - \epsilon_{n\mathbf{k}\sigma}) \quad (7.1)$$

and

$$\begin{aligned}
 D_{\text{TB}}^{\sigma}(\epsilon) &= \sum_{\mathbf{R}, L\nu\mu} \frac{1}{V_{\text{BZ}}} \int_{\text{BZ}} |\tilde{A}_{l,\nu}^{\mathbf{R}\mu\sigma}(\mathbf{k})|^2 d^3k \delta(\epsilon - \epsilon_{n\mathbf{k}\sigma}) \\
 &= \sum_{L\nu\mu} \frac{1}{V_{\text{BZ}}} \int_{\text{BZ}} |A_{l,\nu}^{\mu\sigma}(\mathbf{k})|^2 d^3k \delta(\epsilon - \epsilon_{n\mathbf{k}\sigma}) .
 \end{aligned}
 \tag{7.2}$$

with the  $A$ - and  $B$ -coefficients as defined in (3.21) and  $\tilde{A}_{l,\nu}^{\mathbf{R}\mu\sigma}$  defined in (3.33). Note that  $D_{\text{TB}}^{\sigma}$  can also be obtained from the (DFT) lattice Green function as described in chapter 4 in equation (4.21).

To compare the two densities of states  $D^{\sigma}$  and  $D_{\text{TB}}^{\sigma}$  both were plotted together in one graph for Fe, Co and Ni. Figure 7.7 shows results for Fe and figure 7.8 and 7.9 for Co and Ni. For all three materials, the peak structure of  $D^{\sigma}$  and  $D_{\text{TB}}^{\sigma}$  is identical. The only differences between both densities are small deviations in the height of the peaks. To analyze these deviations quantitatively, the relative deviation  $\Delta D_l^{\sigma}$  of the orbital-resolved density  $D_{\text{TB},l}^{\sigma}$  from the orbital-resolved density  $D_l^{\sigma}$  (with  $l$  denoting the  $s$ ,  $p$  or  $d$ -band density of states) can be calculated by

$$\Delta D_l^{\sigma}(\epsilon) = \frac{D_l^{\sigma}(\epsilon) - D_{\text{TB},l}^{\sigma}(\epsilon)}{D_l^{\sigma}(\epsilon)} ,
 \tag{7.3}$$

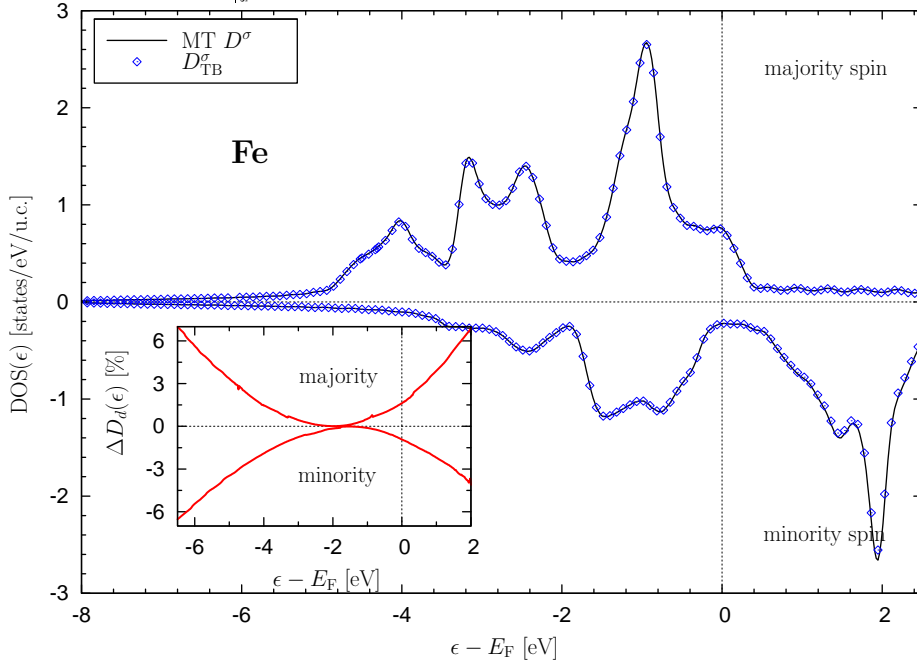


**Figure 7.7:** DOS obtained from DFT calculations for iron (grid of 781 energy points): Comparison of the total DOS  $D^{\sigma}$  with  $D_{\text{TB}}^{\sigma}$  of the electronic states inside one muffin-tin and plot of  $\Delta D_l$  (small frame) for the DOS of  $d$  electrons inside a muffin-tin.

where  $D_l^\sigma$  and  $D_{\text{TB},l}^\sigma$  are obtained from the equations (7.1) and (7.2) for  $D^\sigma$  and  $D_{\text{TB}}^\sigma$  by omitting the sum over the  $l$  quantum number.

In figure 7.7, 7.8 and 7.9  $\Delta D_l^\sigma$  is plotted for the  $d$  electrons in the small frames. I chose to depict the deviation between the densities of the  $d$  states since the  $d$  electrons yield the major contribution to the DOS of all three materials and the deviations of  $D_{\text{TB},d}^\sigma$  from  $D_d^\sigma$  is larger than the deviations between the  $s$  and  $p$  band densities. However, even  $\Delta D_d^\sigma$  does not get larger than a few percent for any of the materials studied here. Furthermore, a significant deviation is reached only far away from the center of gravity of the  $d$  bands, where the contribution of these bands to the density of states  $D_d^\sigma(\epsilon)$  is already close to zero. Hence, only very few states described by the LAPW basis functions are not captured by the TB-FLAPW basis functions.

It might be interesting to mention that the parabolic form of  $\Delta D_d^\sigma$  originates directly from neglecting the energy derivative  $\dot{u}_l$  of the radial function in the LAPW basis function when deriving the TB-FLAPW basis set. The term containing  $\dot{u}_l$  in the expansion of the Kohn-Sham eigenfunctions and enters quadratically in the definition of  $D^\sigma$  given by equation (7.1). This causes the parabolic form of the deviation between  $D_l^\sigma$  and  $D_{\text{TB},l}^\sigma$  since the term proportional to  $\dot{u}_l$  is missing in  $D_{\text{TB},l}^\sigma$ . Furthermore, the radial function  $u_l$  in the expansion of the Kohn-Sham eigenfunction is obtained from the energy-dependent radial function  $u_l(E)$  of the APW basis by

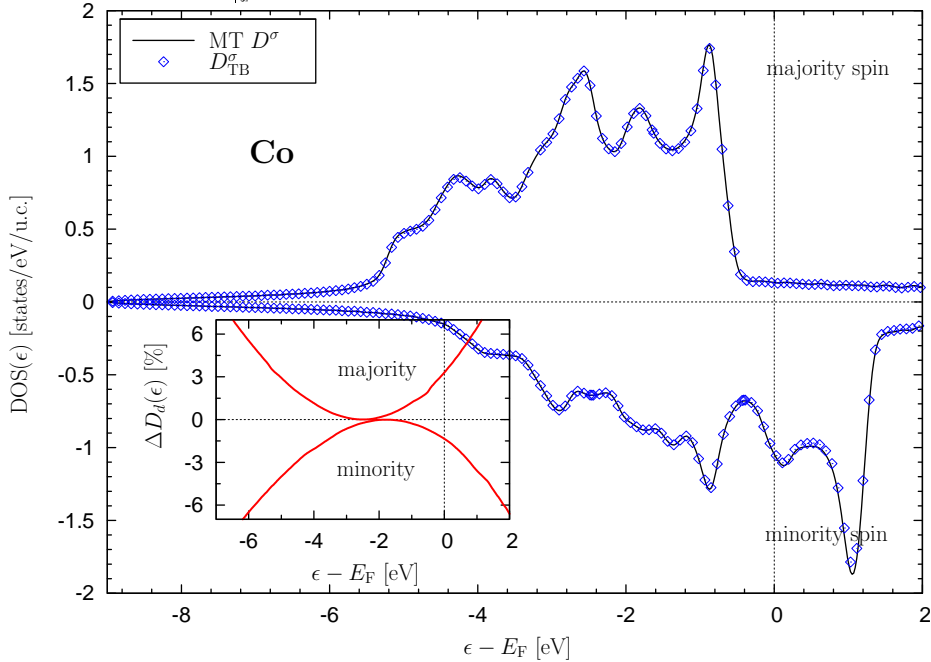


**Figure 7.8:** DOS obtained from DFT calculations for cobalt (grid of 781 energy points): Comparison of the total DOS  $D^\sigma$  with  $D_{\text{TB}}^\sigma$  of the electronic states inside one muffin-tin and plot of  $\Delta D_l$  (small frame) for the DOS of  $d$  electrons inside a muffin-tin.

evaluating  $u_l(E)$  at some fixed energy  $E_l$ . The energies  $E_l$  for the states with orbital numbers  $l = 2$  ( $d$  states) for the majority and minority  $d$  bands of Fe, Co and Ni are listed in the tabular below. Since the energies  $E_l$  are chosen at the center of gravity of the bands to minimize the linearization error entering the LAPW basis functions,  $\dot{u}_l$  becomes zero for  $E = E_l$  yielding  $D_l^\sigma(E_l) = D_{\text{TB},l}^\sigma(E_l)$ . Altogether, the difference in the densities of states  $D_{\text{TB}}^\sigma$  from  $D^\sigma$  inside the muffin tins due to the neglect of the term containing  $\dot{u}_l$  in (7.1) is negligible. An interesting discussion about the influence of the term proportional to  $\dot{u}_l$  in the LAPW basis and the influence of terms containing the second and higher energy derivatives of solutions to the radial scalar-relativistic Dirac equation can be found in the article by Friedrich [FSBK06].

Material	$E_l - E_F$ for the $d$ states [eV]	
	majority spin	minority spin
Iron	-2.0	-1.4
Cobalt	-2.5	-1.8
Nickel	-2.2	-1.8

The other approximation upon deriving the TB-FLAPW basis functions, the total neglect in the LAPW basis representation of the plane waves describing the interstitial region, has a bigger quantitative influence than the neglect of the term in the

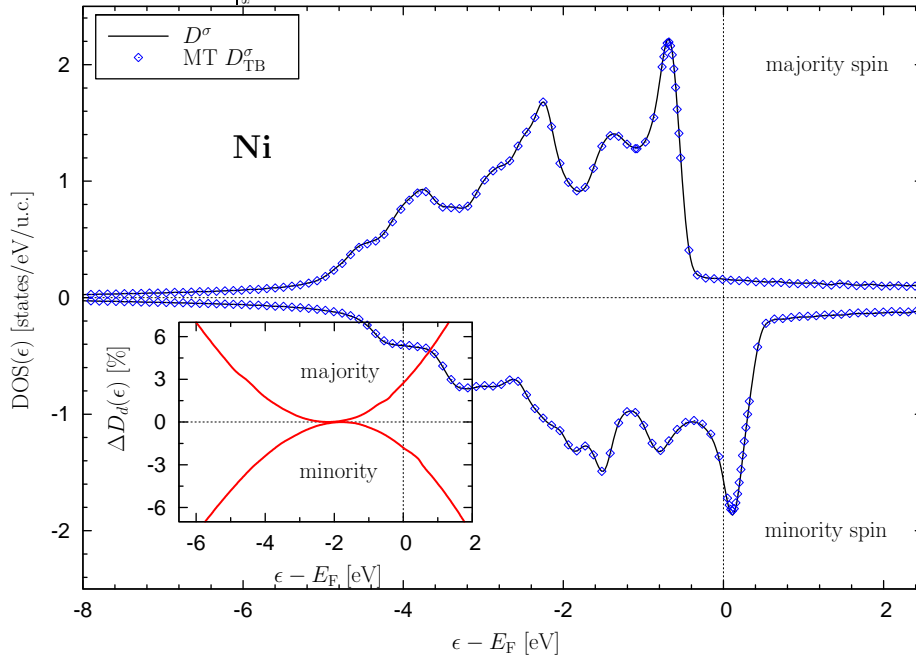


**Figure 7.9:** DOS obtained from DFT calculations for nickel (grid of 1081 energy points): Comparison of the total DOS  $D^\sigma$  with  $D_{\text{TB}}^\sigma$  of the electronic states inside one muffin-tin and plot of  $\Delta D_l$  (small frame) for the DOS of  $d$  electrons inside a muffin-tin.

LAPW basis function containing  $\dot{u}_l$ . This is due to the fact that the second approximation to the LAPW basis functions is equivalent to the total neglect of contributions of the electronic states situated in the interstitial region. Consequently, in the TB-FLAPW basis representation only the charges situated inside the muffin-tin regions are accounted for. However, due to the choice of the muffin-tin radius to be as large as possible and due to the fact that all materials to be examined have a close-packed crystal structure, most of the electron charge is indeed situated inside the muffin tins. This can be demonstrated by integrating the density of states  $D_{\text{TB}}^\sigma$  over the energy up to the Fermi level, which yields the charge inside the muffin-tin region. This can be compared to the total number of valence electrons. Both quantities are listed in the table below for calculations of Fe, Co and Ni.

<b>Material</b>	Charge situated inside each muffin tin	Total number of valence electrons per atom
<b>Iron</b>	6.952	8
<b>Cobalt</b>	8.160	9
<b>Nickel</b>	9.204	10

Although all charges of the valence electrons are not fully accounted for by the description of the electronic system in the TB-FLAPW representation the majority of the charges are taken into account. In particular, the charges situated in the  $d$  bands are captured almost completely by the TB-FLAPW basis representation, since the  $d$  bands are almost completely localized inside the muffin-tin regions. This can be demonstrated by integrating the densities of the  $d$  states  $D_d^\sigma$  and  $D_{\text{TB},d}^\sigma$  over the energy up to the Fermi level and compare how many charges are missing in the density obtained from the TB description of the electronic system.

<b>Material</b>	Charges in the LAPW $d$ states	Charges in the TB-FLAPW $d$ states
<b>Iron</b>	6.1462	6.1418
<b>Cobalt</b>	7.2394	7.2387
<b>Nickel</b>	8.2992	8.2990

The amount of charges not captured by the TB description compared to the LAPW description is smaller than 0.5% for all three materials. Thus, despite the neglect of the charges in the interstitial region, the TB-FLAPW basis functions yield a description both sufficient and accurate enough for the further treatment within DMFT, since it is most important for the calculations within DMFT that the electronic  $d$  states are described accurately.



# 8 Benchmark Calculations within GGA+DMFT for Fe, Co and Ni

In this chapter results from calculations of bulk-crystal properties of the  $3d$  transition metals iron, cobalt and nickel obtained from the new GGA+DMFT scheme are presented. These metals are used for benchmark calculations, since they are intermediately correlated materials due to the partially occupied  $d$  bands and the features of the electronic structure related to the correlation effects are described rather poorly within the LDA or GGA. The description of these materials within GGA+DMFT should improve on the characterization of these features. Therefore, the density of states (DOS), the spectral function and the spin-magnetic moment per atom were calculated within the new implementation of the GGA+DMFT. By comparing the resulting quantities with DFT calculations it is demonstrated how the incorporation of true many-body interactions between electrons changes the features in the electronic structure. Furthermore, the results from the GGA+DMFT approach are found to be in very good agreement with experimental data. This emphasizes the importance of including correlation effects in the description of the electronic system. Furthermore, it can be seen as strong evidence that the FLEX solver used within the DMFT part of the new scheme takes into account the dominant effects responsible for the electronic correlations within the regime of intermediately correlated electron systems. Altogether, the new GGA+DMFT scheme definitely yields an improvement of the bare LDA or GGA description of the electronic structure of the  $3d$  transition metals.

In the first part of the chapter I describe briefly how the DOS, the spectral function and the spin-magnetic moment were calculated. In the second part, I present my results for Fe, Co and Ni.

## 8.1 Calculations

Lattice Green functions are used for all calculations within GGA+DMFT. A lattice Green function within DFT was derived in chapter 4 as a matrix with elements  $G_{\mathbf{R}L,\mathbf{R}'L'}^{0\sigma}$  for each spin  $\sigma$  for the lattice sites  $\mathbf{R}$  and  $\mathbf{R}'$  and for the pair of orbital indices  $L$  and  $L'$  with the combined index  $L = (l, m)$  denoting a certain atomic-like orbital. Within the DMFT part, the single-particle propagator of an interacting particle is given by the lattice Green function with matrix elements  $G_{\mathbf{R}L,\mathbf{R}'L'}^\sigma$  that is derived by solving the Dyson equation (5.15) using  $G_{\mathbf{R}L,\mathbf{R}'L'}^{0\sigma}$  and the self-energy

$\Sigma_{\mathbf{R};LL'}^\sigma$ . The latter is obtained using the FLEX method as described in chapter 5. To use the FLEX method in this context, some input values for the Hubbard  $U$  and Hubbard  $J$  are necessary. The values listed in the table below were taken from the results and discussions presented in [DJcvK99].

Material	Hubbard $U$ [eV]	Hubbard $J$ [eV]
<b>Iron</b>	1.63	1.09
<b>Cobalt</b>	1.63	1.22
<b>Nickel</b>	2.45	1.63

Unfortunately, it is not clear from [DJcvK99] how the muffin-tin radii in the TB-LMTO approach were chosen. However, for a different choice of these radii in the present work different values for  $U$  and  $J$  might be obtained. On the other hand it is also argued in [DJcvK99] that there is no unique way to determine  $U$  and  $J$  for the  $d$  states and that a broad range of values can be found in the literature. For example Grechnev *et al.* used slightly bigger values for  $U$  and  $J$  in [GDMK<sup>+</sup>06] e.g.  $U = 2.3\text{eV}$  and  $J = 0.9\text{eV}$  for Fe. Since the values I used do not differ from those substantially it should not make a big difference in the calculations which values are finally used within a certain energy window. However, no quantitative analysis was carried out so far to support this assumption.

After the single-particle propagator  $G_{\mathbf{R}L,\mathbf{R}'L'}^\sigma$  is determined self-consistently on the basis of the iteration scheme described in chapter 6 it is used to calculate single-particle bulk-crystal properties. In this section it is described in a little more detail how these observables are obtained from  $G_{\mathbf{R}L,\mathbf{R}'L'}^\sigma$ .

### 8.1.1 Density of States (DOS)

The density of states gives the spectrum of the energy eigenstates per atom in the unit cell in real space. From the lattice Green function in real space an  $l$ -resolved density of states  $D_l^\sigma$  for each spin is obtained by

$$D_l^\sigma(\epsilon) = -\frac{1}{\pi} \sum_m \text{Im} G_{\mathbf{R}lm,\mathbf{R}lm}^\sigma(\epsilon), \quad (8.1)$$

which is identical at all lattice sites for elementary solids with one atom per unit cell. The total density of states  $D^\sigma$  for each spin is derived from (8.1) by summation over the  $l$  quantum numbers

$$D^\sigma(\epsilon) = \sum_l D_l^\sigma(\epsilon), \quad (8.2)$$

and the spin-integrated total DOS is determined from (8.2) by summation of the contributions for each spin

$$D(\epsilon) = \sum_{\sigma \in \{\uparrow, \downarrow\}} D^\sigma(\epsilon). \quad (8.3)$$

Note that the densities are all derived from the diagonal elements of the Green-function matrix. Furthermore, it should be mentioned that the DOS and all further quantities are derived from the retarded lattice Green functions. As opposed to the DOS obtained from the time-ordered Green function in equation (4.22), expression (8.1) contains a prefactor of minus one on the right-hand side for all energy arguments of the Green function. In chapter 4 in equation (4.37) it was described how the retarded Green function is connected to the time-ordered Green function which is used to evaluate the diagrammatic expressions obtained from the FLEX method to calculate the self-energy.

Inserting the DFT lattice Green function  $G_{\mathbf{R}L,\mathbf{R}'L'}^{0\sigma}$  into (8.1) yields  $D_{\text{TB}l}^{\sigma}$  as derived from the TB-FLAPW basis functions in the previous chapter. Consequently, (8.2) yields the density  $D_{\text{TB}}^{\sigma}$  introduced in that chapter. Since all quantities introduced in the present chapter are derived from the tight-binding description of the electronic system, the index “TB” is dropped from now on.

To calculate the DOS for the interacting lattice system, the interacting lattice Green function  $G_{\mathbf{R}L,\mathbf{R}'L'}^{\sigma}$  is used to evaluate (8.1), (8.2) and (8.3). The changes in the newly derived DOS compared to the DOS derived from the DFT lattice Green function can be directly related to the self-energy  $\Sigma^{\sigma}$  that is incorporated into  $G^{\sigma}$  by solving the Dyson equation. In quasi-particle language  $\text{Re}(\Sigma^{\sigma})$  gives the energy of the quasi-particles whereas  $\text{Im}(\Sigma^{\sigma})$  is inversely proportional to the life-time of the quasi-particles. The additional energy shifts the peaks in the spectrum of the density of states compared to their position in the DFT description while the finite life-time of the quasi-particle excitations leads to a quasi-particle damping of the peaks in the DOS such that the height of the peaks is reduced and the peaks are simultaneously broadened. These changes can be observed in all spectra calculated within GGA+DMFT.

### 8.1.2 Band Structure and Spectral Function

The spectral function introduced in chapter 4 gives the spectrum of the energy eigenstates in  $\mathbf{k}$ -space. Within DFT the spectral function can be obtained directly from definition (4.23) using the Kohn-Sham eigenfunctions  $\psi_{\mathbf{k},\nu}^{\sigma}$  and the Kohn-Sham eigenvalues  $\epsilon_{\mathbf{k},\nu}^{\sigma}$

$$A^{\sigma}(\mathbf{k}; \epsilon) = \sum_{\nu} \int d^3r |\psi_{\mathbf{k},\nu}^{\sigma}(\mathbf{r})|^2 \delta(\epsilon - \epsilon_{\mathbf{k},\nu}^{\sigma}) = \sum_{\nu} \delta(\epsilon - \epsilon_{\mathbf{k},\nu}^{\sigma}) \quad (8.4)$$

where I already made use of the fact, that the Kohn-Sham eigenfunctions are orthogonal. The spectral function within DFT thus has delta-peak structure.

In figure 8.1 it is depicted schematically how the band structure is derived from the spectral function within DFT. The band structure is the energy dispersion along high-symmetry directions inside the first Brillouin zone (1<sup>st</sup> BZ) of the crystal.

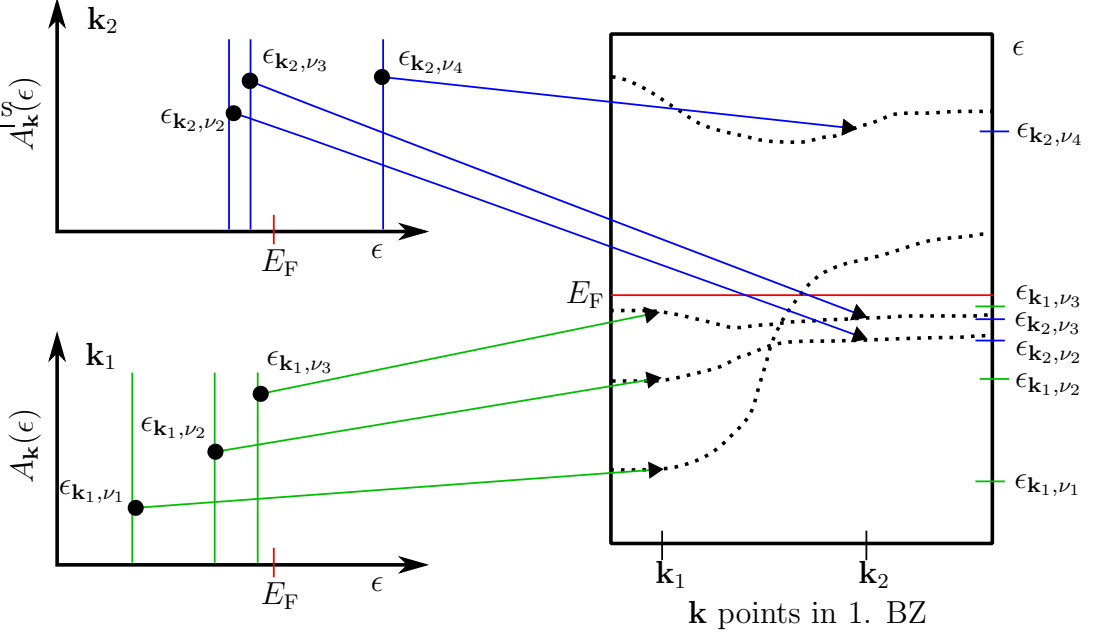


**Figure 8.1:** Schematic description of the derivation of the band structure. The spectral function  $A_{\mathbf{k}}(\epsilon)$  is plotted (left side) for two different  $\mathbf{k}$  vectors  $\mathbf{k}_1$  and  $\mathbf{k}_2$  to determine the bands yielding a contribution to the energy dispersion for the selected  $\mathbf{k}$  point. Plotting the energies over the  $\mathbf{k}$  points (right side) yields the band structure.

In chapter 4 it was described that the spectral function can also be obtained from the one-particle Green function. Using the interacting lattice Green function in  $\mathbf{k}$  space  $G_{LL'}^{\sigma}(\mathbf{k}; \epsilon)$  (or the DFT lattice Green function  $G_{LL'}^{0\sigma}(\mathbf{k}; \epsilon)$ ) the spectral function is given by

$$A^{\sigma}(\mathbf{k}; \epsilon) = -\frac{1}{\pi} \sum_L \text{Im} G_{LL}^{\sigma}(\mathbf{k}; \epsilon). \quad (8.5)$$

If (8.5) is evaluated using the retarded DFT Green function written in the Lehmann representation below

$$G_{LL'}^{0\sigma}(\mathbf{k}; \epsilon) = \frac{1}{N} \sum_{\nu} \frac{(A_{L,\nu}^{\sigma}(\mathbf{k})) (A_{L',\nu}^{\sigma}(\mathbf{k}))^*}{\epsilon - \epsilon_{\mathbf{k},\nu}^{\sigma} + i\eta} \quad (\text{see 4.34})$$

and the formula

$$\frac{1}{x \pm i\eta} = \mathcal{P} \left( \frac{1}{x} \right) \mp i\pi\delta(x) \quad (\text{see 4.19})$$

in the limit  $\eta \rightarrow 0^+$  is applied, where  $\mathcal{P}(1/x)$  is the principal value of  $1/x$ , the DFT

spectral function (8.4) is recovered

$$\begin{aligned} A^\sigma(\mathbf{k}; \epsilon) &\stackrel{\eta \rightarrow 0^+}{=} -\frac{1}{\pi} \sum_L \left( -\frac{1}{N} \sum_\nu |A_{L,\nu}^\sigma(\mathbf{k})|^2 \pi \delta(\epsilon - \epsilon_{\mathbf{k},\nu}^\sigma) \right) \\ &= \sum_\nu \delta(\epsilon - \epsilon_{\mathbf{k},\nu}^\sigma) \end{aligned} \quad (8.6)$$

In the second step, the orthonormality of the TB-FLAPW basis function was used. Note that on the left-hand side  $A^\sigma$  denotes the DFT spectral function whereas on the right-hand side the  $A_{L,\nu}^\sigma$  are the coefficients of the TB-FLAPW basis.

If the interacting lattice Green function is inserted into (8.5) the spectral function no longer has delta-peak structure due to the self-energy contained in  $G_{LL'}^\sigma(\mathbf{k}; \epsilon)$ . Since the imaginary part of the self-energy usually is non-zero, the imaginary part of the lattice Green function is of Lorentzian-like shape approximately given by

$$\text{Im} \left( G_{LL}^\sigma(\mathbf{k}; \epsilon) \right) \sim \frac{\text{Im}(\Sigma^\sigma(\epsilon))}{[\epsilon - \epsilon_{\mathbf{k},\nu}^\sigma + \text{Re}(\Sigma^\sigma(\epsilon))]^2 + [\text{Im}(\Sigma^\sigma(\epsilon))]^2}, \quad (8.7)$$

where it was assumed that the self-energy is not  $\mathbf{k}$ -dependent as is the case within DMFT. The spectral function obtained from  $G_{LL'}^\sigma(\mathbf{k}; \epsilon)$  will therefore also consist of Lorentzian-type peaks with finite height and finite width.

The Lorentzian shape of the spectral density is caused by the same physical effects as the broadening of the peaks of the DOS. Due to the interaction between particles incorporated in the DMFT description of the interacting lattice system excited particles may not stay in the same single-particle eigenstate for all time but may lose some of their energy through scattering events. This leads to the broadening of the peaks in the spectral function, which is proportional to the imaginary part of the self energy which is in turn inversely proportional to the finite life-time of the excited state.

Despite the Lorentzian-shaped spectral features a generalized band structure can still be derived from the spectral function of the interacting lattice electron system. This band structure takes explicitly into account finite quasi-particle life-times. In figure 8.2 the procedure to obtain this generalized band structure is depicted. First, the spectral function  $A^\sigma(\mathbf{k}; \epsilon)$  obtained from the interacting lattice Green function  $G_{LL'}^\sigma(\mathbf{k}; \epsilon)$  is plotted as a function of the energy  $\epsilon$  along some high-symmetry directions in the 1<sup>st</sup> BZ. The resulting peak structure is projected onto the  $(\mathbf{k}, \epsilon)$ -plane with the energies plotted along the vertical and the  $\mathbf{k}$  vectors plotted along the horizontal axis. The broadening of the peaks, being inversely proportional to the quasi-particle life-times, is depicted as a shaded area around the peak maxima, the latter giving the position of the actual bands. Compared to the band structure derived from DFT a shift of the position of the energy bands in the generalized band structure can be observed which is caused by the real part of the self energy as can be seen in equation (8.7). This is again consistent with the changes observed in the DOS.

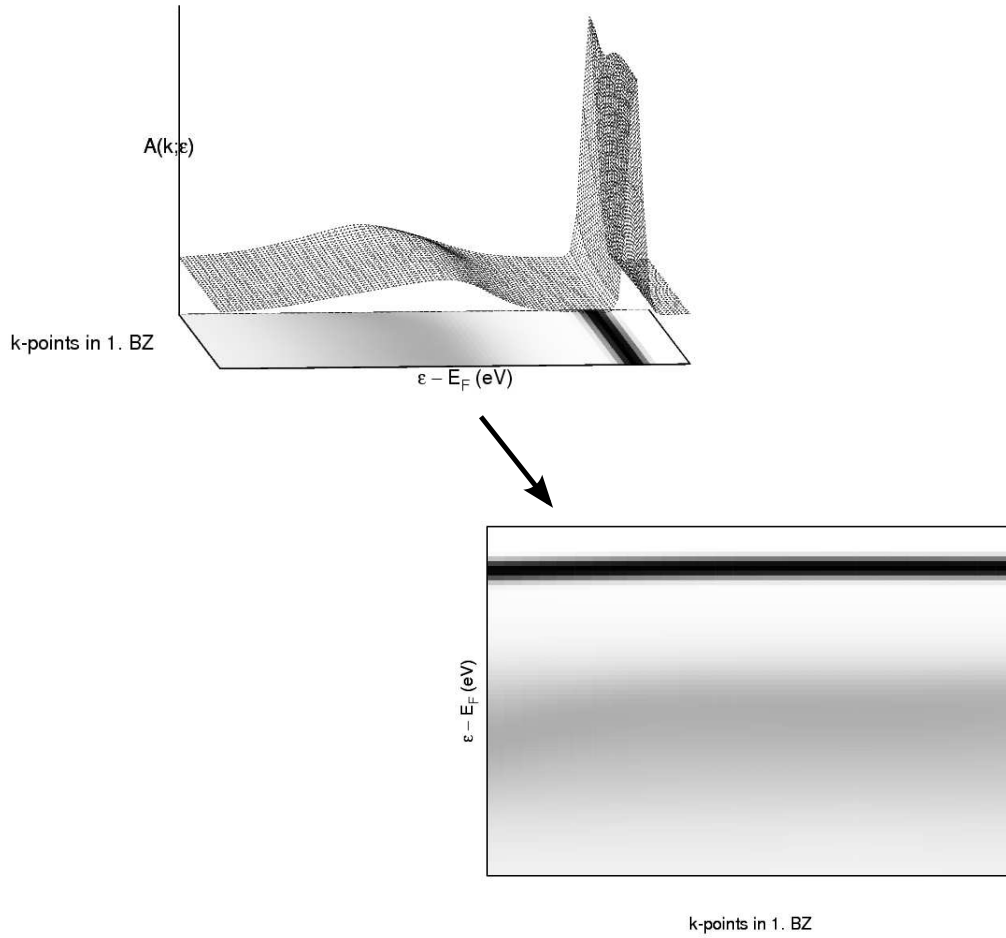


**Figure 8.2:** Example of a fictitious spectral function for a system of interacting electrons (top). The contour lines are projected onto the  $\mathbf{k}, \epsilon$ -plane below the spectral function. The shades of gray encode the amplitude varying between black = maximum height and white = zero height. The complete projection plotted separately in a two-dimensional graph (bottom) yields the generalized band structure.

Although the effects causing the changes in the generalized band structure are the same effects causing the DOS obtained from the GGA+DMFT scheme to differ from the DFT DOS it is instructive to consider both quantities for the materials under investigation. Furthermore, the generalized band structure can be compared to experimental data from ARPES (angular-resolved photo-emission spectroscopy) while the DOS can be compared directly to photo-emission spectra. This will be discussed in more detail below.

### 8.1.3 Total Spin-Magnetic Moments

The magnetization density is derived from the spin-electron densities  $n_{\uparrow}(\mathbf{r})$  and  $n_{\downarrow}(\mathbf{r})$  according to

$$m(\mathbf{r}) = n_{\uparrow}(\mathbf{r}) - n_{\downarrow}(\mathbf{r}) \quad (\text{see 2.6})$$

as described in chapter 2. For the materials studied here, only the total spin-magnetic moment  $\mu_{\text{spin}}$  derived from the integrated spin-electron densities  $n^{\sigma}$  were calculated

$$\mu_{\text{spin}} = \int_{\text{MT}} m(\mathbf{r}) d^3r = n^{\uparrow} - n^{\downarrow} \quad (8.8)$$

and the integrated spin-electron densities are obtained from the lattice Green function in real space by

$$n^{\sigma} = -\frac{1}{\pi} \int_{-\infty}^{E_{\text{F}}} \sum_L \text{Im} G_{\mathbf{R}L, \mathbf{R}L}^{\sigma}(\epsilon) d\epsilon. \quad (8.9)$$

## 8.2 Results for Nickel (Ni)

**Density of States.** The first graphs presented for nickel in figure 8.3 show the spin-resolved total muffin-tin density of states  $D^{\sigma}$  obtained from DFT calculations within the FLAPW which is compared with the density of states obtained from the interacting lattice Green function determined within GGA+DMFT. On the right side, the real and imaginary part of the self-energy contained in the GGA+DMFT description of the electron system of Ni are shown. These self-energy contributions are to be discussed first, since the changes in the DOS obtained from the GGA+DMFT method can be directly related to the self-energy.

The self-energy was determined within FLEX assuming cubic symmetry for all materials and the self-energy contributions were only calculated to describe the interaction between electrons occupying  $d$  states. The crystal field in solids with cubic symmetry splits the 5 electronic  $d$  bands into three-times degenerate  $t_{2g}$  bands and two-times degenerated  $e_g$  bands. Consequently, the self-energy contributions from the majority and the minority spins also split into two contributions  $\Sigma_{t_{2g}}^{\sigma}$  and  $\Sigma_{e_g}^{\sigma}$  for each spin yielding four different self-energy contributions in total. Since the difference between  $\Sigma_{t_{2g}}^{\sigma}$  and  $\Sigma_{e_g}^{\sigma}$  due to the crystal field splitting of the  $d$  bands is rather small I will not discuss it in detail.

The differences in the self-energy contributions for the majority spins compared to the minority's contribution is much larger. This can be qualitatively understood by analyzing equation (6.16) yielding the second order contribution to the FLEX self-energy. From this expression the following equations for  $\Sigma_{t_{2g}}^{\sigma(2)}$  and  $\Sigma_{e_g}^{\sigma(2)}$  are

obtained

$$\begin{aligned}
 \Sigma_{t_{2g}}^{\sigma(2)}(\epsilon) &= (U - J)^2 \left[ 2I_{t_{2g}t_{2g}t_{2g}}^{\sigma\sigma\sigma}(\epsilon) + 2I_{t_{2g}e_g e_g}^{\sigma\sigma\sigma}(\epsilon) \right] \\
 &\quad + U^2 \left[ 3I_{t_{2g}t_{2g}t_{2g}}^{\sigma-\sigma-\sigma}(\epsilon) + 2I_{t_{2g}e_g e_g}^{\sigma-\sigma-\sigma}(\epsilon) \right], \\
 \Sigma_{e_g}^{\sigma(2)}(\epsilon) &= (U - J)^2 \left[ 3I_{e_g t_{2g} t_{2g}}^{\sigma\sigma\sigma}(\epsilon) + I_{e_g e_g e_g}^{\sigma\sigma\sigma}(\epsilon) \right] \\
 &\quad + U^2 \left[ 3I_{e_g t_{2g} t_{2g}}^{\sigma-\sigma-\sigma}(\epsilon) + 2I_{e_g e_g e_g}^{\sigma-\sigma-\sigma}(\epsilon) \right]
 \end{aligned} \tag{8.10}$$

and

$$I_{LL'L''}^{\sigma\sigma'\sigma''}(\epsilon) = \int \int \frac{d\epsilon' d\epsilon''}{(2\pi)^2} \mathcal{G}_L^{0\sigma}(\epsilon - \epsilon') \mathcal{G}_{L'}^{0\sigma'}(\epsilon' + \epsilon') \mathcal{G}_{L''}^{0\sigma''}(\epsilon''). \tag{8.11}$$

Because  $J$  is comparable to  $U$  the largest contribution to  $\Sigma_{t_{2g}}^{\sigma(2)}$  and  $\Sigma_{e_g}^{\sigma(2)}$  comes from states with opposite spins. Furthermore, the first convolution in (8.11) yielding

$$\tilde{I}_{L'L''}^{\sigma'\sigma''}(\epsilon') = \text{Im} \mathcal{G}_{L'}^{0\sigma'}(\epsilon' + \epsilon'') \text{Im} \mathcal{G}_{L''}^{0\sigma''}(\epsilon'') \tag{8.12}$$

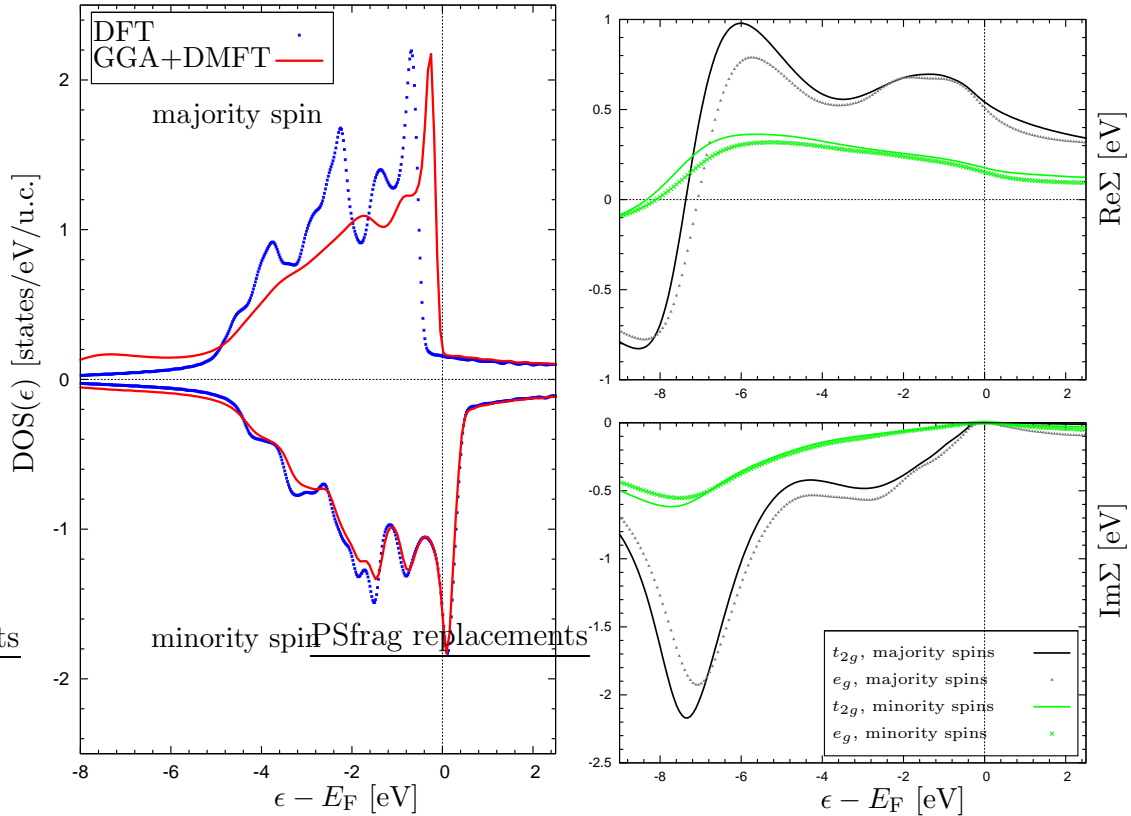
is large for half-filled bands  $L'$  and  $L''$  while the second convolution leading to

$$\text{Im} I_{LL'L''}^{\sigma\sigma'\sigma''}(\epsilon) = \text{Im} \mathcal{G}_L^{0\sigma}(\epsilon - \epsilon') \tilde{I}_{L'L''}^{\sigma'\sigma''}(\epsilon') \tag{8.13}$$

is large for a completely filled band  $L$ . These two conditions are fulfilled for the majority states but they are not fulfilled for the minority states. Therefore, the self-energy for the majority electrons is larger than for the minority electrons and the majority bands are consequently influenced more strongly by the electron correlation.

Finally, it should be mentioned, that the imaginary parts of all self-energy contributions yield  $\text{Im} \Sigma(\epsilon) \propto (\epsilon - E_F)^2$  around the Fermi energy in accordance with the Fermi liquid theory for metals predicting this kind of behavior for the self-energy of metals in the vicinity of the Fermi level. The behavior of the real part of the self-energy however seems to be rather odd because  $\text{Re} \Sigma^\sigma(E_F)$  should also be zero according to Luttinger's theorem. However, Luttinger's theorem is only rigid for one-band models. For now it remains an open question how this behavior of the real part of the self-energy at the Fermi level can be understood.

Since the self-energy contributions are much larger for the majority spin, the GGA+DMFT spin-resolved density of states in figure 8.3 for the majority spin shows some significant differences compared to the DFT DOS whereas the minority-spin DOS obtained from DFT calculations is barely changed in GGA+DMFT. The majority-spin bands in GGA+DMFT move closer to the Fermi level while simultaneously a narrowing of the bands can be observed. This behavior originates from the positive real part of the self-energy for energies larger than  $-7$  eV that moves the center of gravity of the bands closer to the Fermi level. The smearing of the features of the DFT DOS within GGA+DMFT is caused by the imaginary part of the self-energy leading to the broadening of the sharp peaks of the DFT DOS. The

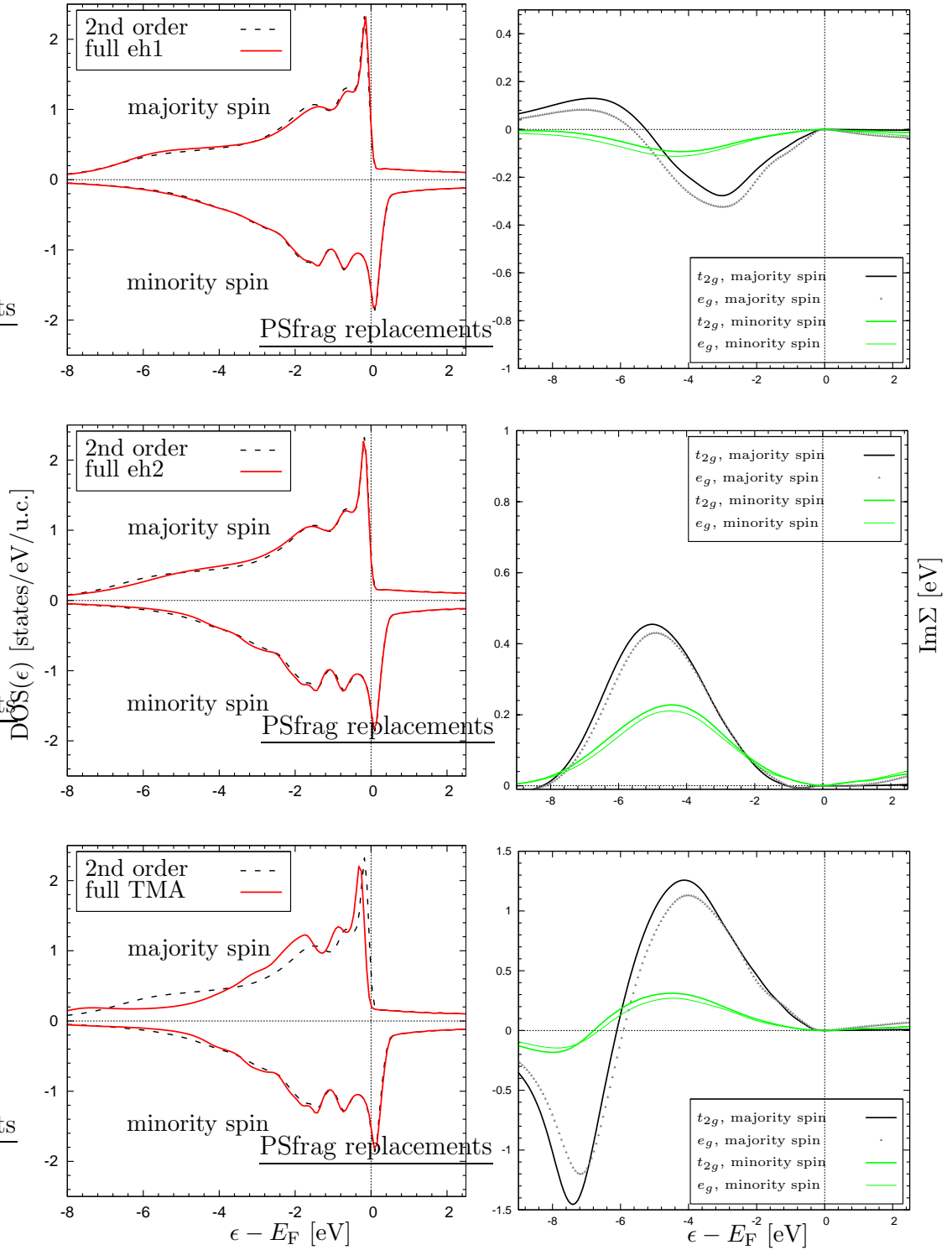


**Figure 8.3:**

*Left:* Majority and minority DOS for fcc nickel obtained within GGA+DMFT (red) compared with the DFT DOS (blue).

*Right:* Real (top) and imaginary part (bottom) of the self-energy contained in the GGA+DMFT calculations on the left. Contributions to the majority-spin self-energy are black and those to the minority-spin self-energy are green. The crystal field splits the self-energy contributions for both spin directions into  $e_g$  and  $t_{2g}$  contributions.

broadening becomes stronger with decreasing energies as  $\text{Im}\Sigma$  is zero at  $E_F$  and increases for energies smaller than  $E_F$ . One of the most remarkable features in the DOS obtained from GGA+DMFT is the forming of a new peak, the so-called satellite, around  $-7$  eV in the majority-spin DOS. The large peak of the imaginary part of the self-energy around  $-7.3$  eV denotes the existence of some long-living quasi-particle excitations in this region. The step descent between  $-6$  and  $-8$  eV as well as the negative peak at  $-8$  eV of the real part of the self-energy indicates a shift of the weights of the low-lying valence bands to lower energies. This is consistent with the common explanation for the appearance of the satellite in nickel (see e.g. [Ary92]) that is caused by two holes that interact by multi-scattering processes thus forming a virtual bound state. The holes are created, if e.g. one electron is emitted from the  $d$  bands during a photo-emission process and a second  $d$  electron at the same site is

**Figure 8.4:**

*Left:* DOS of fcc nickel obtained within GGA+DMFT calculated using only the second-order self-energy contribution (dashed lines) and the second-order plus one higher-order contribution of the self-energy.

*Right:* Imaginary part of the self-energy contributions  $\Sigma^{\sigma \text{ eh1}}(3)$  (top row),  $\Sigma^{\sigma \text{ eh2}}(3)$  (second row),  $\Sigma^{\sigma \text{ pp}}(3)$  (last row) including crystal-field splitting effects. Contributions to the majority-spin self-energy are black and those to the minority-spin self-energy are green.

excited to a state slightly above the Fermi energy. The resulting configuration in the atomic picture corresponding to  $3d^74s^2$  is separated from the main band ( $3d^84s$ ) by more than  $-6$  eV. Due to the selection rules, electrons at the bottom of the  $d$  bands, that hybridize with the  $s$ - $p$  bands, have the largest probability to be excited to the empty  $d$  states. Consequently, the spectral weight going to the satellite mainly comes from the bottom of the  $d$  band as observed in figure 8.3.

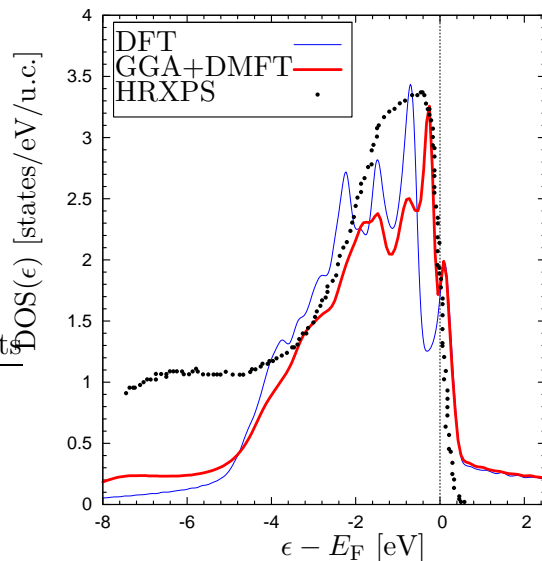
The construction of the self-energy within FLEX enables us to analyze, if the multiple scattering of two holes really is the dominant effect responsible for the formation of the satellite. This can be done by evaluating the single contributions to the self-energy from the different subclasses of the diagrams for the self-energy separately for each contribution. A DOS containing only self-energy contributions derived from one subclass of diagrams can be calculated then. It was shown that the self-energy expression obtained from the FLEX method can be expressed within the framework of DMFT as a sum over the contributions from four different subclasses

$$\Sigma^\sigma(\epsilon) = \Sigma^{\sigma(2)}(\epsilon) + \Sigma^{\sigma\text{pp}(3)}(\epsilon) + \Sigma^{\sigma\text{eh1}(3)}(\epsilon) + \Sigma^{\sigma\text{eh2}(3)}(\epsilon), \quad (\text{see 6.14})$$

where  $\Sigma^{\sigma(2)}$  is the second-order self-energy contribution and  $\Sigma^{\sigma\text{pp}(3)}$  is the contribution from the multiple particle-particle scattering processes further referred to as T-matrix approximation (TMA) starting from third order. The last two terms originates from the electron-hole channel and  $\Sigma^{\sigma\text{eh1}(3)}$  contains all contributions describing multiple scattering processes between an electron and a hole and  $\Sigma^{\sigma\text{eh2}(3)}$  describes the screening of the Coulomb interaction. In figure 8.4 the DOS calculated within GGA+DMFT are presented, that incorporate only one of the self-energy contributions of higher order and the second-order self-energy contribution (e.g. in the first row the DOS obtained from the self-energy  $\Sigma'^\sigma = \Sigma^{\sigma(2)} + \Sigma^{\sigma\text{eh1}(3)}$  is depicted). In each graph, the DOS obtained from including only the second-order self-energy contribution  $\Sigma^{\sigma(2)}$  in the GGA+DMFT scheme is also shown for several reasons: the second-order contribution has to be present in all calculations incorporating some higher-order corrections. If the additional changes due to these higher-order terms are to be studied it is reasonable to also compare them directly to the results containing only the second-order corrections. It furthermore proves, that the second-order term is the dominant term for all three different channels of the self-energy corrections. When comparing the contributions depicted in the graphs of 8.4 it is obvious, that the TMA yields the major contribution to the total DOS obtained from GGA+DMFT. Furthermore, it can be seen that the particle-particle interaction captured by the TMA really is responsible for the formation of the quasi-particle peak in the majority-spin DOS whereas the contributions from the two electron-hole channels are minor. This is confirmed by the presentation of the imaginary parts of the self-energy contributions  $\Sigma^{\sigma\text{eh1}(3)}$ ,  $\Sigma^{\sigma\text{eh2}(3)}$  and  $\Sigma^{\sigma\text{pp}(3)}$  also depicted in figure 8.4 on the right. Note that the imaginary part of the self-energy within the TMA is more than a factor two larger than the contributions from the other channels. Furthermore, the quasi-particle life-time of the particles causing the satellite also originates solely from the particle-particle channel.

Finally, the calculations of the DOS shall be compared to some experimental data. The density of states is the spectrum of the energy-resolved eigenstates per atom in the unit cell in real space. Hence, it can be compared directly to photo-emission spectra obtained from measurements of states below the Fermi energy or inverse photo-emission spectra obtained from experiments probing states above the Fermi level. The measurement of spin-resolved photo-emission spectra seems to be rather difficult and it was not possible to find experimental data with a sufficient level of accuracy and resolution. However, some measurements of the high-resolution x-ray photo-emission spectrum (HRXPS) of the spin-integrated DOS for Fe were reported in [SK96]. In figure 8.5 the spin-integrated DOS as obtained within DFT (blue) and GGA+DMFT is plotted together with the HRXP spectrum (black dots). The experimental data are given in arbitrary units. Thus, the height of the experimental curve was rescaled to match the height of the theoretical spectra. Note that only the spectrum of the occupied electronic states can be obtained from photo-emission spectroscopy. Hence, the contributions to the DOS above the Fermi level calculated within DFT and GGA+DMFT are not captured in this experimental setup. Furthermore, the experimental curve does not decrease as quickly as predicted by the calculations for the lower-lying energies. This originates from effects occurring during the measurement e.g. instrumental broadening, matrix-element modulation or the appearance of an inelastic tail due to electron-electron scattering. An interesting discussion of these effects can be found e.g. in the article by Höchst, Goldmann and Hüfner [HGH76] on the measurement of the XP spectrum of iron. Despite these discrepancies in the HRXP spectrum it is evident, that the data agree well with the calculations from GGA+DMFT. The band narrowing, the shift of the main peak towards the Fermi level as well as the formation of the satellite are all reproduced by the GGA+DMFT calculation in accordance with the measured data. Only the experimentally obtained position of the satellite is slightly higher than the position as predicted by GGA+DMFT. The moving of the satellite closer to the Fermi level

**Figure 8.5:** Comparison between the spin-integrated DOS for fcc nickel obtained within DFT (blue) and GGA+DMFT (red) and from measurements deploying high resolution x-ray photo-emission spectroscopy (HRXPS, black dots). HRXPS can only determine the occupied electronic states below  $E_F$ , hence the resonances in the calculated DOS above the Fermi level are not recorded by HRXPS.



could originate from screening of the Coulomb potential not included sufficiently in GGA+DMFT. This assumption would have to be verified in further studies.

**Spin Magnetic Moments and Exchange Splitting.** From DFT calculations carried out with FLEUR a spin-magnetic moment of  $0.66\mu_B$  was obtained which is slightly above the experimental value of  $0.60\mu_B$  [SAS92]. The GGA+DMFT scheme yields a spin-magnetic moment of exactly  $0.60\mu_B$ . The exchange splitting denoting the energy difference between the peak positions of the majority and minority-spin  $d$  band was not calculated explicitly but it can be taken approximately from the DOS in figure 8.3. The DFT calculations yield approximately 0.8 eV whereas in GGA+DMFT the splitting is reduced by a factor of two which is already much closer to the experimental value between 0.2 and 0.3 eV. Hence, a clear improvement of the description of properties related to the electronic structure is also observed here when taking correlation effects into account within GGA+DMFT.

**Spectral Function and Band Structure** The spectral function for fcc nickel was calculated as described in the previous section using both the DFT lattice Green function and the interacting lattice Green function. As described in detail in section 8.1.2, the band structure within DFT and a generalized band structure within GGA+DMFT can be obtained from the spectral function. Both the DFT band structure and the generalized band structure for the majority bands are depicted in the upper graph in figures 8.6 whereas the graph at the bottom shows the band structures for the minority bands. The band structures for the majority and minority-spin electrons are plotted along distinct high symmetry lines in the first Brillouin zone (1<sup>st</sup> BZ).

The most pronounced feature in the GGA+DMFT band structure is the smearing of the bands due to the finite quasi-particle life-times. The smearing is much stronger for the majority-spin electrons than for the minority spin which is in accordance with the changes observed in the GGA+DMFT DOS. It can also be observed that the  $d$  bands below and above the Fermi energy move closer to the Fermi level causing the reduction of the spin splitting described earlier. This shifts of the  $d$  bands relative to the position of the  $d$  bands obtained from DFT calculations as well as the smearing of bands has been observed for all three materials Fe, Co and Ni. Since the electronic correlation has a stronger influence on the majority states as explained above the shifting and smearing is always much more pronounced for the majority bands than for the minority bands.

The band structure can be compared with measurements of the energy dispersion in the 1<sup>st</sup> BZ obtained from angular-resolved photo-emission spectroscopy (ARPES). In the generalized band structure for the majority-spin bands data measured by Eastman, Himpsel and Knapp (magenta) [EHK78], by Himpsel *et al.* (light blue) [HKE79] and by Eberhardt and Plummer (green) [EP80] were added. The data points close to the Fermi energy all agree well with the calculated band structure

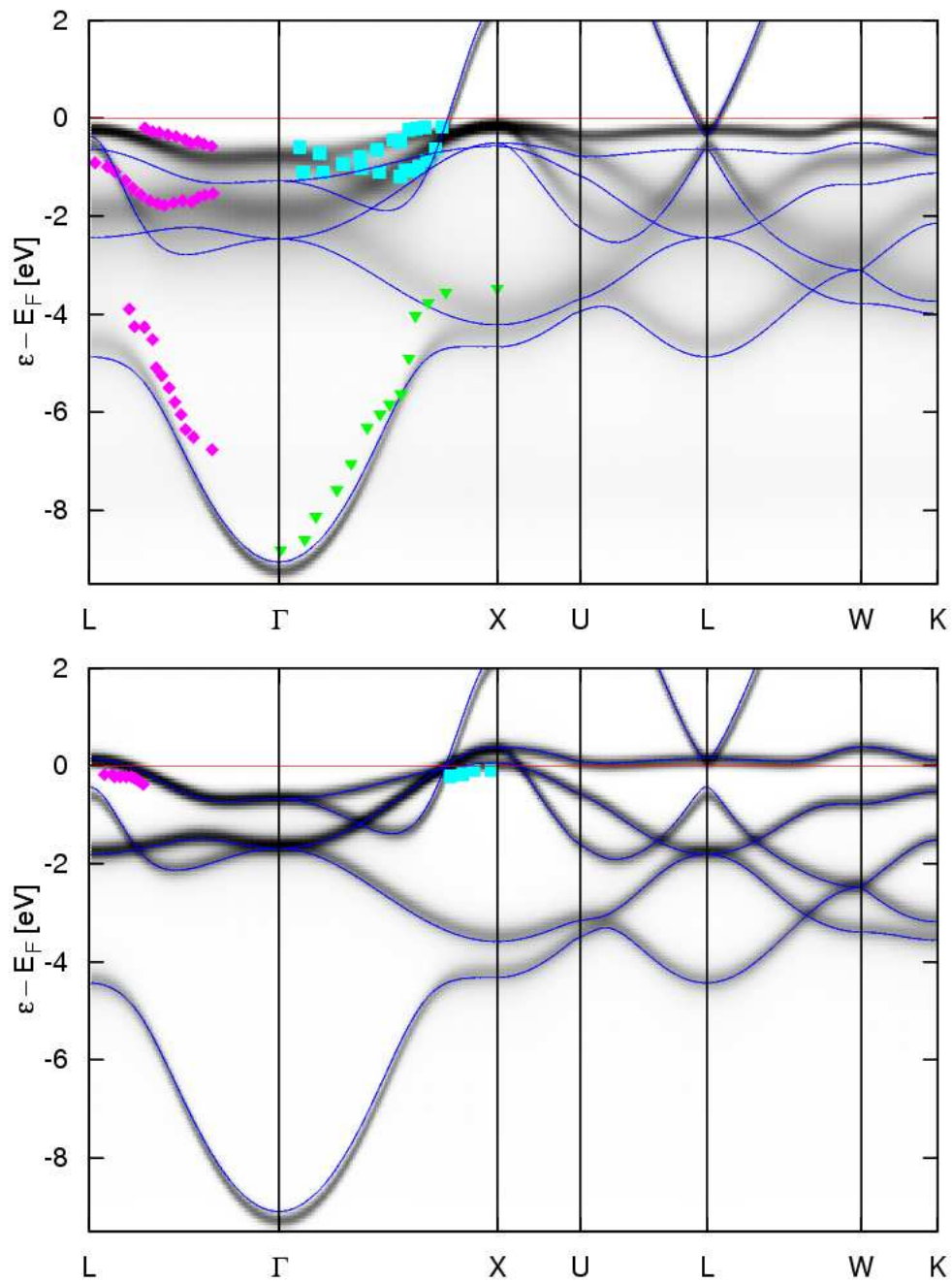


**Figure 8.6:** Generalized band structure obtained from GGA+DMFT and DFT band structure (blue curve) calculated for the majority-spin electrons (top) and minority-spin electrons (bottom) for fcc nickel. The different symbols all denote data obtained from ARPES from [EHK78] (magenta), [HKE79] (light blue) and [EP80] (green)

---

but for the low-lying  $s$  band between the  $\Gamma$  point and the  $X$  point, a constant shift between the measurement and the band calculated within GGA+DMFT is observed. Since this shift is observed in comparison with data from independent measurements it is most likely that the GGA+DMFT calculation does not yield the correct energy dispersion here. To improve on the GGA+DMFT description correlation effects for the electrons in  $s$  bands have to be taken into account but these were not included in the GGA+DMFT scheme here. Thus, for the  $s$  bands only the DFT bands are reproduced within GGA+DMFT that are known to yield an inaccurate description of the energy dispersion. For the minority-spin bands only few data could be found in [EHK78] and [HKE79] measured close to the Fermi level. As for the majority spins, these data are in good agreement with the calculated band structure.

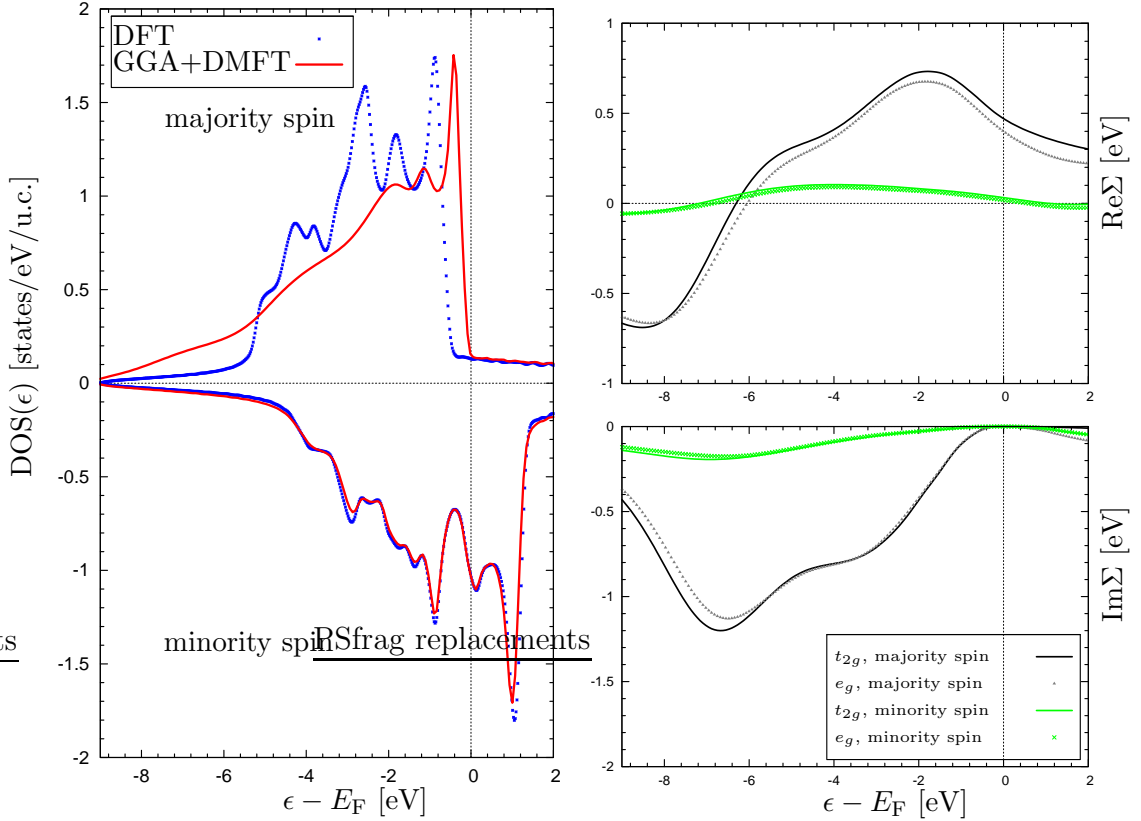


**Figure 8.7:**

*Left:* Majority and minority DOS for fcc cobalt obtained within GGA+DMFT (red) compared with the DFT DOS (blue).

*Right:* Real (top) and imaginary part (bottom) of the self-energy contained in the GGA+DMFT calculations on the left. Contributions to the majority-spin self-energy are black and those to the minority-spin self-energy are green. The crystal field splits the self-energy contributions for both spin directions into  $e_g$  and  $t_{2g}$  contributions.

### 8.3 Results for Cobalt (Co)

**Density of States.** To start the discussion of the results for cobalt the total DOS obtained from DFT calculations and GGA+DMFT calculations as well as the real and imaginary part of the self-energy contained in the GGA+DMFT calculations are shown in figure 8.7. In principle, most of the changes found in the GGA+DMFT description of nickel can also be found in the spectra of cobalt. The majority spin DOS within GGA+DMFT shows some significant effects of band narrowing while the center of gravity of the peak caused by the  $d$ -band states moves closer to the Fermi level. A shift of some spectral weight of the lower part of the DFT spectrum towards even lower energies producing a shoulder at about  $-7$  eV can also be observed and

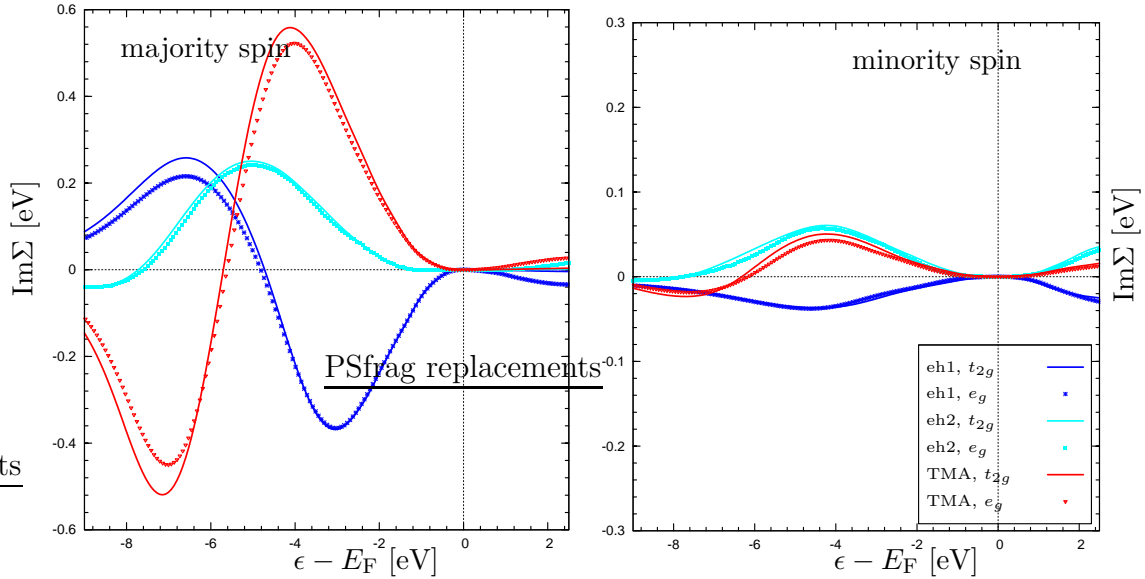


**Figure 8.8:** Imaginary part of the self-energy contributions for fcc Co derived from the different subclasses of diagrams within FLEX. The red curves depict contributions from the particle-particle channel (TMA), the light blue from the eh1 channel and the dark blue from the eh2 channel. The left graph gives the contributions for the majority spins, the right for the minority spins.

is examined in a little more detail below. The DOS obtained within GGA+DMFT for the minority spin states is practically identical with the DFT DOS.

All changes in the DOS can be directly related to the real and imaginary part of the self-energy in the same way it was done for nickel. The imaginary part shows the correct behavior close to the Fermi level whereas for the real part of the self-energy the same odd behaviour at the Fermi energy can be reported as for Ni. The effects of the crystal-field splitting on the self-energy contributions is minor, whereas the difference between the self-energy contributions of the majority and minority-spin states is more severe. However, the contributions are smaller compared to nickel and altogether cobalt has the smallest self-energy contribution for the minority-spin states of all three materials Fe, Co and Ni.

While the narrowing of the bands close to Fermi level is caused by the positive contribution in the real part of the self-energy for energies larger than  $-6$  eV, the negative peak at around  $-8$  eV as well as the negative peak in the imaginary part of the self-energy at about  $-7$  eV indicates the formation of a satellite structure as observed in the DOS of nickel. This could be the origin of the shoulder observed in the DOS of cobalt around  $-7$  eV. I assume, that the physical effect causing this quasi-particle excitation is the same as that producing the satellite peak in the DOS of nickel, namely the repeated scattering of two holes. To verify this assumption,

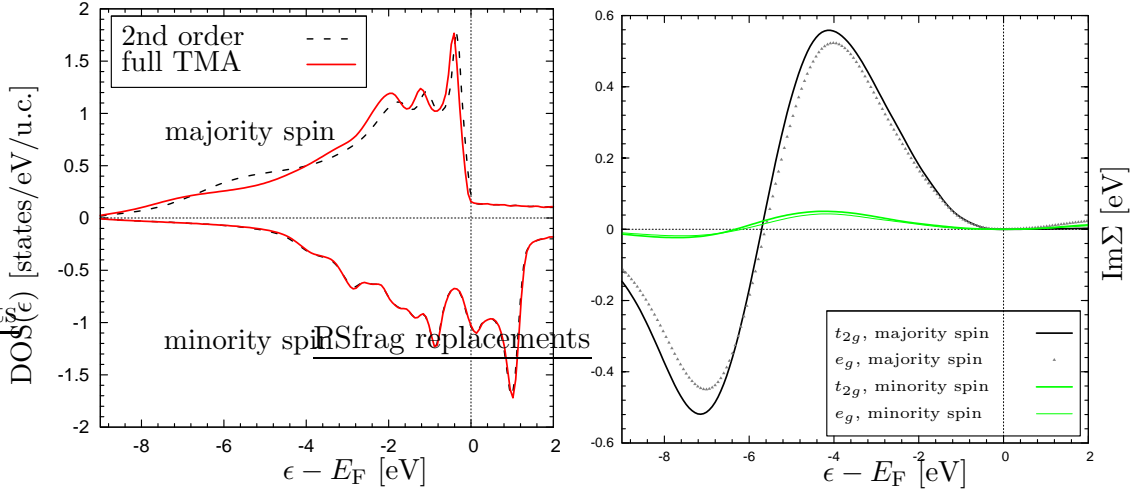


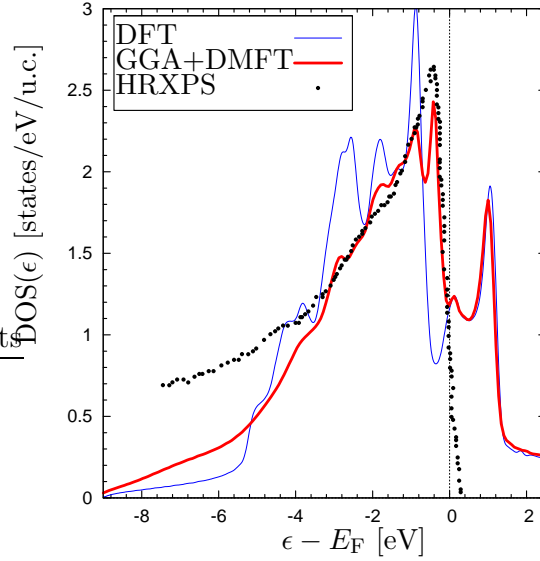
**Figure 8.9:** *Left:* DOS of fcc cobalt obtained within GGA+DMFT calculated using only the second-order self-energy contribution (dashed lines) and the self-energy obtained from the TMA. *Right:* Imaginary part of the self-energy contributions  $\Sigma^{\sigma \text{PP}}^{(3)}$  (last row) including crystal field splitting effects. Contributions to the majority-spin self-energy are black for the minority-spin green.

the imaginary parts of the different self-energy contributions from the TMA, the eh1 channel and the eh2 channel for the majority-spin states are plotted in one graph in figure 8.8 and the contributions for the minority-spin states in a second graph also in figure 8.8. Although the contributions are weaker the peak structure of the contributions for the different channels is very similar to that observed in nickel. The TMA yields the largest contribution whereas the self-energy corrections due to the electron-hole interactions should only cause minor changes. Note that the self-energy contributions calculated for the minority-spin states are an order of magnitude smaller than for the majority spin states.

Due to the structural analogies to nickel, the DOS from the TMA and also from the second-order self-energy contribution are depicted in 8.9 together with the imaginary part of the self-energy obtained within the TMA. In the DOS of the majority-spin states the forming of a satellite can really be observed. The satellite features are even more pronounced than in the total DOS in figure 8.7 containing all self-energy contributions. This is probably caused by the additional self-energy contributions from the eh1 and eh2 channel contained in the total DOS. The peaks of the imaginary part of the self-energy contribution from the eh1 channel at  $-7$  eV and from the eh2 channel at around  $-5$  eV as observed in figure 8.8 cause the satellite features to be washed out due to additionally quasi-particle damping. Nevertheless, a shift of some quasi-particle weight causing a satellite-like peak is clearly visible in 8.9.

Finally, the calculation of the DOS for fcc cobalt shall also be compared to exper-

**Figure 8.10:** Comparison between the spin-integrated DOS for fcc cobalt obtained within DFT (blue) and GGA+DMFT (red) and from measurements deploying high resolution x-ray photo-emission spectroscopy (HRXPS, black dots). HRXPS can only determine the occupied electronic states below  $E_F$ , hence the resonances in the calculated DOS above the Fermi level are not recorded by HRXPS.



imental data. For the same reasons mentioned in the discussion of the results for nickel, only the spin-integrated DOS obtained from DFT and GGA+DMFT calculations are compared to a high-resolution x-ray photo-emission spectrum (HRXPS) taken again from [SK96]. While the DFT results clearly show some deviation from the experimentally obtained spectrum, the GGA+DMFT result is in excellent agreement with the HRXP spectrum with respect to the position of the main peak as well as the shape and width of the peaks. As explained in detail in the last section, the photo-emission spectroscopy can not describe the states in the DOS above the Fermi level and the tail in the spectrum at low energies comes from side-effects during the measurement.

**Spin Magnetic Moments and Exchange Splitting.** For hcp cobalt a spin-magnetic moment of  $1.52\mu_B$  is measured in experiments [SAS92]. In this work cobalt could only be calculated in the fcc phase and a spin-magnetic moment obtained from experiments for this phase could not be found. Hence, the spin-magnetic moments calculated within DFT and GGA+DMFT can not be compared directly to the data. As for nickel, the moment obtained from DFT ( $1.72\mu_B$ ) is larger than the moment calculated within GGA+DMFT ( $1.65\mu_B$ ). The same tendency is observed for the spin splitting which is large within DFT (2.0 eV) and decreases within GGA+DMFT (1.4 eV). For the hcp phase a spin splitting of 0.9 eV was measured (see [SAS92]).

**Spectral Function and Band Structure** From the spectral function calculated with the DFT lattice Green function the DFT band structure was obtained as depicted in figure 8.11 for the majority-spin bands (graph on top) and for the minority-spin bands (graph on the bottom). In the same graphes the generalized band structures obtained from the spectral function using the interacting GGA+DMFT Green function are also presented. As opposed to nickel, it is not possible to compare these results

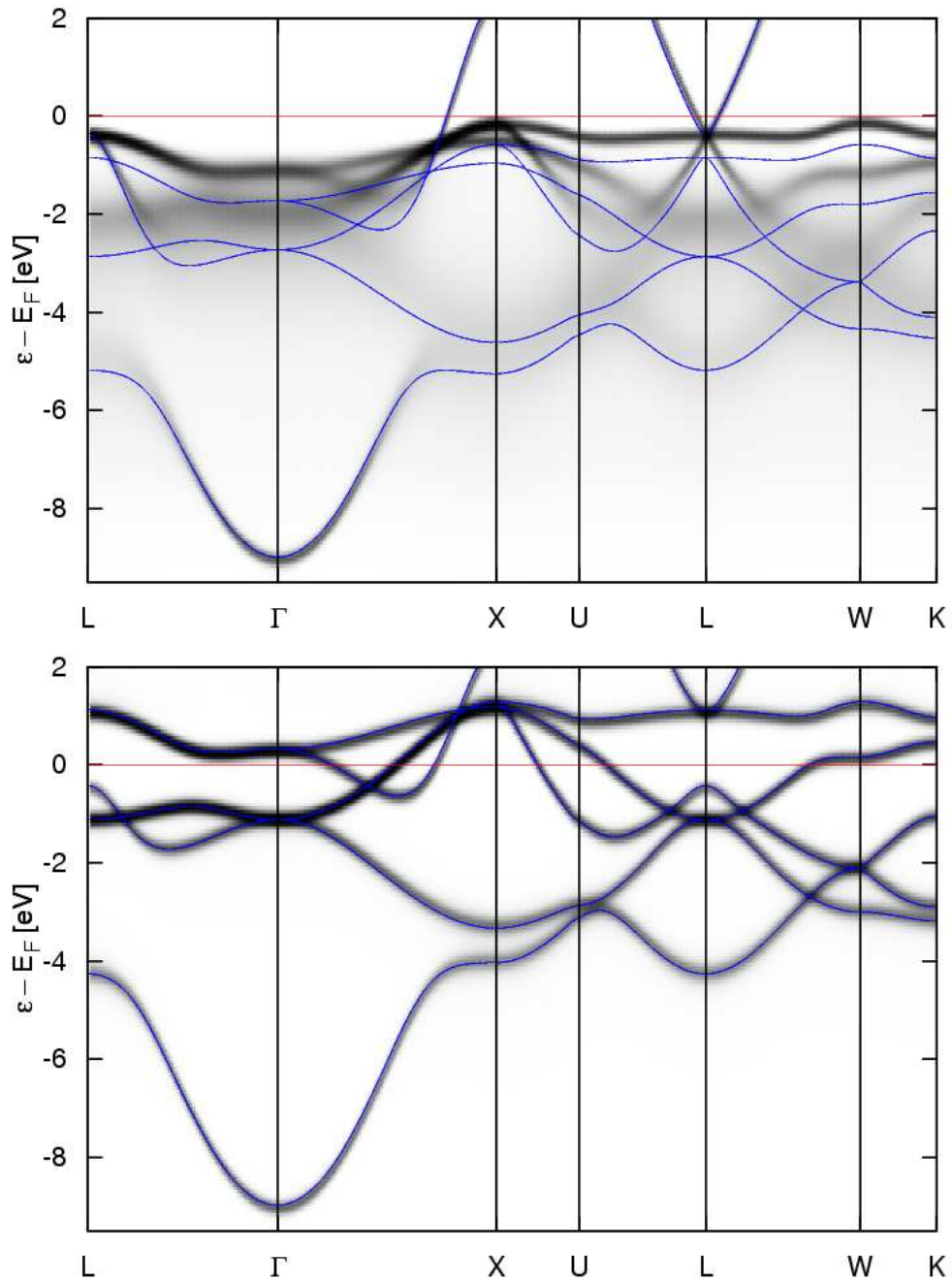


**Figure 8.11:** Generalized band structure obtained from GGA+DMFT and DFT band structure (blue curve) calculated for the majority-spin electrons (top) and minority-spin electrons (bottom) for fcc cobalt.

with experimental data, since the calculations were performed for cobalt with an fcc structure and data are only available for cobalt in a hcp phase. However, it can be verified again, that the  $d$  bands for the majority-spin states move closer to the Fermi level and are washed out due to finite quasi-particle life-times if correlation effects are incorporated within the framework of GGA+DMFT. Once again, these effects are much less pronounced for the minority-spin states.

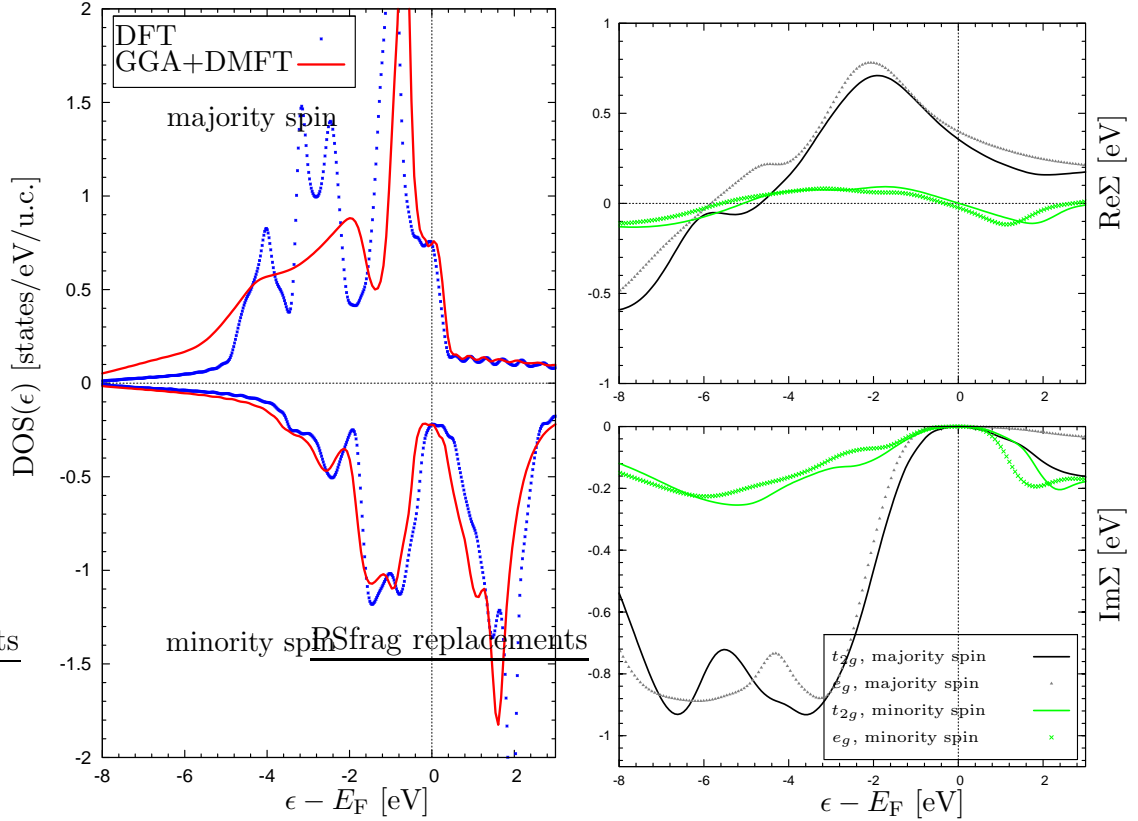


**Figure 8.12:**

*Left:* Majority and minority DOS for bcc iron obtained within GGA+DMFT (red) compared with the DFT DOS (blue).

*Right:* Real (top) and imaginary part (bottom) of the self-energy contained in the GGA+DMFT calculations on the left. Contributions to the majority-spin self-energy are black and those to the minority-spin self-energy are green. The crystal field splits the self-energy contributions for both spin directions into  $e_g$  and  $t_{2g}$  contributions.

## 8.4 Results for Iron (Fe)

To evaluate the results obtained for bcc iron again a comparison between the DFT DOS and the GGA+DMFT DOS together with the real and imaginary parts of the self-energy contained in the GGA+DMFT results in figure 8.12 is presented. The correlation effects in iron as described by the self-energy are roughly as strong as in cobalt, but the self-energy of iron shows a richer structure. The self-energy contributions to the minority-spin states are again much smaller than for the majority spins and the deviation between  $\Sigma_{t_{2g}}^\sigma$  and  $\Sigma_{e_g}^\sigma$  originating from the crystal-field splitting of the  $d$  bands is marginal. It is worth mentioning that the deviation in the majority-

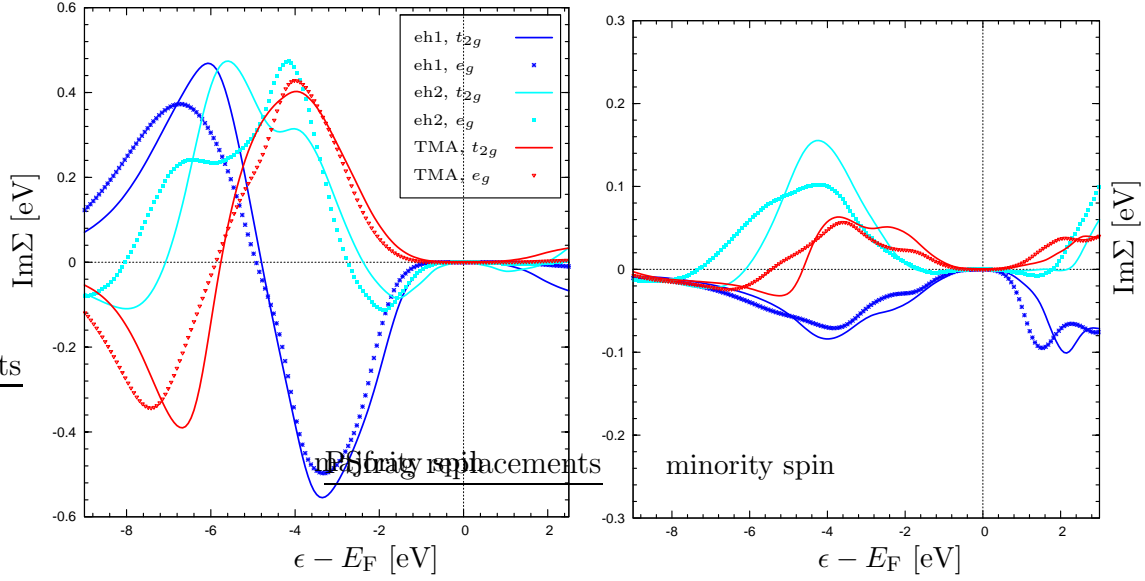


**Figure 8.13:** Imaginary part of the self-energy contributions for bcc Fe derived from the different subclasses of diagrams within FLEX. The red curves depict contributions from the particle-particle channel (TMA), the light blue from the eh1 channel and the dark blue from the eh2 channel. The left graph gives the contributions for the majority spins, the right for the minority spins.

spin contributions between the different contributions  $\Sigma_{t_{2g}}^\sigma$  and  $\Sigma_{e_g}^\sigma$  is strongest in iron. The obvious differences between  $\Sigma_{t_{2g}}^\sigma$  and  $\Sigma_{e_g}^\sigma$  for the majority-spin contributions might be an interesting topic to be investigated in future work. Furthermore, the imaginary part of iron has a second peak around  $-3$  eV that is as pronounced as the peak around  $-7$  eV. In the imaginary parts of nickel and cobalt only the latter peak is present whereas around  $-3$  eV only a small shoulder can be observed (see figure 8.3 for nickel and 8.7 for cobalt).

It was demonstrated for nickel and cobalt that the peak in the imaginary part of the self-energy is caused by particle-particle interactions captured in the TMA. Hence, the second peak observed for iron must arise from the electron-hole interaction. This assumption can be verified by comparing the distinct contributions to the self-energy  $\Sigma^{\sigma \text{ pp} (3)}$  stemming from the particle-particle channel and  $\Sigma^{\sigma \text{ eh1} (3)}$  and  $\Sigma^{\sigma \text{ eh2} (3)}$  from the particle-hole channels 1 and 2. The imaginary parts for all three contribution are depicted for the  $e_g$  and  $t_{2g}$  bands in figure 8.13 for the majority-spin states on the left and for the minorities on the right. The self-energy part from the particle-particle channel shows the same behavior as for nickel and cobalt but the scattering processes between electrons and holes captured in the electron-hole channel 1 yield a much stronger contribution than in Ni and Co and dominate among all self-energy contributions for iron. For iron with fewer valence electrons than nickel and cobalt, the increasing amount of holes in the valence band obviously leads to an increase

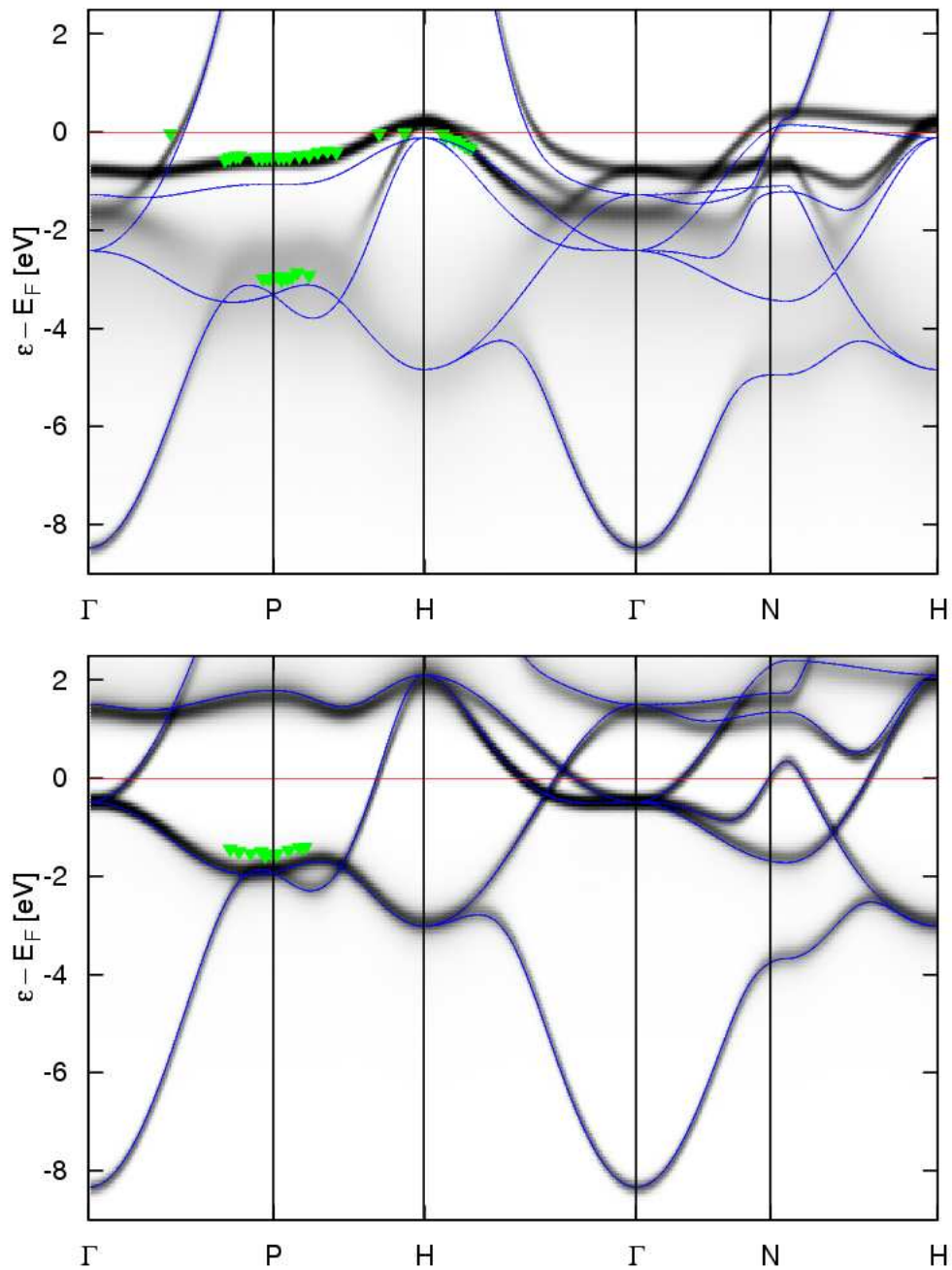
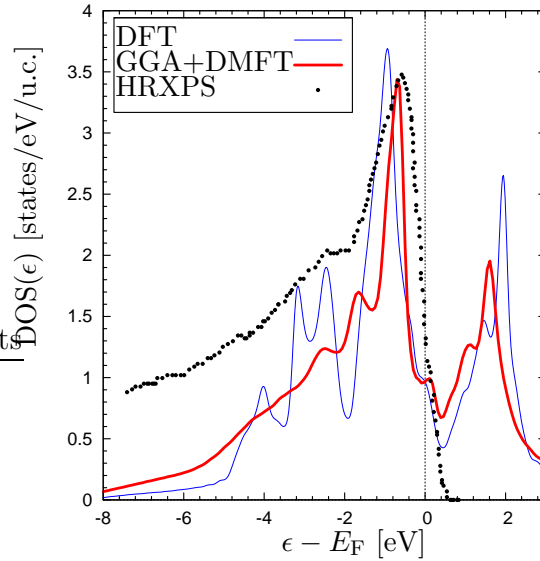


**Figure 8.14:** Generalized band structure obtained from GGA+DMFT and DFT band structure (blue curve) calculated for the majority-spin electrons (top) and minority-spin electrons (bottom) in bcc iron. The green triangles are experimental data form ARPES measurements from [EJW<sup>+</sup>79].

**Figure 8.15:** Comparison between the spin-integrated DOS for bcc iron obtained within DFT (blue) and GGA+DMFT (red) and from measurements deploying high resolution x-ray photo-emission spectroscopy (HRXPS, black dots). HRXPS can only determine the occupied electronic states below  $E_F$ , hence the resonances in the calculated DOS above the Fermi level are not recorded by HRXPS.



of the correlation effects caused by electron-hole interaction. The strong self-energy contribution from the electron-hole channel 1 obviously causes the second peak in the total self-energy contribution to the majority spin bands in 8.12.

In the GGA+DMFT DOS in 8.12 the imaginary part of the self-energy leads to a strong broadening and damping of the peak structure obtained from DFT calculations for the majority spins for energies below  $-2$  eV. Again, this effect is much smaller for the minority-spin states. For both majority and minority-spin states a significant shift of the main peaks close to the Fermi level is observed as well as some shifting of the weight of the lower-lying bands to even lower-lying energies for the majority-spin bands. These shifts are directly related to the real part of the self-energy in the same way as described for nickel and cobalt.

The spin-integrated DOS for iron is compared to experimental data stemming from the same high-resolution x-ray photo-emission experiments as for nickel and cobalt [SK96]. In figure 8.15 the experimental spectrum is plotted together with the results from the DFT and GGA+DMFT calculation. Once again, GGA+DMFT results are in better agreement with the peak positions and the peak structure of the experimental data than the DFT results underlining again the importance of correlation effects for the formation of the electronic structure in Fe.

**Spin Magnetic Moments and Exchange Splitting.** The spin-magnetic moment for iron measured in experiment is given by  $\mu_{\text{spin}} = 2.13\mu_B$ . From DFT calculations with FLEUR a moment of  $2.26\mu_B$  was obtained whereas GGA+DMFT yields  $2.12\mu_B$ . Furthermore, the spin splitting obtained from GGA+DMFT as seen in figure 8.12 of roughly 2.2 eV is much closer to the experimental value of 2.1 eV than the DFT result of 2.7 eV. The experimental results were again taken from [SAS92].

**Spectral Function and Band Structure** Finally, the DFT band structures and the generalized band structures obtained from the spectral function calculated within GGA+DMFT are presented in 8.14. The generalized band structure shows again the smearing of the bands and the shift of the bands as expected when incorporating correlation effects. Data derived from ARPES measurements carried out by Eastman *et al.* [EJW<sup>+</sup>79] are plotted as green triangles marks on top of the generalized band structures. These data agree well with the generalized band structure obtained from GGA+DMFT.

# 9 Auger Spectra of Fe, Co and Ni

In the atomic Auger decay [Aug25] first a deep electron vacancy (hole) created e.g. by a photo-emission process recombines with an outer electron. When the outer electron moves closer to the core it transfers part of its energy to a second electron — the so-called Auger electron — which is ejected into the energy continuum, leaving two holes in the outer shells of the atom. In Auger electron spectroscopy (AES) or Auger photo-electron coincidence spectroscopy (APECS) information about the final two-hole state as well as the formation of this state are obtained by measuring the energy dispersion of the Auger electron.

Compared to the atomic ones, solid-state Auger transitions introduce qualitatively new features, since the core states are approximately the same as in isolated atoms while the valence states are significantly different. For example, Auger transitions in the late  $3d$  transition metals involving two valence holes in the final state, so-called core-valence-valence (CVV) transitions, are known to exhibit a considerable sensitivity to electronic correlations in the valence band. A theory of CVV spectra within GGA+DMFT is introduced in this chapter. A two-particle density of states for Fe, Co and Ni mimicking the spectrum of the Auger electron is derived upon this theoretical framework. It is demonstrated how interactions between two holes in the  $d$  valence bands can be incorporated into the spectra within the framework of GGA+DMFT through the particle-particle ladder approximation from the FLEX method. Calculating the two-particle density of states with and without taking correlation effects into account as well as contrasting these results with experimental data reveals the influence of the electronic correlation on CVV Auger transitions and provides further insight into the CVV Auger processes of Fe, Co and Ni.

## 9.1 The Physics of the Auger Process

I would like to first examine the physical nature of the Auger process in solids in some more detail. This will be helpful to understand the modeling of the Auger process within GGA+DMFT described in the next section.

In figure 9.1 the two steps of a CVV Auger transition in a solid are depicted. In the first step (A), an x-ray photon with energy

$$E^\gamma = \hbar\omega \tag{9.1}$$

removes an electron from a core level of a lattice atom of energy  $\epsilon^{\text{core}}$ . The photo-

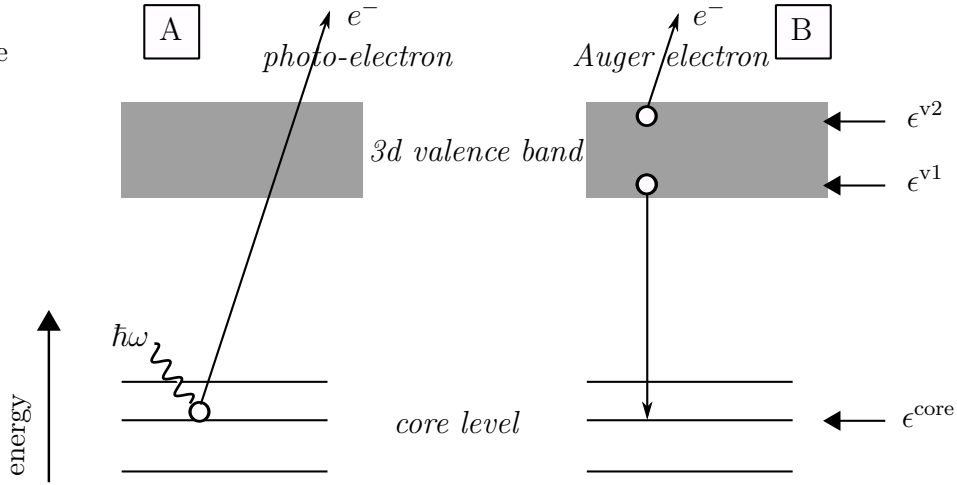


**Figure 9.1:** Schematic description of the two steps (A) and (B) of a CVV Auger transition, here for a 3d transition metal.

electron thus has a kinetic energy of

$$E_{\text{kin}}^{\text{ph}} = E^{\gamma} + \epsilon^{\text{core}} . \quad (9.2)$$

After some time the excited atom relaxes due to the recombination of the hole in the core level with an electron from the valence band. In figure 9.1 this electron had an energy  $\epsilon^{v1}$  (step B) before the recombination. Thus an energy  $\Delta E$  given by

$$\Delta E = \epsilon^{v1} - \epsilon^{\text{core}} \quad (9.3)$$

is released during the process which is given to a second electron in a state with energy  $\epsilon^{v2}$ . The second electron is ejected from the solid with a kinetic energy of

$$E_{\text{kin}}^{\text{Auger}} = \Delta E + \epsilon^{v2} = (\epsilon^{v1} + \epsilon^{v2}) - \epsilon^{\text{core}} . \quad (9.4)$$

There are no strict selection rules for this process as opposed to the case of photo emission (see e.g. the review article about AES by Chang [Cha71]). Therefore, any other electron with a binding energy smaller than the energy  $\Delta E$  could be ejected. Furthermore measurements exhibit a strong dependence of the CVV transition on the total number  $Z$  of electrons at one atomic site. To explain this dependence in detail would be beyond the scope of this introduction but to give at least some idea about the influence of  $Z$ , I like to mention that the atomic Auger process is most likely to occur in atoms with  $Z < 30$  whereas for  $Z > 60$  the relaxation after step A in figure 9.1 occurs in virtue of emission of an X-ray photon with a probability rate of over 90%.

The kinetic energy of the Auger electron is detected in AES but it is quite difficult to derive reliable information from the observed spectra. This is due to the fact

that figure 9.1 does not “tell the whole story” because it only describes the actual Auger process. However, there are a number of other processes taking place in the same energy range such that the observed spectra are often a superposition of the Auger process and some additional effects. Some additional processes contributing to the observed spectra are e.g. the creation of electron-hole pairs by the escaping photo electron when passing through the electron gas of the solid, emission of other core holes from neighboring ions or the appearance of core-core-valence (CCV) Auger transitions, so-called Coster-Kronig transitions. But even in a “normal” Auger process secondary electrons with different energies may be detected since the remaining ion may either relax to the ground state by ejecting the electron or might still be in an excited state after the ejection. These effects can cause damping, broadening or even additional features in the observed spectra and they are often hard to be distinguished from the contribution of the actual Auger process without additional information. (See the article by Thurgate for a detailed listing of a number of processes and their influence on the Auger spectrum [Thu96].)

In Auger photo-electron coincidence spectroscopy (APECS) the Auger electron as well as a photo-electron are detected. It was already mentioned above that there do not exist any strict selection rules for the CVV transition such that the energies  $\epsilon^{v1}$  and  $\epsilon^{v2}$  may differ if the same process is observed twice. However, the conservation of energy ensures that the sum of the energies of the photo electron and the Auger electron must be constant in the case where the two-hole final state and no other processes are observed. The above formula (9.2) through (9.4) yield

$$E_{\text{kin}}^{\text{Auger}} + E_{\text{kin}}^{\text{ph}} = E^{\gamma} + (\epsilon^{v1} + \epsilon^{v2}) \stackrel{!}{=} \text{const} . \quad (9.5)$$

Hence, it is possible to detect “the” photo electron responsible for the ejection of the observed Auger electron. Thus, APECS is able to single out many of the additional processes contributing to the observed Auger spectra. For example the photo-electron analyzer is fixed on one part of the XPS spectrum and the Auger spectrum is scanned to find which parts of the Auger spectrum have their origin in that part of the XPS spectrum. Thus, APECS can in principle provide reliable data of spectra from CVV Auger transition describing the final two-hole state in the valence band. After this small excursion into the field of Auger electron spectroscopy a theoretical description of Auger spectra is derived in the next section.

## 9.2 A Model for Auger Spectra

In this section I will derive a model description of the Auger spectra detected in AES or APECS. The derivation is based on an early model for Auger spectra by Sawatzky [Saw77]. The same assumptions made by Sawatzky hold for the derivation of the model presented here. However, by solving the model within the framework of GGA+DMFT an improved description of Auger spectra is obtained by solving the

derived equations self-consistently. In the earlier theories by Sawatzky [Saw77] or Cini [Cin79] the self-consistency is missing.

First of all the following approximation typically used in the literature (see e.g. [DC94]) to model Auger spectra are also used here

- The two-step approximation assumes that the formation of the core hole and the Auger process are independent.
- The competition with other decay processes is neglected.
- All surface-related effects are neglected.

In [Saw77] it was discussed that the Auger transition rate is determined by matrix element of the type

$$\langle C\sigma_1, \mathbf{k}\sigma_2 | U_{ee} | \mathbf{R}_1 L_1 \sigma'_1, \mathbf{R}_2 L_2 \sigma'_2 \rangle, \quad (9.6)$$

where the states  $|C\sigma_1\rangle$  and  $|\mathbf{k}\sigma_2\rangle$  denote the non-dispersive initial state of the core electron and the state of the escaping free photo-electron, whereas the two final states of the two holes in the valence band are represented in terms of the TB-FLAPW basis introduced in chapter 3. Thus,  $L_i$  specify an orbital at the site  $\mathbf{R}_i$  and the holes carry the spins  $\sigma'_i$  with  $i \in \{1, 2\}$ . The  $U_{ee}$  denotes the Coulomb interaction between the two initial and the two final states. The Auger transition rate is simplified by applying the following additional approximations:

- The contributions of matrix elements with  $\mathbf{R}_1 \neq \mathbf{R}_2$  are neglected. This is well justified for the matrix elements involving the  $d$ -states of the  $3d$  metals since the contribution of the intra-atomic Auger process between valence states with  $\mathbf{R}_1 = \mathbf{R}_2$  is four to five orders of magnitude larger than the inter-atomic contributions due to the localized character of these bands. Furthermore, the contribution of  $s$ - and  $p$ -band electrons for  $\mathbf{R}_1 = \mathbf{R}_2$  is also neglected because of their delocalized character.
- The interaction between the outgoing electron and the ionized material left behind is neglected as far as the shape of the Auger spectra is concerned. This is the so-called sudden approximation.

If it is furthermore assumed that the transition matrix elements are energy-independent, they are constant for each contribution of a specific final two-hole state to the observed Auger spectra. If this approximation for the transition rates is deployed and the final two-hole state is thought to be independent from the first step of the core-electron excitation, the Auger spectrum is simply given by the density of states of this final two-hole state in analogy to the spectra from photo-emission processes that are described by the single-particle density of states as discussed in the previous chapter. The two-hole state can be described within GGA+DMFT in terms of the

two-particle propagator for two holes  $K^{\text{pp}}$ , which in turn can be written in terms of diagrams as

$$\boxed{K^{\text{pp}}} = \begin{array}{c} \longrightarrow \\ \longrightarrow \end{array} + \begin{array}{c} \longrightarrow \\ \longrightarrow \end{array} \boxed{\Gamma^{\text{pp}}} \begin{array}{c} \longrightarrow \\ \longrightarrow \end{array}, \quad (9.7)$$

where  $\Gamma^{\text{pp}}$  is the vertex function encoding all interactions between the two holes in the final state. It is worth mentioning that this general description also incorporates interactions between two electrons in the final state which is shown to yield a non-negligible effect in the calculated spectra later on. Within the FLEX method  $\Gamma^{\text{pp}}$  is approximated by the particle-particle T-matrix and an analytic expression for  $K^{\text{pp}}$  within the T-matrix approximation (TMA) can be derived as

$$K^{\text{pp}}(\epsilon) = \Psi(\epsilon) + \Psi(\epsilon)T^{\text{pp}}(\epsilon)\Psi(\epsilon), \quad (9.8)$$

with the particle-particle T-matrix given by

$$T^{\text{pp}}(\epsilon) = v[1 - v\Psi(\epsilon)]^{-1} \quad (\text{see 5.41})$$

and the bare two-particle propagator given by

$$\Psi(\epsilon) = i \int_{-\infty}^{\infty} \frac{d\epsilon'}{2\pi} G(\epsilon - \epsilon')G(\epsilon'). \quad (\text{see 5.27})$$

For the description of the underlying electronic structure, the multi-band Hubbard model (5.4) is used. Hence, the interacting lattice Green function is used to determine the bare two-particle propagator  $\Psi$  and to calculate the dressed two-particle propagator  $K^{\text{pp}}$ . The interaction  $v$  is the combined interaction defined in equation (5.10). Note that all two-particle quantities are matrices of four orbital indices  $L_1, \dots, L_4$  and two spin indices  $\sigma, \sigma'$  and all matrix elements are in general  $\mathbf{k}$  dependent. The single-particle lattice Green function is a matrix of two orbital indices and one spin index.

To solve equation 9.8, the lattice Green function  $G$  has to be determined. Within GGA+DMFT the  $\mathbf{k}$ -dependence of  $G$  is neglected and  $G$  is determined self-consistently in a single-site approximation (SSA). Consequently, the dressed two-particle propagator  $K^{\text{pp}}$  in equation (9.8) is also obtained within the SSA using the T-matrix approximation from the FLEX method to approximately determine the vertex function. This is the so-called local self-consistent T-matrix approximation (local SC TMA) for the two-particle propagator  $K^{\text{pp}}$ . Finally, in analogy to the single-particle density of states introduced in chapter 8 a spin-integrated two-particle density of states  $D^{\text{pp}}$  can be derived from the imaginary part of the site-diagonal elements of the two-particle propagator  $K_{\mathbf{R}LL'}^{\sigma\sigma' \text{pp}}$

$$D^{\text{pp}}(\epsilon) = -\frac{1}{\pi} \sum_{LL'\sigma\sigma'} \text{Im} K_{\mathbf{R}LL'}^{\sigma\sigma' \text{pp}}(\epsilon). \quad (9.9)$$

The theory of Auger spectra presented above was developed by Drchal and Kudrnovský in 1984 [DK84] to describe the Auger processes in materials like the  $3d$  transition metals with partially filled bands. These authors used a simpler scheme to calculate the lattice Green function self-consistently. It is the first time to the knowledge of the author that the self-consistency is achieved within the framework of DMFT. The theory presented in [DK84] can be viewed as a natural generalization of models developed earlier by Cini in 1976 [Cin76] and Sawatzky in 1977 [Saw77] for Auger processes in materials with completely filled valence bands. In 1979 it was then shown by Cini [Cin79] that a non-self-consistent version of the T-matrix approximation for the two-particle propagator (NSC TMA) yields an adequate description of materials with high band filling. However, it was demonstrated by Drchal and Kudrnovský in [DK84] that the self-consistency is important for the correct prediction of the Auger spectra of materials with partially filled bands. In this work the results from the NSC TMA approach can be recovered by simply replacing all interacting lattice Green functions  $G$  by the non-interacting DFT lattice Green function  $G^0$  in the equations above. This gives the opportunity to study the importance of the self-consistency in the context of the GGA+DMFT description. In the NSC TMA the two-particle Green function  $K_{\text{NSC}}^{\text{PP}}$  is calculated as

$$K_{\text{NSC}}^{\text{PP}}(\epsilon) = \Psi^0(\epsilon) + \Psi^0(\epsilon)T_{\text{NSC}}^{\text{PP}}(\epsilon)\Psi^0(\epsilon), \quad (9.10)$$

with the particle-particle T-matrix calculated with the bare two-particle propagator

$$T_{\text{NSC}}^{\text{PP}}(\epsilon) = v [1 - \Psi^0(\epsilon) v]^{-1} \quad (9.11)$$

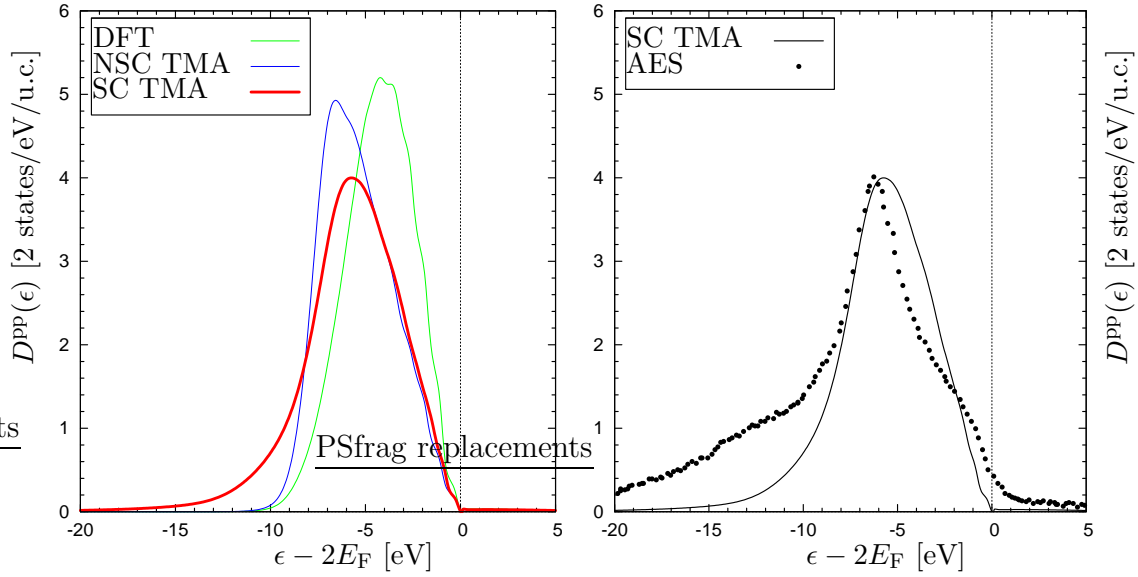
and  $\Psi^0$  is given by

$$\Psi^0(\epsilon) = i \int_{-\infty}^{\infty} \frac{d\epsilon'}{2\pi} G^0(\epsilon - \epsilon') G^0(\epsilon'). \quad (9.12)$$

Finally, the results from GGA+DMFT can also be contrasted with a description of the Auger spectra within DFT. In DFT there is no pair interaction between particles. This can be realized by approximating the two-particle Green function  $K_{\text{bare}}^{\text{PP}}$  by the bare two-particle propagator  $\Psi^0$ . This corresponds to an approximation of  $K^{\text{PP}}$  in (9.10) by the term of zeroth order on the right-hand side. The two-particle propagator is calculated using the DFT lattice Green function as in (9.12). It is clear right from the start that omitting the interaction between the two holes yields an incomplete picture of the underlying physics and cannot describe the Auger spectra sufficiently. However, it allows to extract explicitly the influence of correlation on the Auger spectra by comparing the spectra obtained from the different forms  $K_{\text{bare}}^{\text{PP}}$ ,  $K_{\text{NSC}}^{\text{PP}}$  and  $K^{\text{PP}}$ .

### 9.3 Calculations and Results

In all the calculations in this chapter the same values for the input parameters  $K_{\text{max}}$ ,  $l_{\text{max}}$  and the number of  $\mathbf{k}$  points in the DFT part as well as  $U$  and  $J$  in the DMFT

**Figure 9.2:**

*Left:* Comparison for fcc nickel between the theoretically obtained Auger spectra from DFT (green), NSC TMA (blue) and SC TMA (red).

*Right:* Comparison of the Auger spectra calculated in the SC TMA (straight line) with a spectrum obtained from an AES experiment (dots) from [MNJ84].

part were used as in the calculations presented in the previous two chapters. The formulas to calculate the Auger spectra can be implemented straightforwardly. Note that in all equations the lattice Green functions have to be used as opposed to the formulas in the GGA+DMFT self-consistency scheme where the equations derived from the diagrammatic expressions are evaluated using the bath Green function.

The first results to be discussed are calculations done for nickel. In the previous chapter, it has been demonstrated that interaction processes between two holes are the dominant contribution to the self-energy correction within FLEX (which comprises the particle-particle scattering captured by the T-matrix approximation, the electron-hole scattering and the screening of the Coulomb interaction due to particle-hole pairs). Furthermore, the particle-particle interaction was shown to be strongest in nickel among the three metals Fe, Co and Ni. Last but not least, the single-particle DOS of nickel exhibits a quasi-particle satellite that was directly related to a two-hole interaction process of the same kind as the interaction of the two holes in the final state of the ion after a CVV Auger transition. Therefore, the difference in the Auger spectra calculated in the NSC TMA or the SC TMA compared to the DFT Auger spectra can be best observed in the Auger spectra of nickel.

In figure 9.2 on the left the resulting spectra from the three theoretical approaches

are depicted. On the right the spectra obtained from the SC TMA is shown together with a spectrum from an AES measurement by Mårtensson *et al.* [MNJ84]. The comparison of the theoretical spectra reveals that inclusion of the interaction between the two holes in the final state in the CS TMA causes the weight of the peak observed in the DFT spectrum to shift to lower energies. The Coulomb repulsion between the two holes contributes an additional positive term to the energy of the two-hole final state. Hence, the inclusion of the interaction increases the energy of the final state and in turn decreases the energy of the Auger electrons observed in the spectrum. Deploying the self-consistent TMA leads to an additional damping and broadening of the peak structure relative to the NSC TMA spectrum whereas the position of the main peak does not significantly change in the SC TMA with respect to the peak position in the NSC TMA spectrum. In the SC TMA the two holes are described as dressed particles as opposed to the bare-particle description in the NSC TMA. This renormalization accounts for the interaction of each individual hole with the rest of the medium. However, the change in the energy of one hole due to this renormalization is obviously much smaller than the potential-energy shift due to the direct Coulomb interaction between the two holes while the position of the peak is mainly determined by this latter interaction. This is different from the effects observed in the single-particle densities in the previous chapters where replacing the non-interacting DFT Green function with the interacting Green function caused damping and broadening but also shifts in the observed spectra. In the Auger spectrum only a minor shift of some quasi-particle weight to the left side of the peak can be observed. However, effects of the finite life-times of excited one-particle states causing the damping and broadening of the peaks can also be observed in the two-particle spectrum from the SC TMA spectra much like it was already observed in the single-particle spectra in the previous chapter. Nevertheless, the biggest change in the description of the spectrum is due to the interaction of the two holes which is described well in the SC TMA but is already contained in the NSC TMA spectrum.

If the SC TMA spectrum is compared to the Auger spectrum measured in an experiment by Mårtensson *et al.* [MNJ84] (right side of figure 9.2) it can be seen that the position of the main peak of the Auger spectrum corresponds to the position predicted by the SC TMA. (The height of the measured curve given in arbitrary units was adjusted to the height of the SC TMA spectrum.) Mårtensson *et al.* were able to prove that the main peak is mostly determined by the CVV transition calculated in the SC TMA. This implies that the inclusion of correlation effects in the newly derived theory is vital for an accurate description of Auger spectra.

Unfortunately, it is not possible to analyze the importance of the self-consistency in the description of the two-hole process by further comparing certain features of the two spectra, since the experimental data have to be taken with care. The experimentalists pointed out explicitly in the presentation of their work that the observed spectrum is a superposition of the actual Auger process and three other processes. There is an additional process involving the creation of another pair of holes that contributes some additional weight to the main peak. The shoulder on the left of the

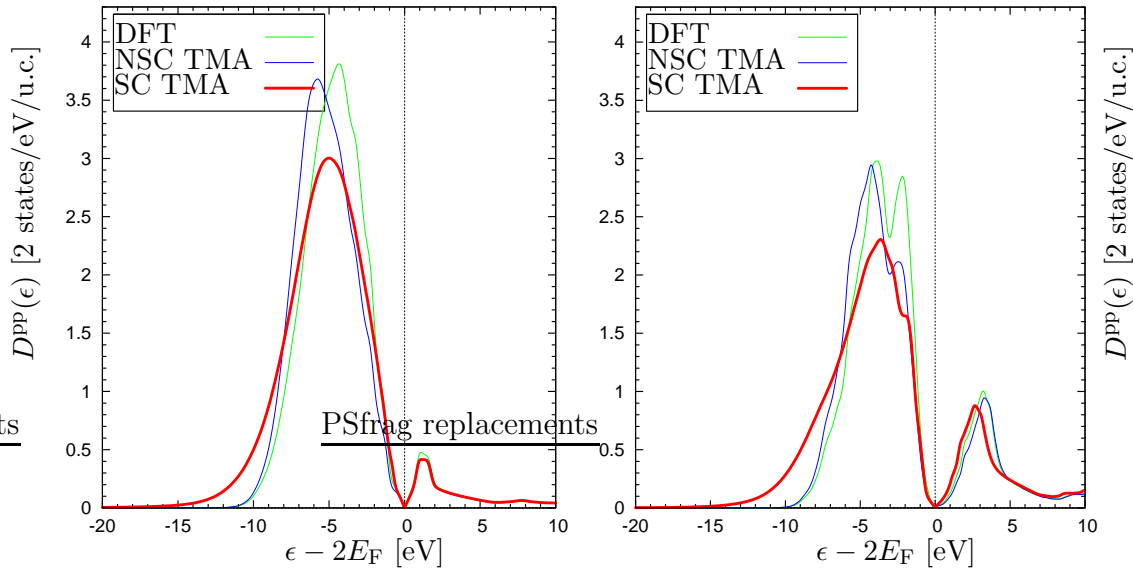


**Figure 9.3:** Comparison between the theoretically obtained Auger spectra from DFT (green), NSC TMA (blue) and SC TMA (red) for fcc cobalt (*left*) and for bcc iron (*right*).

main peak is also caused by a process involving the creation of more than two holes. Both processes are not described within the SC TMA. The shoulder to the right of the main peak is caused by the part of the CVV Auger transition where the two holes in the final state are bandlike. These holes have itinerant character e.g. they can be created at the same site but one hole immediately moves to another site. Due to the single-site approximation in the DMFT part of the GGA+DMFT scheme these bandlike holes are not contained in the SC TMA description of the Auger spectrum, hence, the shoulder is absent in the SC TMA spectrum. The broadening of the features in the AES spectrum is probably caused by finite-temperature effects since a contribution to the spectrum was also observed above two times the Fermi level. All these additional processes make it however impossible to determine, if the additional shift on the left side of the peak in the SC TMA spectrum yields the correct description of the main peak stemming from the CVV transition.

It has been discussed at some length above that it would be ideal to compare the theoretically obtained spectra to results from APECS measurements since the superposition of competing processes in the AES spectra (as observed e.g. in the spectrum of nickel) can be avoided to some extent by the coincidence spectroscopy. Unfortunately, the data available from APECS measurements are yet too few and the resolution is too poor to draw further conclusions in comparison with the calculated spectra. For cobalt and iron even less data were available. Therefore, only the comparison between the theoretically obtained Auger spectra is presented for these materials in figure 9.3. The same trends as observed for nickel can be found but are less pronounced. This is exactly what was to be expected since the hole-hole

interaction is strongest in nickel. In contrast to nickel, the spectra of cobalt and iron also show the formation of appearance-potential spectra manifested by the peak forming at energies higher than two times the Fermi energy. This peak originates from an effect often referred to as inverse CVV Auger transition where two additional correlated electrons in the valence band can be seen. While nickel has the highest number of occupied  $d$  states iron has the lowest of all three materials thus leaving more empty states to be occupied by excited electrons. Therefore, iron has the largest contribution of appearance potential states to the two-particle DOS. In appearance-potential spectroscopy (APS) this part of the two-particle DOS can be studied experimentally.

To conclude this chapter, the importance of correlation effects for the correct description of the Auger spectra of Fe, Co and Ni was demonstrated. With the new theoretical description the Auger process involving dressed particles can be described. Thus the new model is consistent with the ladder approximation for the two-particle Green function. Although the modeling, being an extension of earlier theories eliminates some inconsistencies in these theoretical descriptions, the importance of the self-consistency for the description of experimental data has yet to be demonstrated.

# 10 Chromium – A Case Study of Antiferromagnetism within GGA+DMFT

The  $3d$  transition metal chromium has been studied extensively ever since Shull and Wilkinson first demonstrated in 1953 that chromium is an antiferromagnet (AFM) [SW53]. Although the electronic structure of Cr is well known today on a qualitative level the standard *ab initio* approaches like DFT do not describe all its properties correctly in a quantitative manner. In particular within LSDA the averaged spin-magnetic moment per atom is predicted correctly while the equilibrium lattice constant is much smaller than the experimental lattice constant. As opposed to that within GGA the equilibrium lattice constant is very close to the lattice constant found from experiments, but the averaged spin-magnetic moment per atom is too large.

In this chapter an extension of the GGA+DMFT scheme is introduced to study bulk chromium in a commensurate antiferromagnetic configuration. This yields the opportunity to analyze local correlation effects for electrons in the  $d$  bands of Cr and their influence on the antiferromagnetism and it might remove some deficiencies from the DFT description of this material.

## 10.1 A Model for Chromium as Commensurate AFM

Chromium is a  $3d$  transition metal with a bcc crystal structure and about half-band filling. Below a Néel temperature of  $T_N = 311\text{K}$  Cr exhibits itinerant antiferromagnetic behavior: the spin-magnetic moments of the atoms in the (001) planes couple ferromagnetically and the coupling from layer to layers along the (001) direction is antiferromagnetic. This so-called layered antiferromagnetism (LAF) is depicted in figure 10.1 for one bcc unit cell. For the sake of completeness it should be mentioned that the surface of Cr is found to be magnetic both in experiment and theory (see e.g. the article by Bihlmayer, Asada and Blügel [BAB00]). In this work, however, only the bulk electronic structure of Cr will be studied. The ground state of Cr is a spin-density wave (SDW) state where the LAF structure is modulated by a wave vector  $\mathbf{q} = (2\pi/a_0)(0, 0, q)$  with  $q = 0.952 \approx \frac{19}{20}$ . The experimentally determined lattice constant  $a_0 = 2.88 \text{ \AA}$  is taken from [SA92]. Based on measurements of the periodicity

of the SDW Shirane and Takei estimated that the maximum of the spin-density wave amplitude is as large as  $0.59\mu_B$  corresponding to an average spin-magnetic moment of  $0.46\mu_B$  per atom [ST62]. This value of the spin-magnetic moment is much smaller than might be expected from the fact that the  $3d$  bands are half-filled indicating the proximity of the magnetic properties of Cr to a magnetic instability as pointed out by Singh and Ashkenazi [SA92].

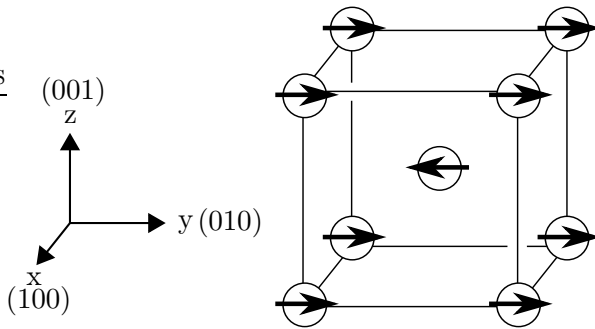


**Figure 10.1:** Bcc unit cell of chromium. The arrows denote the spin-magnetic moment per atom

of the bcc unit cell are of equal magnitude but point in opposite directions as depicted in figure 10.1. It was demonstrated by Koehler *et al.* [KMTM66] that this structure can be actually stabilized by alloying with less than 1% Mn. Thus, the commensurate phase is very close to the true ground-state of pure Cr and it is therefore instructive to perform calculations for this much simpler structure.

George *et al.* [GKKR96] reported for incommensurate magnetic orderings like the spin-density wave modulated ground-state of Cr that no simple set of mean-field equations can be written within DMFT. Consequently, the GGA+DMFT scheme as derived in this work can not be applied to describe the exact electronic structure of the ground state of Cr. However, calculations can be carried out assuming a commensurate antiferromagnetic structure in which the spins at the corner and the center of the

## 10.2 Calculating Commensurate AFM within GGA+DMFT

**Generating Input Data within DFT.** The adapted GGA+DMFT scheme to calculate electronic structures exhibiting commensurate antiferromagnetic ordering needs input from a converged DFT calculation and again the FLEUR code was used to generate this input. Chromium with commensurate antiferromagnetic structure can be modeled by a unit cell of simple cubic structure with two atoms, one at the corner and one at the center of the cell, with opposite spin-magnetic moments. The experimental lattice constant was used in all calculations. Furthermore the parameters  $K_{\max}$  and  $l_{\max}$  were set to 3.4 and 8 in all calculations.

The choice of the number of  $\mathbf{k}$  points has to be done carefully, since the magnetic properties of chromium are sensitive to the Brillouin-zone sampling which reflects

the proximity to the magnetic instability close to the experimental lattice constant as mentioned above. Therefore a large number of 969  $\mathbf{k}$  points in the irreducible part of the 1<sup>st</sup> BZ was used in the iterations to solve the Kohn-Sham equations. With this sampling the Cr moment is within  $0.002\mu_B$  of the converged value calculated for the experimental lattice constant. The densities of states and the eigenvalues to construct the DFT lattice Green function were determined with an even larger number of 1140  $\mathbf{k}$  points.

Finally a parametrization of the exchange-correlation potential has to be chosen. As pointed out in the introduction of this chapter, one may chose for Cr between a GGA yielding accurate lattice constants but too high values for the spin-magnetic moment, or a LDA parametrization which usually gives a value for the spin-magnetic moment close to experiment but underestimates the lattice constant substantially. Furthermore, it was shown by Singh and Ashkenazi [SA92] that the LDA actually predicts the ground state of chromium to be paramagnetic if the equilibrium lattice constant determined within LDA is used instead of the experimental lattice constant. As in previous calculations for Fe, Co and Ni I therefore use the PBE parametrization within the GGA.

**Construction of the Lattice Green Functions.** The two most important steps in the derivation of the new LDA+DMFT scheme are the construction of the lattice Green function within DFT for a crystal symmetry with two atoms per unit cell and the incorporation of this lattice Green function into the GGA+DMFT self-consistency cycle. The construction of the Green function can be done straightforwardly as described in chapter 4 and I only recall the most important steps here.

The general form of the TB-FLAPW basis functions is used

$$\chi_L^{\mu\sigma}(\mathbf{r}^\mu) = u_l^\sigma(r^\mu) Y_L(\hat{\mathbf{r}}^\mu), \quad (\text{see 3.29})$$

where  $L = (l, m)$  is the combined orbital index,  $\mu$  denotes the muffin tin inside the unit cell thus corresponding to a label of the different atoms per unit cell and  $\mathbf{r}^\mu$  gives the position inside the muffin tin  $\mu$ . If the Kohn-Sham eigenfunctions are expanded in terms of the general form of the TB-FLAPW basis functions and the lattice Green function is constructed using this expansion of the Kohn-Sham eigenstates the Green function is obtained as a matrix with elements

$$G_{LL'}^{0\mu\mu'\sigma}(\mathbf{k}; \epsilon) = \frac{1}{N} \sum_{\nu} \frac{(A_{L,\nu}^{\mu\sigma}(\mathbf{k})) (A_{L',\nu}^{\mu'\sigma}(\mathbf{k}))^*}{\epsilon - \epsilon_{\mathbf{k},\nu}^\sigma \pm i\eta}. \quad (\text{see 4.34})$$

The number  $N$  gives the number of atoms in the crystal and  $\epsilon_{\mathbf{k},\nu}^\sigma$  are the Kohn-Sham eigenvalues. The deviation between this Green function and the Green function for a crystal structure with one atom per unit cell stems from the restriction of  $\mathbf{k}$  to the first Brillouin zone which differs in both cases.

For chromium with two different atoms  $\mu \in \{A, B\}$  in the unit cell, the DFT lattice Green function in  $\mathbf{k}$  space can be written in the following matrix form

$$G^{0\sigma}(\mathbf{k}; \epsilon) = \begin{pmatrix} G^{0AA\sigma}(\mathbf{k}; \epsilon) & G^{0AB\sigma}(\mathbf{k}; \epsilon) \\ G^{0BA\sigma}(\mathbf{k}; \epsilon) & G^{0BB\sigma}(\mathbf{k}; \epsilon) \end{pmatrix}. \quad (10.1)$$

From the Green function in  $\mathbf{k}$  space a Green function in real space is obtained using the lattice Fourier transformation introduced in chapter 4. The Fourier transformation can be applied to each matrix element separately. Thus, we can make use of the fact that within DMFT only the local elements of the Green functions are needed, i.e. only the sub-matrices  $G^{0AA\sigma}(\mathbf{k}; \epsilon)$  and  $G^{0BB\sigma}(\mathbf{k}; \epsilon)$  need to be transformed into real space. The lattice transformation for these matrix elements however is of the simple form

$$G^{0\mu\mu\sigma}(\epsilon) = \sum_{\mathbf{k}} G^{0\mu\mu\sigma}(\mathbf{k}; \epsilon). \quad (10.2)$$

**The new GGA+DMFT Iteration Cycle.** As discussed by George *et al.* [GKKR96] within DMFT the same mean-field equations as derived for crystal structures with a single atom per unit cell can be derived for each atom  $A$  and  $B$  from the two sublattices of Cr. This is due to the single-site approximation in DMFT. If the mean-field equations presented in chapter 6 now hold for each atom separately the sub-matrices  $G^{0AA\sigma}(\epsilon)$  and  $G^{0BB\sigma}(\epsilon)$  can be used directly as input in the first iteration step for the FLEX solver to calculate a self-energy contribution  $\Sigma^{AA\sigma}(\epsilon)$  and  $\Sigma^{BB\sigma}(\epsilon)$  for each atomic site. The resulting matrix

$$\Sigma^{\sigma}(\epsilon) = \begin{pmatrix} \Sigma^{AA\sigma}(\epsilon) & 0 \\ 0 & \Sigma^{BB\sigma}(\epsilon) \end{pmatrix}. \quad (10.3)$$

is used together with the DFT lattice Green function in  $\mathbf{k}$  space from equation (10.1) to solve a Dyson equation yielding the interacting lattice Green function  $G$  in  $\mathbf{k}$  space as a matrix of the same form as the DFT lattice Green function in (10.1). The sub-matrices  $G^{AA\sigma}(\epsilon)$  and  $G^{BB\sigma}(\epsilon)$  of the interacting lattice Green function can now be obtained by applying the lattice Fourier transformation to the newly derived Green function  $G$ . The bath Green function for each atom is obtained from these sub-matrices using the same formulas as in the case of a single atom per unit cell since the mean-field equations hold. The bath Green functions are then used to calculate new self-energy matrix elements  $\Sigma^{AA\sigma}(\epsilon)$  and  $\Sigma^{BB\sigma}(\epsilon)$  and this scheme is iterated until convergence is reached.

Due to the specific structure of chromium, i.e. all local properties of an atom  $A$  in the unit cell in real space are the same as the other atom  $B$  with reversed spin, the self-energy contribution has to be calculated only once e.g. for atom  $A$ . To obtain the self-energy for atom  $B$  the relation

$$\Sigma^{BB\sigma}(\epsilon) = \Sigma^{AA-\sigma}(\epsilon) \quad (10.4)$$

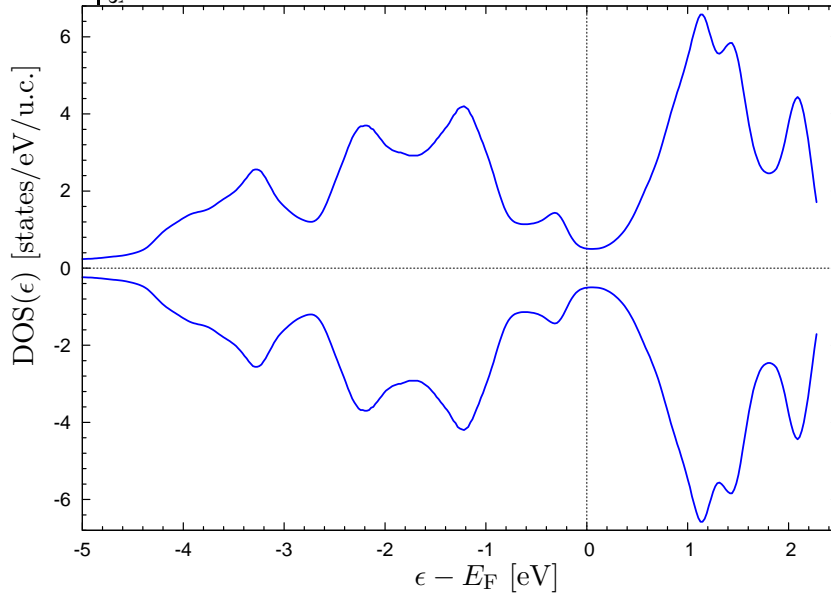


**Figure 10.2:** GGA density of states per unit cell of bulk chromium with a simple cubic unit cell for each spin orientation.

can be used. The same relation also holds for the local parts of the Green function in real space

$$G^{BB\sigma}(\epsilon) = G^{AA-\sigma}(\epsilon). \quad (10.5)$$

Applying these relations reduces the numerical effort drastically. Finally some input values have to be chosen for the calculations within many-body perturbation theory. A Hubbard  $U$  of 1.36 eV was used and a Hubbard  $J$  of 0.82 eV. I will now present the results from calculations for Cr as obtained from the newly derived GGA+DMFT scheme.

## 10.3 Results for Chromium

Like for Fe, Co and Ni, I first discuss the density of states of Cr calculated in a commensurate configuration. The density of states is derived from the site-diagonal elements of the interacting lattice Green function in real space just like for the other materials. In figure 10.2 the DFT DOS per unit cell is depicted. The simple cubic cell was chosen such that it contains two atoms with exactly antiparallel aligned spin-magnetic moments per atom. Consequently, when considering the density of states in the whole unit cell an equal amount of states is occupied with spin up electrons and spin down electrons thus the total density in the unit cell is indistinguishable from that of a paramagnet as can be seen in figure 10.2.

The true magnetic character of the Cr atoms is revealed if the DOS per atom in real space is examined. Figure 10.3 shows the density of states at one atomic site. The

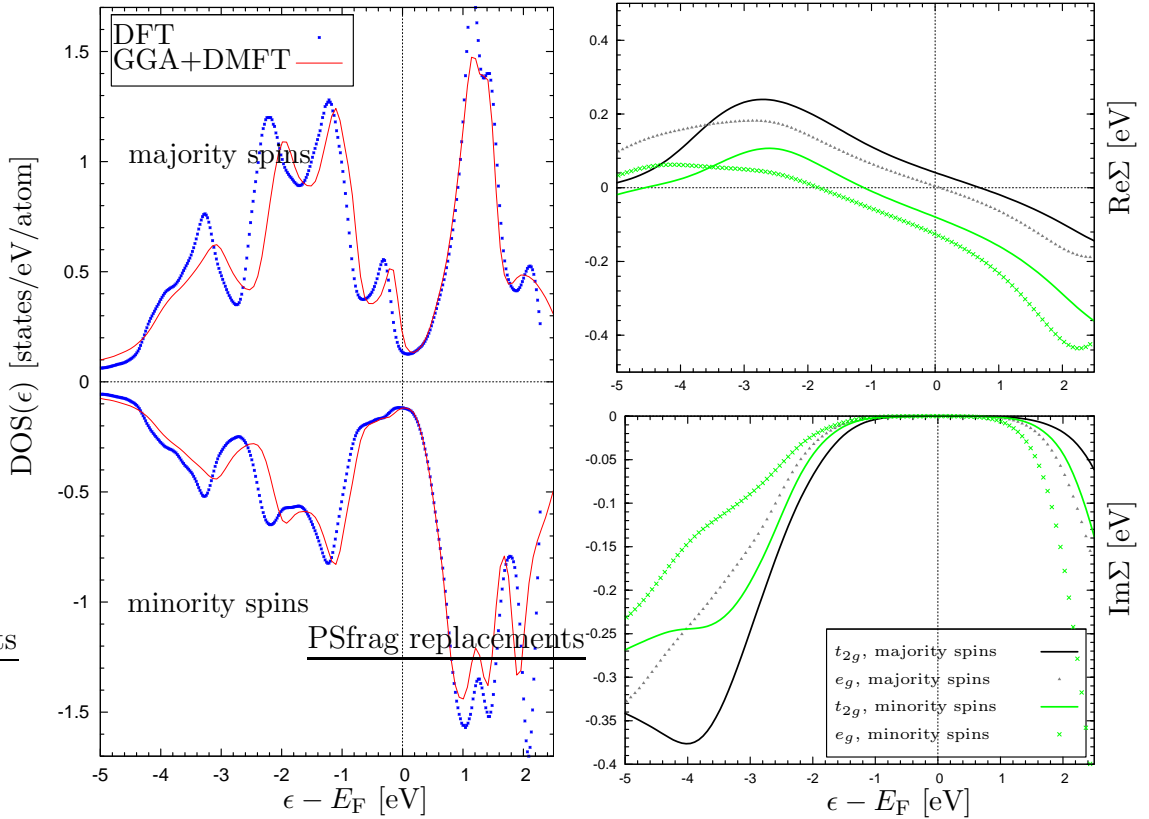


**Figure 10.3:**

*Left:* Majority and minority DOS per atom for simple cubic chromium obtained within GGA+DMFT (red) compared with the DFT DOS (blue).

*Right:* Real (top) and imaginary part (bottom) of the self-energy contained in the GGA+DMFT calculations. Contributions to the majority-spin self-energy are black and those to the minority-spin are green. The crystal field splits the self-energy contributions for both spin directions into  $e_g$  and  $t_{2g}$  contributions.

peak structure for an atom from a layer coupled antiferromagnetically to the layer of the observed atom would exhibit the same DOS but with the peak structures of the minority spin corresponding to the DOS of the majority spins in the other layer and vice versa. In figure 10.3 the DOS per atom as obtained within DFT is compared to the DOS obtained from the new GGA+DMFT scheme. The same changes as for Fe, Co and Ni can be observed, in particular broadening and damping of the DFT peak structure and band narrowing occur and the bands move closer to the Fermi level. On the right side of figure 10.3, the real and imaginary parts of the self-energy contributions from the description of Cr within GGA+DMFT are plotted. In contrast to the self-energy corrections for Fe, Co and Ni, the influence of the crystal field, resulting in a splitting of the self-energy contributions calculated for one spin

direction into two contributions  $\Sigma_{t_{2g}}^\sigma$  and  $\Sigma_{e_g}^\sigma$ , is stronger and of the same magnitude as the difference in the self-energies calculated for the two distinct orientation of the electron spin. Altogether, the self-energy corrections are rather small, in particular close to the Fermi level the imaginary part almost drops to zero. The changes in the GGA+DMFT DOS may be related to the self-energy contributions as was done before for Ni, Co and Fe.

I would like to examine now whether the GGA+DMFT approach yields a spin-magnetic moment for Cr closer to the experimental value than the DFT spin-magnetic moment. It was explained in subsection 8.1.3 that the spin-magnetic moment is the difference of the integrated spin-electron densities. The spin-magnetic moments determined within the DFT part, within GGA+DMFT and from experiment are listed below.

Method	spin-magnetic moment [ $\mu_B$ ]
DFT	1.177
GGA+DMFT	1.091
experiment	0.49

It can be seen that the GGA+DMFT scheme yields a small correction of the spin-magnetic moment into the right direction when comparing the DFT spin-magnetic

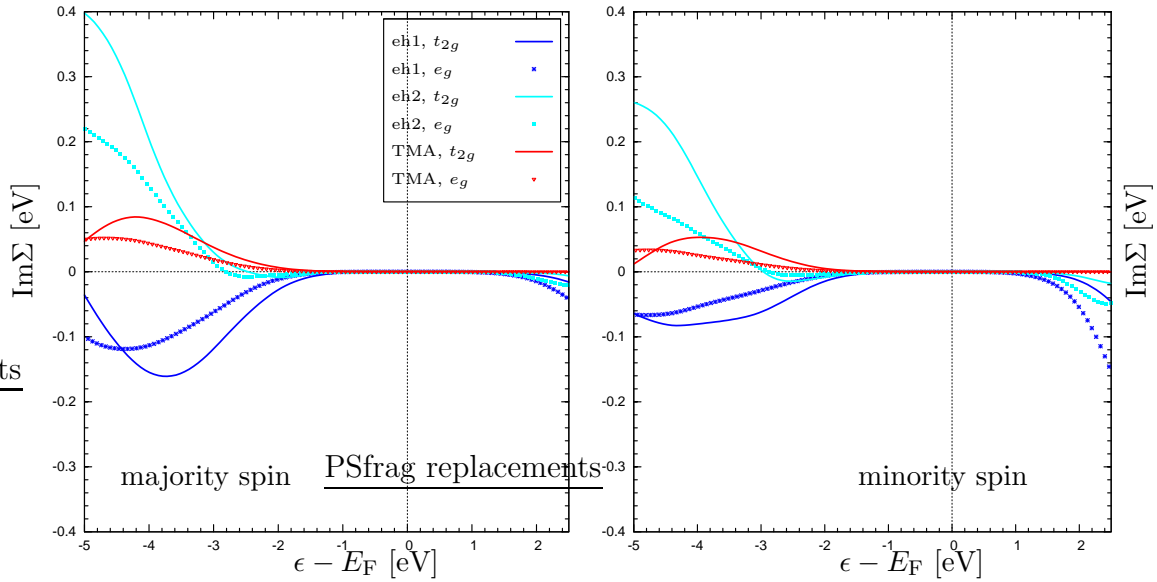


**Figure 10.4:** Imaginary part of the self-energy contributions for simple cubic Cr derived from the different subclasses of diagrams within FLEX. The red curve depicts contributions from the particle-particle channel (TMA), the light blue from the eh1 channel and the dark blue from the eh2 channel. The left graph gives the contributions for the majority spins, the right one for the minority spins.

moment to the moment obtained from experiment. Nevertheless, the agreement with the experimental value is still very poor. I assume that the disagreement stems from the perturbative nature of the GGA+DMFT approach. Within the GGA+DMFT scheme many-body effects are considered to yield a perturbative correction to the GGA description. Hence, if the starting point of the perturbative correction is far away from the expected values as is the case for the spin-magnetic moment within GGA the many-body correction will not lead to a substantially different description. However, it can not be clearly determined from the results obtained so far if the choice of the starting point for the application of the many-body perturbation theory causes the results to differ from experimental findings or whether there are other effects

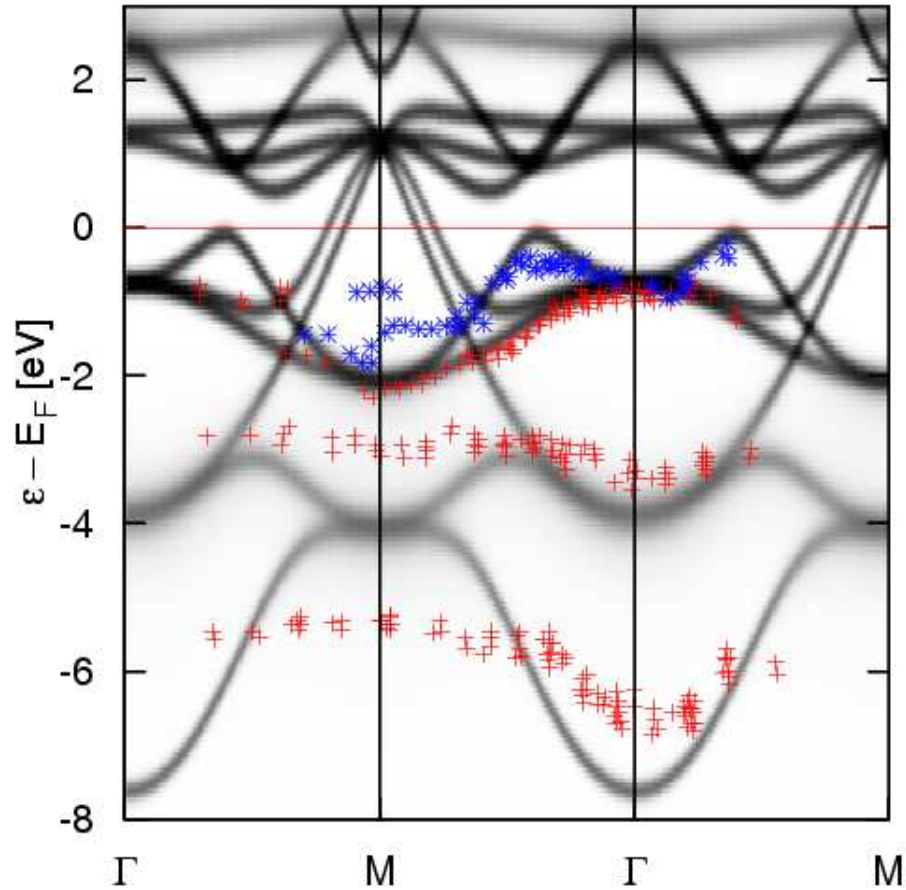


**Figure 10.5:** A part of the band structure of AFM Cr calculated within GGA+DMFT is compared to the data of ARPES measurements along the (110) direction in the bulk BZ (the repeated-zone scheme) from Sakisaka [SKO<sup>+</sup>88]. The red crosses and blue stars were measured by the same group but the blue stars correspond to weaker signals. The smearing of the calculated bands originates from finite life-time effects.

e.g. the neglect of the spin-density wave character of the ground state that give rise to the discrepancy between the theoretical and experimental values. Further tests would have to be carried out to clarify this.

To conclude the discussion of the DOS the imaginary parts of the different self-energy contributions from the TMA, the two electron-hole channels eh1 and eh2 for the majority-spin states are plotted in the left graph in figure 10.4 and the contributions for the minority-spin states are plotted in the right graph in figure 10.4. The contributions from the TMA are even smaller than in iron whereas the contribution of the eh2 channel is increased and obviously yields the main contribution to the self-energy correction. On the whole the self-energy parts do not exhibit a very rich structure. The very small values in all channels close to the Fermi level might be worth mentioning since the absence of almost any self-energy corrections in a window of 2 eV around the Fermi energy has not been observed for any of the other materials.

In the remaining part of the chapter, the band structure of Cr is to be examined. The band structure was derived from the spectral function which can be obtained in turn from the  $\mathbf{k}$ -dependent lattice Green function as described in chapter 8. I first present two plots comparing the calculated band dispersion along distinct symmetry lines of the 1<sup>st</sup> Brillouin zone with experimental data. At the end of the chapter in figure 10.7 the complete band structure obtained from DFT calculations as well as GGA+DMFT calculations is presented.

In figure 10.5 the band structure calculated along the (110) direction in the 1<sup>st</sup> bulk Brillouin zone (repeated-zone scheme) is compared to data obtained from ARPES measurements by Sakisaka *et al.* [SKO<sup>+</sup>88]. For the low-lying  $s$  bands a systematic deviation between the almost dispersionless measured data and the calculated band structure can be observed. This is similar to the observation made for nickel where

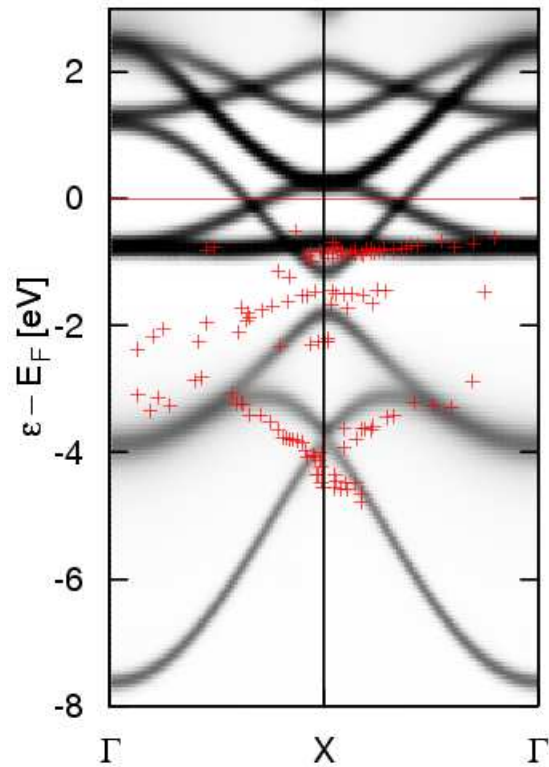


**Figure 10.6:** The experimentally observed band dispersion (red crosses) from [KRLS85] along the (010) symmetry line in AFM commensurate Cr in the bulk BZ (the repeated-zone scheme) is compared to the band structure calculated within GGA+DMFT.

the low-lying bands were not described accurately due to the fact that no self-energy corrections for these bands is calculated within the present GGA+DMFT scheme. Thus, the  $s$  bands are determined from the DFT bands which are known to yield a good qualitative but not a quantitative description of the band dispersion. It is however quite peculiar that the measured data do almost show no dispersion and they should be taken with care. The data for the higher occupied bands agree quite nicely with the calculated spectra, however, Sakisaka *et al.* observed some resonances around the first M point around  $-1$  eV that do not correspond to any part of the calculated band structure. Unfortunately, it can not be determined with the present data, if this stems from errors in the measurement or whether it might be an error in the theoretical description of the band structure. Since the data seem to scatter quite randomly and no additional band or bands can be determined that might be missing in the calculated band structure I assume it to be more likely that the experimental data are inaccurate.

In the second figure 10.6 measurements along the (010) direction are compared to the theoretically determined band structure. The data were obtained in ARPES experiments by Klebanoff *et al.* [KRLS85]. The low-lying bands are again only reproduced qualitatively by the GGA+DMFT results which can be attributed to the reasons mentioned above. Again, some features were observed experimentally

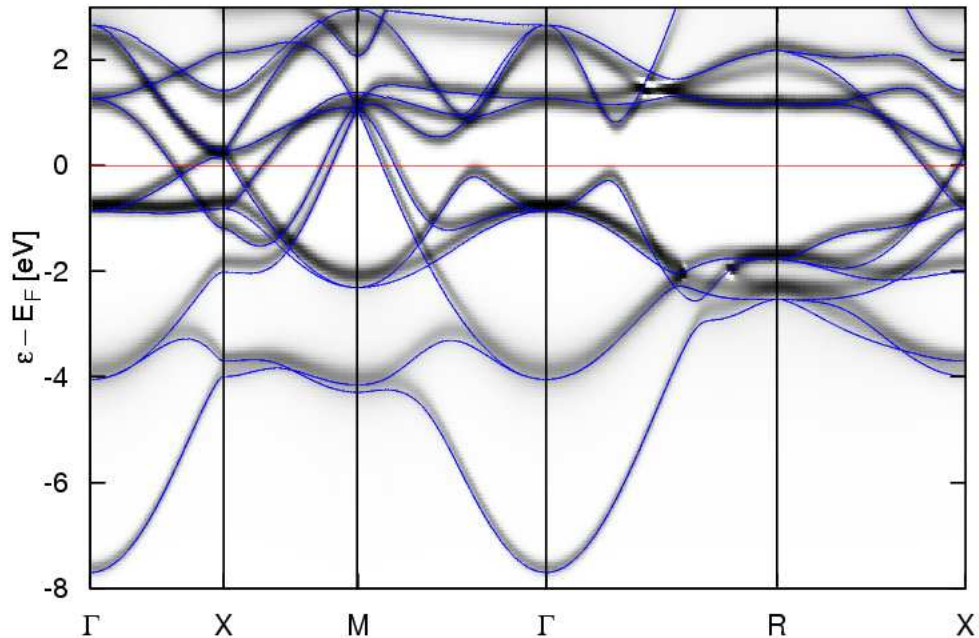


**Figure 10.7:** Generalized band structure obtained from GGA+DMFT and DFT band structure (blue curve) calculated for the AFM commensurate ground state of bulk Cr in a simple cubic unit cell.

that can not be related to any part of the calculated band structure, whereas other parts of the spectra agree well with the GGA+DMFT bands. One reason for the discrepancies might of course be the assumed commensurate AFM as opposed to the actual incommensurate structure. However, the differences in the two structures are supposed to be rather small. Hence, for a deeper understanding of these differences further studies are necessary.

I close the chapter by presenting the complete band structure obtained from DFT calculations in figure 10.7 and compare it to the generalized band structure from GGA+DMFT calculations. In the GGA+DMFT band structure the  $d$  bands move closer to the Fermi level and the bands are washed out due to the finite life-time effects as is also the case for Fe, Co and Ni. These effects are however less pronounced than for example in nickel, since the self-energy corrections in Cr are much smaller.

The band structure exhibits a large variety of almost two- and four-fold degenerated levels. It was discussed by Skriver [Skr81] that this might be a manifestation of the close relationship to a band structure that can be obtained if a bcc band structure is folded back into the first Brillouin zone of the simple cubic lattice. Furthermore, two gaps can be seen between the  $d$  bands left and right to the  $\Gamma$  point positioned in the center of each band structure here. The gaps are held responsible for the stabilization of the antiferromagnetic phase.

Summarizing it has been demonstrated that the description of Cr in a commensurate form within GGA+DMFT yields some changes in the DOS and the band structure due to the incorporation of electronic correlation among the  $d$  electrons. This has however a minor effect on the spin-magnetic moment per atom which might be related to some conceptual problems of the GGA+DMFT scheme in the present form. To verify these assumptions further investigations would be necessary.



# 11 Conclusion and Outlook

**Conclusion.** At the end of this thesis I would like to go back to the very beginning and recall the main goal: I started out with the task to introduce a scheme to incorporate electronic correlation into the standard *ab initio* DFT description of magnetic  $3d$  metals. In particular it was intended to improve on the characterization of the material properties sensitive to correlation effects. In order to achieve that the GGA+DMFT approach was introduced. In the first part of my work I demonstrated how an existing DMFT implementation employing the fluctuation-exchange (FLEX) method as a solver for the DMFT impurity problem can be merged with the linearized augmented-plane-wave DFT code FLEUR. Special attention was devoted to the description of the FLEX method and a thorough and consistent derivation of the FLEX diagrams describing the self-energy of the  $d$  electron systems of the  $3d$  transition metals was presented. In the second part I applied the new GGA+DMFT scheme to obtain the one-particle densities of states and two-particle densities of states (Auger spectra) of the prototype ferromagnetic materials iron, cobalt and nickel both in real space and in  $\mathbf{k}$  space. All spectra exhibit features seen in experiments that are related to electronic correlations. The same applies to the spin-magnetic moments and the exchange splitting of the  $d$  bands of Fe, Co and Ni obtained from GGA+DMFT calculations. These quantities are in very good agreement with experimental data. On the other hand, a case study of commensurate antiferromagnetic chromium yields only minor changes in the calculated properties due to the incorporation of electronic correlation. The many-body corrections in principle lead to a small improvement of the DFT description of Cr when compared to experimental findings. However, this case study also revealed some limitations of the GGA+DMFT scheme in its present form.

Altogether it was shown in this thesis that the GGA+DMFT approach is an intriguing concept that can be employed successfully in the description of magnetic materials with intermediately correlated electron systems. The GGA+DMFT scheme presented here should however be taken only as a first step towards a complete GGA+DMFT characterization of realistic materials because of some limitations of the present scheme for example the neglect of charges in the interstitial region due to the choice of the TB-FLAPW functions for a basis or the suggested form of the double-counting correction. Some suggestions to improve the present GGA+DMFT implementation as well as some ideas to develop more sophisticated schemes are presented on the following pages. I hope that this thesis will be the starting point for a thorough exploitation of both the fluctuation exchange method and the GGA+DMFT approach for the characterization of the exciting physics of

correlated many-electron systems from first principles.

**Outlook.** I would like to first discuss some limitations of the present GGA+DMFT scheme and how they might be removed. For the applications presented in this thesis satisfactory solutions for these problems have been found, but for applications to a broader range of materials with more complicated configurations more elaborate strategies have to be developed.

First of all, the choice of the basis set is a very elementary but also important part in the construction of the GGA+DMFT scheme. Although the TB-FLAPW basis used in this thesis yields good results for the muffin-tin densities of states for Fe, Co and Ni, the total neglect of the interstitial space imposes a too crude approximation for materials with a larger interstitial region. Furthermore, it is unsatisfactory to employ a basis set leading *a priori* to a neglect of some fraction of the valence charge. A better choice for an atom-centered basis are Wannier functions. They are suitable for calculations within DMFT since they characterize the electrons as situated in orbitals localized at distinct lattice sites. On the other hand a basis transformation from a full LAPW basis obtained from DFT calculations to the Wannier representation can be employed such that all charges are captured by the Wannier functions.

Upon the derivation of the Hubbard-type lattice model in chapter 5 the difficulties in determining the Hubbard  $U$  and  $J$  for calculations of realistic materials have been addressed. In the calculations for chromium some further problems were encountered that are thought to be connected to some inconsistencies in the choice of the so-called double-counting correction. In the context of *ab initio* calculations of realistic materials the Hubbard  $U$  and  $J$  as well as a double-counting correction term can be obtained quite naturally from calculations within the constrained LDA method by McMahan *et al.* [MMS88] and Gunnarsson *et al.* [GAJZ89]. In constrained LDA calculations the  $d$  electrons are confined to the  $d$  orbitals by setting all hopping matrix elements involving  $d$  electrons to zero. Hence, the number of electrons in the  $d$  orbitals is fixed. If the total number of  $d$  electrons  $N_d$  has been determined e.g. from DFT calculations, the total energy  $E$  of the electron system for three different configurations is calculated: for a configuration with  $N_d$  electrons yielding  $E(N_d)$ , a configuration with an additional electron in the  $d$  states giving  $E(N_{d+1})$  and with an electron removed from the  $d$  states leading to  $E(N_{d-1})$ . The screening effects on the interaction among the  $d$  electrons caused by the  $s$  and  $p$  electrons is included in these calculations since  $s$  and  $p$  electrons are still allowed to move and they will redistribute if the number of  $d$  electrons changes. It can be shown that the screened Coulomb interaction  $U$  is then given directly by

$$\begin{aligned} U &= E(N_{d+1}) + E(N_{d-1}) - 2E(N_d) \\ &\approx \epsilon_d(N_d + \frac{1}{2}) - \epsilon_d(N_d - \frac{1}{2}), \end{aligned} \tag{11.1}$$

where in the second step the constrained LDA eigenlevel  $\epsilon_d$  of the orbitals of the confined  $d$  electrons was inserted. The latter can be obtained from the relation

$\epsilon_d(N_d) = \frac{dE(N_d)}{dN_d}$  introduced by Slater [Sla74] and Janak [Jan78]. In a similar way the exchange interaction  $J$  and a double-counting correction term can be obtained from this ansatz.

Last but not least, the FLEX solver used in this thesis is limited to crystals with cubic symmetry. Naturally, one likes to extend its applicability to other crystal symmetries, possibly even surfaces, and fortunately there are no principal obstacles preventing this. Thus, it would only be a matter of programming work to overcome this shortcoming of the present scheme.

In the second part of this outlook I would like to present some ideas how the GGA+DMFT approach could be extended beyond the present scheme. My incentive is to pursue the idea of combining *ab initio* methods for realistic materials with a DMFT-like scheme to incorporate electronic correlation. A cornerstone of all schemes to be presented shall be the FLEX method employed in all cases as “the” DMFT solver to solve the DMFT impurity problem since it has been demonstrated in this work that FLEX is a powerful and efficient technique for the description of intermediately correlated electron systems.

A quite natural extension of the present GGA+DMFT approach seems to be the implementation of a full self-consistent GGA+DMFT scheme converging not only the DMFT calculations but also recalculating the DFT results. Within the DMFT part of the GGA+DMFT scheme a new electron density is obtained directly from the interacting lattice Green function. As this density usually differs from the DFT electron density, it is rather intuitive to also recalculate the DFT solution employing the new density. Furthermore, the changes in the density also affect the screened Coulomb interaction and it should therefore be recalculated as well e.g. within a constrained LDA calculation. Both steps then lead to a new many-body problem that is to be solved within DMFT and this scheme can be iterated until convergence is reached. For this work such a complete self-consistency scheme was not considered. Since the GGA description of Fe, Co and Ni is already close to the experimental results, the DMFT many-body corrections yield no fundamental changes to the DFT description and thus the effects of the changes in the electron distribution on the DFT description are thought to be negligible. Furthermore, the full self-consistency scheme is much more computationally expensive than the present approach. Savrasov and Kotliar introduced such a scheme in their calculations for Pu [SK04] albeit without self-consistency for the screened Coulomb interaction but most implementations of GGA+DMFT-like schemes so far do not employ the full self-consistency.

Non-local correlation plays an important role in the physics of correlated electron system such as high- $T_c$  superconductors or heavy-fermion metals. In general the FLEX method yields an energy and  $\mathbf{k}$ -dependent self-energy and it has already been successfully employed e.g. in calculations for the three-band model for  $\text{CuO}_2$  by Esirgen and Bickers [EB98] to describe superconductivity. Within the present GGA+DMFT approach all spatial fluctuations are frozen due to the single-site approximation employed in DMFT. Consequently, the self-energy becomes  $\mathbf{k}$  indepen-

dent. However, if the DMFT description is extended as suggested by Hettler *et al.* [HTZJ<sup>+</sup>98] using the so-called dynamical cluster approximation (DCA) the momentum conservation relinquished in DMFT can be systematically restored. In the DCA the self-energy is assumed to be only weakly momentum dependent so that it is well approximated on a coarse grid of cluster momentum points  $\mathbf{K}$ . The grid of momentum points is constructed by dividing the 1<sup>st</sup> BZ into  $N_c$  patches around certain points  $\mathbf{K}$  and the self-energy is assumed to be constant within each patch. The DCA contains the DMFT in the limiting case of  $N_c = 1$  and it becomes exact if  $N_c$  goes to infinity. Furthermore, the DCA preserves the translational symmetry, hence the bath couples to each site of the cluster in DCA. Despite the fact that Hettler *et al.* themselves considered this extension of DMFT to be “easily adapted to specific models and various existing exact and perturbative solution techniques for these models” [HTZJ<sup>+</sup>98] so far there exist only few applications of the DCA scheme. For example Hague *et al.* presented a combined scheme employing DCA to treat short-range correlation and the FLEX method to describe long-range correlation [HJS03]. I believe the DCA is an interesting scheme to reintroduce the momentum dependence into the many-particle description of the electron system.

Another extension of DMFT worth mentioning was already introduced in 1996 by Georges *et al.* [GKKR96]. This is the cluster DMFT treating not only one impurity site but a cluster of impurity sites in an averaged environment which has to be calculated self-consistently. This approach seems to be quite natural for the descriptions of materials with more than one atom per unit cell but it could also be interesting to employ it in the description of surface states. Since the number of nearest neighbors of surface atoms is reduced relative to the bulk coordination the nearest-neighbor sites yield a non-negligible contribution to the self-energy of such an atom in contrast to the situation in the bulk crystal where the neighboring contributions to the self-energy are rather small. In cluster DMFT only the spatial fluctuations between the atomic sites in the cluster are restored and the bath couples exclusively to the boundary sites of the cluster, thus translational symmetry is not preserved. Cluster extensions of DMFT have been applied successfully to a couple of model systems e.g. by Lichtenstein and Katsnelson [LK00] in calculations of the *d*-wave superconductivity in the two-dimensional Hubbard model. In the context of a GGA+DMFT-like scheme cluster extensions have been carried out by Poteryaev *et al.* [PLK04].

Finally I like to discuss a new approach designed to remove the deficiencies of the present GGA+DMFT scheme inherited by the underlying DFT description. The idea is to replace the initial DFT description by the *GW* approximation (GWA) and treat correlation effects in a combined *GW*+DMFT scheme as first proposed by Biermann *et al.* [BAG03]. The GWA is systematically derived from perturbation theory. The electrons in a solid are described as quasi-particles interacting via a screened potential that is connected to the self-energy  $\Sigma^{GW}$  obtained from the GWA. The self-energy obtained from the GWA has a similar form as in the Hartree-Fock approximation (HFA) but the Coulomb interaction in the GWA is dynamically

screened. This dynamical screening removes some of the major drawbacks of the HFA like the zero density of states at the Fermi level within metals. The resulting self-energy  $\Sigma^{GW}$  is non-local and energy-dependent. Due to the non-locality of  $\Sigma^{GW}$  long-range screening effects between all electronic states including  $s$  and  $p$  orbitals are naturally incorporated in the GWA yielding a more realistic description of the band structure of the  $s$  and  $p$  electrons than the LDA or GGA that incorporate correlation effects only locally via the exchange-correlation potential  $V_{xc}$  (see e.g. the works by Northrup *et al.* [NHL87, NHL89] and Surh *et al.* [SNL88], who studied quasi-particle spectra of various alkali metals). However, the GWA fails to describe intermediate or strong correlation effects between more localized electrons as was already pointed out in the introduction of this work. This drawback of the  $GW$  method can be removed when combining it with DMFT. The idea presented by Biermann *et al.* in [BAG03] is to take the non-local part of the self-energy from the GWA and the local part from the dynamical impurity model of DMFT. The FLEX solver being a perturbative approach just like the GWA could be applied quite naturally in this context to solve the DMFT impurity problem by simply adding the diagrams calculated in FLEX that are missing in the GWA and treat them locally in the single-site approximation of DMFT just like in the present GGA+DMFT approach. Such a new  $GW$ +DMFT approach does not only have the advantage to treat the  $s$  and  $p$  states in a more realistic manner than the GGA. Within this  $GW$ +DMFT approach the screened Coulomb interaction is also determined from first-principles calculations. As demonstrated by Aryasetiawan [AS06], the  $GW$ +DMFT approach can hence yield a true parameter-free description of the electronic system, in contrast to the presented GGA+DMFT approach that still depends on the Hubbard  $U$  and  $J$ . In practice DFT calculations are usually chosen as a starting point to construct the Green function for  $GW$  calculations. Thus, the problem of the double-counting correction still has to be solved. However, since the self-energy in the GWA is calculated for all electronic degrees of freedom the scheme for a double-counting correction suggested in chapter 10 by simply subtracting  $V_{xc}$  from  $\Sigma^{GW}$  is applicable here and the resulting  $GW$  description usually does not depend strongly on the choice of the starting point for many materials as demonstrated by Fleszar [Fle01]. (Note that for some materials where different starting points yield very different results for example nitride semiconductors that depend sensitively on the position of the semicore  $d$  states, the GWA will also yield different results as pointed out by Rinke *et al.* [RQN<sup>+</sup>05]. Thus the GWA is not entirely independent of the selected starting point.) Nevertheless, the self-energy corrections to the  $s$  and  $p$  states in GWA also remove some of the deficiencies of the DFT descriptions still present in the GGA+DMFT approach. Summarizing, the  $GW$ +DMFT scheme is an intriguing new approach with the potential to yield a most valuable contribution to the description of realistic intermediately and strongly correlated materials. The results of some first applications by Biermann *et al.* in [BAG03] are indeed very promising.



## 12 Acknowledgments - Danksagung

About two years ago I was sitting in a lecture about the theory of solid-state physics organized and held by Professor Stefan Blügel. After classes we started talking, I told Stefan Blügel about my growing interest in the theory of many-body physics and about my plan to spend half a year in Prague in the Czech Republic. Stefan Blügel in his usual enthusiastic manner told me about some of his colleagues in Prague working in the field of electronic correlation in solid-state physics applying some technique called FLEX. Although it all seemed very appealing to me, I actually had no clue what he was talking about. Nevertheless, I decided to go on this small journey from Aachen to Prague finally ending up in Jülich under the guidance of Professor Stefan Blügel. Now, two years later, I dare to say that thanks to Stefan Blügel I could gain some insight into this most exciting field of electronic correlations and that I could even contribute a small part to this most interesting field. I would like to thank Stefan Blügel for making all these things possible as well as for reviewing my diploma thesis. Furthermore, I would like to thank Dr. Erik Koch here as the second examiner of my work.

My journey would most probably have taken another course if I had not met Dr. Ilja Turek and Dr. Vaclav Drchal in Prague. I do not only want to thank Dr. Ilja Turek for the wonderful discussions on physics, that helped me to become acquainted with DFT and LMTO. I also want to thank him for so kindly inviting me into his working group which was not only a big help at the beginning of my stay in Prague but also a pleasure and enrichment during my whole time there. Dr. Vaclav Drchal not only is the developer of the FLEX code that I was kindly allowed to use in my thesis. In Prague and after my time there he was a mentor for me, who introduced me to the topic of many-body problems in solid state physics in his most considerate and thoughtful manner. I am very grateful for his patience in numerous discussions and for his critical evaluation of my work.

Back in Germany I met Dr. Arno Schindlmayr upon arriving in Jülich. Arno has become more than just a supervisor for me. His advice on topic not only of purely physical nature has grown more and more important to me during the last year; and I would certainly not have been able to write this thesis without his support. For all that I would like to thank Arno Schindlmayr here.

I am not going to list all the other dear colleagues of the Theory I institute of the IFF who helped me during the past year, to avoid forgetting someone. However, I would like to thank a few people personally who constantly supported me over the last couple of months: I would like to thank Dr. Gustav Bihlmayer, my office team

Swantje Heers, Andreas Dolfen and Manfred (Manni) Niesert and last but not least Ute Winkler who was always most supportive in all non-physical matters involved in a works like this.

Coming to an end I would like to thank my family and friends. You all have been most supportive over the last couple of months and I received positive feedback from all of you. For that I like to thank you all! My special thanks goes to you, Eva, for all the patience you had and all the understanding you gave me. Without you being there for me I would not have brought my work to this end. I like to say thank you and I really hope that I can be there for you as well when the time comes.

---

Vor gut zwei Jahren saß ich in der Vorlesung “Theoretische Festkörperphysik I” von und mit Professor Stefan Blügel. Nach den Vorlesungen kam man ins Gespräch, ich erzählte Stefan Blügel von meinem Interesse an der Festkörperphysik und meinen Plänen eine Weile nach Prag zu gehen. Stefan Blügel erzählte mir in seiner unverwechselbaren begeisternden Art von seinen Kontakten in Prag, die dort spannende Festkörperphysik mit der FLEX-Methode betrieben. Es hörte sich wirklich spannend an, aber ich hatte nicht die leiseste Ahnung, wovon er mir da eigentlich erzählte. Mitgerissen von seiner Begeisterung nahm ich dennoch dieses kleine Abenteuer Aachen-Prag-Jülich unter der immerwährenden Schirmherrschaft von Professor Stefan Blügel in Angriff. Heute, nach gut zwei Jahre wage ich zu behaupten, dass ich dank Stefan Blügel nun einen Einblick in diesen wirklich spannenden Bereich der Festkörperphysik gewonnen habe und selber einen kleinen Beitrag zu diesem Feld habe leisten können. Dafür und auch für seine Tätigkeit als Erstgutachter meiner Diplomarbeit möchte ich Stefan Blügel ganz herzliche danken. Des weiteren danke ich auch Dr. Erik Koch für seine kritischen und detaillierten Kommentare als Zweitgutachter.

Mein kleines Abenteuer in Prag wäre aber sicher ganz anders verlaufen, wenn ich dort nicht Dr. Ilja Turek und Dr. Vaclav Drchal kennengelernt hätte. Dr. Ilja Turek gilt mein Dank nicht nur für die Fachdiskussionen, in denen er mir DFT and LMTO näher brachte. Ilja Tureks offene Art, mich direkt und vorbehaltlos in seinen Arbeitskreis zu integrieren, hat mir den Start und so manch andere Stunde in Prag leichter gemacht. Dr. Vaclav Drchal ist nicht nur der Entwickler des FLEX-Programms, das ich in meiner Arbeit dankenswerter Weise verwenden durfte. Er war mir in Prag und noch darüber hinaus ein Mentor, der mir auf seine bedachte und stets wohlüberlegte Art die Vielteilchenphysik ein Stück näher gebracht hat. Für seine große Geduld und sein kritisches Urteil bin ich ihm sehr zu Dank verpflichtet.

Zurück in Deutschland traf ich dann in Jülich auf Dr. Arno Schindlmayr. Arno ist für mich mehr als nur ein Ansprechpartner geworden, denn er hat mir im Laufe

des vergangenen Jahres auch in einigen nicht allein physikalischen Problemstellungen immer mit gutem Rat beiseite gestanden. Aber ohne ihn hätte meine Arbeit nicht zu dem hier vorgelegten Ergebnis geführt und auch dafür bin ich Ihm sehr dankbar.

Die vielen Kollegen aus dem Institut Theorie 1 im IFF, die mir mit Rat und Tat beiseite gestanden haben, möchte ich nicht alle namentlich nennen, alleine um mir die Peinlichkeit zu ersparen, jemanden zu vergessen. Allerdings möchte ich gerne einigen Personen hier persönlich danken, die mir immer wieder im Laufe des vergangenen Jahres geholfen haben: Dr. Gustav Bihlmayer, der nicht nur immer eine offene Tür sondern auch ein offenes Ohr für alle meine Fragen hatte, mein Office-Team (You rule!) mit Swantje Heers, Andreas Dolfen und Manfred (Manni) Niesert - ihr habt nicht nur meine Launen ertragen, sondern mir bei so unzählig vielen kleinen und größeren Dingen weitergeholfen, dass ich nur hoffen kann, ihr bleibt mir noch eine Weile als Bürokollegen erhalten. Last but not least möchte ich auch Ute Winkler danken, bei der man nicht nur den besten Kaffee im Institut bekommt, sondern die als gute Seele des Instituts immer hilfsbereit zur Stelle war.

Zum Schluss gilt mein Dank meinen Freunden und meiner Familie. Ich habe in den vergangenen Monaten von allen Seiten Unterstützung und Verständnis erfahren. Für mich ist das keinesfalls selbstverständlich und ich weiß dies von jedem Einzelnen von Euch sehr zu schätzen. Dies gilt besonders für deine Unterstützung, liebe Eva, für deine große Geduld und dein fortwährendes Verständnis, aber auch für dein Interesse, dass mich weiter angespornt und motiviert hat. Ohne dich hätte ich die letzten Wochen und Monate nicht das leisten können, was ich erreicht habe. Ich hoffe, dass ich auch Dir einmal so sehr Stütze sein kann!



# Bibliography

- [AIG<sup>+</sup>04] F. Aryasetiawan, M. Imada, A. Georges, G. Kotliar, S. Biermann, and A. I. Lichtenstein.  
Frequency-Dependent local Interactions and low-energy effective Models from electronic Structure Calculations.  
*Phys. Rev. B*, **70**(19):195104, (2004).
- [And75] O. K. Andersen.  
Linear Methods in Band Theory.  
*Phys. Rev. B*, **12**:3060, (1975).
- [Ary92] F. Aryasetiawan.  
Self-Energy of ferromagnetic Nickel in the *GW* Approximation.  
*Phys. Rev. B*, **46**(20):13051–13064, (1992).
- [AS06] K. Jepsen O. Aryasetiawan, F. Karlsson and U. Schönberger.  
Calculations of Hubbard *U* from first-principles.  
*Phys. Rev. B*, **74**:125106, (2006).
- [Aug25] P. Auger.  
*J. Physique Radium*, **6**:205, (1925).
- [AZA91] V. I. Anisimov, J. Zaanen, and O. K. Andersen.  
Band Theory and Mott Insulators: Hubbard *U* instead of Stoner *I*.  
*Phys. Rev. B*, **44**(3):943–954, (1991).
- [BAB00] G. Bihlmayer, T. Asada, and S. Blügel.  
Electronic and magnetic Structure of the (001) Surfaces of V, Cr and V/Cr.  
*Phys. Rev. B*, **62**(18):R11937–R11940, (2000).
- [BAG03] S. Biermann, F. Aryasetiawan, and A. Georges.  
First-Principles Approach to the electronic Structure of strongly correlated Systems: Combining the *GW* Approximation and Dynamical Mean-Field Theory.  
*Phys. Rev. Lett.*, **90**(8):086402, (2003).
- [BB06] S. Blügel and G. Bihlmayer.  
*Computational Nanoscience: Do It Yourself!*  
NIC Series Volume 31. NIC-Directors, (2006).
- [BBF<sup>+</sup>88] M. N. Baibich, J. M. Broto, A. Fert, F. Nguyen Van Dau, F. Petroff, P. Eitenne, G. Creuzet, A. Friederich, and J. Chazelas.

- Giant Magnetoresistance of (001)Fe/(001)Cr magnetic Superlattices.  
*Phys. Rev. Lett.*, **61**(21):2472–2475, (1988).
- [BDC<sup>+</sup>04] S. Biermann, A. Dallmeyer, C. Carbone, W. Eberhardt, C. Pampuch, O. Rader, M. I. Katsnelson, and A. I. Lichtenstein.  
Observation of Hubbard Bands in  $\gamma$ -Manganese.  
*JETP Letters*, **80**:612–615, (2004).
- [BGSZ89] G. Binasch, P. Grünberg, F. Saurenbach, and W. Zinn.  
Enhanced Magnetoresistance in layered magnetic Structures with anti-ferromagnetic interlayer Exchange.  
*Phys. Rev. B*, **39**(7):4828–4830, (1989).
- [BNSF71] Y. U. Babanov, V. Ye. Naysh, O. B. Sokolov, and V. K. Finashkin.  
Electron-Electron Correlations in Metals. I.  
*Fiz. metal. metalloved.*, **32**(3):472–484, (1971).
- [BNSF73a] Y. U. Babanov, V. Ye. Naysh, O. B. Sokolov, and V. K. Finashkin.  
Electron-Electron Correlations in Metals. II.  
*Fiz. metal. metalloved.*, **35**(6):1123–1131, (1973).
- [BNSF73b] Y. U. Babanov, V. Ye. Naysh, O. B. Sokolov, and V. K. Finashkin.  
Electron-Electron Correlations in Metals. III.  
*Fiz. metal. metalloved.*, **35**(6):1132–1146, (1973).
- [BS89] N. E. Bickers and D. J. Scalapino.  
Conserving Approximations for strongly fluctuating Electron Systems.I.  
Formalism and Computational Approach.  
*Annals of Physics*, **193**:206–251, (1989).
- [CA80] D. M. Ceperley and B. J. Alder.  
Ground State of the Electron Gas by a Stochastic Method.  
*Phys. Rev. Lett.*, **45**(7):566–569, (1980).
- [Cha71] Chuan C. Chang.  
Auger Electron Spectroscopy.  
*Surf. Sci.*, **25**:53–79, (1971).
- [Cin76] M. Cini.  
Lifetimes of excited Electrons in Fe and Ni: First-Principle *GW* and the *T*-Matrix Theory.  
*Solid States Commun.*, **20**:605–607, (1976).
- [Cin79] M. Cini.  
Theory of Auger XVV Spectra of Solids: Many Body Effects in incompletely filled Bands.  
*Surf. Sci.*, **87**:483–500, (1979).
- [DC94] V Drchal and M. Cini.  
Screening and Correlation Effects in CVV Auger Spectra of Transition Metals.

- J. Phys.: Condens. Matter*, **6**:8549–8564, (1994).
- [DJcvK99] V. Drchal, V. Janiš, and J. Kudrnovský.  
Dynamical Electron Correlations in weakly interacting Systems: TB-LMTO Approach to Metals and random Alloys.  
*Phys. Rev. B*, **60**(23):15664–15673, (1999).
- [DK84] V. Drchal and V. Kudrnovský.  
The Auger Spectra of Metals: Effect of Electron Correlations in partially filled narrow Bands.  
*J. Phys. F.: Met. Phys.*, **14**:2443–2453, (1984).
- [EB98] G. Esirgen and N. E. Bickers.  
Fluctuation Exchange Analysis of Superconductivity in the Standard three-band  $CuO_2$  Model.  
*Phys. Rev. B*, **57**(9):5376–5393, (1998).
- [EHK78] D. E. Eastman, F. J. Himpsel, and J. A. Knapp.  
Experimental Band Structure and Temperature-Dependent magnetic Exchange Splitting of Nickel using angle-resolved Photo-emission.  
*Phys. Rev. Lett.*, **40**(23):1514–1517, (1978).
- [EJW<sup>+</sup>79] D. E. Eastman, J. F. Janak, A. R. Williams, R. V. Coleman, and G. Wendin.  
Electronic Structure of magnetic 3d Metals: Ground State, Fermi Surface and Photo-emission Properties.  
*J. Appl. Phys.*, **50**(11):7423–7438, (1979).
- [EP80] W. Eberhardt and E. W. Plummer.  
Angle-resolved Photo-emission Determination of the Band Structure and multielectron Excitations in Ni.  
*Phys. Rev. B*, **21**(8):3245–3255, (1980).
- [Fle01] A. Fleszar.  
LDA,  $GW$ , and Exact-Exchange Kohn-Sham scheme Calculations of the electronic Structure of  $sp$  semiconductors.  
*Phys. Rev. B*, **64**(24):245204, (2001).
- [FSBK06] C. Friedrich, A. Schindlmayr, S. Blügel, and T. Kotani.  
Elimination of the Linearization Error in  $GW$  Calculations based on the linearized Augmented-Plane-Wave Method.  
*Phys. Rev. B*, **74**(4):045104, (2006).
- [FW71] Alexander L. Fetter and John Dirk Walecka.  
*Quantum Theory of Many-Particle Systems*.  
McGraw-Hill, (1971).
- [GAJZ89] O. Gunnarsson, O. K. Andersen, O. Jepsen, and J. Zaanen.  
Density-Functional Calculation of the Parameters in the Anderson Model: Application to Mn in CdTe.  
*Phys. Rev. B*, **39**(3):1708–1722, (1989).

- [GDMK<sup>+</sup>06] A. Grechnev, I. Di Marco, M. I. Katsnelson, A. I. Lichtenstein, J. Wills, and O. Eriksson.  
Theory of Quasi-Particle Spectra for Fe, Co and Ni: Bulk and Surface.  
*Preprint: cond-mat/0610621*, (2006).
- [GK92] A. Georges and G. Kotliar.  
Hubbard Model in infinite Dimensions.  
*Phys. Rev. B*, **45**(12):6479–6483, (1992).
- [GKKR96] A. Georges, G. Kotliar, W. Krauth, and M. J. Rozenberg.  
Dynamical Mean-Field Theory of strongly correlated Fermion Systems  
and the limit of infinite Dimensions.  
*Rev. Mod. Phys.*, **68**(1):13, (1996).
- [HGH76] H. Höchst, A. Goldmann, and S. Hüfner.  
X-Ray Photo-Electron Emission from Iron Metal.  
*Z. Phys. B.*, **24**:245–250, (1976).
- [HJS03] J. P. Hague, M. Jarrell, and T. C. Schulthess.  
A novel FLEX supplemented QMC Approach to the Hubbard Model.  
*Preprint: cond-mat/0312155*, (2003).
- [HK64] P. Hohenberg and W. Kohn.  
Inhomogeneous Electron Gas.  
*Phys. Rev.*, **136**(3B):B864–B871, (1964).
- [HKE79] F. J. Himpsel, J. A. Knapp, and D. E. Eastman.  
Experimental Energy-Band Dispersions and Exchange Splitting for Ni.  
*Phys. Rev. B*, **19**(6):2919–2927, (1979).
- [HNK<sup>+</sup>06] K. Held, I. A. Nekrasov, G. Keller, V. Eyert, N. Blümer, A. K. McMa-  
han, R. T. Scalettar, Th. Pruschke, V. I. Anisimov, and D. Voll-  
hardt.  
Realistic Investigations of correlated Electron Systems with LDA +  
DMFT.  
*Phys. Stat. Sol. (b)*, **11**:2599–2631, (2006).
- [HTZJ<sup>+</sup>98] M. H. Hettler, A. N. Tahvildar-Zadeh, M. Jarrell, T. Pruschke, and  
H. R. Krishnamurthy.  
Nonlocal dynamical Correlations of strongly interacting Electron Sys-  
tems.  
*Phys. Rev. B*, **58**(12):R7475–R7479, (1998).
- [Hub63] J. Hubbard.  
Electron Correlations in narrow Energy Bands.  
*Proc. Roy. Soc*, **276**(1365):238–257, (1963).
- [Hub64a] J. Hubbard.  
Electron Correlations in narrow Energy Bands. II. The Degenerate  
Band Case.  
*Proc. Roy. Soc*, **277**(1369):237–259, (1964).

- [Hub64b] J. Hubbard.  
Electron Correlations in narrow Energy Bands. III. An Improved Solution.  
*Proc. Roy. Soc.*, **281**(1386):401–419, (1964).
- [Jan78] J. F. Janak.  
Proof that  $\frac{\partial E}{\partial n_i} = \epsilon$  in Density-Functional Theory.  
*Phys. Rev. B*, **18**(12):7165–7168, (1978).
- [Jul75] M. Julliere.  
Tunneling between Ferromagnetic Films.  
*Phys. Lett.*, **54A**:225–226, (1975).
- [KA75] D. D. Koellind and G. O. Arbman.  
Use of Energy Derivative of the Radial Solution in an Augmented-Plane-Wave Method: Application to Copper.  
*J. Phys. F (Metal Phys.)*, **5**:2041, (1975).
- [KL99] M. I. Katsnelson and A. I. Lichtenstein.  
LDA++ Approach to the Electronic Structure of Magnets: Correlation Effects in Iron.  
*J. Phys.: Condens. Matter*, **11**:1037–1048, (1999).
- [KMTM66] W. C. Koehler, R. M. Moon, A. L. Trego, and A. R. Mackintosh.  
Antiferromagnetism in Chromium Alloys. I. Neutron Diffraction.  
*Phys. Rev.*, **151**(2):405–413, (1966).
- [KRLS85] L. E. Klebanoff, S. W. Robey, G. Liu, and D. A. Shirley.  
Investigation of the near-surface electronic Structure of Cr(001).  
*Phys. Rev. B*, **31**(10):6379–6394, (1985).
- [KS65] W. Kohn and L. J. Sham.  
Self-Consistent Equations Including Exchange and Correlation Effects.  
*Phys. Rev.*, **140**(4A):A1133–A1138, (1965).
- [LK98] A. I. Lichtenstein and M. I. Katsnelson.  
Ab initio Calculations of Quasi-Particle Band Structure in correlated Systems: LDA++ Approach.  
*Phys. Rev. B*, **57**(12):6884–6895, (1998).
- [LK00] A. I. Lichtenstein and M. I. Katsnelson.  
Antiferromagnetism and d-wave Superconductivity in Cuprates: A Cluster dynamical Mean-Field Theory.  
*Phys. Rev. B*, **62**(14):R9283–R9286, (2000).
- [LKK01] A. I. Lichtenstein, M. I. Katsnelson, and G. Kotliar.  
Finite-Temperature Magnetism of Transition Metals: An ab initio Dynamical Mean-Field Theory.  
*Phys. Rev. Lett.*, **87**(6):067205, (2001).
- [LP80] D. C. Langreth and J. P. Perdew.

- Theory of nonuniform electronic Systems. I. Analysis of the Gradient Approximation and a Generalization that Works.  
*Phys. Rev. B*, **21**(12):5469–5493, (1980).
- [LW68] E. H. Lieb and F. Y. Wu.  
Absence of Mott Transition in an exact Solution of the short-range, One-Band Model in one Dimension.  
*Phys. Rev. Lett.*, **20**:1445–1448, (1968).
- [Mar67] P. M. Marcus.  
Variational Methods in the Computation of Energy Bands.  
*Int. J. Quantum Chem. Suppl.*, **1**:567, (1967).
- [Mat67] Richard D. Mattuck.  
*A Guide to Feynman Diagrams in the Many-Body Problem*.  
European physics series. McGraw-Hill Pub. Co, (1967).
- [MKWM95] J. S. Moodera, Lisa R. Kinder, Terrilyn M. Wong, and R. Meservey.  
Large Magnetoresistance at Room Temperature in ferromagnetic thin Film Tunnel Junctions.  
*Phys. Rev. Lett.*, **74**(16):3273–3276, (1995).
- [MMS88] A. K. McMahan, R. M. Martin, and S. Satpathy.  
Calculated effective Hamiltonian for  $La_2CuO_4$  and Solution in the Impurity Anderson Approximation.  
*Phys. Rev. B*, **38**(10):6650–6666, (1988).
- [MNJ84] N. Mårtensson, R. Nyholm, and B. Johansson.  
Four-Hole Satellites in the  $L_3VV$  Auger and the Valence-Band Spectra from Nickel.  
*Phys. Rev. B*, **30**(4):2245–2248, (1984).
- [MV89] W. Metzner and D. Vollhardt.  
Correlated Lattice Fermions in  $d = \infty$  Dimensions.  
*Phys. Rev. Lett.*, **62**:324–327, (1989).
- [NHL87] J. E. Northrup, M. S. Hybertsen, and S. G. Louie.  
Theory of Quasi-Particle Energies in Alkali Metals.  
*Phys. Rev. Lett.*, **59**(7):819–822, (1987).
- [NHL89] J. E. Northrup, M. S. Hybertsen, and S. G. Louie.  
Quasi-Particle Excitation Spectrum for nearly-free-electron Metals.  
*Phys. Rev. B*, **39**(12):8198–8208, (1989).
- [Ohk91] F. J. Ohkawa.  
Electronic Correlation in the Hubbard Model in  $d = \infty$  Dimension.  
*J. Phys. Soc. Jpn.*, **17**:3218–3221, (1991).
- [Ohk92] F. J. Ohkawa.  
Electron Correlation in the Periodic Anderson Model in  $d = \infty$  Dimensions.

- Phys. Rev. B*, **46**:9016–9026, (1992).
- [PBE96] J. P. Perdew, K. Burke, and M. Ernzerhof.  
Generalized Gradient Approximation made simple.  
*Phys. Rev. Lett.*, **77**(18):3865–3868, (1996).
- [Per85] J. P. Perdew.  
Accurate Density Functional for the Energy: Real-Space Cutoff of the  
Gradient Expansion for the Exchange Hole.  
*Phys. Rev. Lett.*, **55**(16):1665–1668, (1985).
- [PKL<sup>+</sup>06] L. V. Pourovskii, M. I. Katsnelson, A. I. Lichtenstein, L. Havela,  
T. Gouder, F. Wastin, V. Shick, A. B. Drchal, and G. H. Lander.  
Nature of non-magnetic strongly-correlated States in  $\delta$ -Plutonium.  
*Europhys. Lett.*, **74**:479–485, (2006).
- [PLK04] A. I. Poteryaev, A. I. Lichtenstein, and G. Kotliar.  
Nonlocal Coulomb Interactions and Metal-Insulator Transition in  
 $Ti_2O_3$ : A Cluster LDA+DMFT Approach.  
*Phys. Rev. Lett.*, **93**(8):086401, (2004).
- [PR72] M. M. Pant and A. K. Rajagopal.  
Theory of inhomogeneous magnetic Electron Gas.  
*Solid State Commun.*, **10**:1157–1160, (1972).
- [PW92] J. P. Perdew and Y. Wang.  
Accurate and simple analytic Representation of the Electron-Gas Cor-  
relation Energy.  
*Phys. Rev. B*, **45**(23):13244–13249, (1992).
- [PZ81] J. P. Perdew and A. Zunger.  
Self-Interaction Correction to Density-Functional Approximations for  
Many-Electron Systems.  
*Phys. Rev. B*, **23**(10):5048–5079, (1981).
- [RQN<sup>+</sup>05] P. Rinke, A. Qteish, J. Neugebauer, C. Freysoldt, and M. Scheffler.  
Combining *GW* Calculations with Exact-Exchange Density-Functional  
Theory: An Analysis of Valence-Band Photo-emission for Com-  
pound Semiconductors.  
*New J. Phys.*, **7**(126), (2005).
- [SA92] D. J. Singh and J. Ashkenazi.  
Magnetism with Generalized-Gradient-Approximation Density Func-  
tionals.  
*Phys. Rev. B*, **46**(18):11570–11577, (1992).
- [SAK98] M. Springer, F. Aryasetiawan, and K. Karlsson.  
First-Principles *T*-Matrix Theory with Application to the 6 eV Satellite  
in Ni.  
*Phys. Rev. Lett.*, **80**(11):2389–2392, 1998.

- [SAS92] M. M. Steiner, R. C. Albers, and L. J. Sham.  
Quasi-Particle Properties of Fe, Co, and Ni.  
*Phys. Rev. B*, **45**(23):13272–13284, (1992).
- [Saw77] G. A. Sawatzky.  
Quasiatomic Auger Spectra in narrow-band Metals.  
*Phys. Rev. Lett.*, **39**(8):504–507, (1977).
- [SDA94] I. V. Solovyev, P. H. Dederichs, and V. I. Anisimov.  
Corrected atomic Limit in the Local-Density Approximation and the  
electronic Structure of *d* Impurities in Rb.  
*Phys. Rev. B*, **50**(23):16861–16871, (1994).
- [Sin94] David J. Singh.  
*Plane Waves, Pseudopotentials and the LAPW Method*.  
Kluwer Academic Publ., (1994).
- [SK96] S. K. See and L.E. Klebanoff.  
Spin-resolved Density of States of 3*d* Metals.  
*J. Appl. Phys.*, **79**:4796–4798, (1996).
- [SK04] S. Y. Savrasov and G. Kotliar.  
Spectral Density Functionals for electronic Structure Calculations.  
*Phys. Rev. B*, **69**:245101–1–245101–24, (2004).
- [SKO<sup>+</sup>88] Y. Sakisaka, T. Komeda, M. Onchi, H. Kato, S. Suzuki, K. Edamoto,  
and Y. Aiura.  
Angle-resolved Photo-emission from Cr(110): Observation of a Bulk  
magnetic Phase Transition.  
*Phys. Rev. B*, **38**(2):1131–1138, (1988).
- [Skr81] H. L. Skriver.  
The electronic Structure of antiferromagnetic Chromium.  
*J. Phys. F.: Metal Phys.*, **11**:97–111, (1981).
- [Sla37] J. C. Slater.  
Wave Functions in a Periodic Potential.  
*Phys. Rev.*, **51**:151, (1937).
- [Sla74] J. C. Slater.  
*The Self-Consistent Field for Molecules and Solids*, volume 4 of *Quantum Theory of Molecules and Solids*.  
McGraw-Hill Pub. Co, (1974).
- [SNL88] M. P. Surh, J. E. Northrup, and S. G. Louie.  
Occupied Quasi-Particle Bandwidth of Potassium.  
*Phys. Rev. B*, **38**(9):5976–5980, (1988).
- [ST62] G. Shirane and W. J. Tahei.  
Neutron-Diffraction of Chromium single Crystals.  
*J. Phys. Soc. Japan Suppl.*, **17**(BIII 35-8), (1962).

- [SW53] C. G. Shull and M. K. Wilkinson.  
Neutron Diffraction Studies of Various Transition Elements.  
*Rev. Mod. Phys.*, **25**(1):100–107, (1953).
- [Thu96] S.M. Thurgate.  
Auger Photo-Electron Coincidence Experiments from Solids.  
*J. Electron Spectroscop. Rel. Phenom.*, **81**:1–31, (1996).
- [vBH72] U. von von Barth and L. Hedin.  
A local Exchange-Correlation Potential for the Spin-Polarized Case.I.  
*J. Phys. C: Solid State Phys*, **5**:1629–1642, (1972).
- [Wij86] H. P. J. Wijn, editor.  
*3d, 4d and 5d Elements, Alloys and Compounds*, volume **19a** of  
*Landolt-Börnstein - Group III Condensed Matter*.  
Springer-Verlag, (1986).
- [ZCE04] V.P. Zhukov, E. V. Chulkov, and P.M. Echenique.  
Lifetimes of excited Electrons in Fe and Ni: First-Principle *GW* and  
the *T*-Matrix Theory.  
*Phys. Rev. Lett.*, **93**, (2004).